THE UNIVERSITY OF
WARWICK

University of Warwick institutional repository: http://go.warwick.ac.uk/wrap

A Thesis Submitted for the Degree of PhD at the University of Warwick

http://go.warwick.ac.uk/wrap/67159

This thesis is made available online and is protected by original copyright.

Please scroll down to view the document itself.

Please refer to the repository record for this item for information to help you to cite it. Our policy information is available from the repository home page.

New Oxides for Catalysis from Hydrothermal Synthesis

by

Craig Ian Hiley

Thesis submitted for the degree of

Doctor of Philosophy in Chemistry

Department of Chemistry, University of Warwick

September 2014

Table of Contents

2. Experimental

5. Redox Properties of Doped Cerium Oxides

6. Hydrothermal Synthesis and Characterisation of New Ruthenium(V) Oxides

Appendix

Acknowledgements

Firstly I would like to extend my sincerest thanks to Professor Richard Walton. It has been a marvellous privilege to be a member of his group for the last five years. His endless guidance, encouragement, curiosity, patience and humour have made this thesis possible. He has, without doubt, been a super-visor.

I would like to thank Janet Fisher and David Thompsett for their supervision and valuable input. Trips to Johnson Matthey Technology Centre were infinitely more productive and enjoyable than they would have been without Janet's help, perpetual optimism and attention to detail. I am grateful to several other people at Johnson Matthey, particularly Noelia Cortes-Felix for help with TPR and OSC measurements and several informative conversations.

The rest of the Walton group, past and present, have all proven to be a constant source of help. Helen Playford's instruction in the use of GSAS; her help with several elements of crystallography, magnetometry and general 'organised-ness' have been invaluable. Luke Daniels needs to be sincerely thanked for the collection of gargantuan amounts of TGA data and help with assorted data collection. I thank Hilni Harunsani for kindly collecting Raman spectra of some of my samples. I have been accompanied by pretty much every member of the group at some time or another on experiments at ISIS or Diamond, and I would like to thank them all for help with data collection at these facilities (and, during the night shift on B18, insight into how sleep deprivation affects sanity).

I thank Martin Lees for help in collecting and interpreting magnetic susceptibility and heat capacity data reported in this thesis. Reza Jalilikashtiban is thanked for providing all the TEM images presented herein. I thank Stefano Agrestini for his

hard work in providing an initial model for the magnetic structure of $SrRu_2O_6$. The instrument scientists Silvia Ramos, Giannantonio Cibin, Andrew Dent, Diego Gianolio and Stephen Parry have all provided expertise that made the many XAFS experiments on B18 possible. I am immensely grateful to Ron Smith for collection of powder neutron diffraction data through the Gem Xpress data collection service he runs. I am also grateful to Chiu Tang, Alex Hannon, Pascal Manuel, Dmitry Khalyavin and Matt Tucker for help with data collection and analysis at Diamond and ISIS.

Last, but by no means the least, I would like to thank Rosanna for her support, endless cups of tea and continual distraction over the last few months.

Declaration

This thesis is submitted to the University of Warwick in support of my application for the degree of Doctor of Philosophy. It has been composed by myself and has not been submitted in any previous application for any degree.

The work presented (including data generated and data analysis) was carried out by the author except in the case outlined below:

Pd K-edge and Pt L_{III}-edge EXAFS analysis results presented in Chapter 4 were provided by Richard Walton.

Parts of this thesis have been published by the author:

"Ruthenium(V) Oxides from Low-Temperature Hydrothermal Synthesis", Hiley, C. I.; Lees, M. R.; Fisher, J. M.; Thompsett, D.; Agrestini, S.; Smith, R. I.; Walton, R. I. *Angew. Chem. Int. Ed.* **2014**, *53*, 4423.

The following publication contains data collected in part by the author:

"Water-Splitting Electrocatalysis in Acid Conditions Using Ruthenate-Iridate Pyrochlores", Sardar, K.; Petrucco, E.; Hiley, C. I.; Sharman, J. D. B.; Wells, P. P.; Russell, A. E.; Kashtiban, R. J.; Sloan, J.; Walton, R. I. *Angew. Chem. Int. Ed.* **2014**, *53*, 10960.

Abstract

In this thesis the one-pot subcritical hydrothermal synthesis of several novel complex oxides with potential applications in catalysis is reported.

The hydrothermal synthesis of nanocrystalline pentavalent ion-substituted cerium dioxide is reported. The materials were all characterised by powder diffraction and a range of spectroscopic techniques in order to elucidate their structures. Up to approximately 30% pentavalent ion-substitution the mixed metal oxides continue to adopt the fluorite unit cell, and the lattice parameter decreases as substitution increases. The choice of mineraliser in the hydrothermal reaction was found to affect the composition and structure of the oxide: when prepared in NaOH, Na is incorporated into the structure as well as the pentavalent ion, and the combination of these allows charge balance to be achieved without the need for Ce reduction or the incorporation of interstitial oxygen. The inclusion of Na greatly improves both the measured oxygen storage capacity and the stability of the fluorite phases, as measured by *in situ* powder X-ray diffraction.

Precious metals Pt and Pd have also been successfully incorporated into the fluorite ceria structure by hydrothermal synthesis, with up to 20 – 25% precious metal substitution. A study of both the average structure and local environment of the precious metals leads to the conclusion that neither precious metal sits on the same crystallographic site as the Ce. Pd adopts a square-planar geometry by shifting ¼ of a unit cell in one direction, to sit in an oxide plane, and thereby expanding the unit cell. The Pt exists a distorted octahedral environment. These oxides were found to be inherently unstable, with precious metal extruded from the fluorite under even mildly reducing conditions.

The hydrothermal reaction of $KRuO_4$ with AO_2 (*A* = Ca, Sr, Ba) peroxides at 200 °C yields a range of previously unreported ruthenium oxides. $Ca_{1.5}Ru_2O_7$, an *A*-site deficient pyrochlore containing a mixed Ru(V/VI) *B*-site. $SrRu_2O_6$ adopts the $PbSb_2O_6$ structure and contains antiferromagnetically ordered Ru(V) moments. *In situ* powder neutron diffraction shows that this ordering persists up to 563 K, an extraordinarily high temperature. $Ba_2Ru_3O_9(OH)$ is an example of a new structure type, which is made up of puckered layers of quasi-trimeric edge-sharing $Ru^{(V)}O_6$ octahedra which are corner-linked together with layers of Ba atoms separating them. $Ba_4Ru_3O_{12}$ is an 8H hexagonal perovskite with a previously unreported stacking order, containing Ru with an average oxidation state of +5.33. Structural refinements and magnetometry of all new materials are presented.

Chapter 1: Introduction

1.1 Functional Metal Oxides

1.1.1 Properties and Uses

Metal oxides exhibit a wealth of properties that make them crucial in every aspect of modern life. Their durability and wide-ranging, vivid colours meant they were first used as pigments and dyes at least eight thousand years ago,[1] an important application to this day.[2] Metal oxides became particularly important in the 20th Century, finding uses as components in electronic devices with widespread applications in areas ranging from medicine to communications;[3,4] heterogeneous catalysts;[5] solar cell components;[6] Li-ion battery materials[7,8] and solid oxide fuel cell electrolytes.[8,9] Whilst binary oxides (*i.e.* compounds containing only one metal and oxygen such as TiO_2 or Fe_2O_3) have extensive applications, complex oxides (compounds containing more than one metal and oxygen) are increasingly being looked to for new functionalities.[10] Novel properties of complex metal oxides such as high-temperature superconductivity[11] and multiferroicity[12] continue to be discovered and exploited.[13]

Structurally, complex metal oxides can be classified into two groups. Firstly, there are those where the metals are on distinct crystallographic sites, such as the perovskite structure, with ABO_3 stoichiometry (where A and B are electropositive elements). Secondly, there are solid solutions and doped metal oxides, where metal sites have a random mixture of metals such as the rutile solid solution $Sn_xTi_{1-x}O_2$ ($0.0 \leq x \leq 0.1$).[14]

The wide range of synthetic routes available for the formation of oxides means that they exhibit can a range of morphologies from large, single crystals[15] and thin

films;[16] to nanostructures[17,18] such as nanowires;[19] to nano- and mesoporous oxides.[20] For many applications the crystal morphology adopted by an oxide is just as important as its atomic structure. For example, whilst an oxide thin film might be desirable for an electronic device[21] or solar cell[22] it would clearly be inappropriate for heterogeneous catalysis, where one of the most important features is a high surface area in order the maximise the solid-fluid interface.[23]

1.1.2 Preparative Techniques

The selection of available synthesis routes of metal oxides is just as broad as their uses. They can crudely be separated into solid-state, solution and gas-deposition methods.[24] Solid-state synthesis (such as the ceramic method) typically needs high temperatures in order to allow ion migration over distances on the scale of microns.[25] Gas deposition techniques (almost exclusively chemical vapour deposition, CVD) lend themselves to preparation of thin films.[4] Typically, volatile metal complexes such as acetylacetonates are mixed and evaporated. The metal oxide product is made directly onto a substrate film. Solution-based methods[26] (principally sol-gel and solvothermal methods) have come to prominence in recent years thanks to the versatile range of reaction conditions and reagents available, and the potential for controlling crystal morphology. Precursors, normally soluble metal salts, are dissolved in a solvent to give atomic level mixing of the metals. The product is then crystallised from solution either by solvent evaporation or the application of heat or a mineraliser. Sometimes a subsequent firing step is needed in order to drive off volatile by-products and to induce higher crystallinity. However, the extreme temperatures used in solid-state methods to promote ion diffusion are not normally necessary since the coprecipitation of metal precursors means that mixing is already complete. This presents two major advantages of solution-based synthesis over solid-

state synthetic procedures: metastable products that are not stable at high temperatures can be isolated; and there is a great deal of scope for particle size control by modifying the both the solution conditions and the reaction temperature.

Some of the more common metal oxide synthetic techniques are described in more detail below. Whilst there is an emphasis on synthesis of ternary and higher order metal oxides, all of the techniques can be extended to binary oxides.

1.1.2.1 The Ceramic Method

By far the oldest and most widespread method of metal oxide synthesis is the ceramic method. Reagents (typically metals, metal oxides or carbonates) are ground together in order to achieve an intimate mixture, which is then heated to temperatures of up to 3000 °C.[27] The reaction progresses by ion diffusion through the solids at the interface between reagents meaning that for complex oxides several grinding/heating cycles are often necessary in order to achieve a phase pure product.

This technique has the benefit of simplicity: the metal ratio of the final product will almost certainly be the same as the ratio in the starting materials and products are often very crystalline; both of which make identification of products often very simple. The environment the reaction takes place in can be easily modified by this method. A tube furnace allows the reagents to be exposed to flows of reactive (or inert) gases to further control the outcome of the reaction. For example V_2O_5 can be reduced to V_2O_3 by a flow of H_2 at 1000 °C.[28]

However this method has significant drawbacks. Only the most thermodynamically stable products will be obtained by this route due to the extreme temperatures utilised. Ceramic techniques have very little scope for controlling the particle morphology. Furthermore, the large crystals formed have comparatively low surface

areas, making them unsuitable for many applications. For doped materials and solid solutions this approach can lead to local inhomogeneity and concentration gradients, which can be difficult to characterise.

1.1.2.2 Molten Salt Fluxes

Molten salt fluxes can be considered an intermediate between solid-state and solution techniques.[29] Reagents are ground together with an excess of a simple metal salt (such as an alkali halide or hydroxide) with a relatively low melting point, typically within the temperature range 200 – 1500 °C. The mixture is then heated to a temperature above the salt's melting point to give a flux. The flux can be a mixture of salts to give a eutectic system, whereby the melting point of this mixture is lower than the melting point of either individual salt. For example, NaOH and KOH have melting points of 323 °C and 360 °C, respectively, whilst their eutectic has the considerably lower melting point of 165 °C.[30] The molten salt can be considered a solvent for reagent ions which significantly lowers the temperature at which ions can diffuse and thereby react.[31] The flux itself often doubles as a reagent, leading to incorporation of ions from it into the final product.

There are several advantages of using a molten salt flux. The ability to modify various parameters such the salt(s) used as the flux; the temperature reached and the cooling rate gives a great deal of control of the particle morphology.[32] The considerably lower temperatures used (compared to ceramic techniques) allow metastable products to be isolated.[29] The electropositivity of the flux also means that metals in their higher oxidation states can be stabilised, which has been exploited to great effect for synthesis of intricate complex oxides containing 4*d* and 5*d* transition metals in high oxidation states, such as Ir(VI),[32-34] and early-series actinides (Th, U and Np) in oxidation states ranging from III to VI.[35]

1.1.2.3 Sol-Gel Methods

Although technically a *sol-gel process* should only refer to procedures in which a *sol* (a colloidal suspension of small particles dispersed in a liquid phase) becomes a *gel* (a three dimensional solid network spread throughout a liquid medium), it has become a more general term for a synthesis of inorganic solids precipitated from solution.[36]

Historically, the sol was prepared by hydrolysis of a metal alkoxide or other organic precursor, and the gel is formed by the condensation of this sol. This gel is an amorphous 3-D network of metal ions bridged by anionic (O^{2-} or OH^{-}) linkers. The solvent is then removed from the gel by either evaporation or by supercritical solvent extraction. The final stage is sintering, where the gel or dried gel is heated to temperatures from 300 °C to 1000 °C. The organic component is driven off and crystallinity is induced, giving the final product.[25,29,37] There is significant scope for control of particle size and morphology by this method. A wealth of parameters such as precursor concentration, the organic chelating agent and the hydrolysis rate (which can be controlled by the acid or base catalyst) all have a profound effect on the gel formed. The method of solvent extraction can create either well dispersed or heavily agglomerated particles,[26] and much of this structure remains intact after firing.

Significant deviations from the perfect scheme exist. For instance, condensation often forms a dense precipitate, rather than a gel, which can be filtered from solution and dried. Synthetic procedures without a firing step can be used to yield a nanoparticulate or amorphous product. The Pechini method is a specific modification for synthesising thin films and nanocrystalline powders whereby the network consists of metals connected by polymerised chelating agents, rather than by short

M – O – M bonds. The firing step brings about pyrolysis of the organic ligands. This causes rapid nucleation and nanocrystalline products.[38,39]

1.1.2. Hydrothermal and Solvothermal Synthesis

Rabenau defined *hydrothermal synthesis* as a reaction carried out in an aqueous medium, in a sealed container above 100 °C (*i.e.* above the boiling point of water).[40] This creates an autogeneous pressure – a pressure generated internally by the vapour pressure of the water, as opposed to an externally applied pressure. Hydrothermal synthesis takes its name from geological processes responsible for the formation of many minerals which take place under similar conditions.[41] It was first demonstrated as a synthetic technique in the 19th Century to make microcrystalline quartz. More recently it is one of the only industrially viable methods for production of chromium(IV) oxide, a magnetic oxide used in tape cassettes in the second half of the 20th Century,[42] and porous materials such as zeolites.[43]

In an idealised hydrothermal reaction completely soluble reagents are dissolved in water in order to achieve atomic-scale mixing. The solution is then sealed in an autoclave and heated to a temperature above 100 °C (though reactions above the critical temperature – ~374 °C – are less common). Solid products crystallise from solution, which can then simply be filtered off. In reality however, the reactions are much more complex. Reagents are often practically insoluble at room temperature, though under hydrothermal conditions they are often much more soluble.[44] Furthermore mineralisers (such as pH modifiers) sometimes must be added to reactions to increase reagent solubility or to induce crystallisation of the product.

There is no requirement for the solvent to be water, and *solvothermal synthesis* is a general term for any reaction that takes place in a sealed container above the boiling

point of the solvent.[45] This has several applications. It is useful for making anhydrous products, or where the precursors (or, of course, products) are unstable in water. The solvent can be selected to give optimal solubility of the reagents, and in many cases the solvent can take part in the reaction.[46]

Above the supercritical temperature of the solvent, there is no longer a distinction between liquid and gas and only one continuous phase exists. The properties of supercritical fluids, such as dielectric constant and density, can be tuned as a function of temperature and pressure, which in turn gives excellent control of particle size and the phase of the product obtained.[47] However, under solvothermal conditions, pressure no longer obeys the ideal gas law and can increase rapidly as a function of temperature and container fill fraction, particularly beyond the solvent's critical temperature.[40,48] This means more robust autoclaves are necessary in order to carry out these reactions, and industrial scale reactions are problematic. Far more common are subcritical solvothermal reactions, where solvents' properties such as viscosity can still differ greatly compared to ambient conditions,[45] and which can be carried out using commercially available autoclaves. Lower temperatures are also less energy intensive, which further serves to make them of interest for large scale applications.

Unlike sol-gel and other solution based routes, solvothermal synthesis often yields crystalline products without need of post-synthetic annealing. This makes it the ideal route to preparing metastable products and a key tool in exploration of the so-called 'energy landscape' of materials,[49,50] a multi-dimensional Gibbs energy surface for a given composition. A wide range of variables available in solvothermal synthesis such as reaction time,[51] solvent,[52] temperature[53] and pH[54] have profound implications for the structure and morphology of products. Surfactants can be used to yield novel

crystal morphologies.[55] Microwave-heated hydrothermal synthesis has been shown to distribute heat evenly through the reaction creating highly uniform nanoparticles.[56,57]

This thesis will focus on new synthesis methods for oxides of cerium and ruthenium and the following sections will review their crystal chemistry and the synthesis routes to such materials.

1.2 Cerium (IV) Oxide

1.2.1 Cerium Dioxide

Cerium dioxide, also known as ceria, adopts the fluorite (named after the structure adopted by CaF_2) structure, space group $Fm\bar{3}m$ (Figure 1. 1a). It is a cubic close-packed type arrangement of eight-coordinate cerium atoms with oxygen filling the tetrahedral holes between them (Figure 1. 1).[5] Its pale yellow colour has been ascribed to $O^{2-} \leftarrow Ce^{4+}$ charge transfer.[58,59]

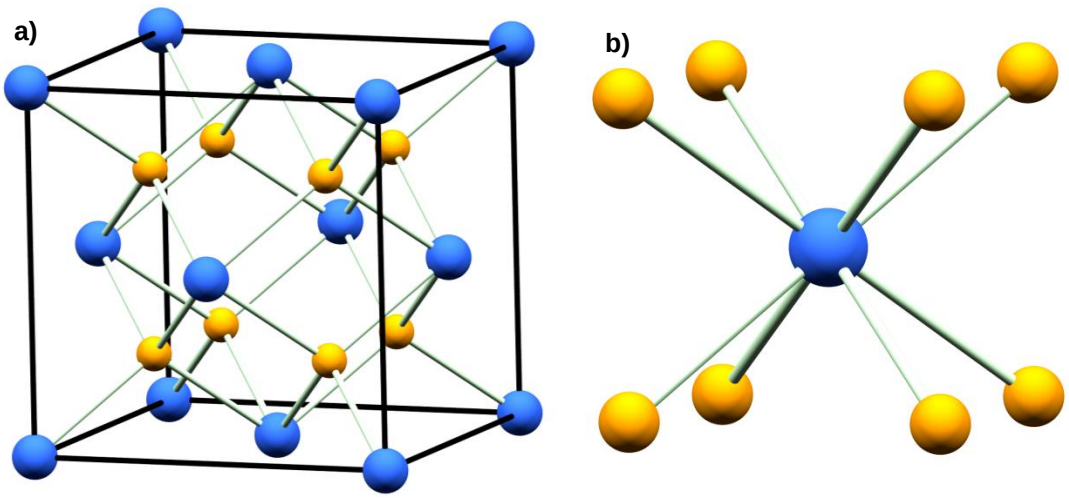

Figure 1. 1a) A CeO_2 unit cell with cerium atoms in blue and oxygen atoms in orange. b) A cerium atom cubically coordinated to eight oxygen atoms.

At elevated temperatures and low oxygen partial pressures CeO_2 is susceptible to reduction to give nonstoichiometric $CeO_{2-\delta}$ whilst still maintaining the overall average fluorite structure to a high degree of oxide vacancy, such that $0 < \delta < 0.5$.[60] Phase diagrams constructed from diffraction, thermal expansion and specific heat suggests that when reduced at temperatures above 650 °C, δ is a continuous value between 0 and 0.182 and depends on the oxygen partial pressure and temperature. However, when it is reduced at temperatures below 450 °C, there are a number of discrete values δ can take.[61-63] Oxygen deficient ceria readily re-oxidises in oxidising conditions (Equation 1. 1). This facile redox cycle makes ceria a key component in automotive three-way catalytic convertors, where it is essential that the fuel-air ratio remains close to the stoichiometric point.[64] It is enabled by both the Ce(IV) – Ce(III) inter-convertibility and the high oxide mobility due to the open fluorite structure.[5] This high oxide mobility also makes ceria and doped ceria materials an excellent solid electrolyte for fuel cells.[65]

$$CeO_2 \rightleftharpoons CeO_{2-\delta} + \frac{\delta}{2}O_2$$

Equation 1. 1 Cerium dioxide equilibrium

In order to maximise the surface area for heterogeneous catalytic applications, cerium oxides are ideally nanocrystalline.[23] In addition to being easier to reduce, the physical properties of nanocrystalline ceria are substantially different from those of bulk ceria. For crystallite sizes of less than 10 nm, the lattice parameter has been reported to increase logarithmically, [66-68] possibly due to an increased proportion of Ce^{3+} at the surface,[67] or strain as a result of increased surface energy.[69] Furthermore, electronic paramagnetic resonance studies suggest the presence of O_2^- superoxide species formed on the surface at particle sizes of 4 – 5 nm.[69]

1.2.2 Doping of Cerium Dioxide

CeO_2 is able to accommodate a huge range of dopant ions whilst retaining its original fluorite structure. Whilst some work has been conducted on replacing oxide for other anions, such as fluoride,[70] a majority of research focuses on substitution of Ce for other metals. Incorporation of almost all main group metals, transition metals and lanthanides has been reported to varying degrees (Figure 1. 2). This can have a range of benefits for catalysis. Substitution by cations of lower oxidation state creates oxide vacancies which increase oxide ion mobility.[71] Isovalent ion substitution creates lattice distortions which also increases oxide mobility.[64,72,73] In addition to this doping can also improve thermal stability by preventing sintering at high temperatures.[74] Furthermore, many transition metals, such as Fe^{3+} and Pd^{2+}, have redox properties of their own, which can significantly lower the oxide's reduction temperature.[75]

1.2.2.1 Alkali and Alkali Earth Metal-Substitution in Cerium Dioxide

There are very few reports of group 1 metal substitution into ceria. This can be explained by alkali metals' large ionic radii compared to that of Ce^{4+}. Eight-coordinate Ce^{4+} has an ionic radius of 0.97 Å, whilst Na^+ is 1.18 Å in the same environment;[76] more than 20% larger. Furthermore, the low valence means a large proportion of oxide vacancies are needed to achieve charge neutrality. Alkali metal dispersed on the surface of the ceria has been shown to reduce the temperature at which ethane was oxidised[77] and at which the water-gas shift reaction occurred.[78-80] The first report of Na inclusion was by Wright *et al.*[81] They reported 1.85% Na substitution in hydrothermally prepared ceria-zirconia solid solutions which drastically lowered the temperature at which it was reduced. Subsequently Pearce *et*

al. suggested up to 7% Na substitutional doping of CeO_2 was achieved by solid state firing, causing an unexpected decrease in lattice parameter.[82]

The divalent alkali earth metals Mg and Ca are more easily incorporated than monovalent alkali metals into the ceria lattice as their ionic radii (0.89 Å and 1.12 Å, respectively)[76] are more similar to that of Ce^{4+}. Whilst early reports of Mg, Ca and Sr substitution suggested only low levels of doping were possible,[83] much subsequent work has shown this is inaccurate. Solid solutions of the form $Ce_{1-x}M_xO_{2-x}$ (M = Mg, Ca, Sr; $x \leq 0.20$) have shown greatly improved oxide and electronic conductivity[82,84-98] and oxygen storage capacity[99,100] due to oxide vacancy formation. Although the majority of alkali earth-doped cerium oxides were prepared by high temperature solid state procedures, some reports of hydrothermal synthesis of cerium-alkali metal oxide solid solutions do exist.[90,91,97]

Ceria doped with low levels of Ta^{5+} and 'counterdoped' with Ca^{2+} in a 2:1 ratio (in order to achieve charge balance without the need for oxide or metal vacancies forming) was found to exhibit electrical conductivity identical to that of CeO_2.[101]

As a result of the tendency of Ba^{2+} to adopt a twelve-coordinate environment in oxides, the formation of the perovskite phase $BaCe^{IV}O_3$ is facile,[102] making the preparation of Ba-substituted ceria difficult. Nonetheless, ceria with Ce co-substituted by Ba, Sr and La has been prepared by coprecipitation of nitrate salts and calcination at 1450 °C (with 5% Ba substitution),[92] and the hydrothermal reaction of Ce, Bi and Ba nitrates in aqueous NaOH created a mixed oxide adopting the fluorite structure with ~7% Ba on the metal sites.[97]

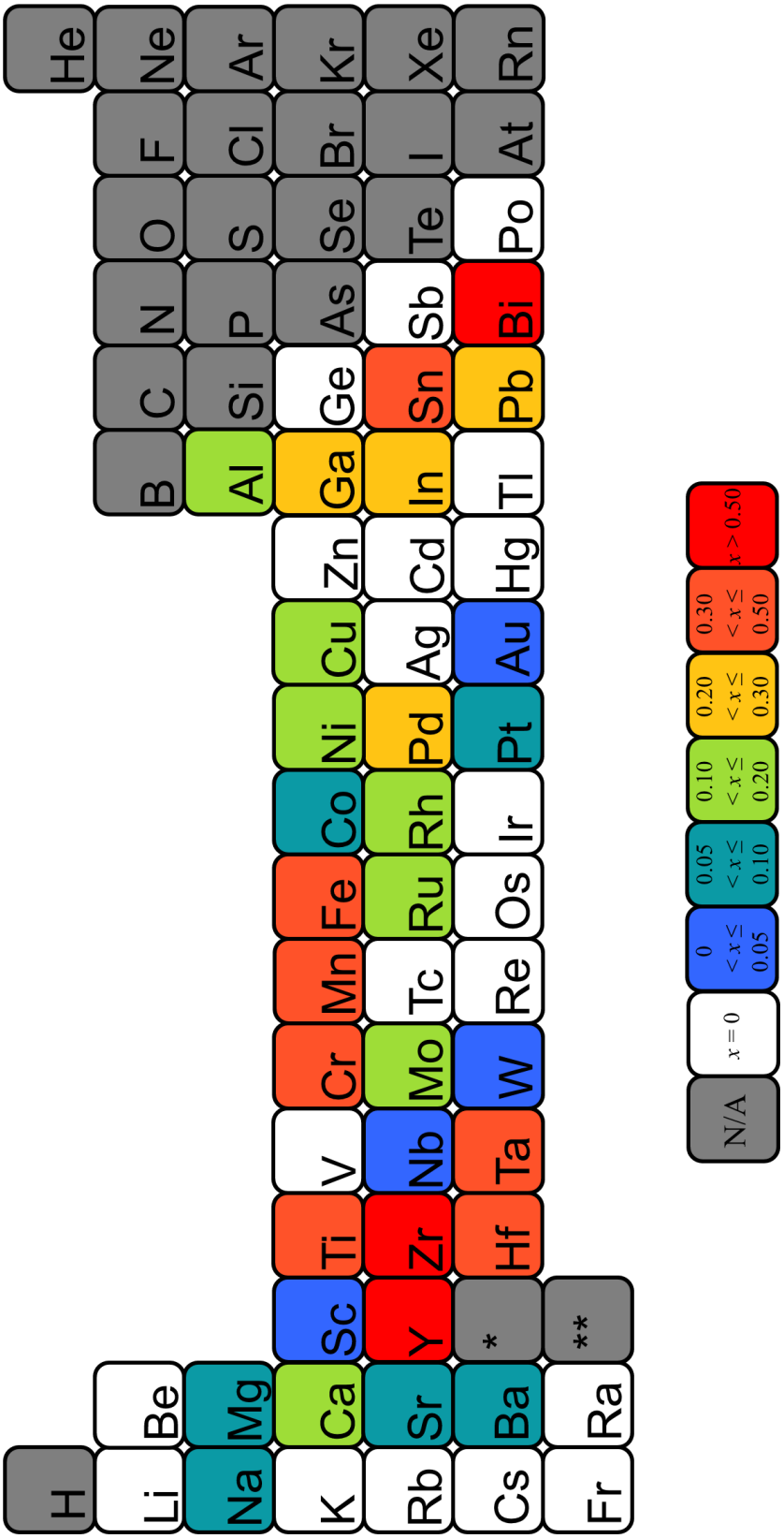

Figure 1. 2 Periodic table showing the maximum reported value of x *in solid solutions* $Ce_{1-x}M_xO_{2-\delta}$*, where M is a main group or transition metal ion. References in text. Maximum solubilities of grey elements were not determined.*

1.2.2.2 Transition Metal-Substitution in Cerium Dioxide

Almost every transition metal can be incorporated into ceria to some extent (Figure 1. 2). In general, the 3*d* and 4*d* metals have been shown to exhibit higher solubility than the 5*d* metals, possibly due to their ionic radii being typically closer to that of Ce^{4+} and their ability to occupy eight-coordinate sites. However, it is equally possible that 5*d* metals' scarcity mean they are the focus of less research and their maximum solubilities have not yet been determined.

High temperature preparations of mixed scandium-cerium oxides of the form $Ce_{1-x}Sc_xO_{2-0.5x}$ have been reported for $x \leq 0.05$.[83,103] NMR studies of very low level doping (x = 0.05, 0.005) showed oxide vacancies were localised around Sc, creating a mixed seven- and eight-coordinate environment.[104,105] Upon formation of further oxide vacancies at elevated temperatures the proportion of seven-coordinate Sc increased suggesting oxide vacancies are stabilised by the present of aliovalent ions in CeO_2.[106,107] Solid solutions of $Ce_{1-x}Y_xO_{2-0.5x}$ over the complete range $0 \leq x \leq 1$ can be prepared.[83] Eight-coordinate Y^{3+} has an ionic radius almost identical to that of Ce^{4+}, at 1.02 Å. Y_2O_3 adopts the C-type sesquioxide structure, which is closely related to the fluorite structure,[108] which is also adopted by the mixed oxide for values of x beyond 0.50.[74,85,109,110] Although when $x \leq 0.50$ the average fluorite structure is retained, Rietveld and pair distribution function (PDF) analyses of neutron and X-ray powder diffraction data suggest the structure consists of domains of Y_2O_3 in a CeO_2 matrix.[111] The excellent ionic conductivity[86,112,113] exhibited in $Ce_{1-x}Y_xO_{2-0.5x}$ is attributed to the similarity between ionic radii.[114-118] A range of preparation techniques have been utilised such as solid state synthesis,[112] coprecipitation of metal carbonates,[119] solution combustion[74] and hydrothermal synthesis;[120] each giving a different crystallite morphology.

Although the ionic radius of Ti^{4+} is significantly smaller than that of Ce^{4+}, solid solutions of the form $Ce_{1-x}Ti_xO_{2-\delta}$ up to a value of x = 0.40 retain the fluorite structure, leading to a contraction of the unit cell length.[74,121,122] At values of x > 0.40, mixtures of both fluorite and anatase phases form,[121] though a sol-gel preparation leads to a mixed-metal monoclinic phase with an undetermined structure.[122] Ti-doped cerium dioxide has been shown to exhibit improved redox properties,[121,122] particularly when co-doped with precious metals.[121,123] Furthermore, ceria's activity for CO_2 splitting has recently been found to be improved by Ti substitution.[118] Ceria-zirconia solid solutions ($Ce_{1-x}Zr_xO_2$) have been the focus of much research and are widely used in commercial catalysts,[64] thanks to their excellent thermal stability[72] and improved reducibility compared to ceria.[60,124] Solid solutions across the full composition range $0 \leq x \leq 1$ can be prepared, although the fluorite structure is only maintained when $x \leq$ 0.10. At room temperature ZrO_2 adopts a baddeleyite-type structure, a monoclinic ($P2_1/c$) distortion of the fluorite structure containing seven-coordinate Zr sites, which also forms in the mixed oxide where $x \geq 0.90$. Intermediate between these compositions exists a tetragonal phase ($P4_2/nmc$).[5] A huge range of approaches to synthesis of $Ce_{1-x}Zr_xO_2$ solid solutions[81,125-132] means that morphology is highly tuneable.[72,81,131-133] Zr^{4+} and Hf^{4+} have similar ionic radii (0.84 Å and 0.83 Å, respectively) and like ZrO_2, HfO_2 also adopts the baddeleyite structure. Although the maximum value of x of cerium-hafnium solid solutions prepared by conventional solution methods is 0.25,[118,127-129,134] up to 50% Hf substitution into ceria has been achieved by a solution combustion technique.[123,125] $Ce_{1-x}Hf_xO_2$ mixed oxides were found to exhibit improved CO conversion at reduced temperatures, compared to $Ce_{1-x}Zr_xO_2$ solid solutions.[127]

Group 5 metals (V, Nb, Ta) tend to be stable in the +5 oxidation state in oxides.[28] The zircon-type oxide structure $Ce^{III}M^{V}O_4$ is known to form in the case of all three metals. $CeNbO_4$ can accommodate interstitial oxygen, to partially oxidise the Ce to give $Ce^{3+2\delta}NbO_{4+\delta}$.[135] $CeVO_4$ forms easily from the solid state reaction of CeO_2 and V_2O_5 at 600 °C,[136] and as a result no V-doped CeO_2 has been reported. This can be rationalised by the much smaller ionic radius of V^{5+} (0.54 Å for six-coordinate V) compared to Ce^{4+} (0.97 Å). Nb^{5+} and Ta^{5+} (both are 0.74 Å in an eight-coordinate environment) are significantly larger than V, and though their ionic radii are still smaller than that of Ce^{4+}, mixed fluorite oxides of the form $Ce_{1-x}Nb_xO_{2+0.5x}$ and $Ce_{1-x}Ta_xO_{2+0.5x}$ have been reported. Some early reports focus on extremely low values of x (< 0.01) for both Nb[137-139] and Ta[101,138] where substitution was inferred by electronic properties. The maximum value of x for Nb-doped ceria made by coprecipitation was found to be around 0.01-0.02, after which $CeNbO_4$ began to form as an impurity.[140-142] A value of $x = 0.10$ for both Nb and Ta was later suggested,[143] though very little change in lattice parameter was observed for either and the formation of a mixed oxide was not certain. A coprecipitation method yielded a CeO_2-Mn_2O_3 mixture with Nb_2O_5 either highly dispersed on the surface of the oxides or present as an amorphous phase,[144] which exhibited low temperature soot oxidation and high selectivity for NO_x oxidation.[145] $Ce_{0.96}Ta_{0.04}O_{2.02}$ has been identified as having high electronic conductivity[146] and both $Ce_{0.90}Ta_{0.10}O_{2.05}$[147] and $Ce_{0.5}Ta_{0.5}O_{2.25}$[148] were found to be excellent catalysts for solar water splitting.

Cr-substituted ceria with formula $Ce_{0.67}Cr_{0.33}O_{2.11}$ was first synthesised by a hydrothermal reaction.[149] The Cr oxidation state was determined by X-ray photoelectron spectroscopy (XPS) and thermogravimetric analysis (TGA) to be a mixture of IV and VI in a 2:1 ratio, respectively. Charge balance was thought to be

achieved by the incorporation of extra oxide in interstitial sites. Like cerium oxide solid solutions containing Group 5 metals, this oxide was found to be extremely active for low temperature splitting of water,[150] though its practicality for use commercially is doubtful due to the toxicity of Cr(VI). $Ce_{1-x}Mo_xO_{2+\delta}$ fluorite-type oxides where $x \leq 0.10$ have been prepared by solid state synthesis at 1000 °C.[151] This technique was then adapted to synthesise rare earth metal co-doped ceria with formula $Ce_{0.9-x}RE_xMo_{0.1}O_{2+\delta}$ (RE = Y, Sm, Gd; $x \leq 0.50$).[112,152] XPS and XAFS studies of similar samples indicated Mo was present as Mo(VI).[153] A sol-gel method has been used to synthesise $Ce_{0.85}Mo_{0.15}O_{2+\delta}$, the highest reported degree of Mo substitution.[154] A coprecipitation procedure has been used to make several co-doped oxides with general formula $Ce_{0.86-x}RE_xMo_{0.14}O_{2+\delta}$ (RE = Y, Dy, Er, Gd, Pr, Sm, Tb, Ho).[113,155-158] Only one report of W-doped CeO_2 can be found, where 0.26% of the metal sites were occupied by W,[138] which resulted in high electronic conductivity.

Of the Group 7 metals, only Mn has been reported to be substituted into CeO_2 (up to $x = 0.50$).[159-162] All compositions contain Mn in the +3 oxidation state, and have been demonstrated to reduce NO selectively at low temperatures.[160] The oxides are commonly prepared by coprecipitation,[100,144,159-163] though less substituted samples have been prepared by solid state synthesis.[164]

Like Mn, Fe has been substituted into CeO_2 up to $x = 0.50$.[165-167] The first reported Fe-substituted CeO_2 sample ($Ce_{0.85}Fe_{0.15}O_2$) was prepared by hydrothermal synthesis,[75] though subsequently several techniques have been implemented including coprecipitation,[168-170] solution combustion[171-173] and sonochemical methods.[174,175] Very recently microscopy has suggested that a coprecipitation with no heating step results in CeO_2 and amorphous FeOOH.[176] $Ce_{0.85}Ru_{0.15}O_2$ (the most Ru-substituted CeO_2 found in the literature) was prepared hydrothermally in the

presence of a melamine complexing agent, but Ru-substituted ceria has also been prepared by sonication[174] and solution combustion.[177-179] No difference in catalytic activity was seen for methane reforming,[177] though CO_2 methanation was found to be catalysed at a lower temperature, compared to the reaction on unsubstituted ceria.[179] No substitution of Os has been reported in the literature.

The highest value of x in $Ce_{1-x}Co_xO_2$ is 0.10, which was achieved by electrodeposition onto a fluorine-doped tin oxide substrate,[180] though other methods such as solution combustion[179] and coprecipitation[181] have achieved phase-pure samples up to $0.05 \leq x \leq 0.07$. $Ce_{0.95}Co_{0.05}O_{2-\delta}$ has been shown to exhibit ferromagnetic ordering of the $Co^{2+/3+}$.[182] Very low levels of Rh-substitution (x = 0.01, 0.005) has been achieved by solution combustion.[183,184] Recently, synthesis of $Ce_{1-x}Rh_xO_{2-\delta}$ with a range of values of x up to 0.15 were reported, but the materials were inherently unstable to any kind of thermal treatment.[185] Like Re and Os, no Ir-substitution of ceria has been reported to date.

Mahammadunnisia *et al*. reported the synthesis of $Ce_{1-x}Ni_xO_{2-\delta}$ ($0 \leq x \leq 0.15$) by solution-combustion,[186] a significantly higher level of substitution than prepared hydrothermally,[187,188] coprecipitation[189] or solid state synthesis.[190] Although little has been published on Ni-substitution, Pd- and Pt-substitution has received a lot of interest. This is probably due to the use of these noble metals in existing ceria catalysts and a drive to disperse these on (or in) ceria more efficiently,[191] due to the high price of these metals. With this in mind, it is unsurprising that the majority of researchers are interested in substitution of 2% or less. The group of Hegde has extensively researched substituting < 10 at% Pd and/or Pt into both CeO_2 and transition metal-substituted (*e.g.* $Ce_{0.83}Ti_{0.15}Pt_{0.02}O_{2-\delta}$) CeO_2.[123,171,183,192-197] Misch *et al*. reported the synthesis of $Ce_{1-x}Pd_xO_{2-\delta}$ ($0 \leq x \leq 0.10$) by spray pyrolysis, a fluorite

which exhibits improved methane oxidation.[198] Recently Pd-substitution into ceria by a coprecipitation from a microemulsion with up to $x = 0.21$.[199] $Ce_{0.89}Pd_{0.11}O_{2-\delta}$ prepared by this route was shown to be an effective catalyst for CO oxidation.[199] Although Pd^{2+} would be expected to have a strong preference square-planar coordination, Pd extended X-ray absorption fine structure (EXAFS) experiments have suggested distorted or partially occupied eight-coordinate environments[192,196] However, the model used to fit data in these EXAFS experiments includes correlations not found in the crystal structure, so the veracity of their results is unclear.

Fluorites of the form $Ce_{1-x}Cu_xO_{2-\delta}$ ($0 \leq x \leq 0.20$) have been prepared by both sol-gel/coprecipitation methods,[100,200-204] and solution combustion.[205-208] H_2 temperature programmed reduction (TPR) showed a large, low-temperature uptake and Cu EXAFS suggested three-coordinate Cu(II) species were present.[206] Although no reports of Ag-doping have been published, low levels of Au-substitution ($x = 0.03 – 0.034$) into CeO_2 have been reported, by a reflux reaction which exhibited high water-gas shift and CO oxidation activity.[209,210]

None of the Group 12 metals (Zn, Cd, Hg) has been successfully substituted into ceria.

1.2.2.3 Post-Transition Metal-Substitution in Cerium Dioxide

$Ce_{0.50}Zr_{0.30}Al_{0.20}O_{2-\delta}$ has been prepared by a hydrothermal route.[211] A small lattice contraction of the fluorite cell was observed, as would be expected with substitution by Al ions (six coordinate Al^{3+} has an ionic radius of 0.535 Å[76]). $Ce_{0.75}Ga_{0.25}O_{2-\delta}$ prepared by coprecipitation has been shown to possess enhanced reducibility[212] increased surface acidity[213] and increased oxygen storage capacity.[214] Attempts to

prepare $Ce_{1-x}In_xO_{2-\delta}$ by coprecipitation proved unsuccessful.[82,100] However when the perovskite type phase $BaCe_{1-x}In_xO_{3-\delta}$ (x = 0.1, 0.2, 0.3; prepared by solid state synthesis) was heated under a flow of CO_2 the metastable fluorite $Ce_{1-x}In_xO_{2-\delta}$ and $BaCO_3$ were found to form.[215] No Tl-doping of ceria has been reported.

Ge-substitution has not been reported in CeO_2. However, a range of methods have proven successful in the synthesis of $Ce_{1-x}Sn_xO_{2-\delta}$. Hegde's group have determined the maximum value of x = 0.5 by solution combustion.[216] Sn-substituted CeO_2 has demonstrated improved oxygen storage capacity[118,217] and CO conversion[120,218] $Ce_{1-x}Pb_xO_{2-\delta}$ (x = 0.08,[100] 0.1[99]) synthesised by coprecipitation have been reported, with very little shift in lattice parameter, which can be explained by the similar ionic radii of eight-coordinate Ce^{4+} and Pb^{2+} (0.97 Å and 1.29 Å, respectively[76]). A hydrothermal synthesis yielded a Pb-substituted oxide up to x = 0.20.[219] $Ce_{0.80}Pb_{0.20}O_{2-\delta}$ made in this way exhibited an improved oxygen storage capacity.

No reports of Sb-substituted CeO_2 have been published to the best of the author's knowledge. A report of the synthesis of 'a defect pyrochlore $CeSbO_3$'[220] was called into question shortly after publication, and was instead identified as a mixture of CeO_2 and Sb_2O_3.[221] On the other hand, Bi-doped CeO_2 has been widely reported in the literature. Thanks to its comparable ionic radius (eight coordinate Bi^{3+} has an ionic radius of 1.17 Å, compared to the radius of Ce^{4+} of 0.97 Å)[76] a relatively high level of substitution has been achieved through a range of solution-based methods: a Pechini synthesis yielded $Ce_{1-x}Bi_xO_{2-\delta}$ ($0 \leq x \leq 0.5$),[222,223] whilst several reports of hydrothermal synthesis have found different maximum values for x,[97,224-227] the highest of these being 0.6.[227] Bi X-ray absorption near edge spectroscopy (XANES) confirmed an average Bi oxidation state of +3, though all the materials were found to be inherently unstable under reducing conditions at even mild temperatures.[227]

1.3 Applications of Cerium (IV) Oxides

Cerium oxides have found a wide range of uses as both catalyst supports and as the active catalyst themselves. As well as being investigated for catalysing a huge range of organic reactions (such as transformylation of amines,[228] hydrogenation of alkynes,[229] dry reforming of methane[177] and CO_2 thermochemical splitting[118] in 2014 alone) cerium oxides find most interest as solid oxide fuel cell electrolytes, automobile exhaust three-way catalysts and water-gas shift reaction catalysts.[78,197,202,209,230-232]

1.3.1 Automobile Exhaust Three-Way Catalysts[5]

By far the most widespread use of cerium(IV) oxides is as an oxygen buffer in automobile three-way catalysts, and with ever stricter emissions standards worldwide (Figure 1. 3[233,234]), more efficient three-way catalysts are in high demand.

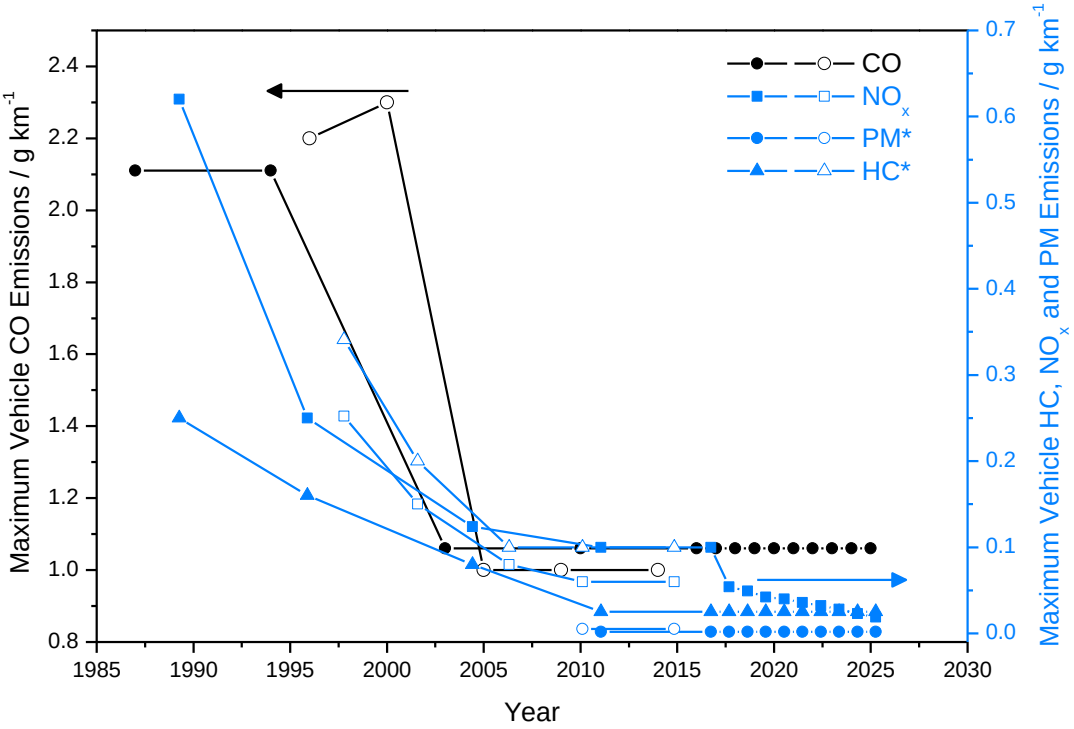

*Figure 1. 3 Vehicle emissions standards in the USA (Closed symbols) and EU (open symbols). *PM = particulate matter, HC = hydrocarbon,* i.e. *unburned fuel. Data taken from references 233 and 234.*

A three-way catalytic convertor simultaneously oxidises CO and unburned hydrocarbons, and reduces nitrogen oxides, NO_x. A three-way convertor is typically comprised of three constituent parts:

- a monolith, typically made of a ceramic material with a honeycomb structure (pores ~1 mm), through which the exhaust gas flows, typically made of Al_2O_3 or other refractory material. This often has a further washcoat of high surface area Al_2O_3 to improve surface area;
- a thin coating of an oxygen-storage material, invariably ceria/substituted ceria;
- precious metal nanoparticles on the surface.

Although other materials have oxygen storage capacity, only substituted cerium oxides have been shown to exhibit rapid oxygen release and uptake kinetics, resistance to sulphur poisoning and excellent thermal stability.[5]

This oxygen storage material is necessary to maintain a precise oxygen-fuel ratio. The efficiency of a three-way catalyst is very high, as long as the oxygen-fuel ratio is maintained close to the stoichiometric point.[64] Deviation of even a few per cent can dramatically impede conversion efficiency (Figure 1. 4). Although a carburettor is used, it does not react quickly enough to maintain a 'tight' control on the air-fuel ratio. At the moderate temperatures at which three-way catalysts operate (~500 – 800 °C) CeO_2 rapidly releases and takes up oxygen in fuel rich and lean gas streams, respectively.

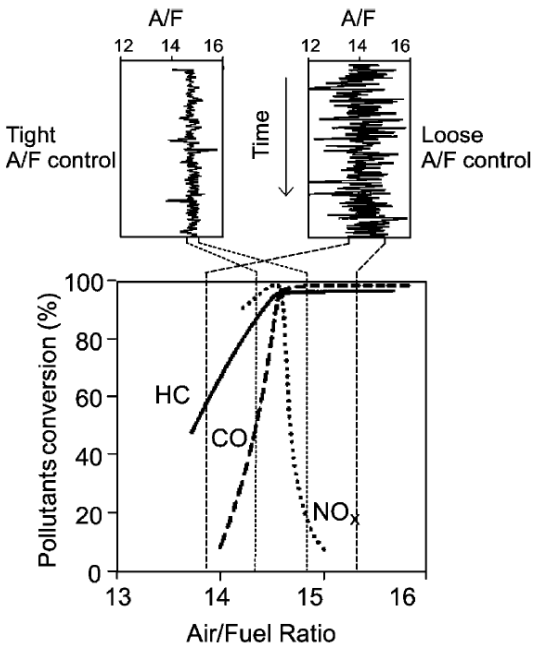

Figure 1. 4 Three-way catalysis conversion of hydrocarbons (HC), CO and NO_x as a function of air-fuel ratio. Also shown are representative air-fuel ratio vs *time of 'loosely' (i.e. under only carburettor control – no oxygen storage material) and 'tightly' (carburettor and oxygen storage material) controlled air-fuel. Taken from Di Monte and Kaspar.*[64]

1.4 Complex Ruthenium Oxides

Complex precious metal (*i.e.* Ru, Rh, Pd, Os, Ir and Pt) oxides form a wide variety of structures.[235-238] They routinely contain strongly electropositive elements (such as alkaline metals, alkaline earth metals and lanthanides), which, by an inductive effect, helps to stabilise them in oxidation states not found in binary oxides.[191] The perovskite structure and perovskite-type oxides are commonly adopted, with multiple examples for each platinum group metal. Also known are several oxides adopting the pyrochlore, spinel and delafossite structures.[191] Ruthenium has perhaps the richest oxide chemistry of the platinum group metals. It is extremely flexible in its oxidation state (Ru oxidation states +2,[239] +3,[240] +4, +5, +6[28,241] and +7[28] have all been reported in condensed complex oxides), and is less prone to reduction at elevated temperatures than the other platinum group metals.

1.4.1 Alkaline Earth Metal (Ca, Sr, Ba) Ruthenium Oxides

1.4.1.1 Perovskite-type structures

Alkaline earth metal ruthenium oxides form a wide variety of structures. Perovskites and perovskite-related phases – namely Ruddlesden-Popper phases and hexagonal perovskites – are exceedingly common (Table 1. 1), and exhibit a wide variety of diverse and exotic magnetic properties. For example, the Ruddlesden-Popper phase Sr_2RuO_4 is an unusual *p*-wave superconductor which contains no Cu, whilst the perovskite $SrRuO_3$ is a metallic conductor and is ferromagnetic.

Table 1. 1 Reported perovskite-type alkaline earth metal ruthenium oxides stable at room temperature and pressure. Further details of Ba ruthenate hexagonal perovskites in Table 6.10.

Structure Type		Ca	Sr	Ba
Perovskite		$CaRuO_3$ *Pnma*[242,243]	$SrRuO_3$ *Pbnm*[242,243]	
Hexagonal Perovskite	**4H**			$BaRuO_3$[244]
	6H			$Ba_4Ru_3MO_{12}$ (*M* = Li, Mg, Zn)[245]; $Ba_3MRu_2O_9$ (*M* = Na, Li, Ni, Co, Zn Ce, Pr, Tb)[241,246,247]
	8H		$Sr_4Ru_3O_{12}$[248]	$Ba_4Ru_3NaO_{12}$[245]; $Ba_5Ru_2O_{10}$[249]
	9R			$BaRuO_3$[250]
	10H			$BaRuO_3$[251]
Ruddlesden-Popper $A_{n+1}Ru_nO_{3n+1}$	***n* = 1**	*Pbca* / $P2_1/c$[252-254]	*I*4/*mmm*[255-257]	*I*4/*mmm*[258]
	***n* = 2**	*Bb*21*m*[259]	*I*4/*mmm* [257]	
	***n* = 3**		*Pbam*[260]	

The perovskite structure, at its simplest, is a cubic structure with chemical formula ABX_3, where cations *A* and *B* are twelve- and six-coordinate, respectively. *A* is typically significantly larger than *B*, and in cubic perovskites the tolerance factor, *t*, should fall between 0.9 and 1:[261]

$$t = \frac{r_A + r_X}{\sqrt{2}(r_B + r_X)}$$

Equation 1. 2 The Goldschmidt tolerance factor, t, *calculated from ionic radii,* r, *of constituent ions.*

When this tolerance factor is below ~0.90, symmetry lowering distortion of the perovskite occurs, leading to tetragonal or orthorhombic distortion of the unit cell, as observed in $CaRuO_3$ (Figure 1. 5a). Conversely, when the tolerance factor > 1, hexagonal perovskites are favoured (see Section 6.5.2).

Ruddlesden-Popper phases consist of *n* 'slices' of the ABX_3 perovskite structure which are displaced relative to each other and are separated by a terminal AO 'cladding layer', to give a general formula $A_{n+1}B_nX_{3n+1}$, Figure 1. 5b, c.[262]

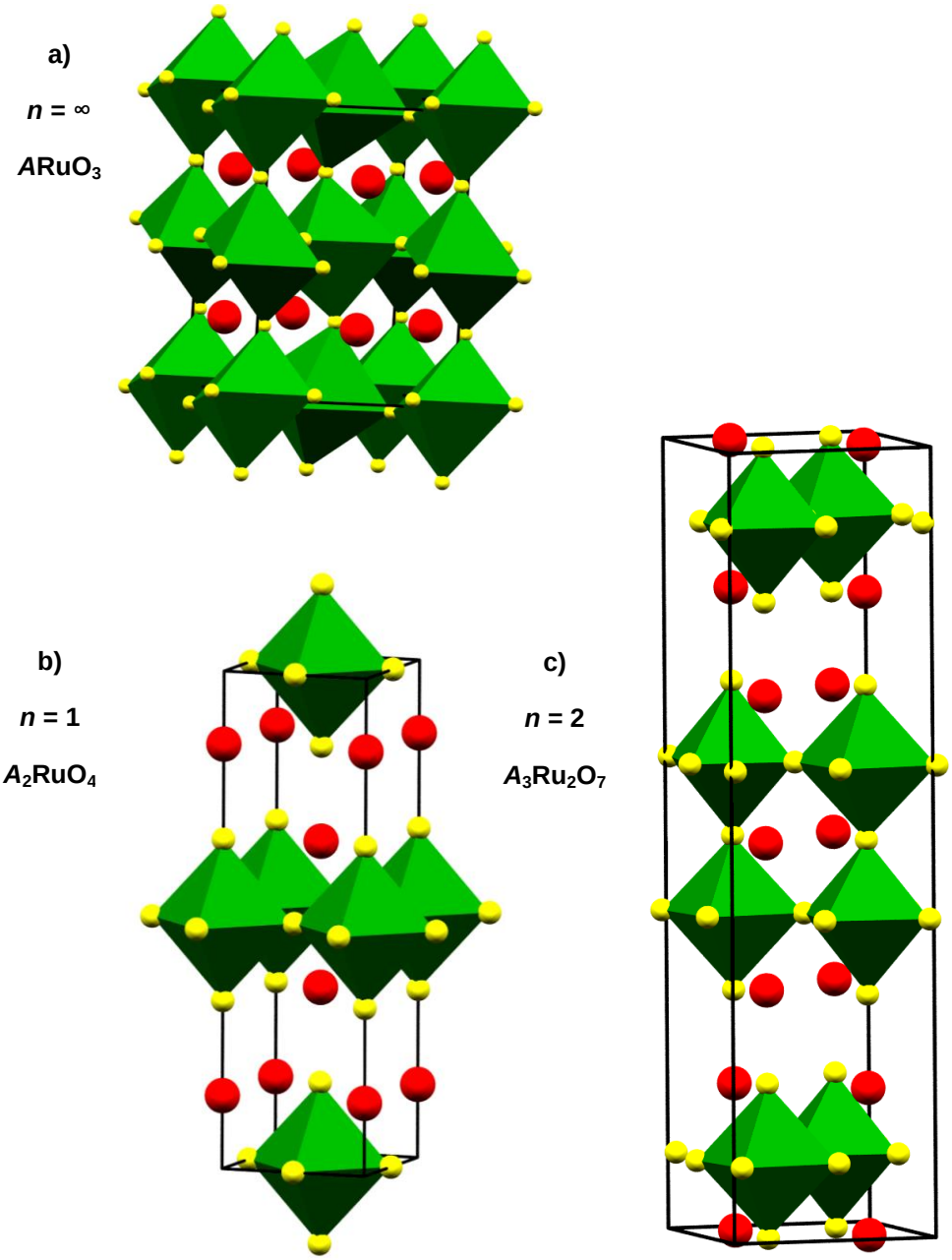

*Figure 1. 5a) The orthorhombic perovskite $ARuO_3$. b) The Ruddlesden-Popper phase (*n = *1),* A_2RuO_4. *c) The Ruddlesden-Popper phase (*n = *2)* $A_3Ru_2O_7$. A *atoms in red, RuO_6 octahedra in green, with yellow oxygen atoms.*

1.4.1.2 Other Alkaline Earth Metal Ruthenium Oxides

In the Ca – Ru system, the only other phase found after a review of the literature was the pyrochlore $Ca_2Ru_2O_7$, prepared by high-temperature, high-pressure hydrothermal synthesis.[263] This is the only calcium ruthenate which contains Ru in the +5 oxidation state.

A similar high-temperature, high pressure hydrothermal synthesis has been shown to yield a strontium ruthenate not related to the perovskite structure, $Sr_2Ru_3O_{10}$. It has a monoclinic (*C*2/*m*) structure, which is built of chains of edge-sharing $Ru^{5.33+}O_6$ octahedra interconnected by corner-sharing RuO_6 octahedra, forming layers in the *bc*-plane with Sr ions separating them.[264]

The Ba – Ru oxide system contains many non-perovskite structures. Although the syntheses of Ba_4RuO_6, Ba_9RuO_{11}, $BaRu_4O_9$ and Ba_3RuO_5 has been reported,[265,266] their diffraction patterns have yet to be successfully indexed. The orthorhombic (originally thought to be monoclinic[267]) $Ba_3Ru^{4+}{}_4O_{10}$ consists of a mixture of face- and corner-sharing octahedra, which form checkerboard-type layers separated by Ba ions (see Section 6.4.4).[268] A monoclinic phase, $Ba_2Ru^{4.57+}{}_7O_{18}$ (isostructural with $Ba_2M_7F_{18}$ (M = Zn, Ni)) was synthesised, consisting of alternating layers of Ru_4O_{16} edge-sharing octahedral clusters and Ru_3O_{14} trimeric edge-sharing octahedral chains.[251] $Ba_5Ru^{4+}{}_3O_{12}$, prepared by firing of RuO_2 and $BaCO_3$ at 1200 °C, consists of isolated quasi-trimeric face-sharing RuO_6 octahedral chains surrounded by Ba atoms.[267]

1.5 Aims of This Work

Despite the range of substituents doped into ceria detailed above there is still a need for materials with improved oxygen storage capacity at lower temperatures, with uses in automobile three-way catalytic convertors and emerging applications such as thermochemical water-splitting.[269] The aim of the work described in this thesis was to synthesise hydrothermally high surface area cerium dioxide doped with a range of substituents which have not been prepared previously or have been poorly

characterised. The substituents studied can be broadly split into two groups: pentavalent metal ions (Sb^{5+}, Nb^{5+}, Ta^{5+}) and platinum group metals (Pd and Pt). The redox properties of these oxides will be explored to assess their suitability for catalysis.

There are few reports of significant pentavalent doping of ceria, and how a pentavalent ion is incorporated into the fluorite structure is poorly understood. A hydrothermal route to these oxides will be explored and the structure of these materials will be explored by diffraction and spectroscopic methods. There have been some reports of Pd and Pt incorporation into CeO_2. However, there have been no reports of hydrothermal synthesis of these oxides, and it is poorly understood how these ions are incorporated into the ceria lattice. A hydrothermal synthetic route to these will be investigated, and the structure and redox properties of these materials will be investigated.

In addition to the substituted cerium(IV) oxides, new hydrothermally-prepared alkali earth metal, ruthenium oxides with potential use as oxygen-evolution catalysts were also prepared. The majority of previously synthesised ruthenates have been prepared by solid state synthesis. No previous work on low temperature hydrothermal synthesis of alkaline earth ruthenates exists to the best of the author's knowledge, and metastable products can often be isolated by a hydrothermal approach.[45] The structure and magnetism of these materials will be explored.

1.6 References

(1) Noll, W.; Holm, R.; Born, L. *Angew. Chem. Int. Ed.* **1975**, *14*, 602.
(2) Braun, J. H.; Baidins, A.; Marganski, R. E. *Prog. Org. Coat.* **1992**, *20*, 105.
(3) Zubko, P.; Gariglio, S.; Gabay, M.; Ghosez, P.; Triscone, J. M. *Annu. Rev. Condens. Matter Phys.* **2011**, *2*, 141.
(4) Leskelä, M.; Mölsä, H.; Niinistö, L. *Supercond. Sci. Technol.* **1993**, *6*, 627.
(5) Trovarelli, A. *Catalysis by Ceria and Related Materials*; Imperial College Press, 2013.
(6) Gratzel, M. *Nature* **2001**, *414*, 338.
(7) Goodenough, J. B. *J. Solid State Electrochem.* **2012**, *16*, 2019.
(8) Yuan, C.; Wu, H. B.; Xie, Y.; Lou, X. W. *Angew. Chem. Int. Ed.* **2014**, *53*, 1488.
(9) Ormerod, R. M. *Chem. Soc. Rev.* **2003**, *32*, 17.
(10) Tokura, Y.; Hwang, H. Y. *Nat. Mater.* **2008**, *7*, 694.
(11) Bednorz, J. G.; Müller, K. A. *Z. Physik B - Condensed Matter* **1986**, *64*, 189.
(12) Cheong, S.-W.; Mostovoy, M. *Nat. Mater.* **2007**, *6*, 13.
(13) Ogale, S. B.; Venkatesan, T. V.; Blamire, M. *Functional Metal Oxides: New Science and Novel Applications*; Wiley, 2013.
(14) Harunsani, M. H.; Oropeza, F. E.; Palgrave, R. G.; Egdell, R. G. *Chem. Mater.* **2010**, *22*, 1551.
(15) zur Loye, H.-C.; Layland, R. C.; Smith, M. D.; Claridge, J. B. *J. Cryst. Growth* **2000**, *211*, 452.
(16) Dawber, M.; Rabe, K. M.; Scott, J. F. *Rev. Mod. Phys.* **2005**, *77*, 1083.
(17) Wu, J.; Cao, J.; Han, W. Q.; Janotti, A.; Kim, H. C. *Functional Metal Oxide Nanostructures*; Springer, 2011.
(18) Lou, X. W.; Wang, Y.; Yuan, C. L.; Lee, J. Y.; Archer, L. A. *Adv. Mater.* **2006**, *18*, 2325.
(19) Xia, Y.; Yang, P.; Sun, Y.; Wu, Y.; Mayers, B.; Gates, B.; Yin, Y.; Kim, F.; Yan, H. *Adv. Mater.* **2003**, *15*, 353.
(20) Soler-illia, G. J. D.; Sanchez, C.; Lebeau, B.; Patarin, J. *Chem. Rev.* **2002**, *102*, 4093.
(21) Wang, J.; Neaton, J. B.; Zheng, H.; Nagarajan, V.; Ogale, S. B.; Liu, B.; Viehland, D.; Vaithyanathan, V.; Schlom, D. G.; Waghmare, U. V.; Spaldin, N. A.; Rabe, K. M.; Wuttig, M.; Ramesh, R. *Science* **2003**, *299*, 1719.
(22) Chopra, K. L.; Paulson, P. D.; Dutta, V. *Prog. Photovoltaics* **2004**, *12*, 69.
(23) Bell, A. T. *Science* **2003**, *299*, 1688.
(24) Atkins, P. *Shriver and Atkins' Inorganic Chemistry*; OUP Oxford, 2010.
(25) Rao, C. N. R.; Gopalakrishnan, J. *Acc. Chem. Res.* **1987**, *20*, 228.
(26) Cushing, B. L.; Kolesnichenko, V. L.; O'Connor, C. J. *Chem. Rev.* **2004**, *104*, 3893.
(27) Schubert, U.; Hüsing, N. *Synthesis of Inorganic Materials*; Wiley-VCH: Weinheim, 2004.
(28) Greenwood, N. N.; Earnshaw, A. *Chemistry of the Elements*; 2nd ed.; Butterworth–Heinemann, 1997.
(29) Gopalakrishnan, J. *Chem. Mater.* **1995**, *7*, 1265.
(30) Liu, H.; Hu, C.; Wang, Z. L. *Nano Lett.* **2006**, *6*, 1535.
(31) Elwell, D.; Scheel, H. J. *Crystal Growth from High-temperature Solutions*; Academic Press, 1975.
(32) Bugaris, D. E.; zur Loye, H.-C. *Angew. Chem. Int. Ed.* **2012**, *51*, 3780.

(33) Mugavero III, S. J.; Gemmill, W. R.; Roof, I. P.; zur Loye, H.-C. *J. Solid State Chem.* **2009**, *182*, 1950.
(34) Mugavero, S. J.; Smith, M. D.; Yoon, W.-S.; zur Loye, H.-C. *Angew. Chem. Int. Ed.* **2009**, *48*, 215.
(35) Bugaris, D. E.; Ibers, J. A. *Dalton Trans.* **2010**, *39*, 5949.
(36) Kakihana, M. *J. Sol-Gel Sci. Technol.* **1996**, *6*, 7.
(37) Livage, J.; Henry, M.; Sanchez, C. *Prog. Solid State Chem.* **1988**, *18*, 259.
(38) Lessing, P. A. *Am. Ceram. Soc. Bull.* **1989**, *68*, 1002.
(39) Marcilly, C.; Courty, P.; Delmon, B. *J. Am. Ceram. Soc.* **1970**, *53*, 56.
(40) Rabenau, A. *Angew. Chem. Int. Ed.* **1985**, *24*, 1026.
(41) Lyell, C. *A Manual of Elementary Geology*; Little, Brown and Company: Boston, 1855.
(42) Chen, H.; Hiller, D. M.; Hudson, J.; Westenbroek, C. *IEEE Trans. Magn.* **1984**, *20*, 24.
(43) Davis, M. E.; Lobo, R. F. *Chem. Mater.* **1992**, *4*, 756.
(44) Knauss, K. G.; Dibley, M. J.; Bourcier, W. L.; Shaw, H. F. *Appl. Geochem.* **2001**, *16*, 1115.
(45) Walton, R. I. *Chem. Soc. Rev.* **2002**, *31*, 230.
(46) Lewis, L. C.; Fredericks, W. J. *J. Cryst. Growth* **1970**, *7*, 120.
(47) Reverchon, E.; Adami, R. *J. Supercrit. Fluids* **2006**, *37*, 1.
(48) Rajamathi, M.; Seshadri, R. *Curr. Opin. Solid State Mater. Sci.* **2002**, *6*, 337.
(49) Jansen, M. *Angew. Chem. Int. Ed.* **2002**, *41*, 3746.
(50) Jansen, M.; Pentin, I. V.; Schön, J. C. *Angew. Chem. Int. Ed.* **2012**, *51*, 132.
(51) Modeshia, D. R.; Darton, R. J.; Ashbrook, S. E.; Walton, R. I. *Chem. Commun.* **2009**, 68.
(52) Playford, H. Y.; Hannon, A. C.; Barney, E. R.; Walton, R. I. *Chem. Eur. J.* **2013**, *19*, 2803.
(53) Inoue, M.; Kimura, M.; Inui, T. *Chem. Commun.* **1999**, 957.
(54) Chen; Fan, R. *Chem. Mater.* **2001**, *13*, 802.
(55) Harunsani, M. H.; Woodward, D. I.; Peel, M. D.; Ashbrook, S. E.; Walton, R. I. *J. Solid State Chem.* **2013**, *207*, 117.
(56) Komarneni, S.; Roy, R.; Li, Q. H. *Mater. Res. Bull.* **1992**, *27*, 1393.
(57) Sōmiya, S.; Roy, R. *Bull. Mater. Sci.* **2000**, *23*, 453.
(58) Ranga Rao, G.; Mishra, B. G. *Bull. Catal. Soc. India* **2003**, *2*, 122.
(59) Yuan, Q.; Duan, H.-H.; Li, L.-L.; Sun, L.-D.; Zhang, Y.-W.; Yan, C.-H. *J. Colloid Interface Sci.* **2009**, *335*, 151.
(60) Trovarelli, A. *Catal. Rev.-Sci. Eng.* **1996**, *38*, 439.
(61) Ricken, M.; Nölting, J.; Riess, I. *J. Solid State Chem.* **1984**, *54*, 89.
(62) Riess, I.; Ricken, M.; Nölting, J. *J. Solid State Chem.* **1985**, *57*, 314.
(63) Körner, R.; Ricken, M.; Nölting, J.; Riess, I. *J. Solid State Chem.* **1989**, *78*, 136.
(64) Di Monte, R.; Kaspar, J. *Top. Catal.* **2004**, *28*, 47.
(65) Steele, B. C. H. *Solid State Ion.* **2000**, *129*, 95.
(66) Tsunekawa, S.; Sivamohan, R.; Ito, S.; Kasuya, A.; Fukuda, T. *Nanostruct. Mater.* **1999**, *11*, 141.
(67) Tsunekawa, S.; Ishikawa, K.; Li, Z. Q.; Kawazoe, Y.; Kasuya, A. *Phys. Rev. Lett.* **2000**, *85*, 3440.
(68) Hailstone, R. K.; DiFrancesco, A. G.; Leong, J. G.; Allston, T. D.; Reed, K. J. *J. Phys. Chem. C* **2009**, *113*, 15155.

(69) Xu, J.; Harmer, J.; Li, G.; Chapman, T.; Collier, P.; Longworth, S.; Tsang, S. C. *Chem. Commun.* **2010**, *46*, 1887.
(70) Ahmad, S.; Gopalaiah, K.; Chandrudu, S. N.; Nagarajan, R. *Inorg. Chem.* **2014**, *53*, 2030.
(71) Balazs, G. B.; Glass, R. S. *Solid State Ion.* **1995**, *76*, 155.
(72) Di Monte, R.; Kaspar, J. *J. Mater. Chem.* **2005**, *15*, 633.
(73) Fornasiero, P.; Di Monte, R.; Rao, G. R.; Kaspar, J.; Meriani, S.; Trovarelli, A.; Graziani, M. *J. Catal.* **1995**, *151*, 168.
(74) Singh, P.; Hegde, M. S. *J. Solid State Chem.* **2008**, *181*, 3248.
(75) Li, G.; Smith, R. L.; Inomata, H. *J. Am. Chem. Soc.* **2001**, *123*, 11091.
(76) Shannon, R. D. *Acta Crystallogr. Sect. A* **1976**, *32*, 751.
(77) Kennedy, E. M.; Cant, N. W. *Appl. Catal., A* **1992**, *87*, 171.
(78) Evin, H.; Jacobs, G.; Ruiz-Martinez, J.; Thomas, G.; Davis, B. *Catal. Lett.* **2008**, *120*, 166.
(79) Evin, H. N.; Jacobs, G.; Ruiz-Martinez, J.; Graham, U. M.; Dozier, A.; Thomas, G.; Davis, B. H. *Catal. Lett.* **2008**, *122*, 9.
(80) Jacobs, G.; Davis, B. H. *Int. J. Hydrogen Energy* **2010**, *35*, 3522.
(81) Wright, C. S.; Walton, R. I.; Thompsett, D.; Fisher, J.; Ashbrook, S. E. *Adv. Mater.* **2007**, *19*, 4500.
(82) Pearce, M. C.; Thangadurai, V. *Asia-Pac. J. Chem. Eng.* **2009**, *4*, 33.
(83) Etsell, T. H.; Flengas, S. N. *Chem. Rev.* **1970**, *70*, 339.
(84) Blumenthal, R. N.; Brugner, F. S.; Garnier, J. E. *J. Electrochem. Soc.* **1973**, *120*, 1230.
(85) Kudo, T.; Obayashi, H. *J. Electrochem. Soc.* **1975**, *122*, 142.
(86) Tuller, H. L.; Nowick, A. S. *J. Electrochem. Soc.* **1975**, *122*, 255.
(87) Garnier, J. E.; Blumenthal, R. N.; Panlener, R. J.; Sharma, R. K. *J. Phys. Chem. Solids* **1976**, *37*, 369.
(88) Eguchi, K.; Setoguchi, T.; Inoue, T.; Arai, H. *Solid State Ion.* **1992**, *52*, 165.
(89) Pijolat, M.; Prin, M.; Soustelle, M.; Touret, O.; Nortier, P. *J. Chem. Soc., Faraday Trans.* **1995**, *91*, 3941.
(90) Yamashita, K.; Ramanujachary, K. V.; Greenblatt, M. *Solid State Ion.* **1995**, *81*, 53.
(91) Huang, W.; Shuk, P.; Greenblatt, M. *Chem. Mater.* **1997**, *9*, 2240.
(92) Mori, T.; Drennan, J.; Lee, J.-H.; Li, J.-G.; Ikegami, T. *Solid State Ion.* **2002**, *154–155*, 461.
(93) Banerjee, S.; Devi, P. S. *Solid State Ion.* **2008**, *179*, 661.
(94) Cioatera, N.; Pârvulescu, V.; Rolle, A.; Vannier, R. N. *Solid State Ion.* **2009**, *180*, 681.
(95) Parkash, O.; Singh, N.; Singh, N. K.; Kumar, D. *Solid State Ion.* **2012**, *212*, 100.
(96) Balaguer, M.; Vert, V. B.; Navarrete, L.; Serra, J. M. *J. Power Sources* **2013**, *223*, 214.
(97) Zhao, H.; Feng, S. *Chem. Mater.* **1999**, *11*, 958.
(98) Mogensen, M.; Sammes, N. M.; Tompsett, G. A. *Solid State Ion.* **2000**, *129*, 63.
(99) Zhang, Y.; Andersson, S.; Muhammed, M. *Appl. Catal., B* **1995**, *6*, 325.
(100) Blank, J. H.; Beckers, J.; Collignon, P. F.; Rothenberg, G. *ChemPhysChem* **2007**, *8*, 2490.
(101) Chang, E. K.; Blumenthal, R. N. *J. Solid State Chem.* **1988**, *72*, 330.

(102) Medvedev, D.; Murashkina, A.; Pikalova, E.; Demin, A.; Podias, A.; Tsiakaras, P. *Prog. Mater Sci.* **2014**, *60*, 72.
(103) Gerhardt, R.; Lee, W. K.; Nowick, A. S. *J. Phys. Chem. Solids* **1987**, *48*, 563.
(104) Subbi, J.; Heinmaa, I.; Põder, R.; Kooskora, H. *Solid State Ion.* **2012**, *225*, 488.
(105) Jain, P.; Avila-Paredes, H. J.; Gapuz, C.; Sen, S.; Kim, S. *J. Phys. Chem. C* **2009**, *113*, 6553.
(106) Avila-Paredes, H. J.; Jain, P.; Sen, S.; Kim, S. *Chem. Mater.* **2009**, *22*, 893.
(107) Subbi, J.; Heinmaa, I.; Põder, R.; Kooskora, H. *Solid State Ion.* **2013**, *239*, 15.
(108) Maaskant, W. J. A. *Physica B* **2010**, *405*, 2474.
(109) McCullough, J. D.; Britton, J. D. *J. Am. Chem. Soc.* **1952**, *74*, 5225.
(110) Wang, D. Y.; Park, D. S.; Griffith, J.; Nowick, A. S. *Solid State Ion.* **1981**, *2*, 95.
(111) Coduri, M.; Scavini, M.; Allieta, M.; Brunelli, M.; Ferrero, C. *Chem. Mater.* **2013**, *25*, 4278.
(112) Li, Q.; Thangadurai, V. *J. Mater. Chem.* **2010**, *20*, 7970.
(113) Bo, Q. B.; Sun, G. X.; Meng, J. *J. Phys. Chem. Solids* **2006**, *67*, 732.
(114) Suzuki, T.; Kosacki, I.; Anderson, H. U. *J. Am. Ceram. Soc.* **2002**, *85*, 1492.
(115) Marrocchelli, D.; Bishop, S. R.; Kilner, J. *J. Mater. Chem. A* **2013**, *1*, 7673.
(116) Marrocchelli, D.; Bishop, S. R.; Tuller, H. L.; Watson, G. W.; Yildiz, B. *Phys. Chem. Chem. Phys.* **2012**, *14*, 12070.
(117) Marrocchelli, D.; Bishop, S. R.; Tuller, H. L.; Yildiz, B. *Adv. Funct. Mater.* **2012**, *22*, 1958.
(118) Jiang, Q.; Zhou, G.; Jiang, Z.; Li, C. *Solar Energy* **2014**, *99*, 55.
(119) Li, J.-G.; Ikegami, T.; Wang, Y.; Mori, T. *J. Solid State Chem.* **2002**, *168*, 52.
(120) Xiao, G.; Li, S.; Li, H.; Chen, L. *Microporous Mesoporous Mater.* **2009**, *120*, 426.
(121) Baidya, T.; Gayen, A.; Hegde, M. S.; Ravishankar, N.; Dupont, L. *J. Phys. Chem. B* **2006**, *110*, 5262.
(122) Luo, M.; Chen, J.; Chen, L.; Lu, J.; Feng, Z.; Li, C. *Chem. Mater.* **2001**, *13*, 197.
(123) Baidya, T.; Dutta, G.; Hegde, M. S.; Waghmare, U. V. *Dalton Trans.* **2009**, 455.
(124) Balducci, G.; Fornasiero, P.; Di Monte, R.; Kaspar, J.; Meriani, S.; Graziani, M. *Catal. Lett.* **1995**, *33*, 193.
(125) Baidya, T.; Hegde, M. S.; Gopalakrishnan, J. *J. Phys. Chem. B* **2007**, *111*, 5149.
(126) Dong, Q.; Yin, S.; Guo, C.; Kimura, T.; Sato, T. *RSC Advances* **2012**, *2*, 12770.
(127) Reddy, B. M.; Bharali, P.; Saikia, P.; Park, S. E.; van den Berg, M. W. E.; Muhler, M.; Grunert, W. *J. Phys. Chem. C* **2008**, *112*, 11729.
(128) Reddy, B. M.; Bharali, P.; Thrimurthulu, G.; Saikia, P.; Katta, L.; Park, S.-E. *Catal. Lett.* **2008**, *123*, 327.
(129) Reddy, B. M.; Katta, L.; Thrimurthulu, G. *Catal. Today* **2011**, *175*, 585.
(130) Walton, R. I. *Prog. Cryst. Growth Charact. Mater.* **2011**, *57*, 93.
(131) Zhang, F.; Chen, C.-H.; Hanson, J. C.; Robinson, R. D.; Herman, I. P.; Chan, S.-W. *J. Am. Ceram. Soc.* **2006**, *89*, 1028.
(132) Zhong, S.-L.; Zhang, L.-F.; Wang, L.; Huang, W.-X.; Fan, C.-M.; Xu, A.-W. *J. Phys. Chem. C* **2012**, *116*, 13127.

(133) Guillen-Hurtado, N.; Bueno-Lopez, A.; Garcia-Garcia, A. *J. Mater. Sci.* **2012**, *47*, 3204.
(134) Reddy, B. M.; Bharali, P.; Saikia, P.; Khan, A.; Loridant, S.; Muhler, M.; Grünert, W. *J. Phys. Chem. C* **2007**, *111*, 1878.
(135) Packer, R. J.; Skinner, S. J. *Adv. Mater.* **2010**, *22*, 1613.
(136) Matta, J.; Courcot, D.; Abi-Aad, E.; Aboukaïs, A. *Chem. Mater.* **2002**, *14*, 4118.
(137) Naik, I. K.; Tien, T. Y. *J. Electrochem. Soc.* **1979**, *126*, 562.
(138) De Guire, M. R.; Shingler, M. J.; Dincer, E. *Solid State Ion.* **1992**, *52*, 155.
(139) Yashiro, K.; Suzuki, T.; Kaimai, A.; Matsumoto, H.; Nigara, Y.; Kawada, T.; Mizusaki, J.; Sfeir, J.; Van herle, J. *Solid State Ion.* **2004**, *175*, 341.
(140) Ramirez-Cabrera, E.; Atkinson, A.; Chadwick, D. *Appl. Catal. B-Environ.* **2002**, *36*, 193.
(141) Ramírez-Cabrera, E.; Atkinson, A.; Chadwick, D. *Solid State Ion.* **2000**, *136–137*, 825.
(142) Wilkes, M. F.; Hayden, P.; Bhattacharya, A. K. *J. Catal.* **2003**, *219*, 295.
(143) Zhao, S.; Gorte, R. J. *Appl. Catal., A* **2003**, *248*, 9.
(144) Casapu, M.; Krocher, O.; Mehring, M.; Nachtegaal, M.; Borca, C.; Harfouche, M.; Grolimund, D. *J. Phys. Chem. C* **2010**, *114*, 9791.
(145) Casapu, M.; Bernhard, A.; Peitz, D.; Mehring, M.; Elsener, M.; Kröcher, O. *Appl. Catal., B* **2011**, *103*, 79.
(146) Ananthapadmanabhan, P. V.; Menon, S. B.; Patil, D. S.; Venkatramani, N.; Rohatgi, V. K. *J. Mater. Sci. Lett.* **1992**, *11*, 501.
(147) Kaneko, H.; Taku, S.; Naganuma, Y.; Ishihara, T.; Hasegawa, N.; Tamaura, Y. *J. Sol. Energy Eng. Trans.-ASME* **2010**, *132*, 021202.
(148) Le Gal, A.; Abanades, S. *J. Phys. Chem. C* **2012**, *116*, 13516.
(149) Singh, P.; Hegde, M. S.; Gopalakrishnan, J. *Chem. Mater.* **2008**, *20*, 7268.
(150) Singh, P.; Hegde, M. S. *Chem. Mater.* **2010**, *22*, 762.
(151) Li, Q.; Thangadurai, V. *Fuel Cells* **2009**, *9*, 684.
(152) Vishnu, V. S.; George, G.; Reddy, M. L. P. *Dyes Pigments* **2010**, *85*, 117.
(153) Mazalov, L. N.; Sokolov, V. V.; Mang, Q.; Oglezneva, I. M.; Brenner, N. V.; Trubina, S. V. *Inorg. Mater.* **2006**, *42*, 1222.
(154) Jose, P. F.; Sugunan, S. *Indian J. Chem. Sect A-Inorg. Bio-Inorg. Phys. Theor. Anal. Chem.* **2006**, *45*, 1619.
(155) Bo, Q. B.; Feng, J.; Che, P.; Wang, J. P.; Wang, Q. Y.; Cao, X. Q.; Meng, J. *J. Phys.-Condes. Matter* **2003**, *15*, 5181.
(156) Che, P.; Bo, Q.; Feng, J.; Wang, Q.; Cao, X.; Meng, J. *J. Alloys Compd.* **2006**, *408–412*, 645.
(157) Zhou, D. F.; Xia, Y. J.; Zhu, J. X.; Guo, W.; Meng, J. *J. Am. Ceram. Soc.* **2009**, *92*, 1042.
(158) Zhou, D. F.; Xia, Y. J.; Zhu, J. X.; Meng, J. *Solid State Sci.* **2009**, *11*, 1587.
(159) Machida, M.; Uto, M.; Kurogi, D.; Kijima, T. *Chem. Mater.* **2000**, *12*, 3158.
(160) Machida, M.; Kurogi, D.; Kijima, T. *Chem. Mater.* **2000**, *12*, 3165.
(161) Qi, G.; Yang, R. T. *J. Phys. Chem. B* **2004**, *108*, 15738.
(162) Qi, G.; Yang, R. T.; Chang, R. *Appl. Catal., B* **2004**, *51*, 93.
(163) Luo, J.-Y.; Meng, M.; Yao, J.-S.; Li, X.-G.; Zha, Y.-Q.; Wang, X.; Zhang, T.-Y. *Appl. Catal., B* **2009**, *87*, 92.
(164) Murugan, B.; Ramaswamy, A. V.; Srinivas, D.; Gopinath, C. S.; Ramaswamy, V. *Chem. Mater.* **2005**, *17*, 3983.

(165) Kamimura, Y.; Sato, S.; Takahashi, R.; Sodesawa, T.; Akashi, T. *Appl. Catal., A* **2003**, *252*, 399.
(166) Pérez-Alonso, F. J.; López Granados, M.; Ojeda, M.; Terreros, P.; Rojas, S.; Herranz, T.; Fierro, J. L. G.; Gracia, M.; Gancedo, J. R. *Chem. Mater.* **2005**, *17*, 2329.
(167) Perez-Alonso, F. J.; Melián-Cabrera, I.; López Granados, M.; Kapteijn, F.; Fierro, J. L. G. *J. Catal.* **2006**, *239*, 340.
(168) Bao, H.; Chen, X.; Fang, J.; Jiang, Z.; Huang, W. *Catal. Lett.* **2008**, *125*, 160.
(169) Qiao, D.; Lu, G.; Liu, X.; Guo, Y.; Wang, Y.; Guo, Y. *J. Mater. Sci.* **2011**, *46*, 3500.
(170) Zhang, Z.; Han, D.; Wei, S.; Zhang, Y. *J. Catal.* **2010**, *276*, 16.
(171) Gupta, A.; Kumar, A.; Waghmare, U. V.; Hegde, M. S. *Chem. Mater.* **2009**, *21*, 4880.
(172) Jayakumar, O. D.; Vinu, A.; Guduru, K. V.; Sakuntala, T.; Tyagi, A. K. *J Nanosci. Nanotechnol.* **2010**, *10*, 2299.
(173) Kaneko, H.; Ishihara, H.; Taku, S.; Naganuma, Y.; Hasegawa, N.; Tamaura, Y. *J. Mater. Sci.* **2008**, *43*, 3153.
(174) Shinde, V. M.; Madras, G. *Appl. Catal., B* **2013**, *138–139*, 51.
(175) Singh, P.; Hegde, M. S. *Cryst. Growth Des.* **2010**, *10*, 2995.
(176) Hailstone, R. K.; DiFrancesco, A. G.; Allston, T. D.; Parsiegla, K.; Reed, K. J. *J. Nanopart. Res.* **2014**, *16*, 2267.
(177) Derk, A. R.; Moore, G. M.; Sharma, S.; McFarland, E. W.; Metiu, H. *Top. Catal.* **2014**, *57*, 118.
(178) Mistri, R.; Llorca, J.; Ray, B. C.; Gayen, A. *J. Mol. Catal. A: Chem.* **2013**, *376*, 111.
(179) Sharma, S.; Hu, Z.; Zhang, P.; McFarland, E. W.; Metiu, H. *J. Catal.* **2011**, *278*, 297.
(180) Younis, A.; Chu, D.; Li, S. *Appl. Phys. Lett.* **2013**, *103*, 253504.
(181) Phokha, S.; Pinitsoontorn, S.; Maensiri, S. *J. Appl. Phys.* **2012**, *112*, 113904.
(182) Ou, Y.-N.; Li, G.-R.; Liang, J.-H.; Feng, Z.-P.; Tong, Y.-X. *J. Phys. Chem. C* **2010**, *114*, 13509.
(183) Gayen, A.; Baidya, T.; Biswas, K.; Roy, S.; Hegde, M. S. *Appl. Catal., A* **2006**, *315*, 135.
(184) Gayen, A.; Priolkar, K. R.; Sarode, P. R.; Jayaram, V.; Hegde, M. S.; Subbanna, G. N.; Emura, S. *Chem. Mater.* **2004**, *16*, 2317.
(185) Kurnatowska, M.; Kepinski, L. *Mater. Res. Bull.* **2013**, *48*, 852.
(186) Mahammadunnisa, S.; Reddy, P. M. K.; Lingaiah, N.; Subrahmanyam, C. *Catal. Sci. Technol*, **2013**, *3*, 730.
(187) Li, T.; Xiang, G.; Zhuang, J.; Wang, X. *Chem. Commun.* **2011**, *47*, 6060.
(188) Liu, X.; Zuo, Y.; Li, L.; Huang, X.; Li, G. *RSC Advances* **2014**, *4*, 6397.
(189) Xu, J.; Xue, B.; Liu, Y.-M.; Li, Y.-X.; Cao, Y.; Fan, K.-N. *Appl. Catal., A* **2011**, *405*, 142.
(190) Foschini, C. R.; Souza, D. P. F.; Paulin Filho, P. I.; Varela, J. A. *J. Eur. Ceram. Soc.* **2001**, *21*, 1143.
(191) Kurzman, J. A.; Misch, L. M.; Seshadri, R. *Dalton Trans.* **2013**, *42*, 14653.
(192) Baidya, T.; Priolkar, K. R.; Sarode, P. R.; Hegde, M. S.; Asakura, K.; Tateno, G.; Koike, Y. *J. Chem. Phys.* **2008**, *128*.
(193) Bera, P.; Patil, K. C.; Jayaram, V.; Subbanna, G. N.; Hegde, M. S. *J. Catal.* **2000**, *196*, 293.

(194) Bera, P.; Priolkar, K. R.; Gayen, A.; Sarode, P. R.; Hegde, M. S.; Emura, S.; Kumashiro, R.; Jayaram, V.; Subbanna, G. N. *Chem. Mater.* **2003**, *15*, 2049.
(195) Hegde, M. S.; Madras, G.; Patil, K. C. *Acc. Chem. Res.* **2009**, *42*, 704.
(196) Priolkar, K. R.; Bera, P.; Sarode, P. R.; Hegde, M. S.; Emura, S.; Kumashiro, R.; Lalla, N. P. *Chem. Mater.* **2002**, *14*, 2120.
(197) Sharma, S.; Deshpande, P. A.; Hegde, M. S.; Madras, G. *Ind. Eng. Chem. Res.* **2009**, *48*, 6535.
(198) Misch, L. M.; Kurzman, J. A.; Derk, A. R.; Kim, Y.-I.; Seshadri, R.; Metiu, H.; McFarland, E. W.; Stucky, G. D. *Chem. Mater.* **2011**, *23*, 5432.
(199) Kurnatowska, M.; Kepinski, L.; Mista, W. *Appl. Catal., B* **2012**, *117–118*, 135.
(200) Hočevar, S.; Krašovec, U. O.; Orel, B.; Aricó, A. S.; Kim, H. *Appl. Catal., B* **2000**, *28*, 113.
(201) Jung, C. R.; Han, J.; Nam, S. W.; Lim, T. H.; Hong, S. A.; Lee, H. I. *Catal. Today* **2004**, *93–95*, 183.
(202) Kušar, H.; Hočevar, S.; Levec, J. *Appl. Catal., B* **2006**, *63*, 194.
(203) Sedmak, G.; Hočevar, S.; Levec, J. *J. Catal.* **2003**, *213*, 135.
(204) Wang, X.; Rodriguez, J. A.; Hanson, J. C.; Gamarra, D.; Martínez-Arias, A.; Fernández-García, M. *J. Phys. Chem. B* **2005**, *109*, 19595.
(205) Bera, P.; Aruna, S. T.; Patil, K. C.; Hegde, M. S. *J. Catal.* **1999**, *186*, 36.
(206) Bera, P.; Priolkar, K. R.; Sarode, P. R.; Hegde, M. S.; Emura, S.; Kumashiro, R.; Lalla, N. P. *Chem. Mater.* **2002**, *14*, 3591.
(207) Kaneko, H.; Miura, T.; Ishihara, H.; Taku, S.; Yokoyama, T.; Nakajima, H.; Tamaura, Y. *Energy* **2007**, *32*, 656.
(208) Shan, W.; Shen, W.; Li, C. *Chem. Mater.* **2003**, *15*, 4761.
(209) Fu, Q.; Saltsburg, H.; Flytzani-Stephanopoulos, M. *Science* **2003**, *301*, 935.
(210) Venezia, A. M.; Pantaleo, G.; Longo, A.; Di Carlo, G.; Casaletto, M. P.; Liotta, F. L.; Deganello, G. *J. Phys. Chem. B* **2005**, *109*, 2821.
(211) Dong, Q.; Yin, S.; Guo, C.; Sato, T. *Nanoscale Res. Lett* **2012**, *7*, 542.
(212) Collins, S.; Finos, G.; Alcántara, R.; del Rio, E.; Bernal, S.; Bonivardi, A. *Appl. Catal., A* **2010**, *388*, 202.
(213) Finos, G.; Collins, S.; Blanco, G.; del Rio, E.; Cíes, J. M.; Bernal, S.; Bonivardi, A. *Catal. Today* **2012**, *180*, 9.
(214) Vecchietti, J.; Collins, S.; Xu, W.; Barrio, L.; Stacchiola, D.; Calatayud, M.; Tielens, F.; Delgado, J. J.; Bonivardi, A. *J. Phys. Chem. C* **2013**, *117*, 8822.
(215) Bhella, S. S.; Shafi, S. P.; Trobec, F.; Bieringer, M.; Thangadurai, V. *Inorg. Chem.* **2010**, *49*, 1699.
(216) Baidya, T.; Gupta, A.; Deshpandey, P. A.; Madras, G.; Hegde, M. S. *J. Phys. Chem. C* **2009**, *113*, 4059.
(217) Gupta, A.; Hegde, M. S.; Priolkar, K. R.; Waghmare, U. V.; Sarode, P. R.; Emura, S. *Chem. Mater.* **2009**, *21*, 5836.
(218) Sasikala, R.; Gupta, N. M.; Kulshreshtha, S. K. *Catal. Lett.* **2001**, *71*, 69.
(219) Zhang, G.; Li, L.; Li, G.; Qiu, X.; Yan, G. *Solid State Sci.* **2009**, *11*, 671.
(220) Garcia Casado, P.; Mendiola, A.; Rasines, I. *Inorg. Chem.* **1982**, *21*, 2902.
(221) Hewston, T. A. *Inorg. Chem.* **1983**, *22*, 1967.
(222) Frolova, Y. V.; Kochubey, D. I.; Kriventsov, V. V.; Moroz, E. M.; Neofitides, S.; Sadykov, V. A.; Zyuzin, D. A. *Nucl. Instrum. Methods Phys. Res., Sect. A* **2005**, *543*, 127.
(223) Zhao, H.; Feng, S.; Xu, W. *Mater. Res. Bull.* **2000**, *35*, 2379.
(224) Dikmen, S.; Shuk, P.; Greenblatt, M. *Solid State Ion.* **1998**, *112*, 299.

(225) Jiang, D.; Wang, W.; Gao, E.; Zhang, L.; Sun, S. *J. Phys. Chem. C* **2013**, *117*, 24242.
(226) Li, G.; Mao, Y.; Li, L.; Feng, S.; Wang, M.; Yao, X. *Chem. Mater.* **1999**, *11*, 1259.
(227) Sardar, K.; Playford, H. Y.; Darton, R. J.; Barney, E. R.; Hannon, A. C.; Tompsett, D.; Fisher, J.; Kashtiban, R. J.; Sloan, J.; Ramos, S.; Cibin, G.; Walton, R. I. *Chem. Mater.* **2010**, *22*, 6191.
(228) Wang, Y.; Wang, F.; Zhang, C.; Zhang, J.; Li, M.; Xu, J. *Chem. Commun.* **2014**, *50*, 2438.
(229) Vilé, G.; Bridier, B.; Wichert, J.; Pérez-Ramírez, J. *Angew. Chem. Int. Ed.* **2012**, *51*, 8620.
(230) Gorte, R. J. *AlChE J.* **2010**, *56*, 1126.
(231) Hilaire, S.; Wang, X.; Luo, T.; Gorte, R. J.; Wagner, J. *Appl. Catal. A-Gen.* **2001**, *215*, 271.
(232) Ricote, S.; Jacobs, G.; Milling, M.; Ji, Y.; Patterson, P. M.; Davis, B. H. *Appl. Catal., A* **2006**, *303*, 35.
(233) Mock, P. *EU CO_2 standards for passenger cars and light-commercial vehicles*, The International Council on Clean Transportation, 2013.
(234) Kaspar, J.; Fornasiero, P.; Graziani, M. *Catal. Today* **1999**, *50*, 285.
(235) Müller-Buschbaum, H. *Z. Anorg. Allg. Chem.* **2005**, *631*, 1005.
(236) Müller-Buschbaum, H. *Z. Anorg. Allg. Chem.* **2006**, *632*, 1625.
(237) Müller-Buschbaum, H. *Z. Anorg. Allg. Chem.* **2007**, *633*, 1289.
(238) Müller-Buschbaum, H. *Z. Anorg. Allg. Chem.* **2008**, *634*, 2111.
(239) Denis Romero, F.; Burr, S. J.; McGrady, J. E.; Gianolio, D.; Cibin, G.; Hayward, M. A. *J. Am. Chem. Soc.* **2013**, *135*, 1838.
(240) Sinclair, A.; Rodgers, J. A.; Topping, C. V.; Míšek, M.; Stewart, R. D.; Kockelmann, W.; Bos, J.-W. G.; Attfield, J. P. *Angew. Chem. Int. Ed.* **2014**, *53*, 8343.
(241) Stitzer, K. E.; Smith, M. D.; Gemmill, W. R.; zur Loye, H.-C. *J. Am. Chem. Soc.* **2002**, *124*, 13877.
(242) Bouchard, R. J.; Gillson, J. L. *Mater. Res. Bull.* **1972**, *7*, 873.
(243) Callaghan, A.; Moeller, C. W.; Ward, R. *Inorg. Chem.* **1966**, *5*, 1572.
(244) Hong, S.-T.; Sleight, A. W. *J. Solid State Chem.* **1997**, *128*, 251.
(245) Battle, P. D.; Kim, S. H.; Powell, A. V. *J. Solid State Chem.* **1992**, *101*, 161.
(246) Lightfoot, P.; Battle, P. D. *J. Solid State Chem.* **1990**, *89*, 174.
(247) Doi, Y.; Wakeshima, M.; Hinatsu, Y.; Tobo, A.; Ohoyama, K.; Yamaguchi, Y. *J. Mater. Chem.* **2001**, *11*, 3135.
(248) Renard, C.; Daviero-Minaud, S.; Huve, M.; Abraham, F. *J. Solid State Chem.* **1999**, *144*, 125.
(249) Dussarrat, C.; Fompeyrine, J.; Darriet, J. *Eur. J. Solid State Inorg. Chem.* **1994**, *31*, 289.
(250) Donohue, P. C.; Katz, L.; Ward, R. *Inorg. Chem.* **1965**, *4*, 306.
(251) Ogawa, T.; Sato, H. *J. Alloys Compd.* **2004**, *383*, 313.
(252) Nakatsuji, S.; Ikeda, S. I.; Maeno, Y. *J. Phys. Soc. Jpn.* **1997**, *66*, 1868.
(253) Nakamura, F.; Goko, T.; Ito, M.; Fujita, T.; Nakatsuji, S.; Fukazawa, H.; Maeno, Y.; Alireza, P.; Forsythe, D.; Julian, S. R. *Phys. Rev. B* **2002**, *65*, 220402.
(254) Alexander, C. S.; Cao, G.; Dobrosavljevic, V.; McCall, S.; Crow, J. E.; Lochner, E.; Guertin, R. P. *Phys. Rev. B* **1999**, *60*, R8422.
(255) Lichtenberg, F. *Prog. Solid State Chem.* **2002**, *30*, 103.

(256) Mackenzie, A. P.; Maeno, Y. *Rev. Mod. Phys.* **2003**, *75*, 657.
(257) Malvestuto, M.; Carleschi, E.; Fittipaldi, R.; Gorelov, E.; Pavarini, E.; Cuoco, M.; Maeno, Y.; Parmigiani, F.; Vecchione, A. *Phys. Rev. B* **2011**, *83*, 165121.
(258) Kafalas, J. A.; Longo, J. M. *J. Solid State Chem.* **1972**, *4*, 55.
(259) Yoshida, Y.; Nagai, I.; Ikeda, S.-I.; Shirakawa, N.; Kosaka, M.; Môri, N. *Phys. Rev. B* **2004**, *69*, 220411.
(260) Crawford, M. K.; Harlow, R. L.; Marshall, W.; Li, Z.; Cao, G.; Lindstrom, R. L.; Huang, Q.; Lynn, J. W. *Phys. Rev. B* **2002**, *65*, 214412.
(261) Mitchell, R. H. *Perovskites: Modern and Ancient*; Almaz Press, 2002.
(262) Cole, M. W. *Nature* **2013**, *502*, 455.
(263) Munenaka, T.; Sato, H. *J. Phys. Soc. Jpn.* **2006**, *75*, 103801.
(264) Renard, C.; Daviero-Minaud, S.; Abraham, F. *J. Solid State Chem.* **1999**, *143*, 266.
(265) Gadzhiev, M. I.; Shaplygin, I. S. *Russ. J. Inorg. Chem.* **1984**, *29*, 1230.
(266) Popova, T. L. *Sov. Prog. Chem.* **1982**, *48*, 8.
(267) Dussarrat, C.; Grasset, F.; Bontchev, R.; Darriet, J. *J. Alloys Compd.* **1996**, *233*, 15.
(268) Carim, A. H.; Dera, P.; Finger, L. W.; Mysen, B.; Prewitt, C. T.; Schlom, D. G. *J. Solid State Chem.* **2000**, *149*, 137.
(269) Abanades, S.; Legal, A.; Cordier, A.; Peraudeau, G.; Flamant, G.; Julbe, A. *J. Mater. Sci.* **2010**, *45*, 4163.

Chapter 2: Experimental Techniques

2.1 Introduction

A description of the experimental techniques employed and a brief overview of the principles behind the key techniques are included here. Specific details on synthetic procedures can be found in results Chapters 3 – 6.

2.2 Hydrothermal Synthesis

In this work a range of new materials (detailed in Chapters 3, 4 and 6) were prepared by a hydrothermal synthesis.[1] Typically, reagents were dissolved or suspended in distilled water with stirring and the solution/suspension was sealed in a Teflon-lined 23 ml stainless steel autoclave (Figure 2. 1). Autoclaves were then placed in a pre-heated, fan-assisted oven for 24 hours (temperature depending on target compound). Autoclaves were then removed from the oven and allowed to cool to room temperature before opening and solids were separated from the remaining solution by suction filtration.

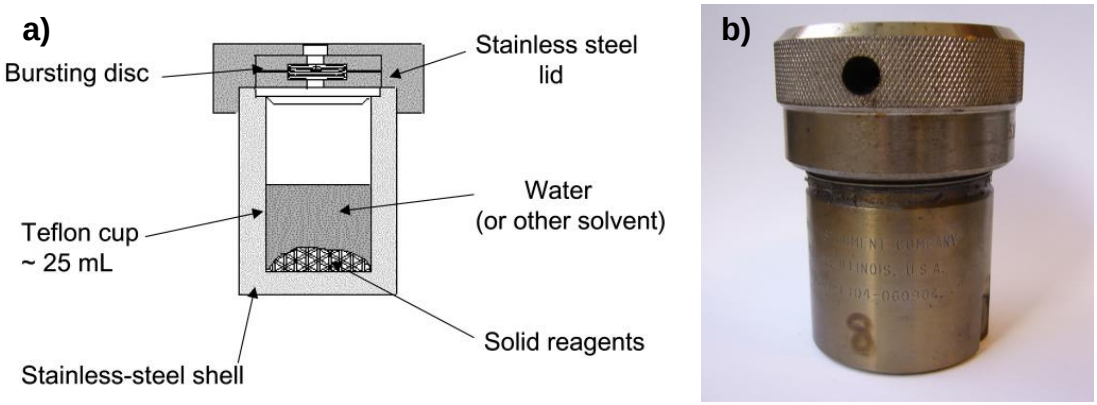

Figure 2. 1a) A schematic and b) a photograph of a Teflon-lined stainless steel autoclave, of the design used for hydrothermal preparations described in this thesis. Schematic taken from review by Walton.[1]

2.3 Powder Diffraction[2]

2.3.1 General Principles

A crystal is a solid where (ideally) all atoms are spatially ordered. This order is defined as a regular, periodic repetition of atoms in space (typically three-dimensional, but lower dimensional crystallinity is also known).

Three-dimensional periodicity can be described by a *unit cell*, a parallelepiped from which a crystal can be completely constructed solely by translational displacements. A unit cell is completely defined by six lattice parameters: *a*, *b*, *c*, *α*, *β* and *γ*, Figure 2. 1. Any unit cell that can be used to describe the structure is allowed, though conventionally the unit cell with the highest symmetry and smallest volume is selected. These lattice parameters and the translational symmetry of the structure gives rise to seven crystal systems (Table 2. 1).

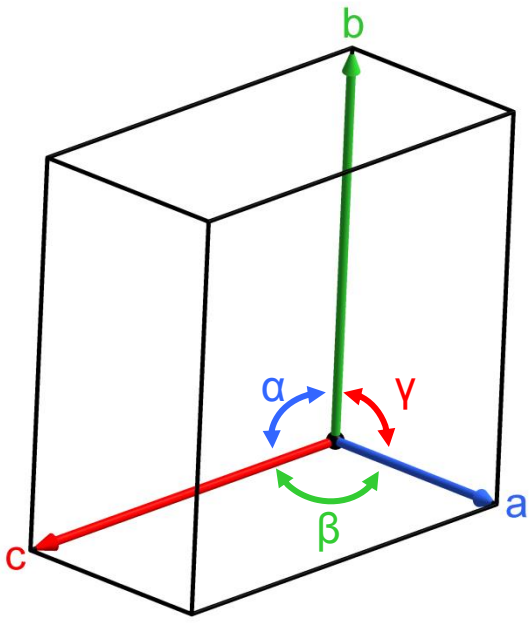

Figure 2. 2 A three-dimensional unit cell.

A *lattice* is a set of imaginary, equivalent points ordered in space. Depending upon the translational symmetry, a lattice can be *primitive*, *body-centred* or *face-centred*, denoted by the shorthand *P*, *I* or *F* (or *C*, if only centred on one face – a *base-centred* lattice) (Figure 2. 3). The only translational symmetry of a primitive lattice is that of the unit cell. A body-centred lattice has a lattice point in the centre of the cell, *i.e.* translational symmetry of $(x + ½, y + ½, z + ½)$. A face-centred lattice has lattice points at the centre of each face, *i.e.* translational symmetry of $(x + ½, y + ½, z)$, $(x + ½, y, z + ½)$ and $(x, y + ½, z + ½)$. A base-centred lattice has only translational symmetry of $(x + ½, y + ½, z)$.

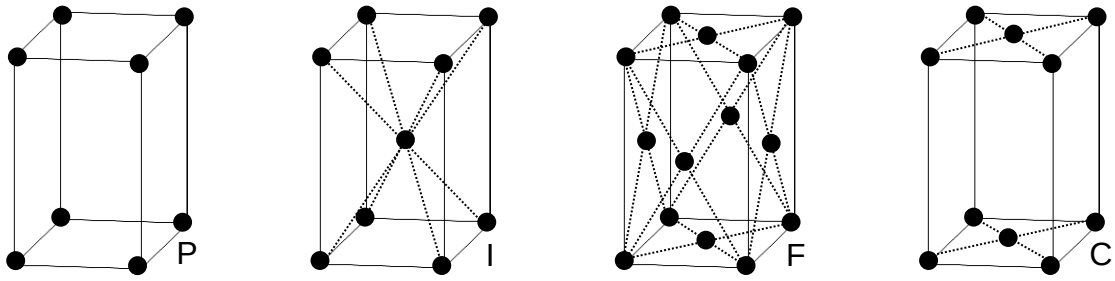

*Figure 2. 3 Primitive (*P*), body-centred (*I*), face-centred (*F*) and base-centred (*C*) unit cells.*

A crystal system and a lattice centring can be combined to give a *Bravais lattice*. Not all crystal lattices can be combined with every type of lattice centring to give a unique Bravais lattice: one half can be reduced to another, smaller Bravais lattice. Hence 14 Bravais lattices exist in three dimensions (Table 2. 1). Addition of further symmetry elements that describe the arrangement of unique atoms within the unit cell (rotation, reflection, improper rotation, screw axis or glide plane) can be applied to generate a space group. From a space group and coordinates of unique atom positions the entire crystal structure can be defined.

Table 2. 1 The symmetry of the seven crystal families and irreducible Bravais lattices.

Crystal Family	Unit Cell Parameters	Unit Cell Symmetry	Bravais Lattices
Triclinic	$a \neq b \neq c$; $\alpha \neq \beta \neq \gamma$	$\bar{1}$	*P*
Monoclinic	$a \neq b \neq c$; $\alpha = \gamma = 90°$; $\beta \neq 90°$	2/m	*P, C*
Orthorhombic	$a \neq b \neq c$; $\alpha = \beta = \gamma = 90°$	mmm	*P, C, I, F*
Tetragonal	$a = b \neq c$; $\alpha = \beta = \gamma = 90°$	4/mmm	*P, I*
Hexagonal/Trigonal	$a = b \neq c$; $\alpha \neq \beta = 90°$; $\gamma = 120°$	6/mmm	*P, R**
Cubic	$a = b = c$; $\alpha = \beta = \gamma = 90°$	m$\bar{3}$m	*P, I, F*

*R = Rhombohedral; translational symmetry of (x + ⅔, y + ⅓, z + ⅓) and (x + ⅓, y + ⅔, z + ⅔).

A crystallographic plane is an imaginary plane in a crystal, described by Miller indices *h*, *k* and *l*. A plane with indices (*hkl*) divides lattice parameters *a*, *b* and *c* into *h*, *k* and *l* equal parts; respectively, *i.e*. the planes intersect the *a*, *b* and *c* cell edges at 1/*h*, 1/*k* and 1/*l*, respectively (Figure 2. 4). When a Miller index = 0, this indicates that the plane is parallel to the corresponding lattice parameter.

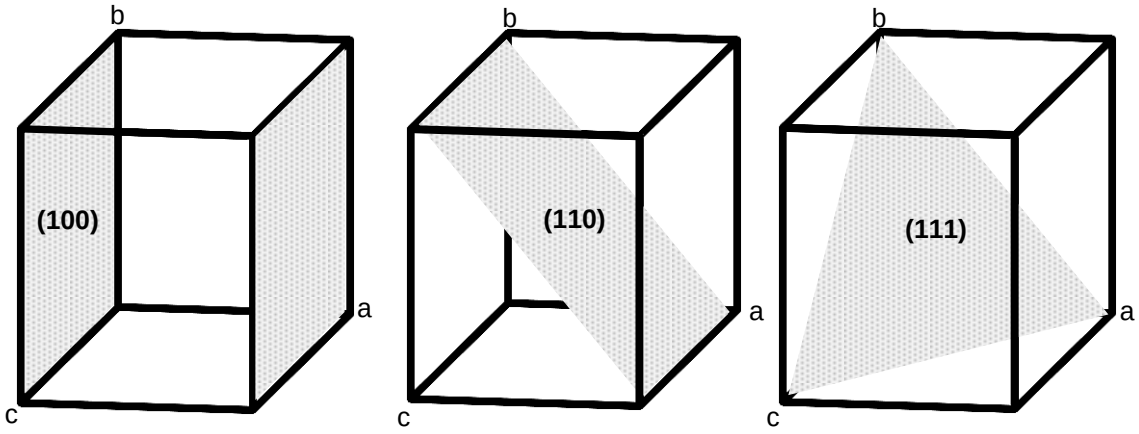

Figure 2. 4 (100), (110) and (111) crystallographic planes.

The distance between crystallographic planes, d_{hkl} can be related to the unit cell lengths. In an orthogonal unit cell this relationship is (non-orthogonal cells have similarly derived, more complex expressions):

$$\frac{1}{d_{hkl}} = \sqrt{\frac{h^2}{a^2} + \frac{k^2}{b^2} + \frac{l^2}{c^2}}$$

Equation 2. 1 Relationship between d*-spacing and lattice parameters.*

2.3.2 The Powder X-ray Diffraction Experiment

X-rays are of an appropriate wavelength to be diffracted by a crystallographic lattice. X-rays are scattered by the electrons in atoms, and a diffraction pattern is the result of interference of X-rays. Constructive interference of an X-ray of wavelength, λ, occurs at certain angles of incidence, θ (Figure 2. 5), which satisfy the Bragg equation:

$$n\lambda = 2d \sin\theta$$

Equation 2. 2 The Bragg equation. n *is an integer corresponding to a number of wavelengths (in practise* n = *1).*

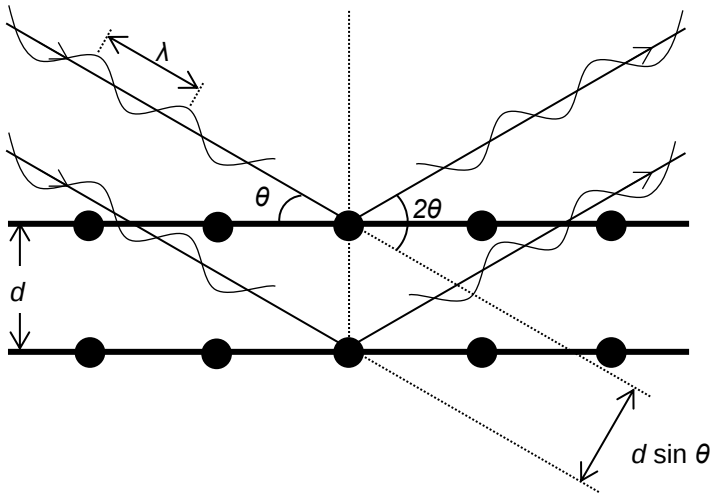

Figure 2. 5 Constructive interference of X-rays according to the Bragg equation.

In an ideal polycrystalline powder, every crystallographic orientation is represented equally. By varying the angle of incidence and detector angle (in either a Bragg-Brentano theta-2 theta or Bragg-Brentano theta-theta configuration[2]) a one-

dimensional *diffraction pattern* can be obtained with detected X-rays plotted as a function of scattering angle 2θ. The constructive interference result in diffraction maxima, referred to as *Bragg reflections* (Figure 2. 6).

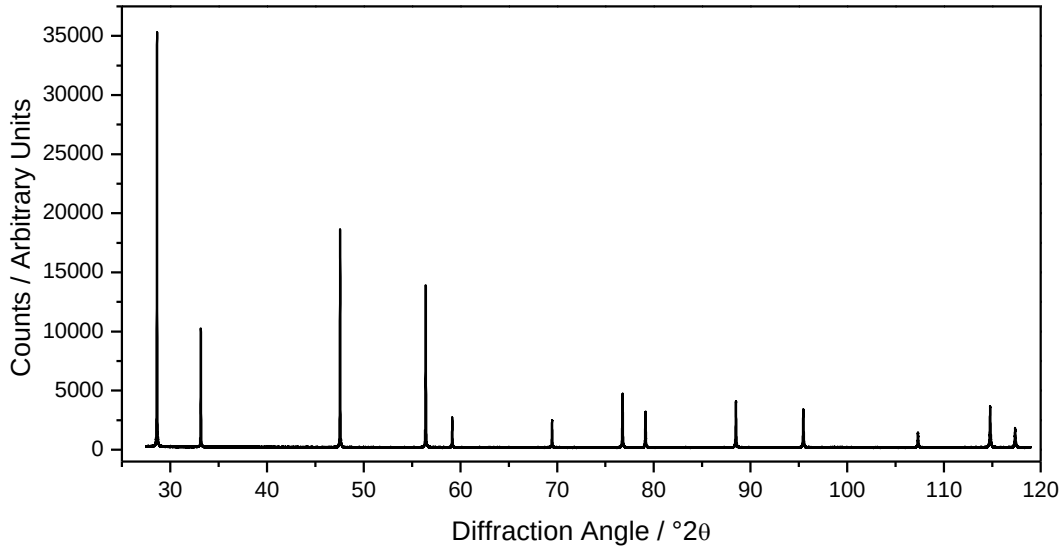

Figure 2. 6 High-resolution powder diffraction pattern of CeO_2 (NIST).

When the crystallite size, τ, decreases below ~1 μm, Bragg reflections' width increases according to the Scherrer equation:

$$\tau = \frac{K\lambda}{\beta \cos\theta}$$

Equation 2. 3 The Scherrer equation, where K is a shape factor (= 0.9) and β is the Bragg peak broadening in radians.

Powder X-ray diffraction (XRD) is one of the key techniques used to characterise materials presented in this thesis. A Bruker D5000 powder diffractometer was used to collect many of the powder diffraction patterns included herein. For this diffractometer samples were pressed into an Al sample holder using a glass slide, which lead to the presence of Al Bragg reflections in the collected diffraction pattern. These peaks were masked for Le Bail and Rietveld fits to the data. Counts

are given in arbitrary units since the intensities are based on X-ray source, X-ray detector, sample size and scanning speed, which varies between each diffractometer and experiment. The step size in a typical scan was 0.01°, and the time per step was 8 s. A Bruker D5005 was used to collect low temperature diffraction data, and a Bruker D8 Advance powder diffractometer was used to collect *in situ* heating powder XRD. Samples were packed into a Macor sample holder which was placed into an Anton Parr XRK900 heating stage. Each individual scan had a step size of 0.008° and a time per step of 0.5 s. Data were collected at room temperature and at 50 °C intervals from 50 °C to 900 °C. The heating ramp rate was 10 °C min^{-1} and a dwell time of 300 s was included before data collection began, in order for the temperature to stabilise. For experiments conducted in reducing conditions 5% H_2 in N_2 was flowed over the sample whilst it was heated to simulate temperature-programmed reduction (TPR) conditions. Whilst TPR profiles cannot be perfectly correlated to *in situ* diffraction data due to the long periods spent at each temperature to allow the collection of high quality diffraction patterns (approximately 1 hour), it provides a useful tool for analysing long term stability at elevated temperatures under oxidising and reducing conditions. This slower heating rate can also give an indication of the absolute reducibility of the materials, whereas faster TPR experiments measure their dynamic reducibility. Furthermore for materials which phase separate, *in situ* diffraction experiments can give insight into the temperature at which this occurs, and give complementary information to allow the assignment of hydrogen uptakes seen in TPR. All of these use un-monochromated Cu $K\alpha_{1,2}$ radiation (λ_1 = 1.5405 Å, λ_2 = 1.5418 Å).

High resolution powder XRD data was collected using a Philips X'pert Pro powder diffractometer with a curved Johansson monochromator to give monochromatic Cu

$K\alpha_1$ X-ray radiation. The sample was rotated (8 rpm) to reduce preferred orientation effects. Scans had a step size of 0.0131° and a time per step of 10 s.

Powder synchrotron XRD data were also collected for $Ba_2Ru_3O_9(OH)$ using beamline I11,[3] Diamond Light Source, U.K. The X-ray wavelength was 0.827154 Å, and a step size of 0.001° and a time per step of 0.01 s were used.

2.3.3 Powder Time-of-Flight Neutron Diffraction

Neutrons, like X-rays, can be diffracted by an atomic lattice. However, unlike X-rays, neutrons are not scattered by electrons but by nuclei of atoms. This has three significant consequences. Firstly, since the X-ray scattering structure factor is determined by the number of electrons the atom possesses, light elements scatter X-rays much more weakly than heavier elements, making determination of positions of light elements difficult with X-rays. Conversely, neutron structure factors have no relationship to atomic number, and vary comparatively little between elements. This is particularly useful for studying metal oxides, since it allows accurate information about oxygen atoms to be extracted that would be difficult to extract from X-ray diffraction data. Secondly, since the nucleus acts as a point source (as opposed to the much larger, diffuse electron cloud), neutron scattering intensity has much less angular dependence than X-ray scattering. This means that more Bragg reflections (at smaller *d*-spacings) can be measured accurately. Thirdly, since the neutron has a spin, they are scattered by magnetic moments. When long-range magnetic order exists, magnetic Bragg reflections are found in the neutron diffraction pattern.

Neutron diffraction data presented in this thesis were collected at ISIS (U.K), a neutron spallation source. Neutrons are generated in pulses and are thus ideally suited to time-of-flight diffraction. Time-of-flight diffractometers consist of

stationary, fixed-angle detectors. Instead of counting neutrons as a function of angle, they can be related to their time-of-flight, *t*, which is directly proportional to *d*-spacing:

$$t = \left(\frac{2m}{h}\right) L \sin\theta \, d$$

Equation 2. 4 Relationship between a neutron time-of-flight and d*-spacing, derived by combining the de Broglie relationship and the Bragg equation, where m is the neutron mass,* h *is the Planck constant and* L *is the total neutron flight distance from the moderator to the detector.*

Room temperature powder neutron diffraction data were collected on the GEM[4,5] instrument at ISIS. Samples were placed into vanadium sample cans either 6 mm or 8 mm in diameter. Diffraction patterns of $SrRu_2O_6$, $Ba_2Ru_3O_9(OH)$ and $Ba_4Ru_3O_{12}$ were collected by Dr. Ronald I. Smith as part of the 'GEM Xpress' service. Diffraction data from $Ca_{1.5}Ru_2O_7$, CeO_2 and $Ce_{1-x}Nb_xO_{2-\delta}$ (x = 0.10, 0.20, 0.30) made hydrothermally in NaOH were collected by Luke Daniels and Helen Playford.

The instrument WISH[6] was used to collect powder neutron diffraction data of $SrRu_2O_6$ at a range of temperatures from 5 to 623 K. The sample was placed in a 8 mm vanadium can which was placed inside a closed cycle refrigerator (CCR) fitted with a hot stage.

2.3.4 Software Used

Rietveld[7] and Le Bail[8] fits were carried out using the software GSAS,[9] implemented mainly using the EXPGUI interface.[10] An initial model for the magnetic structure was proposed by Stefano Agrestini (Max-Planck Insitut, Germany), using the software FullProf.[11] *Ab initio* structure determination of $Ba_2Ru_3O_9(OH)$ and $Ba_4Ru_3O_{12}$ was performed using Fox,[12] further details are provided in Chapter 6.

Crystal structures are visualised using the software Diamond 3.2i.[13]

2.4 General Characterisation Techniques

2.4.1 Electron Microscopy

2.4.1.1 Scanning Electron Microscopy

Scanning electron microscopy was used to determine the crystal morphology of the alkaline earth ruthenates described in Chapter 6. Images were collected using a Zeiss Supra 55-VP scanning electron microscope, which uses a field emission gun with an accelerating voltage of 20 kV to generate an electron beam. A small amount of powder was sprinkled onto a piece of carbon tape. Energy dispersive X-ray analysis was used to give an approximate metal ratio at multiple points of the sample, with the intention of checking sample homogeneity. The software 'Genesis' was used to collect the spectra and quantify the metal ratio.

2.4.1.2 Transmission Electron Microscopy

Transmission electron microscopy images were collected by Reza J. Kashtiban, (Department of Physics, University of Warwick) using either a JEOL 2100 TEM or a JEOL ARM200F TEM. Both operated at 200 kV and have LaB_6 filaments.

2.4.2 Infrared Spectroscopy

Fourier transform infrared spectroscopy (FT-IR) was used to determine the presence of water, hydroxide or ammonium by looking for O – H and N – H stretches at 3600 – 3200 cm^{-1}.[14] Spectra were recorded using a Perkin Elmer Paragon 1000 FT-IR spectrometer in attenuated total reflection mode.

2.4.3 Thermogravimetric Analysis

Thermogravimetric analysis[15] was used to determine mass loss in the oxides as a function of temperature. This was used to infer decomposition temperatures and quantify water content in the oxides prepared. Data were collected by Luke Daniels using a Mettler-Toledo TGA/DSC1 instrument. A small amount of sample (~10 – 20 mg) was placed in an alumina crucible and heated from room temperature to 1000 °C at a rate of 10 °C min^{-1}.

2.4.4 Surface Area Measurement

Surface areas were calculated from N_2-adsorption isotherms using the theory proposed by Brunauer, Emmett and Teller,[16] whereby the number of gas molecules adsorbed onto the surface of the sample is related to the surface area of the material. Isotherms were collected at Johnson Matthey Technology Centre (JMTC, Sonning Common, UK) using a Micromeritics Tristar 3000 porosimeter. Samples (0.05 – 0.25 g) were first placed into a tube and degassed by passing a stream of N_2 over the sample whilst it was heated at 200 °C for 10 hours. The tubes were then evacuated and known amounts of N_2 introduced at cryogenic temperature up to saturation pressure. The relative pressure is measured, from which total adsorbed N_2 is inferred.

2.4.5 Pycnometry

Pycnometry was used to determine the density of some of the oxides prepared. A sample of accurately known mass was placed into a chamber of known volume. The chamber is filled with a volume of He and (after an equilibration time) the pressure was measured. A valve then opens and the gas expands to fill a second chamber of known volume and, after a second equilibration, the pressure is again measured.

Since the product of volume and pressure is constant (in a closed system at constant temperature) and the volumes of both chambers are known, the volume of the sample can be accurately determined, allowing the density to be calculated.

A Micromeritics AccuPyc 1330 gas pycnometer (Department of Physics, University of Warwick) using He gas was used. A 1 cm^3 insert was used, and the device was calibrated using a stainless steel ball-bearing of known volume.

2.4.6 Raman Spectroscopy[17]

Raman spectroscopy can be used to measure vibrational frequencies that correspond to changing polarisability. Unlike infrared spectroscopy, only inelastically scattered photons are observed, which have transferred some energy to excite vibrations. In crystalline materials it is the crystal lattice which vibrates to give macroscopic 'phonon' modes. Different crystal lattices exhibit different phonon modes, and thus Raman spectroscopy can be used to identify lattices.

Data were collected by M. Hilni Harunsani. All data were collected at room temperature, using a Renishaw inVia Raman Microscope equipped with an Ar^+ laser with wavelength 514.5 nm and Renishaw charge-coupled device (CCD) detectors.

2.4.7 Inductively Coupled Plasma-Optical Emission Spectroscopy

The amounts of metals in the prepared materials were determined by optical emission spectroscopy. Samples were digested by HBr to give a solution, which is nebulised into a plasma. Each element has a characteristic atomic spectral line, and the number of atoms of that element is determined by the intensity of the emitted light.

Assays were obtained by both Stephen Goodall (Medac Ltd, U.K.) using a Varian Vista MPX ICP-OES system with a CCD detector; and Matt Gregory, Ana-Maria Rusu and Ian Briggs (JMTC, Sonning Common, UK) using a Perkin Elmer Optima 3300RL ICP-OES system.

2.5 X-ray Absorption Spectroscopy[18]

X-ray absorption spectral data were collected on Beamline B18[19] (Diamond Light Source, U.K.). Samples were diluted with polyethylene powder and pressed into pellets approximately 1 mm thick. Absorption data were collected in transmission mode. Spectra were normalised using ATHENA.[20]

Although the majority of reference materials were purchased, it was necessary to prepare Sb_2O_4 (by heating Sb_2O_3 in air to 500 °C[21]) and $La_{4.87}Ru_2O_{12}$ (by repeatedly grinding together La_2O_3 and RuO_2 in the appropriate ratio together, and heating for 12 hours at 1050 °C[22]).

X-ray absorption spectroscopy concerns the absorption of photons and the ejection of a core electron. These absorptions occur at energies specific to the element. The spectra can be split into two regions: the X-ray Absorption Near Edge Spectroscopy (XANES) region and the Extended X-ray Absorption Fine Structure (EXAFS) region (Figure 2. 7).

The XANES comprises the X-ray absorption edge and a small portion of the post-edge (~50 eV). Local coordination environment can greatly affect the edge's shape, and pre-edge features can be caused by electronic transitions to empty bound states. The edge's position can also be affected by the oxidation state of the atom: the ionisation energy increases as the oxidation state increases.

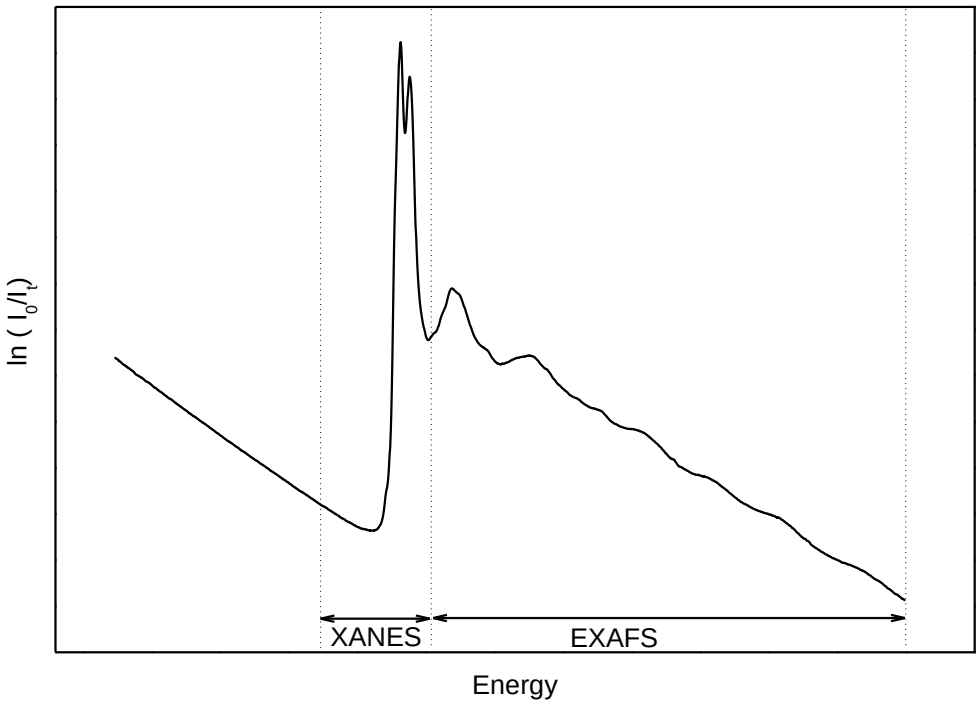

Figure 2. 7 An X-ray absorption spectrum split into the XANES and EXAFS regions.

Atoms surrounding the absorbing atom scatter the photoelectron wave, which causes an interference pattern that alters the probability of the atom's core electrons interacting with X-rays. This causes the ripples seen in the EXAFS region, which can be used to gain information about the local environment of the absorbing atom.[18]

Pd K-edge and Pt L_{III}-edge EXAFS data were analysed by Richard Walton using the software ATHENA.[20]

2.6 Redox Property Measurement

2.6.1 Temperature-Programmed Reduction

Temperature-programmed reduction (TPR) is a widely employed technique,[23-29] used to assess the reducibility of the doped cerias. A reducing gas (typically H_2) is passed over a sample which is heated at a constant rate and the variation of H_2 before and

after contact with the sample is measured. A decrease in the concentration of H_2 is indicative of a reduction of the sample.

The temperature-programmed reduction/oxidation apparatus at JMTC (Figure 2. 8a) was used to collect TPR profiles. H_2 consumption was measured by the variation in thermal conductivity of the gas before and after contact with the sample (Figure 2. 8b). A H_2O trap after the sample absorbs water created by H_2 oxidation. In order to quantify accurately the hydrogen consumption a known quantity (1 ml) of N_2 was injected into the H_2/N_2 gas stream before the experiment began to create a 'calibration peak'. Quantification of H_2 consumption was carried by the integration of TPR profile as a function of time using the program TPROVL (developed in house by JMTC). The results are given as an amount of H atoms oxidised per gram of sample (mmol(H) g^{-1}) to allow convenient calculation of Ce(IV) reduced. Previous work has estimated the error to be ±10% for the total H_2 consumption and ±15% for integration of the high and low segments of the TPR profile.[30] These estimations have been used herein to allow meaningful comparison between integration values. Sample temperature was measured by a thermocouple placed beside the sample tube.

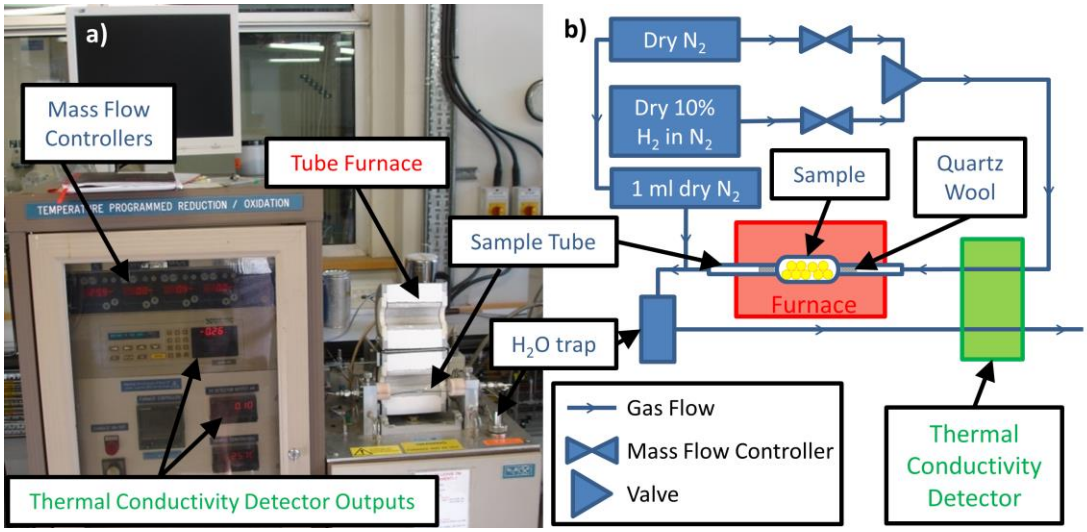

Figure 2. 8 JMTC TPR/O apparatus a) photograph and b) schematic annotated with key components. A secondary valve (not shown) allows TPO to be carried out using 10% O_2 in He.

2.6.2 Dynamic Oxygen Storage Capacity Measurement

Oxygen storage capacity (OSC) measurements were carried out at JMTC using custom made apparatus with the help of Noelia Cortes Felix and Francesco Dolci (JMTC).

To measure dynamic OSC a He gas stream containing alternating pulses of 1% CO and 0.5% O_2 in He, each 250 s in length at a rate of 100 ml min^{-1}, was passed over the oxide (loaded with 0.5 wt% Rh) and the concentration of these feed gases (and CO_2) was monitored by mass spectrometry (Figure 2. 9a). 0.5 wt% Rh was supported onto the oxides by incipient wetness impregnation of an appropriate volume of $Rh(NO_3)_3$ solution and calcination at 500 °C. The sample was pelletised and sieved to give particles sized between 250 and 355 µm and approximately 0.1 g was loosely packed into a quartz capillary. Pelletisation of the sample was necessary in order to stop a fine powder from packing tightly and limiting the flow of gas, whilst a maximum diameter of 355 µm ensured that particles were not too big for diffusion of gases to become rate limiting. The sample was heated in 50 °C increments and held there for several CO – O_2 cycles, Figure 2. 9b. Dynamic OSC was calculated from the measured breakthrough time, t_B of CO by the equation:

$$\mathrm{OSC} = \frac{Q_{CO} \times t_B}{V_m}$$

Equation 2. 5 Dynamic oxygen storage capacity, OSC, is calculated from the CO breakthrough time, t_B *in s.* Q_{CO} *is CO flow rate, 0.0167 ml* s^{-1} *and* V_m *is the ideal molar volume at room temperature,* 24×10^{-3} *ml µmol*$^{-1}$.

t_B is defined as the time taken for CO to be detected after the start of a CO pulse in a gas stream after the gas stream has passed over a sample, Figure 2. 9c. This delay in

CO detection is caused by its oxidation to CO_2 by the fast extraction of O from the oxide. t_0 can be inferred by the detection of the CO_2 (and the absence of O_2).

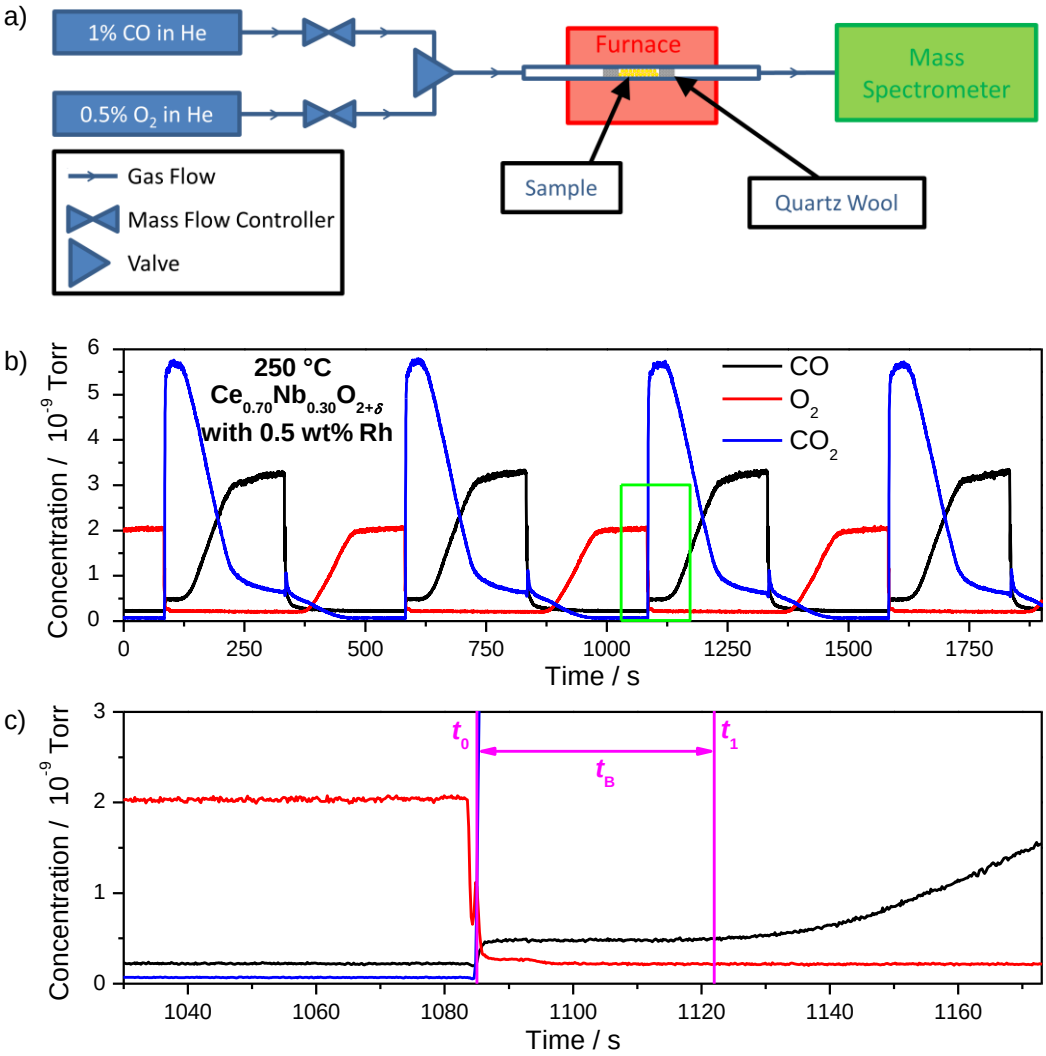

Figure 2. 9a) Schematic of OSC measurement apparatus. b) Concentration of CO, O_2 and CO_2 as a function of time in gas stream after passing over $Ce_{0.70}Nb_{0.30}O_{2+\delta}$ (loaded with 0.5 wt% Rh) at 250 °C. Green box shows area shown in c), a zoomed in view, centred around the start of a CO pulse, at t_0. The time at which the CO concentration begins to increase is shown as t_1.

2.7 Magnetometry

In order to examine the magnetic properties of the alkaline earth ruthenates, magnetic susceptibility data was collected.

A Quantum Design MPMS XL7 SQUID (superconducting quantum interference device) magnetometer was used to collect magnetic susceptibility data as a function of temperature. Data were collected with the assistance of Martin R. Lees. A small amount of sample (10 – 25 mg) was sealed in a small gel capsule, which was placed in the middle of plastic straw. Low temperature data were collected from 5 to 400 K in an applied field of 100 or 1000 Oe.

To collect high temperature susceptibility data from $SrRu_2O_6$, it was pressed into a pellet and a fragment of the pellet was placed in a ceramic tube. This ceramic tube was placed in an oven, which was then placed inside the magnetometer. The oven was heated to 723 K (450 °C) and a 1000 Oe field was applied. The oven was then allowed to cool to room temperature whilst data were collected.

2.8 References

(1) Walton, R. I. *Chem. Soc. Rev.* **2002**, *31*, 230.
(2) Pecharsky, V.; Zavalij, P. *Fundamentals of Powder Diffraction and Structural Characterization of Materials, Second Edition:*; Springer, 2009.
(3) Thompson, S. P.; Parker, J. E.; Potter, J.; Hill, T. P.; Birt, A.; Cobb, T. M.; Yuan, F.; Tang, C. C. *Rev. Sci. Instrum.* **2009**, *80*, 075107.
(4) Hannon, A. C. *Nucl. Instrum. Methods Phys. Res., Sect. A* **2005**, *551*, 88.
(5) Williams, W. G.; Ibberson, R. M.; Day, P.; Enderby, J. E. *Physica B* **1997**, *241–243*, 234.
(6) Chapon, L. C.; Manuel, P.; Radaelli, P. G.; Benson, C.; Perrott, L.; Ansell, S.; Rhodes, N. J.; Raspino, D.; Duxbury, D.; Spill, E.; Norris, J. *Neutron News* **2011**, *22*, 22.
(7) Rietveld, H. M. *J. Appl. Crystallogr.* **1969**, *2*, 65.
(8) Le Bail, A.; Duroy, H.; Fourquet, J. L. *Mater. Res. Bull.* **1988**, *23*, 447.
(9) Larson, A. C.; Van Dreele, R. B. *Los Alamos National Laboratory Report LAUR* **1994**, 86.
(10) Toby, B. H. *J. Appl. Crystallogr.* **2001**, *34*, 210.
(11) Rodríguez-Carvajal, J. *Physica B* **1993**, *192*, 55.
(12) Favre-Nicolin, V.; Cerny, R. *J. Appl. Crystallogr.* **2002**, *35*, 734.
(13) Pennington, W. *J. Appl. Crystallogr.* **1999**, *32*, 1028.
(14) Williams, D. H.; Fleming, I. *Spectroscopic methods in organic chemistry*; McGraw-Hill, 1995.
(15) Atkins, P. *Shriver and Atkins' Inorganic Chemistry*; OUP Oxford, 2010.
(16) Brunauer, S.; Emmett, P. H.; Teller, E. *J. Am. Chem. Soc.* **1938**, *60*, 309.
(17) Nakamoto, K. In *Infrared and Raman Spectra of Inorganic and Coordination Compounds*; John Wiley & Sons, Inc.: 2008, p 1.
(18) Bunker, G. *Introduction to XAFS: A Practical Guide to X-ray Absorption Fine Structure Spectroscopy*; Cambridge University Press, 2010.
(19) Dent, A. J.; Cibin, G.; Ramos, S.; Smith, A. D.; Scott, S. M.; Varandas, L.; Pearson, M. R.; Krumpa, N. A.; Jones, C. P.; Robbins, P. E. *J. Phys. Conf. Ser.* **2009**, *190*, 012039.
(20) Ravel, B.; Newville, M. *J. Synchrotron Rad.* **2005**, *12*, 537.
(21) Greenwood, N. N.; Earnshaw, A. *Chemistry of the Elements*; 2nd ed.; Butterworth–Heinemann, 1997.
(22) Khalifah, P.; Huang, Q.; Ho, D. M.; Zandbergen, H. W.; Cava, R. J. *J. Solid State Chem.* **2000**, *155*, 189.
(23) Bhatia, S.; Beltramini, J.; Do, D. D. *Catal. Today* **1990**, *7*, 309.
(24) Holm, V. C. F.; Clark, A. *J. Catal.* **1968**, *11*, 305.
(25) Hurst, N. W.; Gentry, S. J.; Jones, A.; McNicol, B. D. *Catal. Rev.-Sci. Eng.* **1982**, *24*, 233.
(26) Jenkins, J. W.; McNicol, B. D.; Robertson, S. D. *Chem. Tech.* **1977**, *7*, 316.
(27) Monti, D. A. M.; Baiker, A. *J. Catal.* **1983**, *83*, 323.
(28) Robertson, S. D.; McNicol, B. D.; De Baas, J. H.; Kloet, S. C.; Jenkins, J. W. *J. Catal.* **1975**, *37*, 424.
(29) Rogers, R. N.; Yasuda, S. K.; Zinn, J. *Anal. Chem.* **1960**, *32*, 672.
(30) Dunwoody, P. PhD Thesis, University of Manchester, 2000.

Chapter 3: Hydrothermal Synthesis and Characterisation of Pentavalent Ion-Doped Cerium Oxides

3.1 Introduction

In this chapter hydrothermal syntheses of pentavalent ion-doped ceria of the forms $Ce_{1-x}M_xNa_yO_{2-\delta}$ and $Ce_{1-x}M_xO_{2-\delta}$ (M = Sb, Nb, Ta; $0 \leq x \leq 0.40$) are presented; together with structural characterisation of these oxides to determine the doping the mechanism by which a pentavalent ion is incorporated into the fluorite structure. The redox properties and thermal stability of the oxides is explored in Chapter 5.

Whilst there have been reports of Nb-substitution ($x \leq 0.01 - 0.02$) and Ta-substitution ($x \leq 0.50$), Sb-substitution has not been previously reported (see Chapter 1). No satisfactory conclusion has been drawn as to how these pentavalent ions are incorporated into the fluorite lattice. Extra, interstitial oxide or Ce^{4+} reduction are often cited as possible mechanisms,[1,2] but no detailed study has previously explored this.

3.2 Hydrothermal Synthesis of Pentavalent Ion-Doped Ceria

3.2.1 Hydrothermal Synthesis of Ceria

Ceria was prepared by a hydrothermal route as a reference material for the doped materials described in this chapter, and in Chapter 4. 6 mmol $CeCl_3 \cdot 7H_2O$ was dissolved in 2 ml distilled water, followed by the addition of 2 ml of H_2O_2 (37% aqueous solution). This solution was then stirred for 15 minutes, during which the colour of the solution changed from colourless to a pale yellow/orange colour, indicating Ce^{3+} oxidation to Ce^{4+}. Next 8 ml of either 7.5 mol dm^{-3} NaOH or NH_4OH was added dropwise with effervescence. The red-brown gel was stirred for a further

10-15 minutes before being sealed in a Teflon-lined steel autoclave and heated in a fan oven to 240 °C for 24 hours. The autoclave was cooled to room temperature before filtration and washing with copious amounts of boiling water. The resulting brown solids were dried in an oven at 80 °C overnight and ground in a pestle and mortar to give a fine powder.

3.2.2 Hydrothermal Synthesis of Antimony-Substituted Ceria

To prepare Sb-substituted ceria the same protocol as above (Section 3.2.1) was followed; except in place of $CeCl_3 \cdot 7H_2O$, a (1-*x*):*x* molar ratio of $CeCl_3 \cdot 7H_2O$ and antimony precursor, respectively, was used, to give a total of 6 mmol metal. The antimony precursors $SbCl_5$, $SbCl_3$ and $NaSbO_3 \cdot xH_2O$ were all used to successfully prepare mixed cerium – antimony oxides of the forms $Ce_{1-x}Sb_xNa_yO_{2-\delta}$ and $Ce_{1-x}Sb_xO_{2-\delta}$ ($0.05 \leq x \leq 0.30 - 0.40$, in increments of $x = 0.05$).

3.2.3 Hydrothermal Synthesis of Niobium- and Tantalum-Substituted Ceria

To prepare Nb- and Ta-substituted ceria the same protocol as above (Section 3.2.1) was followed; except in place of $CeCl_3 \cdot 7H_2O$, a (1-*x*):*x* molar ratio of $CeCl_3 \cdot 7H_2O$ and $(Nb/Ta)Cl_5$, respectively, was used to give a total of 6 mmol metal. The maximum value of *x* achieved was either 0.25 or 0.30, depending on metal and base used in the synthesis. The value of *x* was increased in increments of 0.05.

3.3 Powder XRD

3.3.1 Ceria

The powder XRD patterns of CeO_2 prepared hydrothermally in either NaOH or NH_4OH solutions can both be indexed and the profile fitted using the space group $Fm\bar{3}m$ with almost identical lattice parameters (Figure 3. 1). However, the pattern of sample made in NH_4OH exhibits broader Bragg peaks, suggesting a smaller crystallite size.

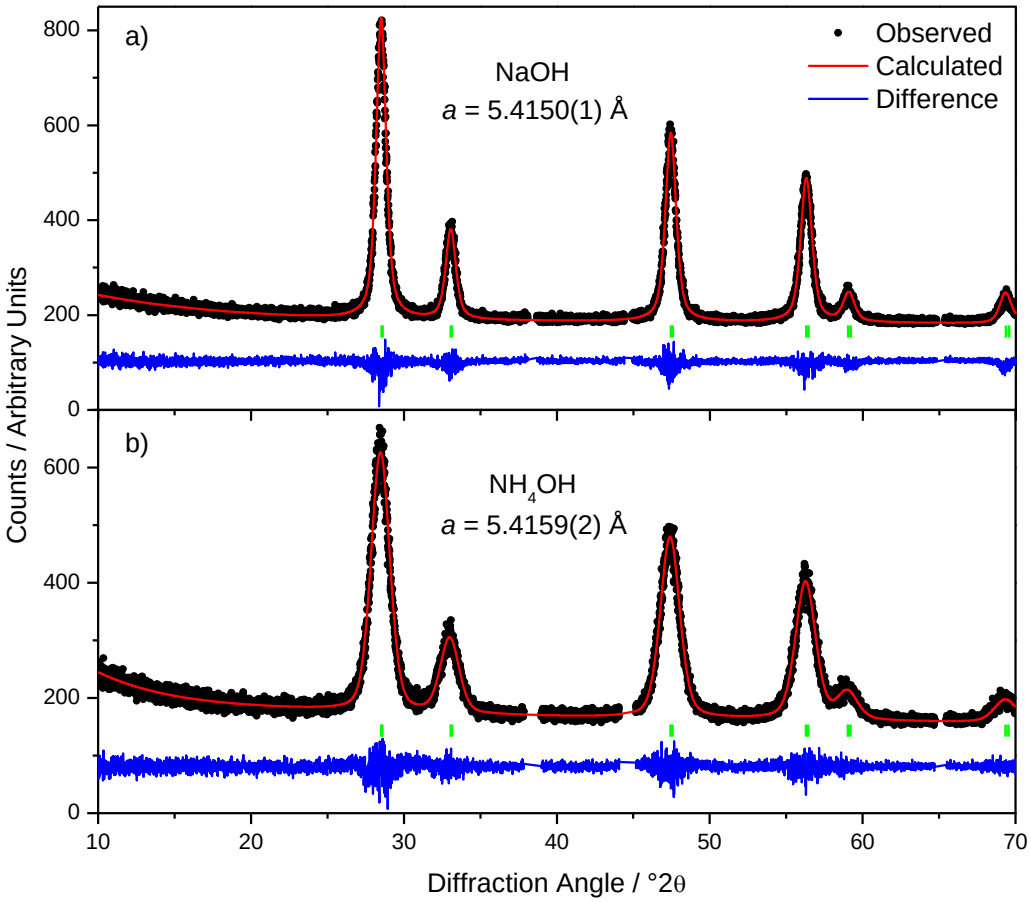

Figure 3. 1 Le Bail fits to powder XRD data (λ = 1.54056 Å) of CeO_2 made hydrothermally using a) NaOH, b) NH_4OH. Peaks due to Al sample holder at 38°, 44° and 65° are the regions excluded.

3.3.2 Sb-Substituted Ceria

Powder XRD patterns of compounds withinitially assumed formula $Ce_{1-x}Sb_xO_{2-\delta}$ prepared in NaOH using $SbCl_5$ as the Sb precursor (Figure 3. 2b-i) can be indexed and the profile fitted to a cubic fluorite cell (space group $Fm\bar{3}m$) within the range $0.05 \leq x \leq 0.40$. When $x > 0.40$ peaks attributed to Sb_2O_3 are observed. Diffraction patterns of $Ce_{1-x}Sb_xO_{2-\delta}$ made using $NaSbO_3$ and $SbCl_3$ (only up to $x = 0.35$) can be indexed to the same space group and can be found in Appendix 1 (Figures A. 1 and A. 2). As x increases the Bragg peaks become broader and the lattice parameter decreases linearly (Figure 3. 3). A similar trend is seen whether $SbCl_5$, $NaSbO_3$ or $SbCl_3$ is used in the hydrothermal reaction. The broadening of the Bragg peaks is likely to be caused by a reduced particle size, though crystallographic strain effects can also cause peak broadening.[3] The lattice contraction is consistent with the smaller atomic radius of Sb compared to that of Ce^{4+} (six-coordinate Sb^{3+} and Sb^{5+} have respective ionic radii of 0.76 Å and 0.6 Å, compared to 0.97 Å for eight-coordinate Ce^{4+}).[4]

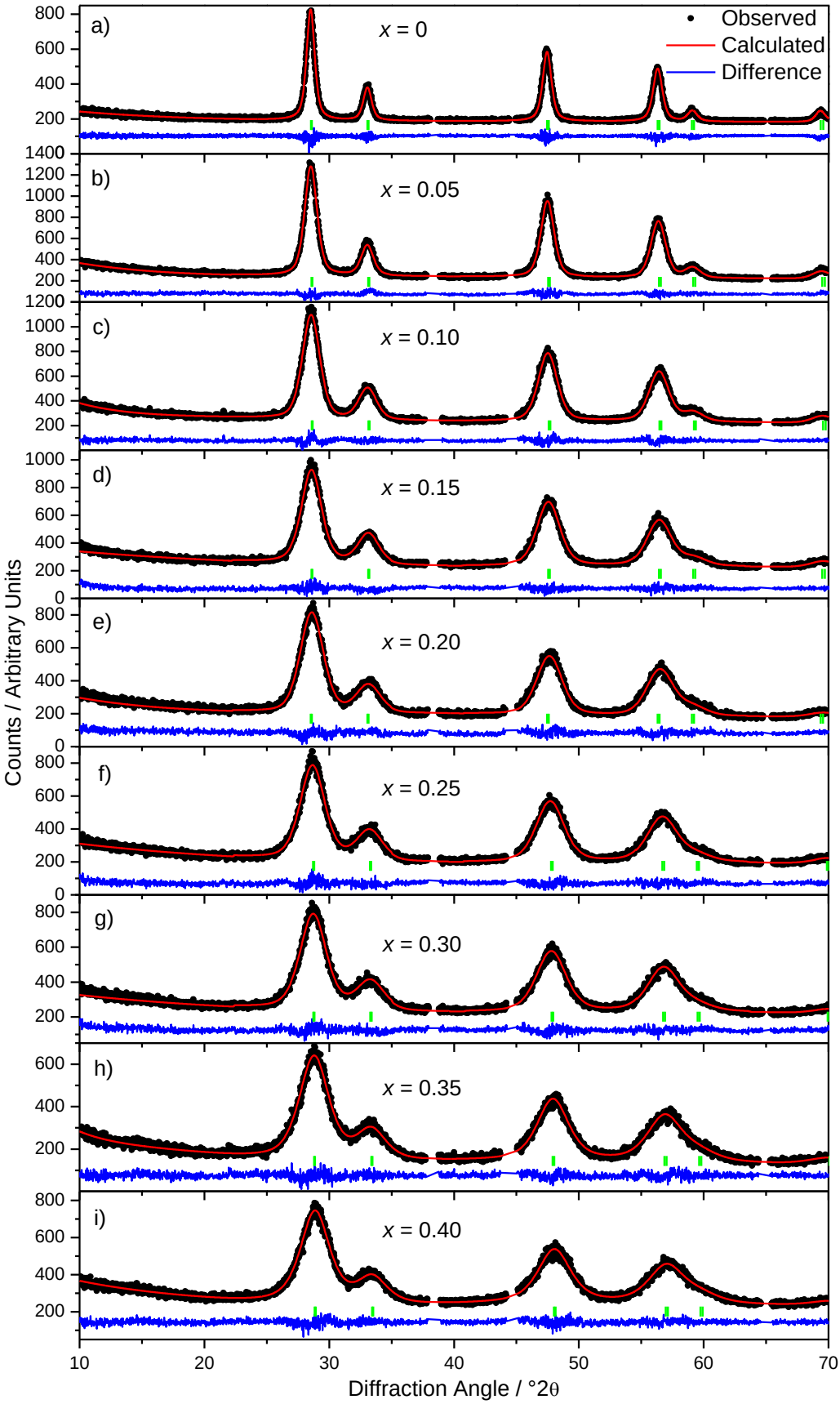

Figure 3. 2a – i) Le Bail fits to powder XRD data (λ = 1.54056 Å) of $Ce_{1-x}Sb_xO_{2-\delta}$ *(0.00 ≤ x ≤ 0.40; respectively) made hydrothermally in NaOH solution (where* $SbCl_5$ *is the Sb reagent). Peaks due to Al sample holder at 38°, 44° and 65° are the regions excluded.*

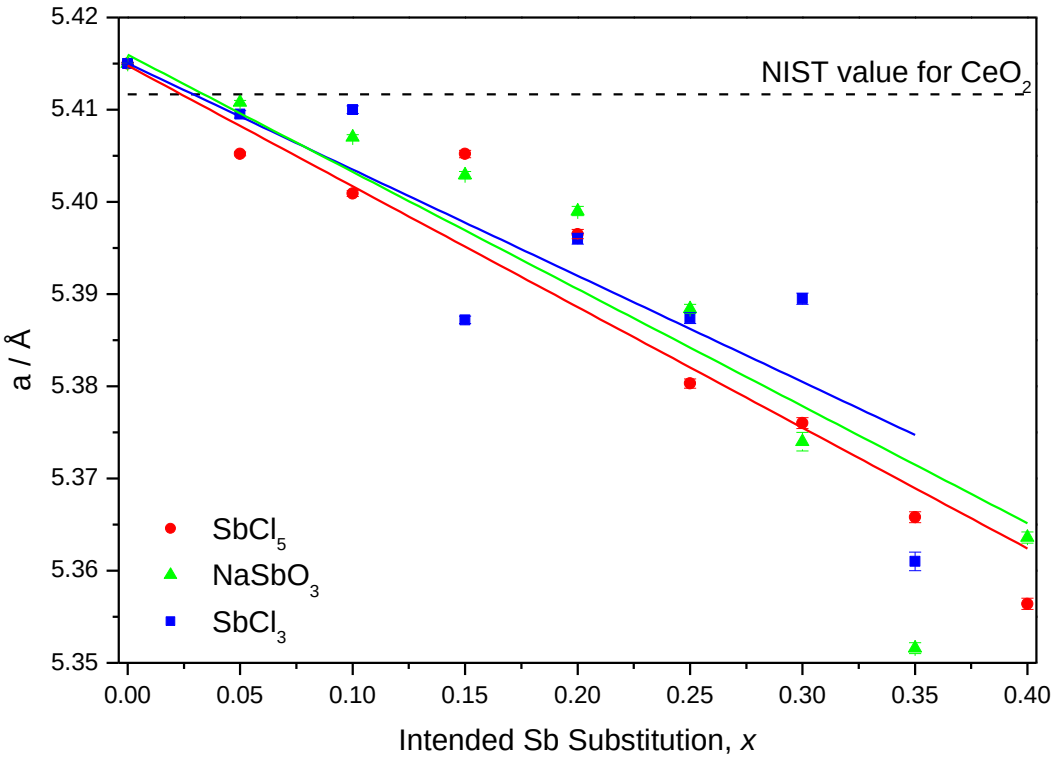

Figure 3. 3 Refined lattice parameter, a, *as a function of* x *in* $Ce_{1-x}Sb_xO_{2-\delta}$ *prepared hydrothermally in NaOH using either* $SbCl_5$, $NaSbO_3$ *or* $SbCl_3$ *as Sb precursor. Linear fits shown as a guide for the eye.*

Powder XRD patterns of $Ce_{1-x}Sb_xO_{2-\delta}$ prepared in NH_4OH, $0.05 \leq x \leq 0.30 - 0.35$ (made using $SbCl_5$, Figure 3. 4; made using $NaSbO_3$ and $SbCl_3$, Figures A. 3 and A. 4 in Appendix, respectively) again can be indexed to a fluorite cell, and when $x > 0.30 - 0.35$ an Sb_2O_3 impurity forms. Again Bragg reflection broadening increases as a function of *x*, and a lattice contraction is observed, regardless of which Sb precursor is used. However, compared to their analogues made in NaOH, the lattice contraction is significantly smaller (Figure 3. 5).

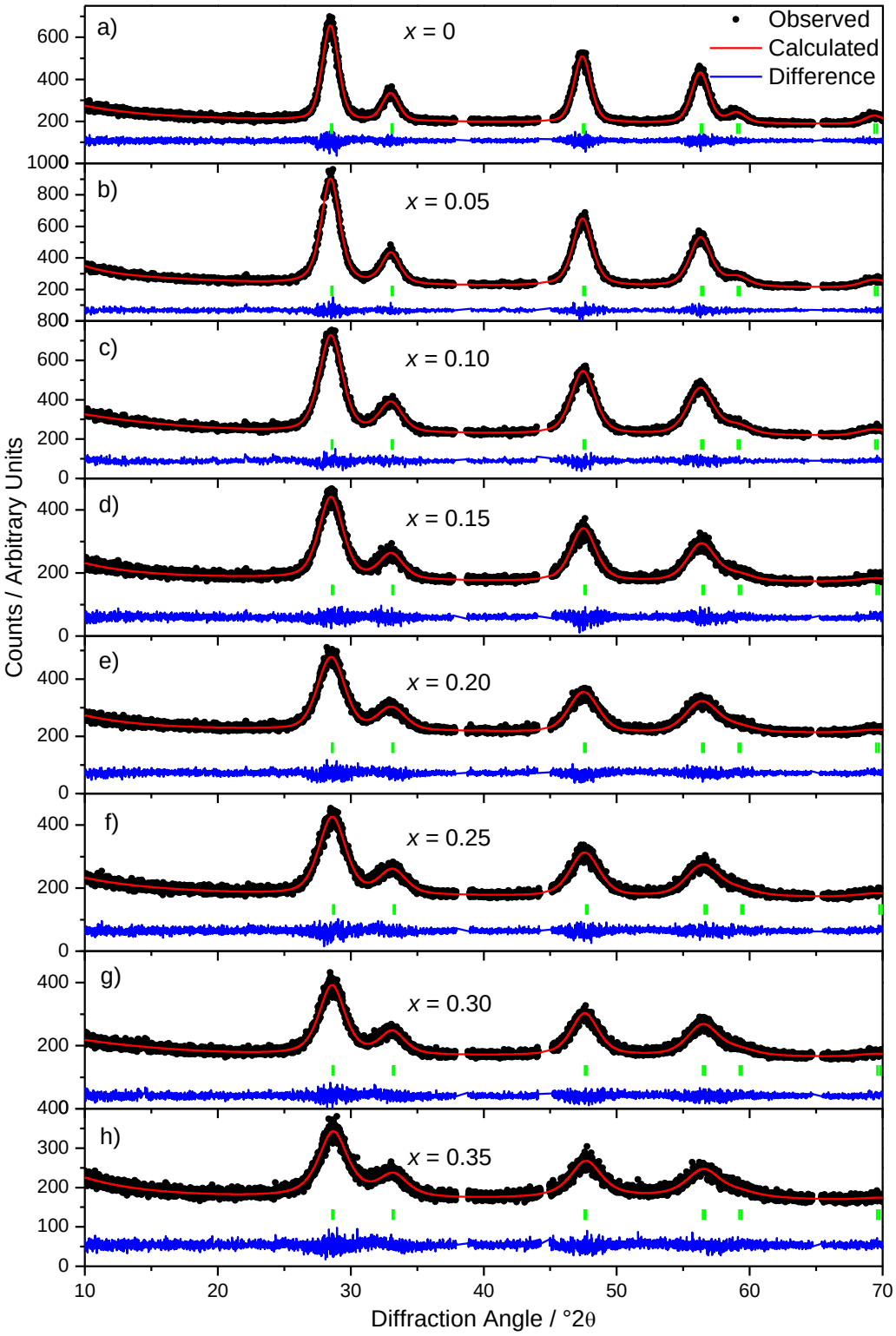

Figure 3. 4 a – i) Le Bail fits to powder XRD data (λ = 1.54056 Å) of $Ce_{1-x}Sb_xO_{2-\delta}$ (0.00 ≤ x ≤ 0.35; respectively) made hydrothermally in NH_4OH solution (where $SbCl_5$ is the Sb reagent). Peaks due to Al sample holder at 38°, 44° and 65° are the regions excluded.

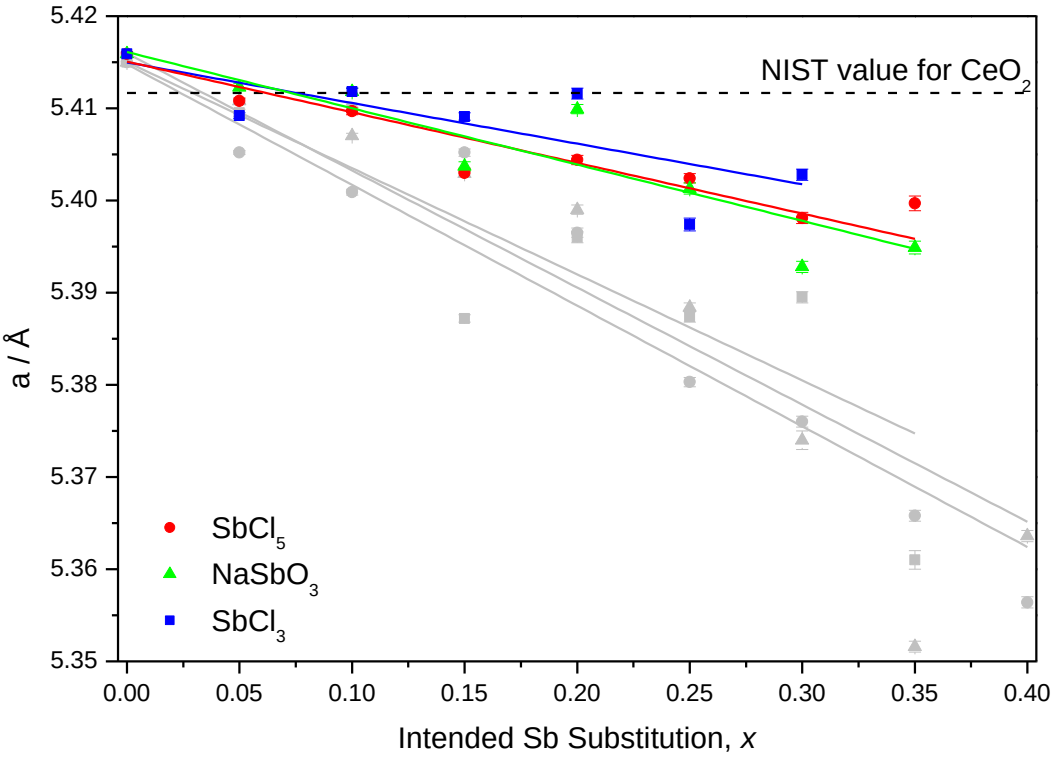

Figure 3. 5 Refined lattice parameter, a, *as a function of* x *in* $Ce_{1-x}Sb_xO_{2-\delta}$ *prepared hydrothermally in* NH_4OH *using either* $SbCl_5$, $NaSbO_3$ *or* $SbCl_3$ *as Sb precursor. The lattice parameters of the samples prepared in NaOH are shown in grey for comparison. Linear fits shown as a guide for the eye.*

3.3.3 Nb- and Ta-Substituted Ceria

Powder XRD of $Ce_{1-x}M_xO_{2-\delta}$ (M = Nb, Ta) prepared in NaOH could be indexed to a cubic fluorite unit cell up to x = 0.30 and x = 0.25 for Nb and Ta, respectively (Figure 3. 6 and Figure 3. 7). Bragg peaks become broader as x increases, indicating a decrease in crystallite size. The fluorite lattice parameter also decreases as a function of x to a similar degree in both $Ce_{1-x}Nb_xO_{2-\delta}$ and $Ce_{1-x}Ta_xO_{2-\delta}$ (Figure 3. 8), in accordance with the similar ionic radii of Nb and Ta which are both considerably smaller than Ce^{4+} (octahedral Nb^{5+} and Ta^{5+} both have ionic radii of 0.64 Å, whilst in an eight-coordinate environment they are both 0.74 Å; eight coordinate Ce^{4+} is 0.97 Å).[4] At higher values of x the perovskites $NaMO_3$ (M = Nb, Ta; as appropriate) began to form as an secondary phase. The formation of these perovskites is not

unexpected; both have been prepared by the hydrothermal reaction of M_2O_5 (M = Nb, Ta) in NaOH.[5,6]

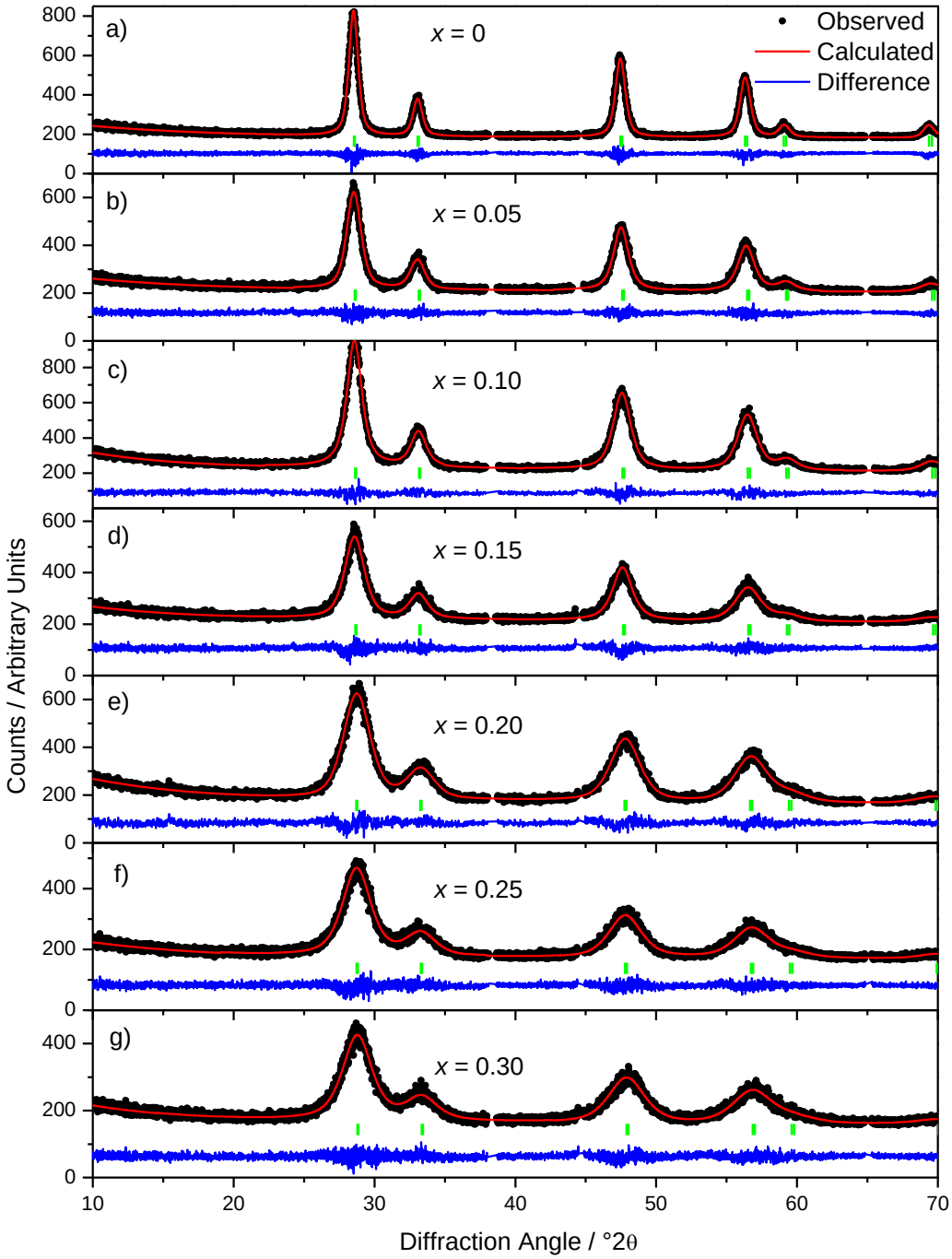

Figure 3. 6 Le Bail fits to powder XRD data (λ = 1.54056 Å) of $Ce_{1-x}Nb_xO_{2-\delta}$ (0.00 ≤ x ≤ 0.30; respectively) made hydrothermally in NaOH solution. Peaks due to Al sample holder at 38°, 44° and 65° are the regions excluded.

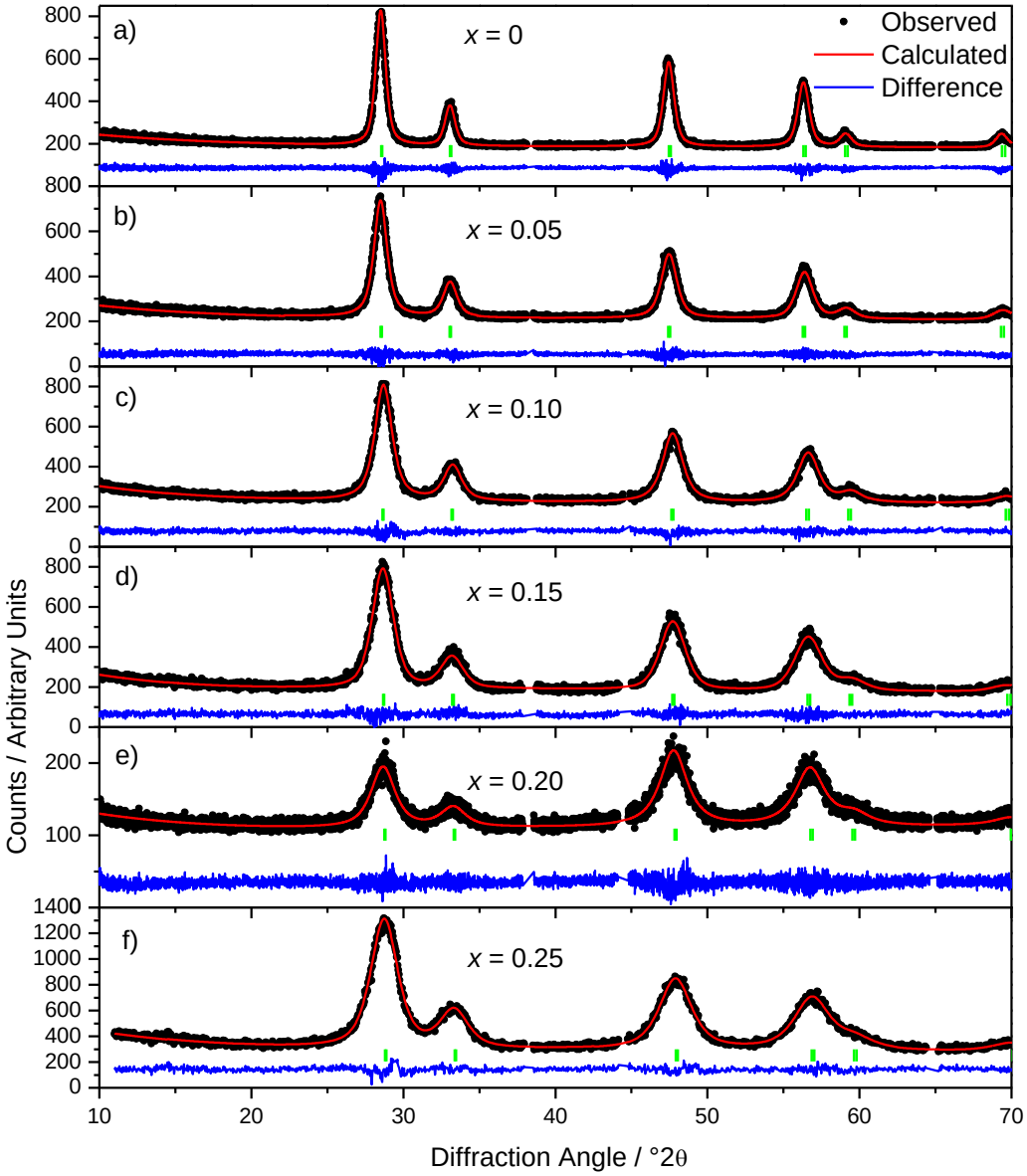

Figure 3. 7 Le Bail fits to powder XRD data (λ = 1.54056 Å) of $Ce_{1-x}Ta_xO_{2-\delta}$ *(0.00 ≤ x ≤ 0.25; respectively) made hydrothermally in NaOH solution Peaks due to Al sample holder at 38°, 44° and 65° are the regions excluded.*

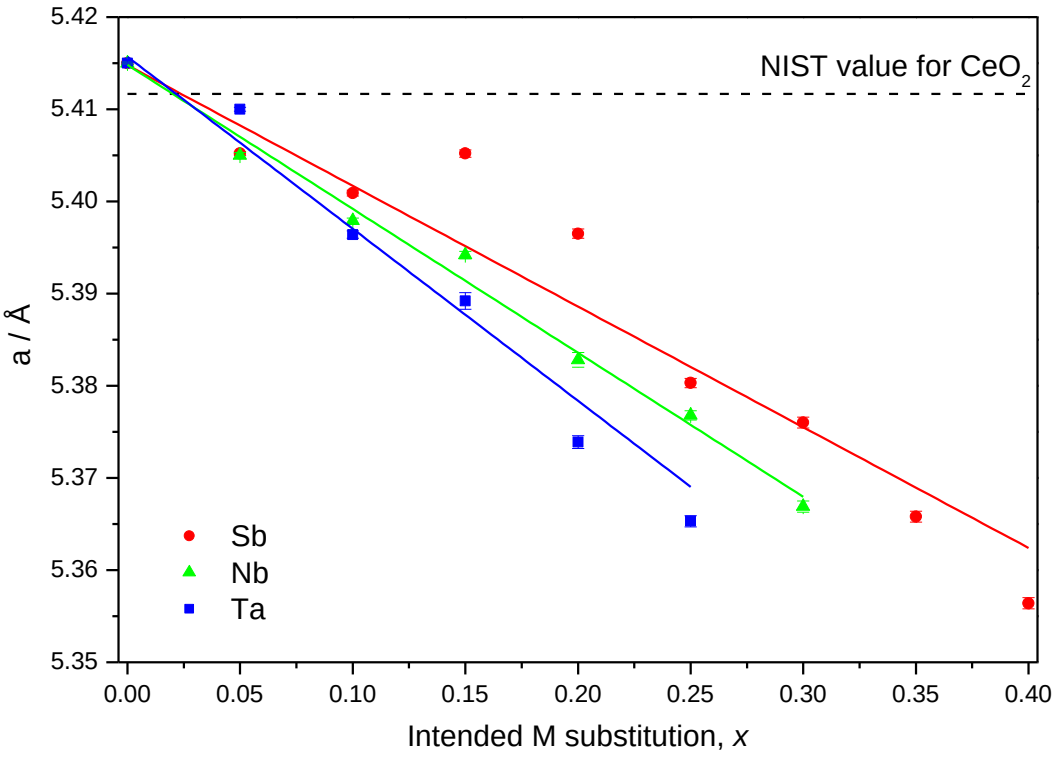

Figure 3. 8 Refined lattice parameter, a, *as a function of* x *of* $Ce_{1-x}M_xO_{2-\delta}$ *(M = Sb (made using* $SbCl_5$ *as Sb precursor), Nb, Ta) prepared hydrothermally in NaOH. Linear fits shown as a guide for the eye.*

Powder XRD of $Ce_{1-x}M_xO_{2-\delta}$ (M = Nb, Ta) prepared by the same technique, but using NH_4OH instead of NaOH in the hydrothermal reaction, shows the products again adopt a cubic fluorite unit cell up to x = 0.25 – 0.30 (Figure 3. 9 and Figure 3. 10, respectively). Diffraction peaks are observed to broaden as *x* increases, suggesting a decreasing particle size. In addition to this, the lattice parameters of the $Ce_{1-x}M_xO_{2-\delta}$ (M = Nb, Ta) made in NH_4OH decrease linearly as a function of *x* (Figure 3. 11) in a similar manner to $Ce_{1-x}Sb_xO_{2-\delta}$ made in NH_4OH (Figure 3. 5). The lattice parameters of these oxides made using NH_4OH decreases less than their analogous oxides made using NaOH, suggesting that the choice of base leads to a difference in structure of the materials.

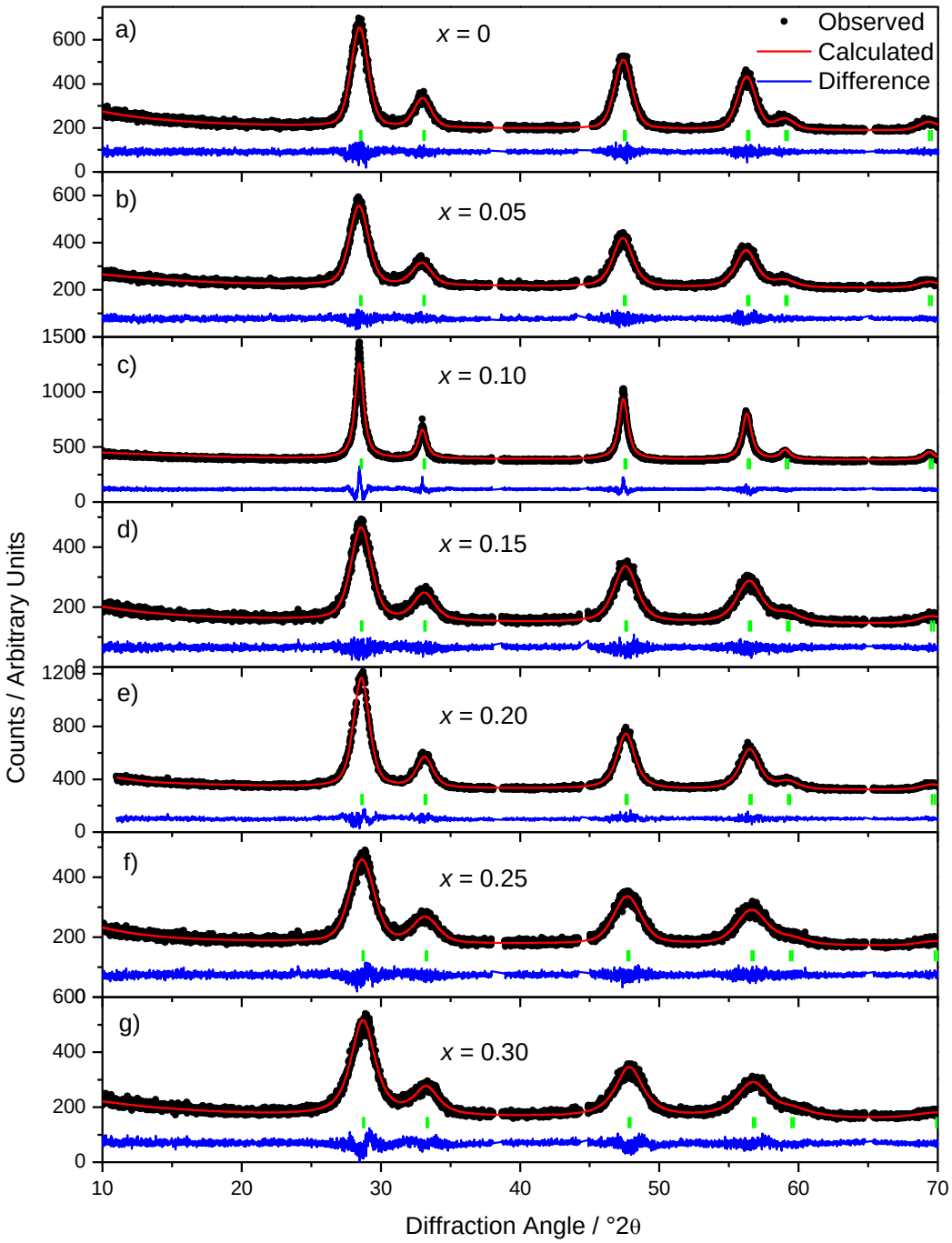

Figure 3. 9 Le Bail fits to powder XRD data (λ = 1.54056 Å) of $Ce_{1-x}Nb_xO_{2-\delta}$ (0.00 ≤ x ≤ 0.30; respectively) made hydrothermally in NH_4OH solution. Peaks due to Al sample holder at 38°, 44° and 65° are the regions excluded.

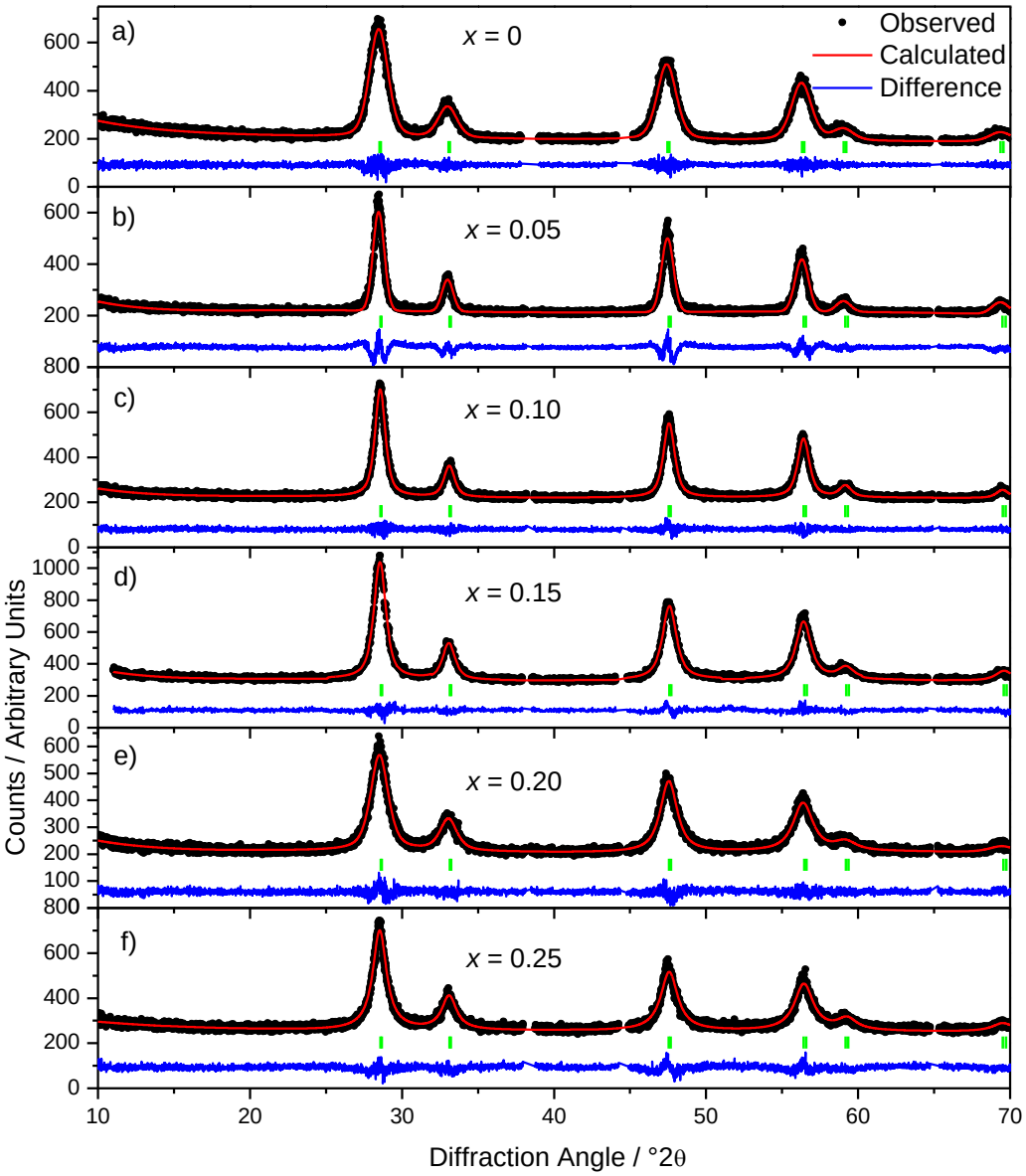

Figure 3. 10 Le Bail fits to powder XRD data (λ = 1.54056 Å) of $Ce_{1-x}Ta_xO_{2-\delta}$ *(0.00 ≤ x ≤ 0.25; respectively) made hydrothermally in* NH_4OH *solution Peaks due to Al sample holder at 38°, 44° and 65° are the regions excluded.*

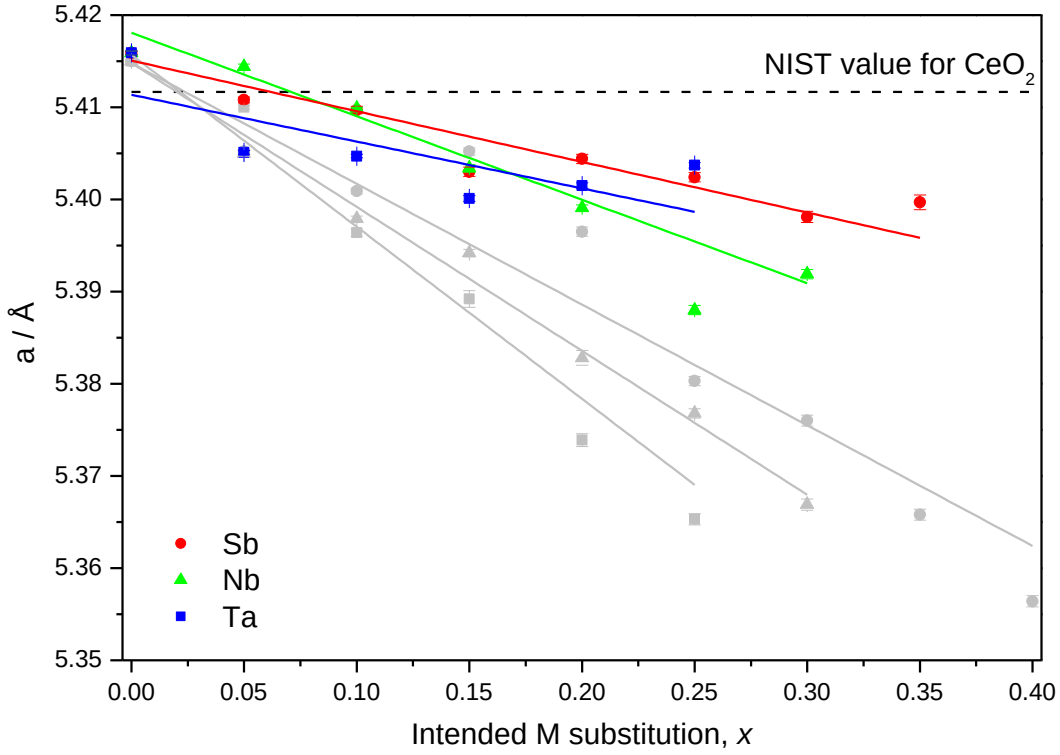

Figure 3. 11 Refined lattice parameter, a, *as a function of* x *in* $Ce_{1-x}M_xO_{2-\delta}$ *(M = Sb (made using* $SbCl_5$ *as Sb precursor), Nb, Ta) prepared hydrothermally in* NH_4OH*. The lattice parameters of the samples prepared in NaOH are shown in grey for comparison. Linear fits shown as a guide for the eye.*

It was unclear as to how a pentavalent ion is substituted into the ceria lattice: commensurate Ce^{3+} reduction has been suggested by modelling of Nb- and Ta-doping (x = 0.036)[7] although no work has been done to prove this experimentally. Another model proposed is co-doping with cations of lower valence, leading to a "cancelling out" of oxide vacancies.[8,9] As such, the possiblilty of Na^+ and/or NH_4^+ (present in the hydrothermal reaction solution) co-substitution cannot be excluded as a potential mechanism, and would explain the difference in lattice parameter of otherwise identical pentavalent ion-substituted ceria prepared in different bases.

A third possibility that was considered is the formation of an oxygen-excess fluorite superlattice,[10] where the fluorite oxygen lattice is fully occupied, and extra oxygen is present in the interstitial sites to achieve charge neutrality. $UO_{2+\delta}$ ($0 \leq \delta \leq 0.25$),

containing a mixture of U^{4+} and U^{5+},[11-14] has been shown to contain an oxide excess whilst maintaining an average fluorite structure.

It is conceivable that pentavalent ions are accommodated in the fluorite ceria lattice by any of these possibilities, or some combination of these. However, powder XRD alone cannot distinguish between these models.

3.4 Further Characterisation

Raman spectroscopy data of $Ce_{1-x}Nb_xO_{2-\delta}$ ($0 \leq x \leq 0.30$) show one broad band centred at around 459 – 465 cm^{-1} (Figure 3. 12), attributed to the F_{2g} Raman mode caused by M – O symmetric stretching in an MO_8 cube, the characteristic stretch in fluorite oxides.[15] This band broadens as Nb content increases, indicative of increasing disorder. There is very little obvious difference between samples prepared in NaOH (Figure 3. 12a) and NH_4OH (Figure 3. 12b).

As Nb content increases a second band begins to appear ~600 cm^{-1}, which is commonly assigned as a phonon mode arising from oxide vacancies.[16-18] This evidence could suggest the presence of an "oxide-excess" in the fluorite is less likely, unless the extra band is caused by excess oxide. There are no other observed Raman bands, confirming that no other phases are present.

TGA of $Ce_{1-x}Sb_xO_{2-\delta}$ ($0 \leq x \leq 0.30$) and $Ce_{1-x}Nb_xO_{2-\delta}$ ($0 \leq x \leq 0.25$) made in NaOH (Figure 3. 13a and Figure 3. 14a) shows a steady mass loss which tends to increase in magnitude with increasing *x*. It is difficult to ascertain what proportion of this is due to the loss of surface water; since the surface area increases with increasing *x* (see Chapter 5).

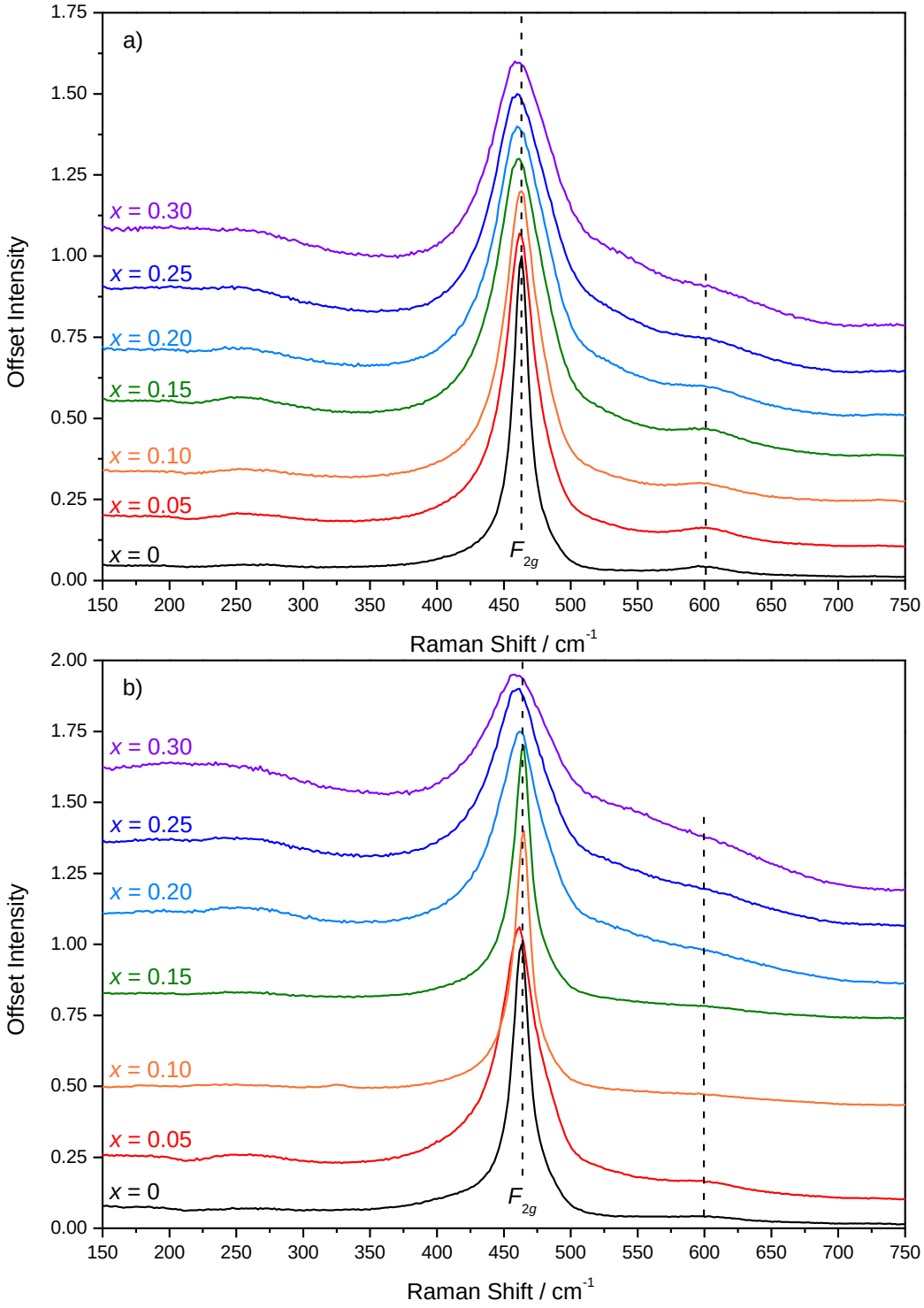

Figure 3. 12 Raman spectra of $Ce_{1-x}Nb_xO_{2-\delta}$ ($0 \leq x \leq 0.30$) prepared hydrothermally in a) NaOH, b) NH_4OH.

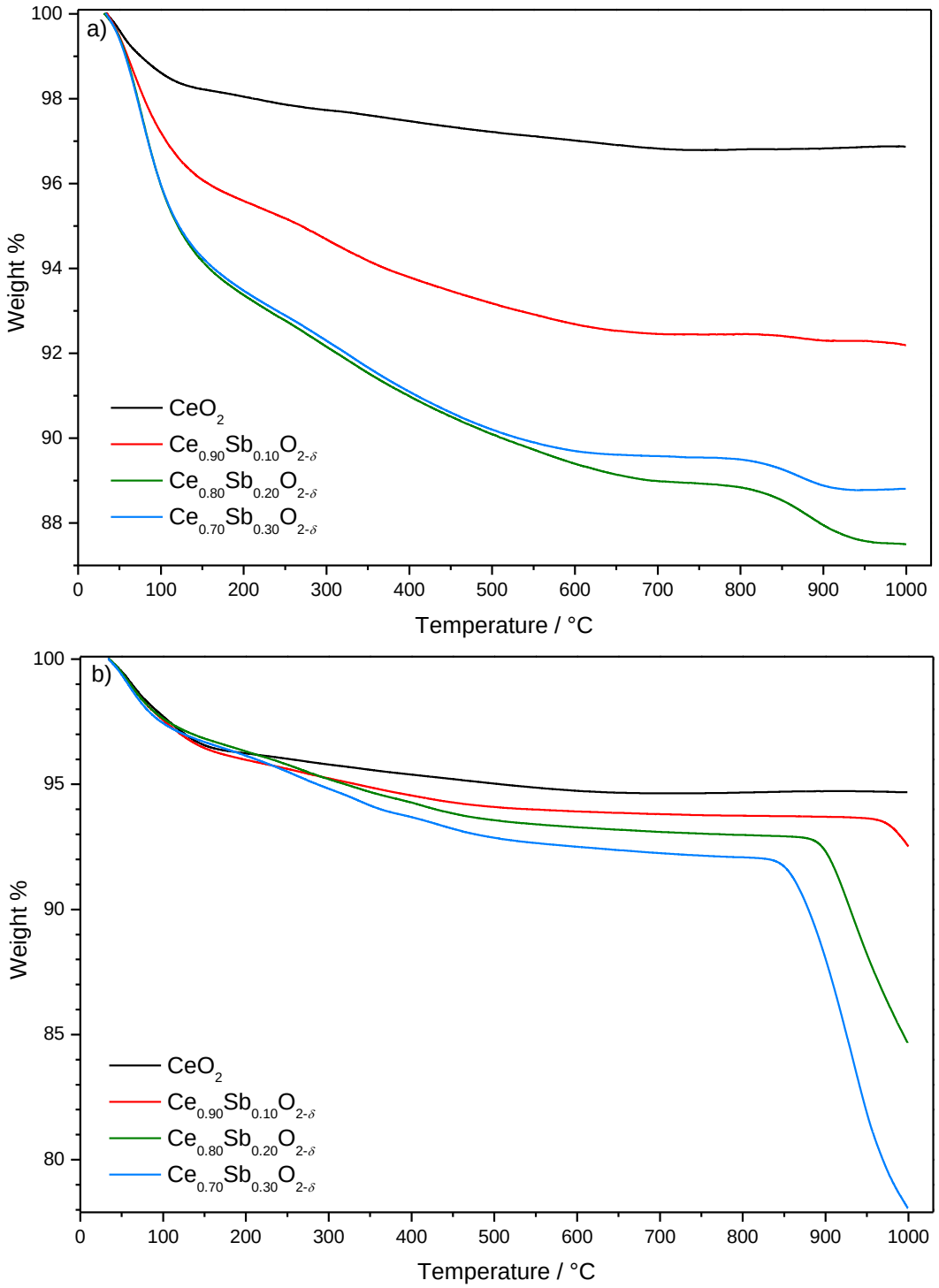

Figure 3. 13 TGA of $Ce_{1-x}Sb_xO_{2-\delta}$ ($0 \leq x \leq 0.30$) prepared hydrothermally in a) NaOH and b) NH_4OH.

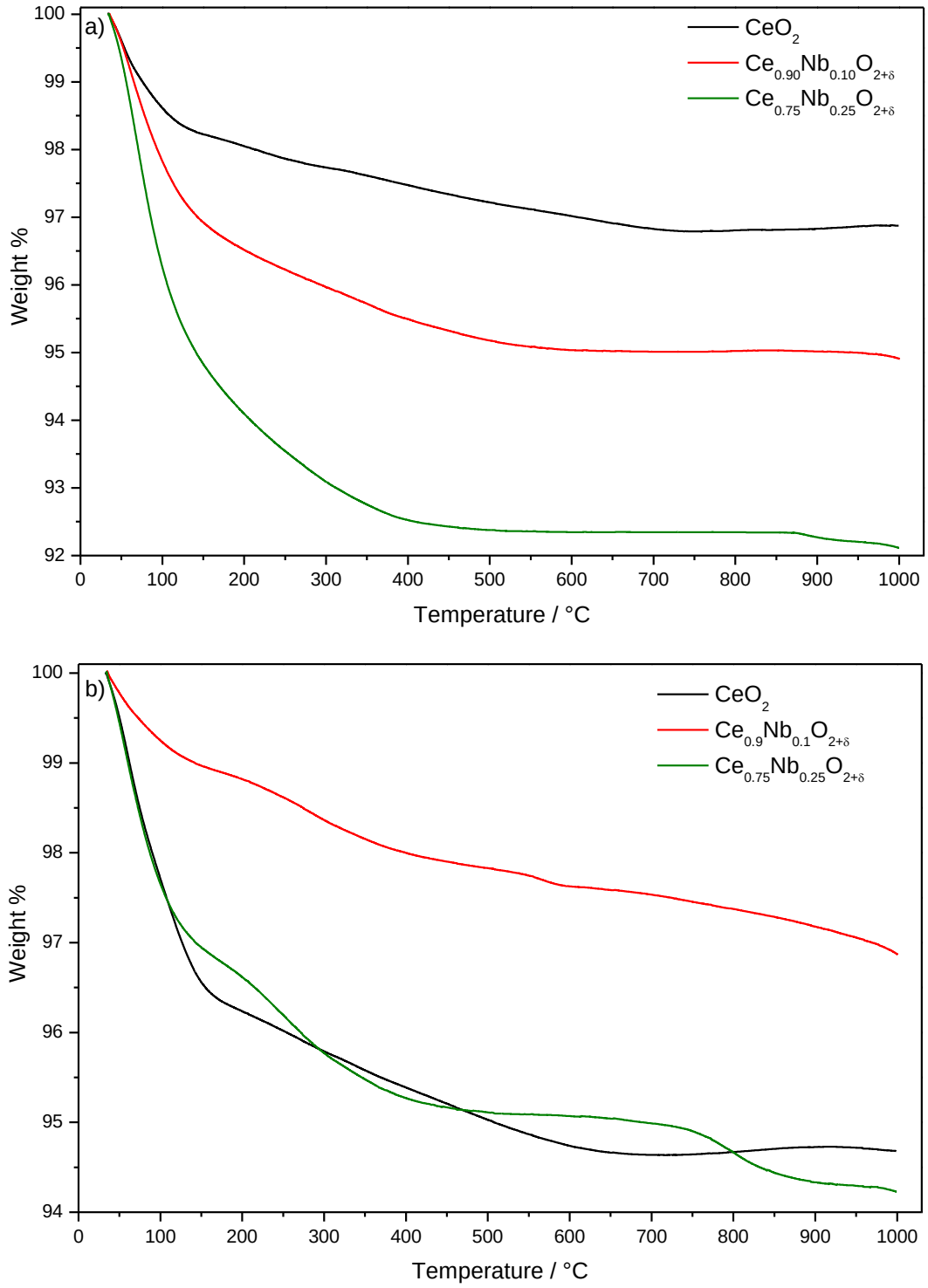

Figure 3. 14 TGA of $Ce_{1-x}Nb_xO_{2-\delta}$ ($0 \leq x \leq 0.25$) prepared hydrothermally in a) NaOH and b) NH_4OH.

TGA of $Ce_{1-x}M_xO_{2-\delta}$ (M = Sb, Nb; $0 \leq x \leq 0.25 - 0.30$) made hydrothermally in NH_4OH (Figure 3. 13b and Figure 3. 14b, respectively) also show mass losses at low temperature which can be attributed at least partially to surface H_2O. $Ce_{1-x}Sb_xO_{2-\delta}$ made in NH_4OH exhibits a large drop in mass above 850 °C which is ascribed to

oxygen loss resulting from Sb(V) reduction. $Sb_2O_5 \cdot xH_2O$ is known to reduce to Sb_2O_4 (a mixed Sb(III/V) phase), suggesting the Sb(V) is unstable at high temperature,[19] see below for assignment of the Sb oxidation state. TGA of $Ce_{1-x}Nb_xO_{2-\delta}$ made in NH_4OH shows no such mass loss, illustrative of Nb(V)'s high stability.

ICP-OES elemental analysis of $Ce_{1-x}M_xO_{2-\delta}$ (M = Sb, Nb; Table 3. 2 and Table 3. 1, respectively) made in NaOH and NH_4OH shows a Ce:M ratio very close to the intended values of *x*. However, in the samples made in NaOH, an amount of Na was also observed, which increases with Nb content. A very small amount (0.17 wt%) of Na was observed in "CeO_2" which could be incorporated into the structure. Na has previously been shown to be incorporated into $Ce_{1-x-y}Zr_xO_2$ prepared hydrothermally,[20] leading to oxide vacancies and improved redox properties. The ionic radius of eight coordinate Na^+ is 1.18 Å,[4] is slightly larger than eight-coordinate Ce^{4+} (0.97 Å), though Na is quite flexible in its coordination number and it may not be occupying a Ce 4*a* site. The very small amount of Na in CeO_2 could be due to surface species, despite thorough washing with boiling water. However, the increasing proportion of Na with increasing Sb or Nb content suggests that this cannot be the sole cause (even though the surface area increases as *x* increases (Chapter 5), the Na content increase is not proportional to this).

Table 3. 2 ICP-OES measured metal content by mass of $Ce_{1-x}Sb_xO_{2-\delta}$ (made using $SbCl_5$ as Sb precursor) with calculated formula assuming remaining mass is oxide.

Intended *x*	**Base**	Ce / %	Sb / %	Na / %	Calculated Formula
0	NaOH	81.42(30)	N/A	0.17(30)	$Ce_{0.99(3)}Na_{0.01(2)}O_{1.95(8)}$
0.05	NaOH	72.35(30)	3.51(30)	0.73(30)	$Ce_{0.89(4)}Sb_{0.050(4)}Na_{0.06(2)}O_{2.5(1)}$
0.10	NaOH	69.71(30)	7.44(30)	0.41(30)	$Ce_{0.86(3)}Sb_{0.106(5)}Na_{0.03(2)}O_{2.4(1)}$
0.20	NaOH	58.09(30)	15.46(30)	1.32(30)	$Ce_{0.69(2)}Sb_{0.212(7)}Na_{0.09(2)}O_{2.6(1)}$
0.30	NaOH	52.16(30)	19.98(30)	2.24(30)	$Ce_{0.59(5)}Sb_{0.259(8)}Na_{0.15(2)}O_{2.5(1)}$
0.05	NH_4OH	78.88(30)	3.35(30)	N/A	$Ce_{0.953(7)}Sb_{0.047(3)}O_{1.88(7)}$
0.20	NH_4OH	62.85(30)	14.26(30)	N/A	$Ce_{0.793(7)}Sb_{0.207(4)}O_{2.53(7)}$

Table 3. 1 ICP-OES measured metal content by mass of $Ce_{1-x}Nb_xO_{2-\delta}$ with calculated formula assuming remaining mass is oxide.

Intended *x*	**Base**	Ce / %	Nb / %	Na / %	Calculated Formula
0.05	NaOH	68.23(30)	2.57(30)	0.40(30)	$Ce_{0.92(3)}Nb_{0.053(6)}Na_{0.03(2)}O_{3.4(2)}$
0.10	NaOH	68.8(3)	5.25(30)	1.20(30)	$Ce_{0.82(2)}Nb_{0.096(6)}Na_{0.09(2)}O_{2.6(1)}$
0.20	NaOH	60.1(3)	10.3(3)	1.63(30)	$Ce_{0.70(2)}Nb_{0.182(7)}Na_{0.12(2)}O_{2.9(1)}$
0.30	NaOH	53.5(3)	15.5(3)	2.12(30)	$Ce_{0.60(2)}Nb_{0.261(9)}Na_{0.14(2)}O_{2.8(1)}$

An ICP-OES elemental analysis of $Ce_{0.70}Nb_{0.30}O_{2-\delta}$ (nominal composition) to determine the concentration of trace metals (Appendix 2, Table A.1) showed no significant amount of any other metal, ruling out the presence of other lanthanides or transition metals (potentially present in the starting products) co-doped into the structure.

Several of the oxides had a large amount of mass unaccounted for, attributed solely to structural oxide in Table 3. 2 and Table 3. 1. However in reality, a proportion of this mass is likely to be present as surface water, making determination of oxide content from ICP-OES impossible.

The presence of increasing amounts of Na (as *x* increases) suggests that Na incorporation is helping to achieve charge balance. IR spectroscopy of $Ce_{0.70}Nb_{0.30}O_{2-\delta}$ made in NH_4OH (Chapter 5) possibly shows a weak N – H stretch, though it is impossible to determine if this is on the surface or in the fluorite structure.

HR-TEM images of CeO_2 made in NaOH and NH_4OH (Figure 3. 15a and b; respectively) show that both have a similar particle size, around 10 nm in diameter, and atomic resolution images clearly show individual atoms, showing a high degree of atomic order within individual crystallites. TEM of $Ce_{1-x}Nb_xO_{2-\delta}$ made in NaOH (x = 0.10, 0.25; Figure 3. 16a and b; respectively) and NH_4OH (x = 0.10, 0.25; Figure 3. 16c and d; respectively) show that irrespective of the base used the particle size decreases as *x* increases (to as low as ~5 nm in $Ce_{0.75}Nb_{0.25}O_{2-\delta}$) and individual atoms become less visible indicating that the internal strain or disorder is increasing. A similar effect is observed in $Ce_{1-x}Sb_xO_{2-\delta}$ (Figure 3. 17). This suggests that the pentavalent dopant hinders crystallite growth or limits particle size. This observation is consistant with powder XRD Scherrer broadening (Section 3.3) and surface area measurements (Chapter 5) which also suggest a particle size reduction with increasing *x*.

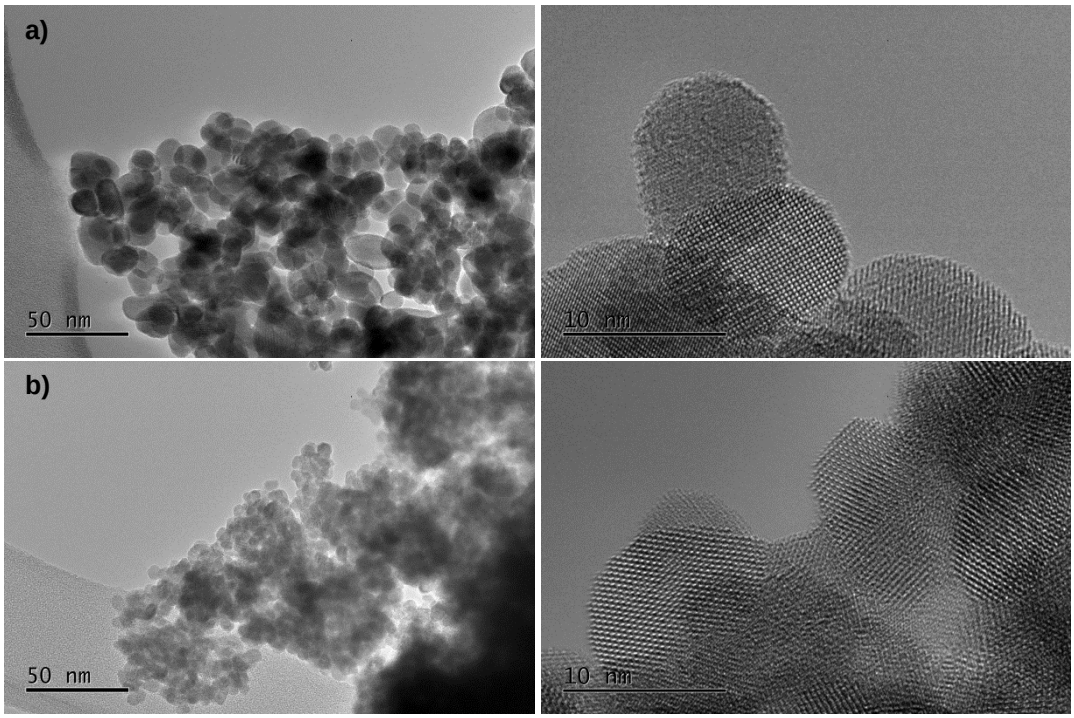

Figure 3. 15 Transmission electron micrographs of CeO_2 made hydrothermally in a) NaOH and b) NH_4OH. Right-hand panels show high resolution micrographs of individual crystallites.

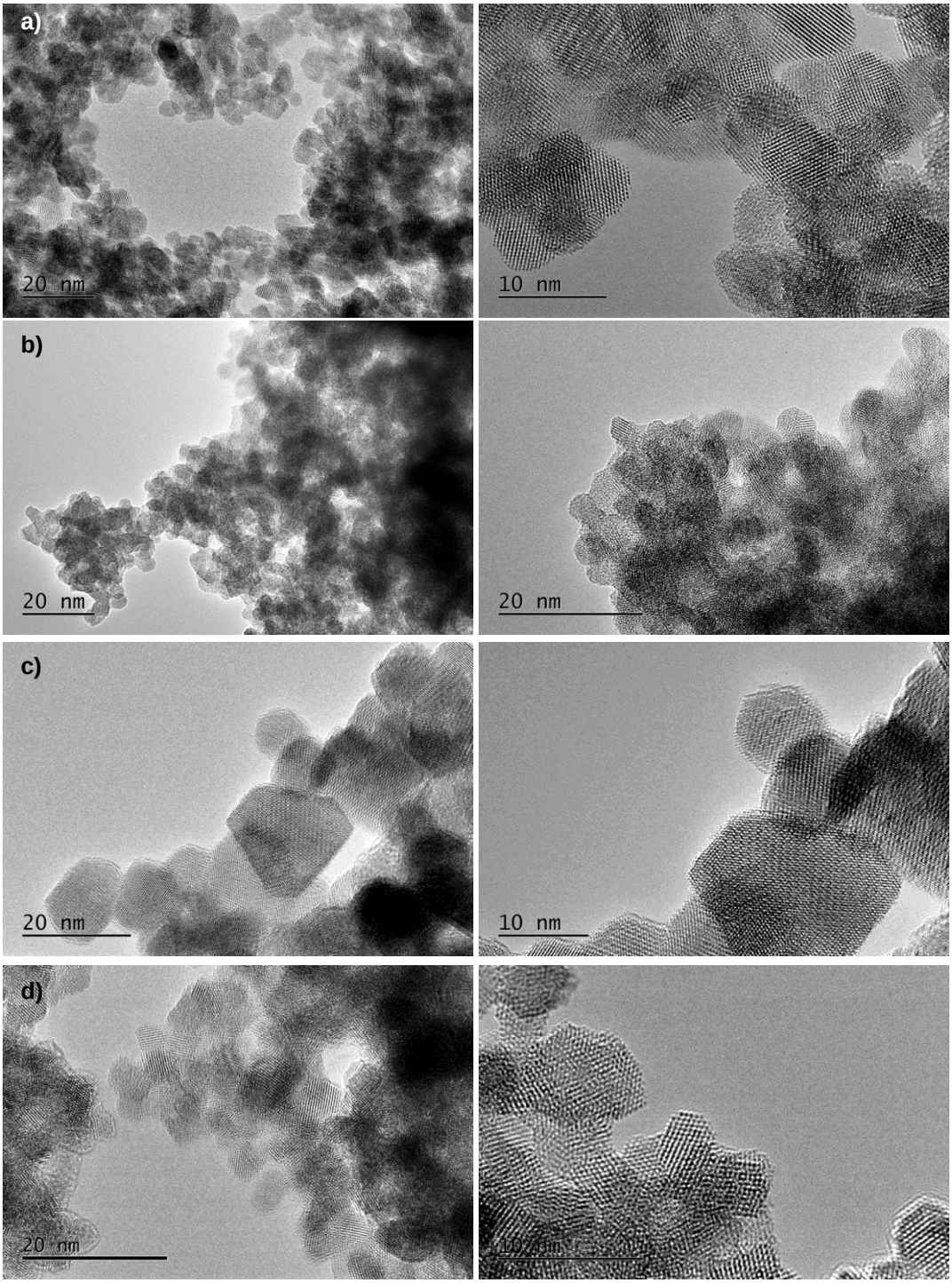

Figure 3. 16 Transmission electron micrographs of a) $Ce_{0.90}Nb_{0.10}O_{2-\delta}$ made in NaOH, b) $Ce_{0.80}Nb_{0.25}O_{2-\delta}$ made in NaOH, c) $Ce_{0.90}Nb_{0.10}O_{2-\delta}$ made in NH_4OH, d) $Ce_{0.80}Nb_{0.25}O_{2-\delta}$ made in NH_4OH. Right-hand panels show high resolution micrographs of individual crystallites.

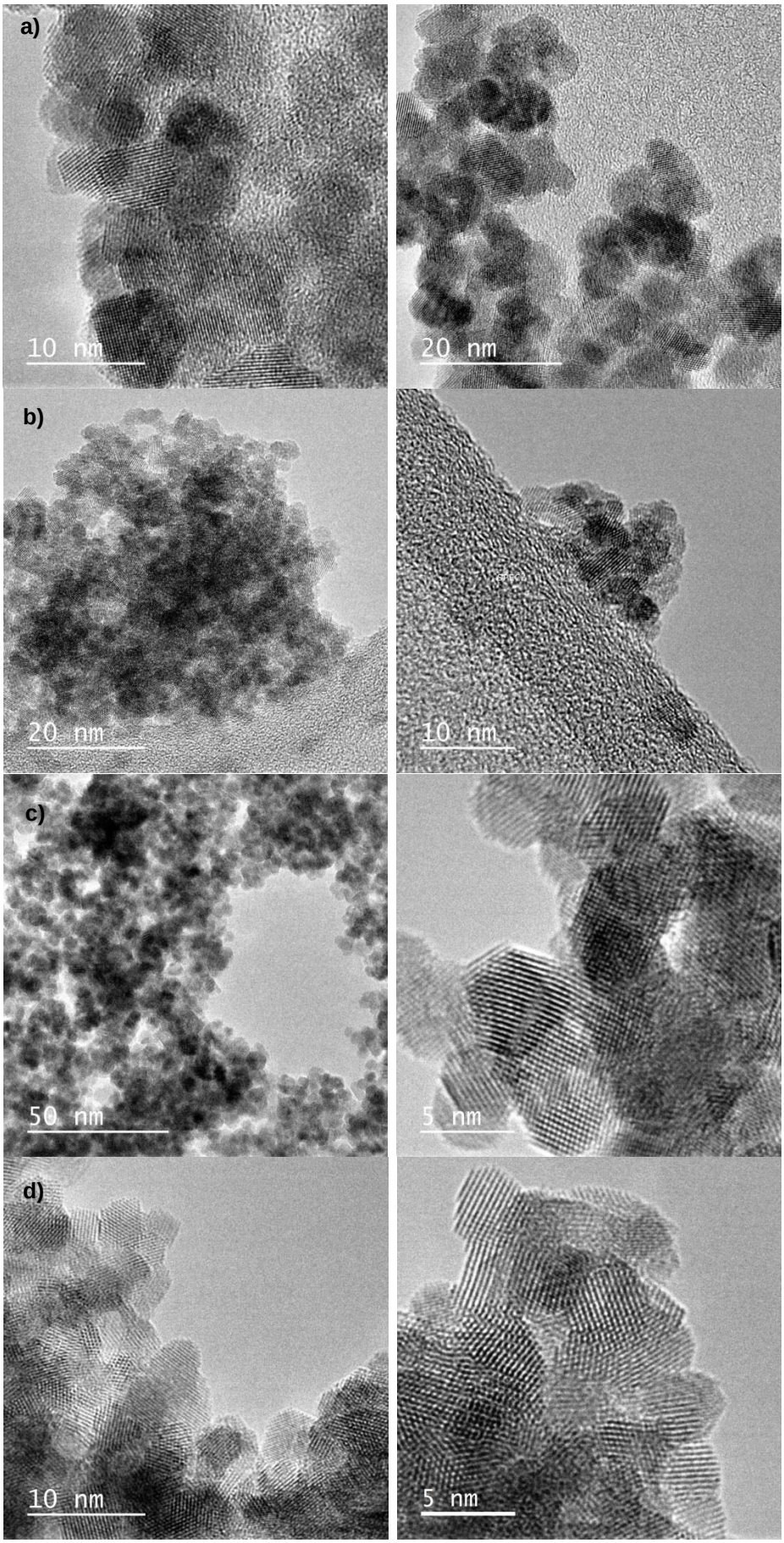

Figure 3. 17 Transmission electron micrographs of a) $Ce_{0.90}Nb_{0.10}O_{2-\delta}$ made in NaOH, b) $Ce_{0.80}Nb_{0.25}O_{2-\delta}$ made in NaOH, c) $Ce_{0.90}Nb_{0.10}O_{2-\delta}$ made in NH_4OH, d) $Ce_{0.80}Nb_{0.25}O_{2-\delta}$ made in NH_4OH. Right-hand panels show high resolution micrographs of individual crystallites.

EDX of $Ce_{1-x}M_xO_{2-\delta}$ (M = Sb, Nb; Table 3. 3 and Table 3. 4, respectively) made hydrothermally in NaOH or NH_4OH at several regions show that there is little variation in *x*.

Table 3. 3 Measured values of x *from EDX elemental analysis (from high resolution TEM) of* $Ce_{0.95}Sb_{0.05}O_{2-\delta}$ *and* $Ce_{0.70}Sb_{0.30}O_{2-\delta}$ *made hydrothermally in NaOH or* NH_4OH.

Intended *x*	Base	Average *x*	Spectra Collected	Min *x*	Max *x*	Standard Deviation
0.05	NaOH	0.032	6	0.020	0.041	0.007
0.30	NaOH	0.208	5	0.144	0.250	0.044
0.05	NH_4OH	0.043	5	0.041	0.047	0.003
0.30	NH_4OH	0.262	5	0.202	0.320	0.053

Table 3. 4 Measured values of x *from EDX elemental analysis (from high resolution TEM) of* $Ce_{0.90}Nb_{0.10}O_{2-\delta}$ *and* $Ce_{0.75}Nb_{0.25}O_{2-\delta}$ *made hydrothermally in NaOH or* NH_4OH.

Intended *x*	Base	Average *x*	Spectra Collected	Min *x*	Max *x*	Standard Deviation
0.10	NaOH	0.120	3	0.109	0.130	0.010
0.25	NaOH	0.252	3	0.244	0.266	0.013
0.10	NH_4OH	0.076	11	0.041	0.105	0.023
0.25	NH_4OH	0.228	7	0.203	0.246	0.015

3.5 X-ray Absorption Spectroscopy

3.5.1 Ce L_{III}-Edge XANES

Ce L_{III}-edge XANES of $Ce_{1-x}M_xO_{2-\delta}$ (M = Sb, Nb, Ta; Figure 3. 18, Figure 3. 19 and Figure 3. 20; respectively) shows the edge position remains close to the position observed in the CeO_2 spectrum. In all cases the near edge region consists of a double peak, characteristic of the Ce^{4+} ion and attributed to two different transitions from the 2*p* level; to either the 5*d* or 4*f* levels.[21,22] This suggests that in all cases the Ce oxidation state is +4, meaning that Ce^{4+} reduction is not responsible for pentavalent ion inclusion in the fluorite structure.

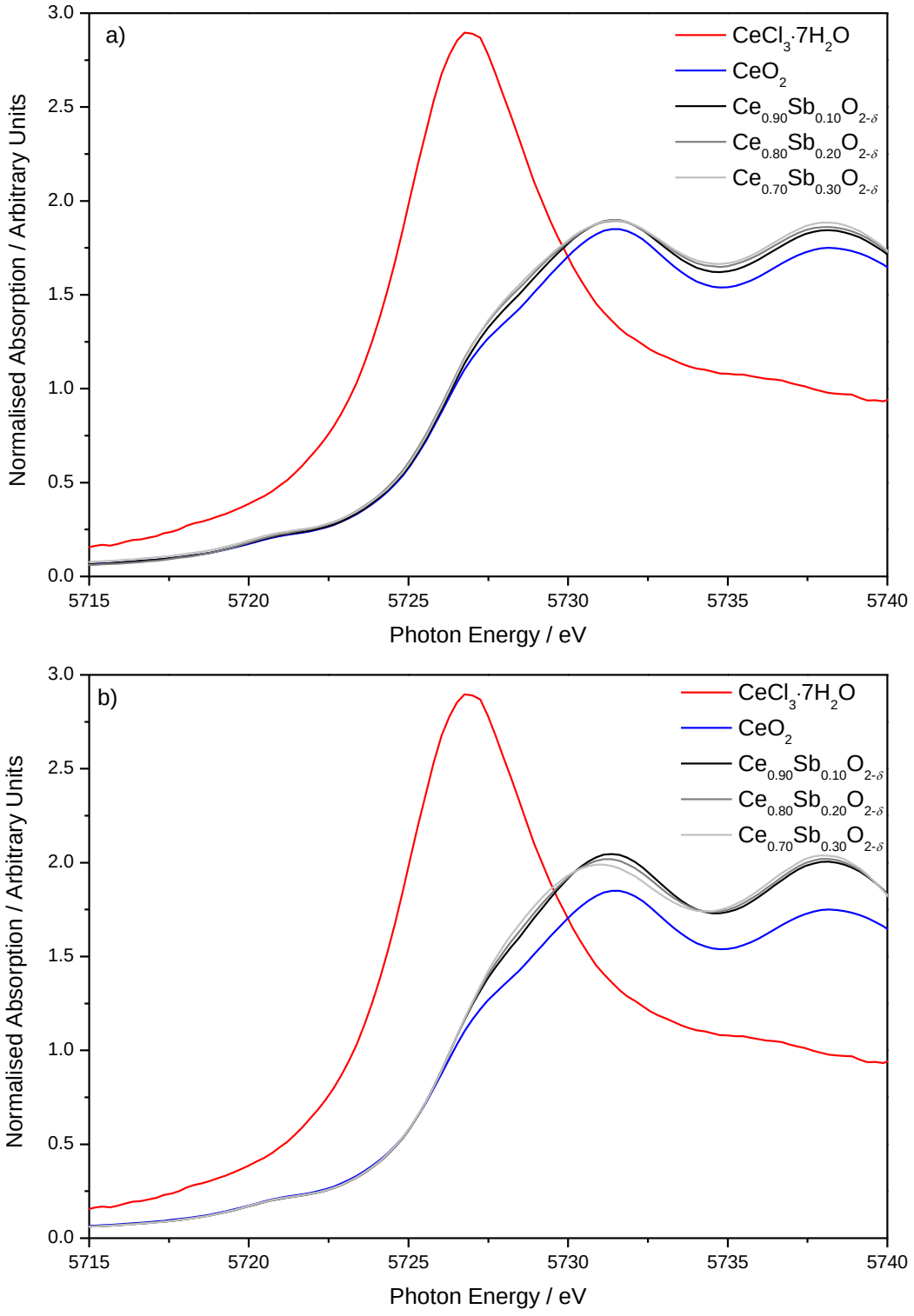

Figure 3. 18 Ce L_{III}-edge XANES spectra of $Ce_{1-x}Sb_xO_{2-\delta}$ (x = 0.10, 0.20, 0.30) made in a) NaOH, b) NH_4OH, compared to Ce^{3+} ($CeCl_3 \cdot 7H_2O$, Sigma-Aldrich) and Ce^{4+} (CeO_2, Sigma-Aldrich) references.

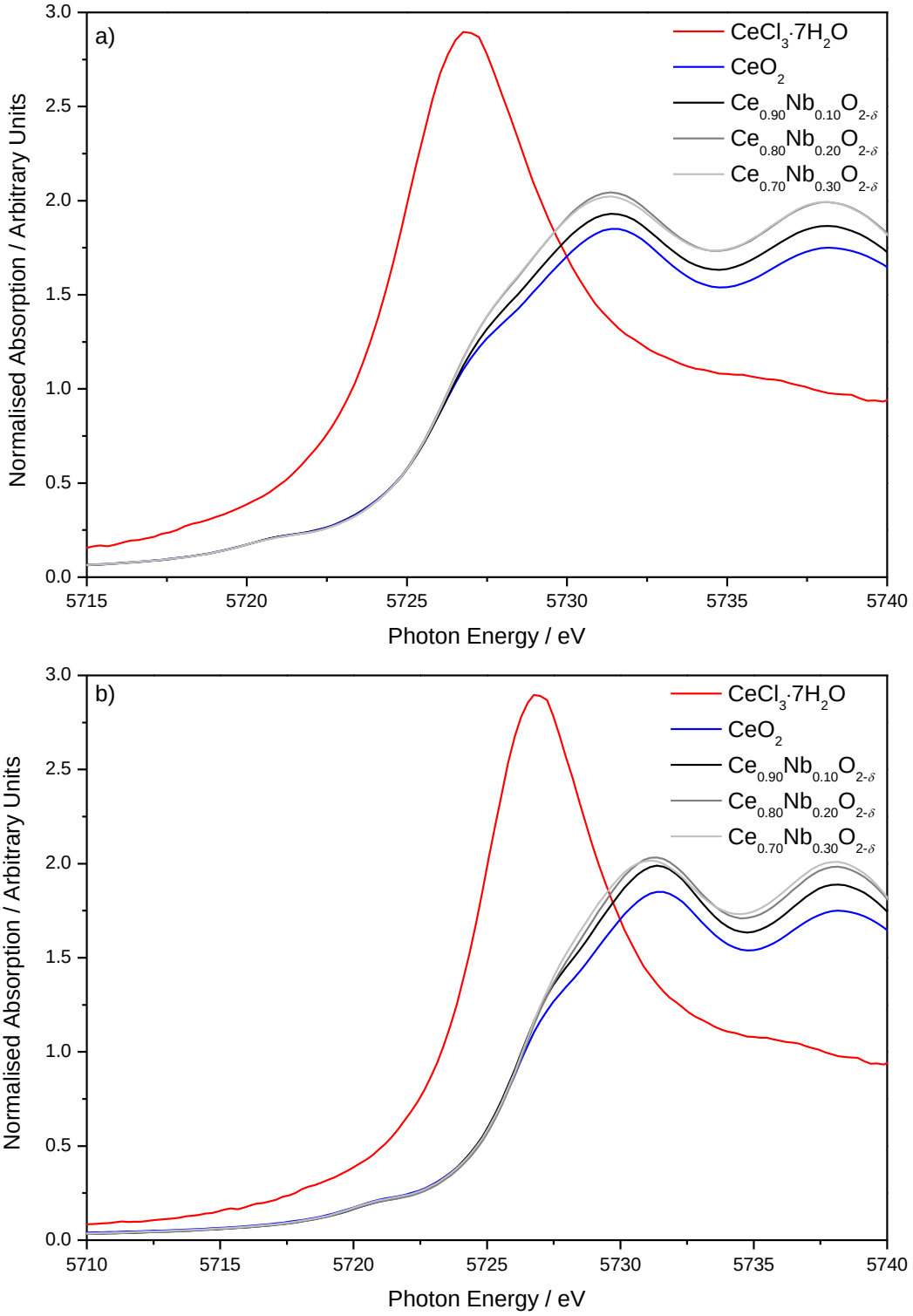

Figure 3. 19 Ce L_{III}-edge XANES spectra of $Ce_{1-x}Nb_xO_{2-\delta}$ (x = 0.10, 0.20, 0.30) made in a) NaOH, b) NH_4OH, compared to Ce^{3+} ($CeCl_3 \cdot 7H_2O$, Sigma-Aldrich) and Ce^{4+} (CeO_2, Sigma-Aldrich) references.

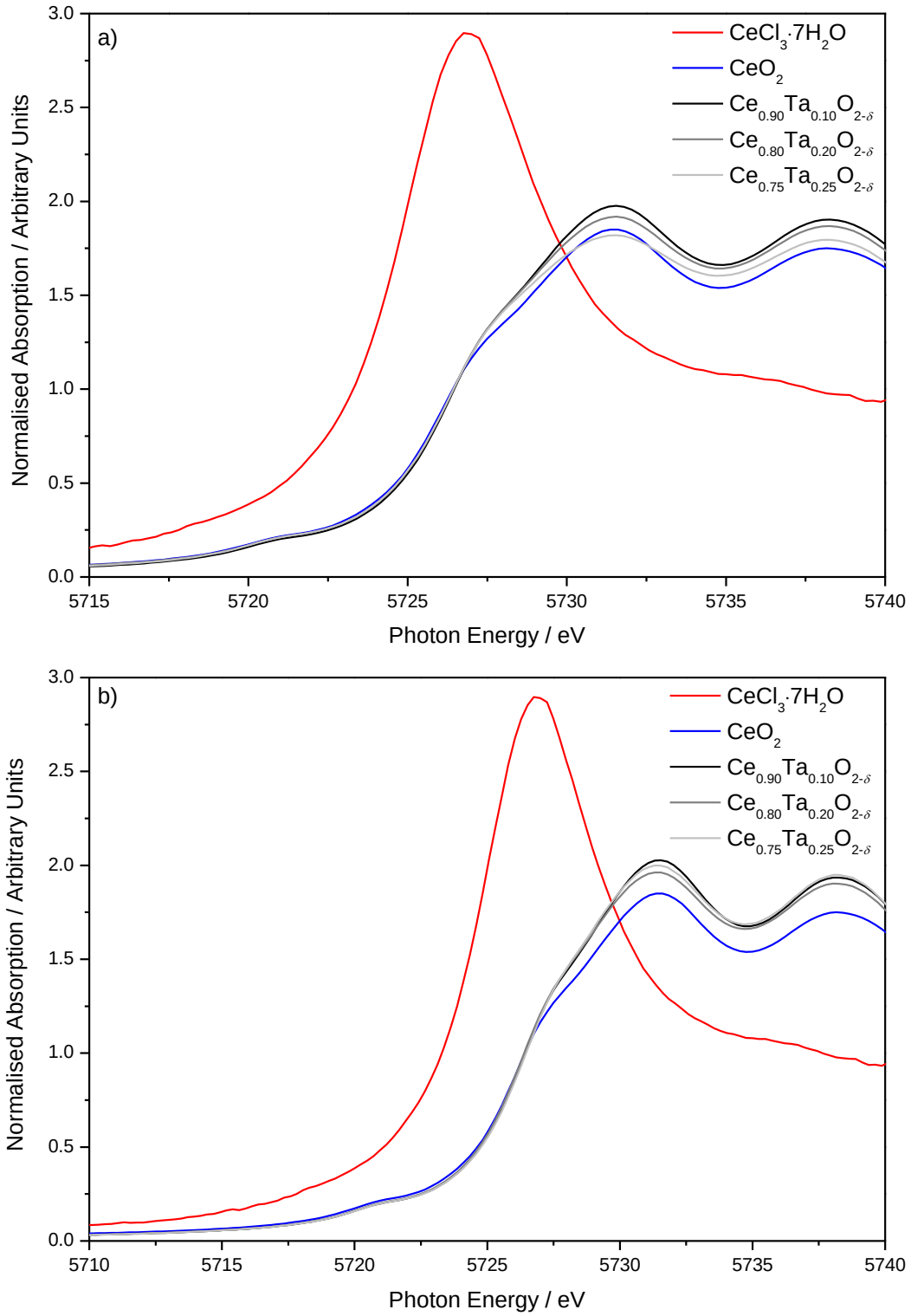

Figure 3. 20 Ce L_{III}-edge XANES spectra of $Ce_{1-x}Ta_xO_{2-\delta}$ (x = 0.10, 0.20, 0.25) made in a) NaOH, b) NH_4OH, compared to Ce^{3+} ($CeCl_3 \cdot 7H_2O$, Sigma-Aldrich) and Ce^{4+} (CeO_2, Sigma-Aldrich) references.

3.5.2 Sb K-Edge, Nb K-Edge and Ta L_{III}-Edge XANES

Sb is stable in both the +3 and +5 oxidation states.[19] Sb^{3+} inclusion into the fluorite lattice might be expected, since $Ce_{1-x}Bi_xO_{2-\delta}$ containing Bi^{3+} has been previously hydrothermally synthesised,[22] and oxide vacancies – which form easily in the fluorite structure – could be used to achieve charge balance. Sb K-edge XANES spectra of $Ce_{1-x}Sb_xO_{2-\delta}$ made in NaOH (Figure 3. 21a) and NH_4OH (Figure 3. 21b), however, have an edge position very close to that of $NaSbO_3$, suggesting an average oxidation state of +5.

As expected (due to the stability of the Nb and Ta +5 oxidation state[23]), the Nb K- and Ta L_{III}-edge positions in $Ce_{1-x}Nb_xO_{2-\delta}$ (Figure 3. 22) and $Ce_{1-x}Ta_xO_{2-\delta}$ (Figure 3. 23) respectively, were found to be very close to Nb^{5+} and Ta^{5+} references.

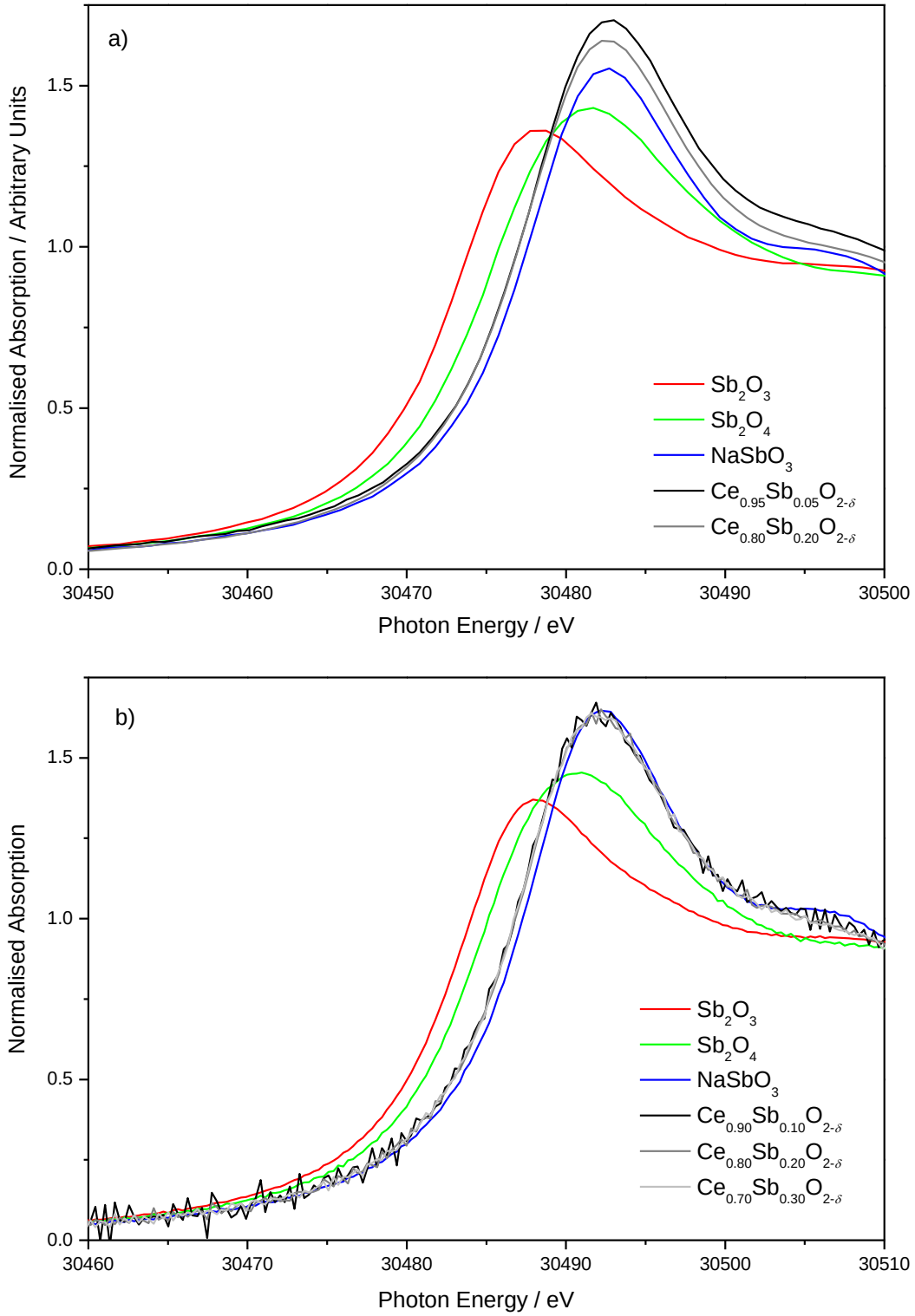

Figure 3. 21 Sb K-edge XANES spectra of $Ce_{1-x}Sb_xO_{2-\delta}$ (x = 0.10, 0.20, 0.30, made using $SbCl_5$) made in a) NaOH, b) NH_4OH, compared to Sb^{3+} (Sb_2O_3, Sigma-Aldrich), Sb^{4+} (Sb_2O_4) and Sb^{5+} ($NaSbO_3$, Alfa Aesar) references.

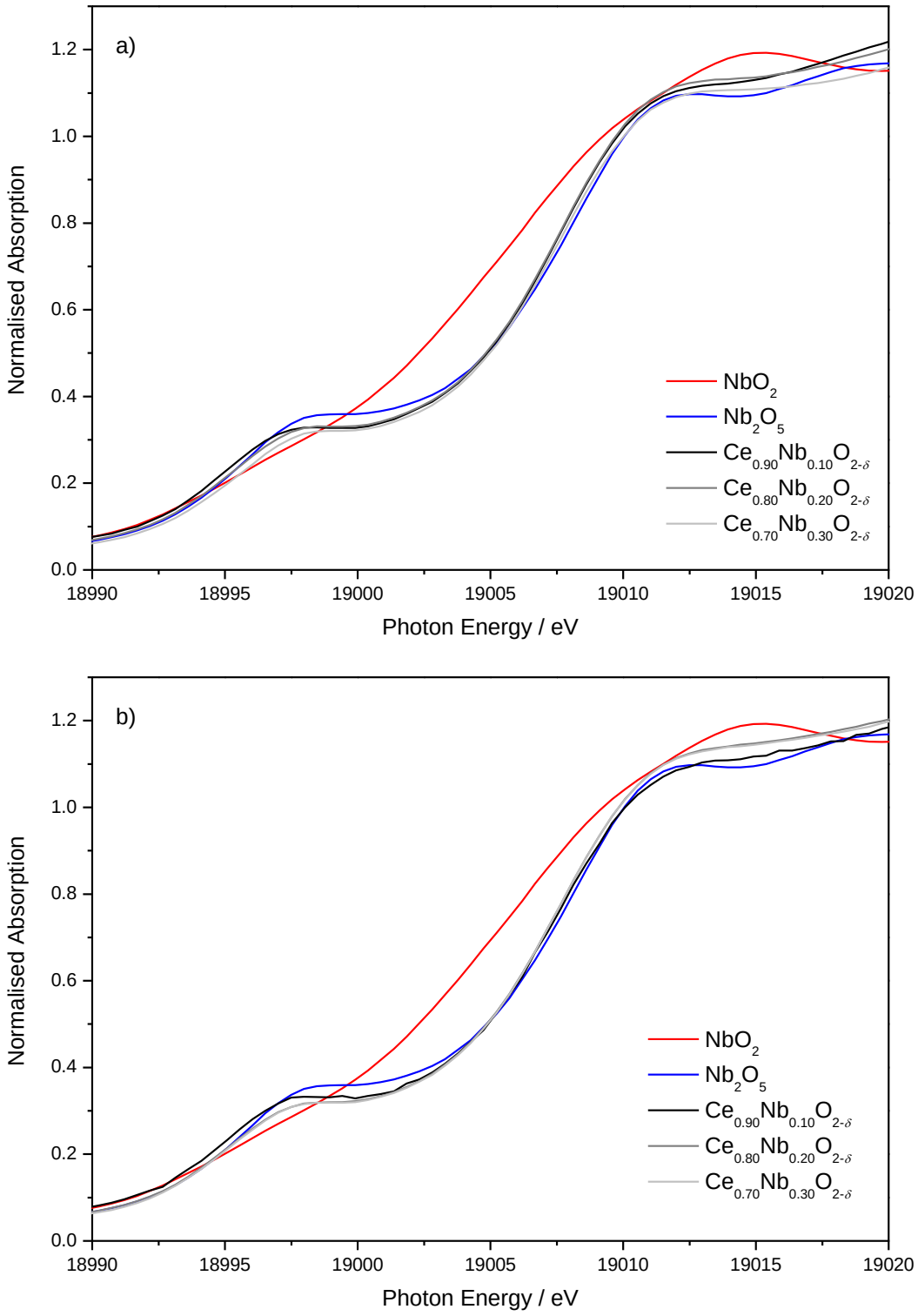

Figure 3. 22 Nb K-edge XANES spectra of $Ce_{1-x}Nb_xO_{2-\delta}$ (x = 0.10, 0.20, 0.30) made in a) NaOH, b) NH_4OH, compared to Nb^{4+} (NbO_2) and Nb^{5+} (Nb_2O_5, Sigma-Aldrich) references.

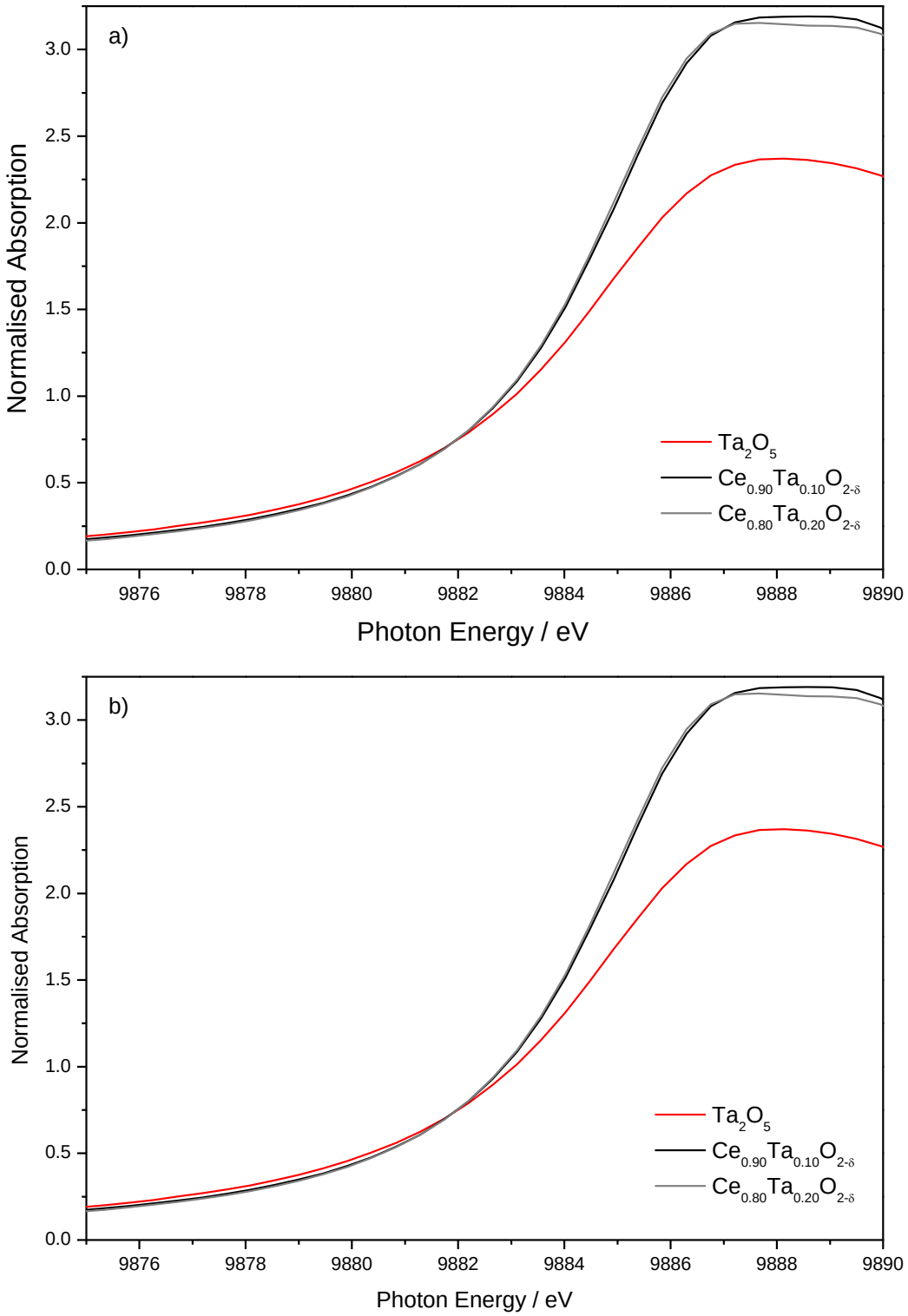

Figure 3. 23 Ta K-edge XANES spectra of $Ce_{1-x}Ta_xO_{2-\delta}$ (x = 0.10, 0.20) *made in a) NaOH, b)* NH_4OH, *compared to* Ta^+ (Ta_2O_5, Sigma-Aldrich) *references.*

3.6 Powder Neutron Diffraction

Powder neutron diffraction patterns collected on GEM (ISIS, U.K.) of CeO_2 and $Ce_{1-x}Nb_xO_{2-\delta}$ (x = 0.10, 0.20, 0.30) made in NaOH (Figure 3. 24) and CeO_2 and $Ce_{0.80}Nb_{0.20}O_{2-\delta}$ made in NH_4OH (and fired in air at 500 °C, Figure 3. 25) all have Bragg reflections which can be indexed to a cubic fluorite. Na was not included in the Rietveld model in order to achieve a stable refinement. Eight-coordinate Na has a similar ionic radius to eight-coordinate Ce^{4+} and is thus expected to occupy the 4*a* site. The scattering lengths of Ce and Na (4.84 fm and 3.63 fm;[24] respectively) are also quite similar, making a unique fit difficult, particularly when Nb is also occupying the 4*a* site. The Ce and Nb occupancies were constrained so that the total occupancy of the 4*a* site = 1, in order to achieve a meaningful result.

The Bragg peaks become broader as x increases, as observed in powder XRD and attributed to crystallite size and strain effects. However, as x increases the Rietveld fits to the data using the simple cubic fluorite model become significantly worse – peaks become increasingly asymmetric and peak intensities are not accurately reproduced in the calculated pattern. This is indicative of significant local disorder, which would be expected if Nb were not sitting on the Ce 4*a* site in order to have an octahedral coordination environment. This would also distort the cubic oxide lattice. This distortion causes a large discrepancy in the site occupancy factors and atomic displacement parameters obtained from the Rietveld refinements (Table 3. 6 – Table 3. 10), particularly at high values of x, where distortion is greatest.

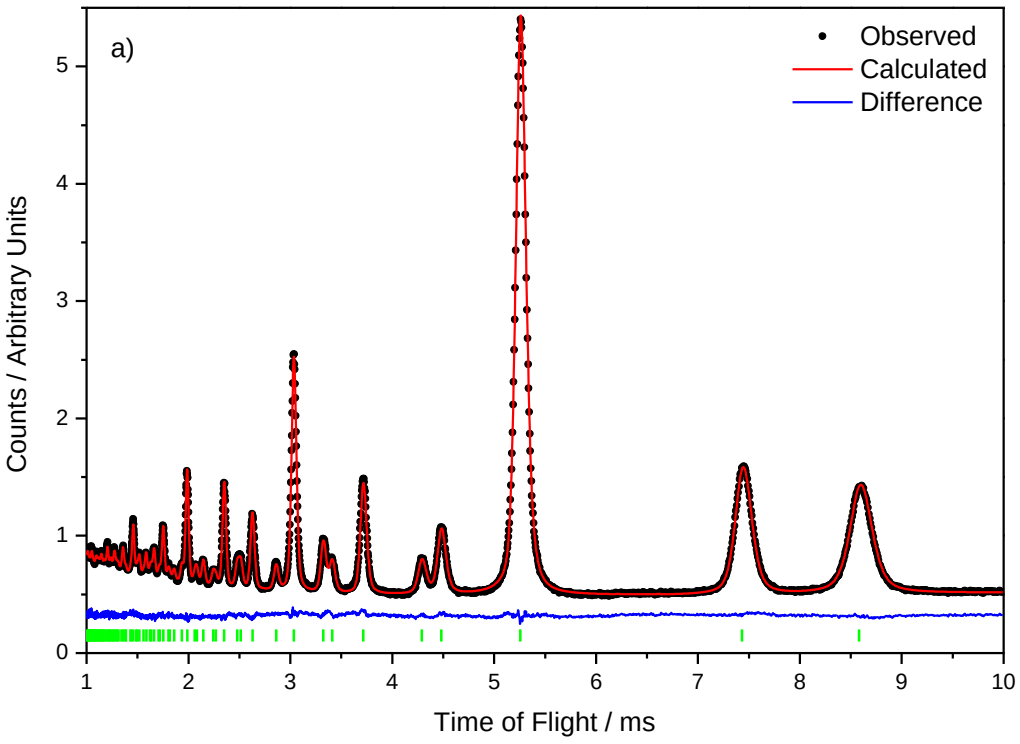
a)
Observed
Calculated
Difference
Counts / Arbitrary Units
Time of Flight / ms

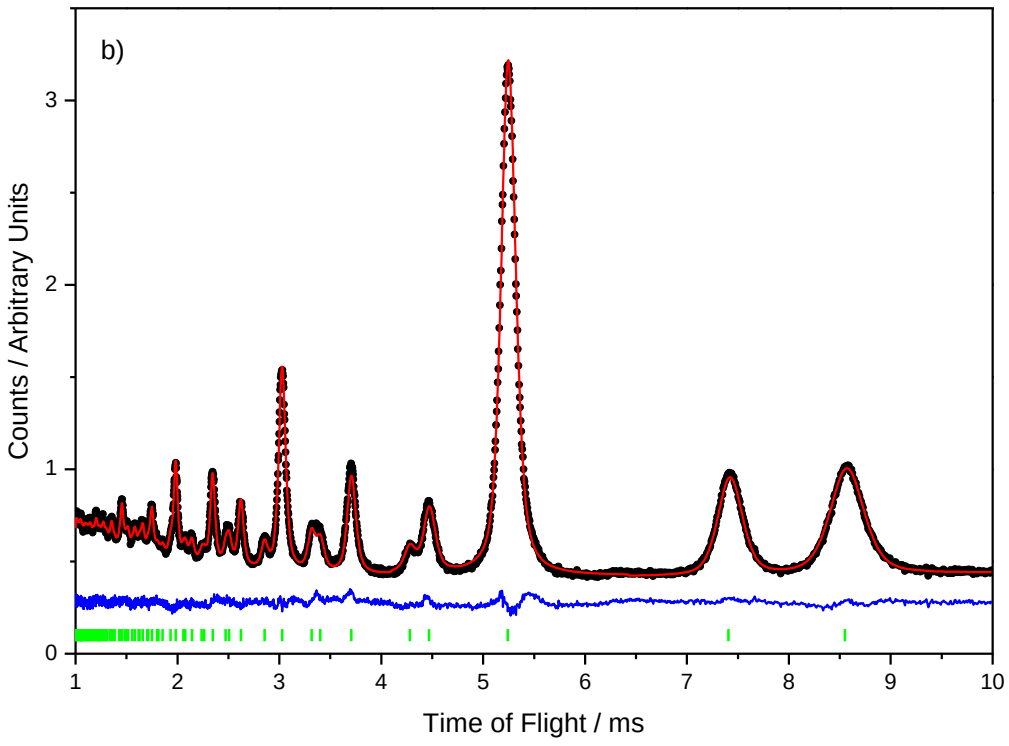
b)
Counts / Arbitrary Units
Time of Flight / ms

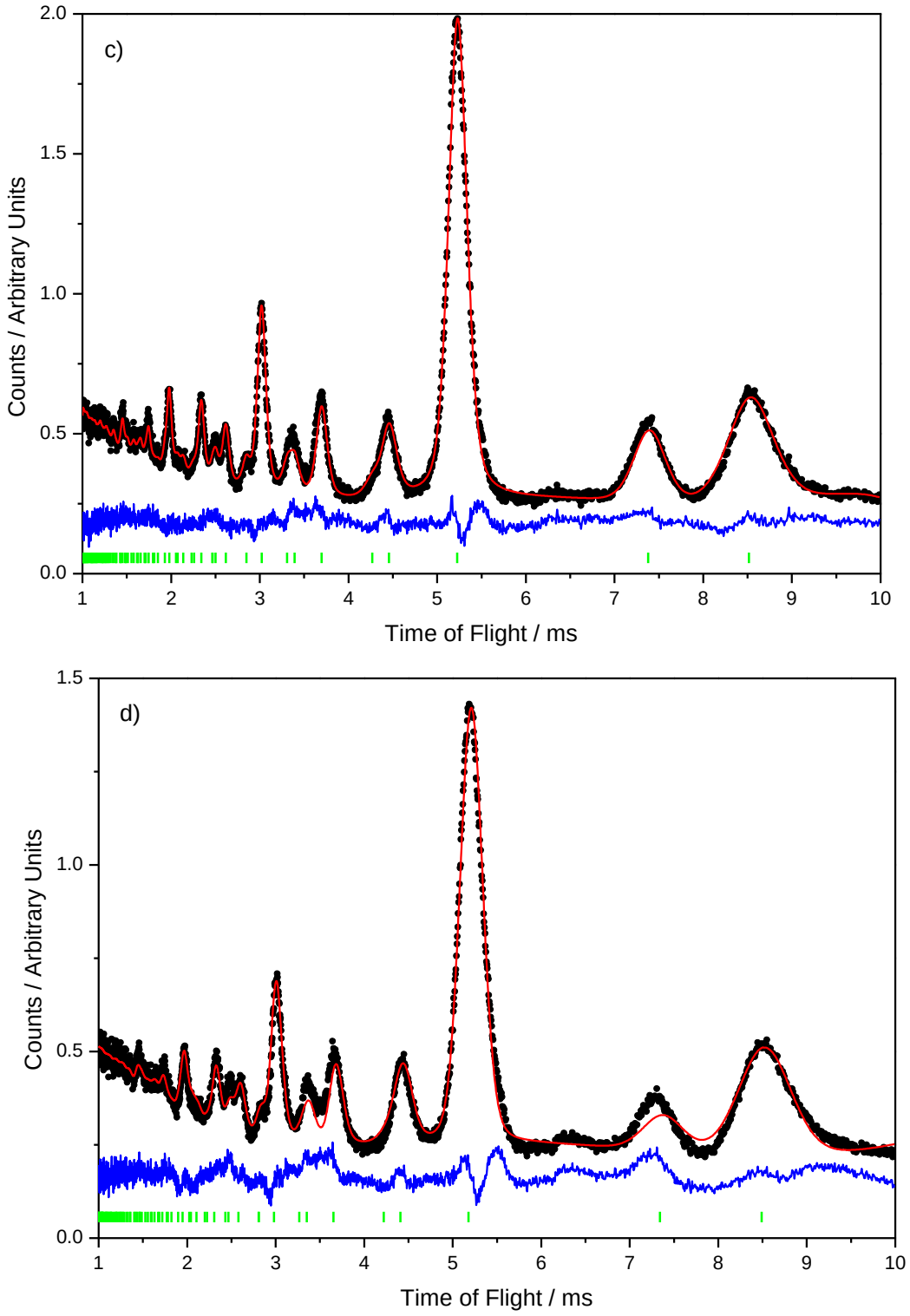

Figure 3. 24 Rietveld fits to room temperature powder neutron diffraction data of a) CeO_2, b) $Ce_{0.90}Nb_{0.10}O_{2-\delta}$, c) $Ce_{0.80}Nb_{0.20}O_{2-\delta}$ and d) $Ce_{0.70}Nb_{0.30}O_{2-\delta}$ all made hydrothermally in NaOH. Tick marks denote expected $Fm\bar{3}m$ *positions. All diffraction patterns from GEM Bank 3 (mean scattering angle 2θ = 34.96°).*

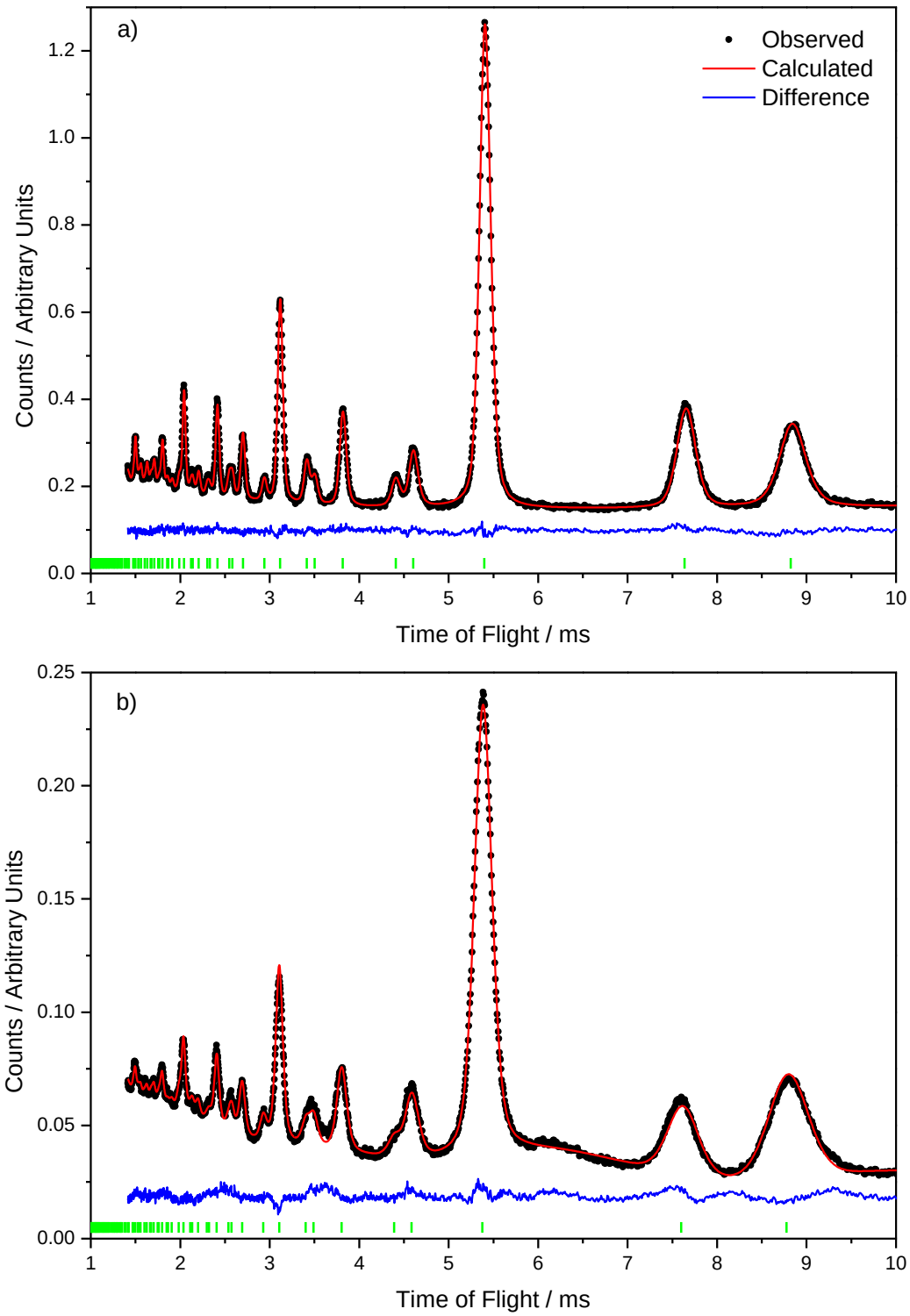

Figure 3. 25 Rietveld fits to room temperature powder neutron diffraction data of a) CeO_2, b) $Ce_{0.80}Nb_{0.20}O_{2-\delta}$, both made hydrothermally in NH_4OH. Tick marks denote expected $Fm\bar{3}m$ *positions. All diffraction patterns from GEM Bank 3 (mean scattering angle* $2\theta = 34.96°$*).*

Table 3. 6 Refined atomic parameters of CeO_2 prepared hydrothermally in NaOH to powder neutron diffraction data (GEM banks 3 and 5). Space group $Fm\bar{3}m$, *a = 5.40228(3) Å;* χ^2 *= 4.45;* R_{wp} *= 2.21% (1.89% and 2.39% for respective banks);* R_p *= 1.71% (1.48% and 1.89% for respective banks).*

Atom	Wyckoff	*x*	*y*	*z*	Occupancy	ADP / Å^2
Ce	4*a*	0	0	0	1	0.00389(4)
O	8*c*	0.25	0.25	0.25	1	0.00694(2)

Table 3. 7 Refined atomic parameters of $Ce_{0.90}Nb_{0.10}O_{2-\delta}$ prepared hydrothermally in NaOH to powder neutron diffraction data (GEM banks 3 and 5). Space group $Fm\bar{3}m$, *a = 5.39454(8) Å;* χ^2 *= 3.62;* R_{wp} *= 2.19% (1.98% and 2.31% for respective banks);* R_p *= 1.80% (1.56% and 1.99% for respective banks).*

Atom	Wyckoff	*x*	*y*	*z*	Occupancy	ADP / Å^2
Ce	4*a*	0	0	0	0.872(3)	0.00365(5)
Nb	4*a*	0	0	0	0.128(3)	0.00365(5)
O	8*c*	0.25	0.25	0.25	1.006(1)	0.00864(4)

Table 3. 5 Refined atomic parameters of $Ce_{0.80}Nb_{0.20}O_{2-\delta}$ prepared hydrothermally in NaOH to powder neutron diffraction data (GEM banks 3 and 5). Space group $Fm\bar{3}m$, *a = 5.3760(3) Å;* χ^2 *= 2.64;* R_{wp} *= 2.07% (2.09% and 2.06% for respective banks);* R_p *= 1.68% (1.63% and 1.73% for respective banks).*

Atom	Wyckoff	*x*	*y*	*z*	Occupancy	ADP / Å^2
Ce	4*a*	0	0	0	0.728(6)	0.0061(1)
Nb	4*a*	0	0	0	0.272(6)	0.0061(1)
O	8*c*	0.25	0.25	0.25	0.935(2)	0.0090(1)

Table 3. 8 Refined atomic parameters of $Ce_{0.70}Nb_{0.30}O_{2-\delta}$ prepared hydrothermally in NaOH to powder neutron diffraction data (GEM banks 3 and 5). Space group $Fm\bar{3}m$, *a = 5.3647(4) Å;* χ^2 *= 5.50;* R_{wp} *= 2.16% (2.22% and 2.12% for respective banks);* R_p *= 1.73% (1.76% and 1.71% for respective banks).*

Atom	Wyckoff	*x*	*y*	*z*	Occupancy	ADP / Å^2
Ce	4*a*	0	0	0	0.456(6)	0.00292(8)
Nb	4*a*	0	0	0	0.544(6)	0.00292(8)
O	8*c*	0.25	0.25	0.25	0.959(2)	0.0175(2)

Table 3. 9 Refined atomic parameters of CeO_2 prepared hydrothermally in NH_4OH to powder neutron diffraction data (GEM banks 3 and 5). Space group $Fm\bar{3}m$, *a = 5.41131(5) Å;* χ^2 *= 1.24;* R_{wp} *= 1.83% (1.95% and 1.74% for respective banks);* R_p *= 1.46% (1.52% and 1.39% for respective banks).*

Atom	Wyckoff	*x*	*y*	*z*	Occupancy	ADP / Å^2
Ce	4*a*	0	0	0	1	0.00333(6)
O	8*c*	0.25	0.25	0.25	1	0.00664(3)

Table 3. 10 Refined atomic parameters of $Ce_{0.80}Nb_{0.20}O_{2-\delta}$ prepared hydrothermally in NH_4OH to powder neutron diffraction data (GEM banks 3 and 5). Space group $Fm\bar{3}m$, *a = 5.413(1) Å;* χ^2 *= 4.02;* R_{wp} *= 2.12% (1.80% and 2.29% for respective banks);* R_p *= 1.56% (1.44% and 1.67% for respective banks).*

Atom	Wyckoff	*x*	*y*	*z*	Occupancy	ADP / Å^2
Ce	4*a*	0	0	0	0.75(2)	0.0048(3)
Nb	4*a*	0	0	0	0.25(2)	0.0048(3)
O	8*c*	0.25	0.25	0.25	1.006(6)	0.0142(3)

3.7 Discussion and Conclusions

In this chapter it has been shown for the first time that a range of ions in the +5 oxidation state can be substituted into the CeO_2 fluorite structure in a nanocrystalline morphology by hydrothermal synthesis. This chapter has attempted to address this and determine how a pentavalent ion is incorporated into CeO_2; when prepared hydrothermally.

Whilst some reports of pentavalent ion substitution exist, authors tend not to address the mechanism by which this is occurring. Those that do, offer conflicting models with little proof.[1,2] The most plausible models proposed are:

1. Reduction of Ce^{4+} to achieve charge balance. Surface reduction of Ce^{4+} has been predicted by computational methods[7] but has not previously been tested experimentally.
2. Incorporation of a second cation of lower valence into the structure. This has been demonstrated in a very dilute system, $Ce_{0.9985}Ta_{0.0010}Ca_{0.0005}O_2$,[8] but no further to the best of my knowledge.
3. Incorporation of excess oxygen into the structure, as found for $UO_{2+\delta}$.

Ce L_{III}-edge XANES (Section 3.5.1) shows that the average oxidation state of Ce remains close to +4 in $Ce_{1-x}M_xO_{2-\delta}$ (M = Sb^{5+}, Nb^{5+}, Ta^{5+}; $0 \leq x \leq 0.25 - 0.40$) with no sign of Ce reduction as x increases, ruling out Ce^{4+} reduction (Model 1).

Lattice parameters of $Ce_{1-x}M_xO_{2-\delta}$, as determined by powder diffraction techniques, show a decrease as a function of x, in accordance with the reduced ionic radii of the pentavalent ions compared to that of eight-coordinate Ce^{4+}. However, the oxides made hydrothermally in NaOH show a larger decrease in lattice parameter than their

analogous samples prepared in NH_4OH. This suggests that the base is not merely a mineraliser for the reaction, but is also acting as a reagent. In order to achieve charge balance (with no oxide non-stoichiometry or cation vacancies) one Na atom could be substituted for a Ce atom for every three Nb (or Sb or Ta) atoms substituted into the structure, in Kröger-Vink notation:

$$4Ce_{Ce}^{\times} \Rightarrow 3Nb_{Ce}^{\bullet} + Na_{Ce}'''$$

Elemental analysis shows an approximately linear increase in the amount of Na in $Ce_{1-x}M_xO_{2-\delta}$ (M = Sb, Nb) as x increases (Figure 3. 26). The amount of Na present is consistently larger than the amount needed for charge balance of the form described above. There are two possible explanations for this. There is always the possibility of Na species on the surface which are not removed by washing with boiling water that would contribute to the total Na content. This is not likely to be the sole reason for the presence of Na however; although the surface area of the oxide increases as a function of x (see Chapter 5), it only increases by a factor of three from CeO_2 to $Ce_{0.70}Nb_{0.30}O_{2-\delta}$, far smaller than the increase in the amount of Na present. It is for this reason that it is concluded that, for the materials made hydrothermally in NaOH, Na incorporation is at least partially the mechanism by which pentavalent ions are substituted into the fluorite structure. However, it is still unclear as to how pentavalent ions are substituted into the lattice when NH_4OH is used instead of NaOH in the synthesis.

The other explanation for the larger-than-expected increase in Na content is that extra Na is being incorporated into the fluorite, with oxide vacancies balancing the charge. This could explain why an appreciable amount of Na was detected in "CeO_2" prepared hydrothermally.

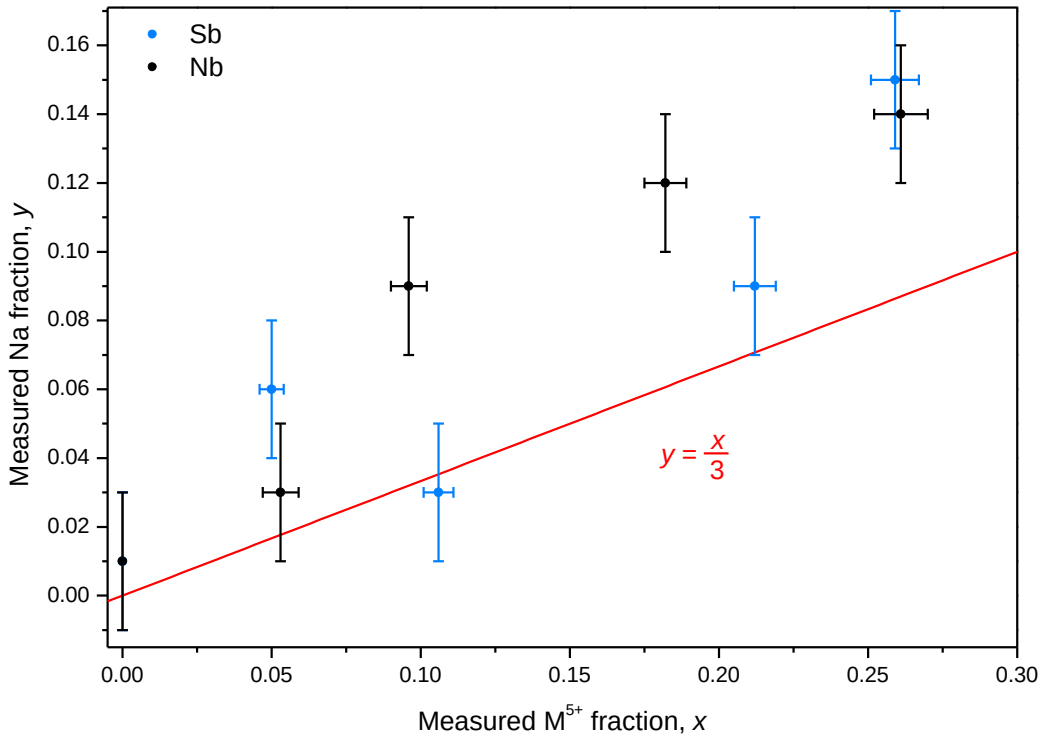

Figure 3. 26 Measured (by ICP-OES) Na molar fraction y *as a function of* M^{5+} *molar fraction; where* $Ce_{1-x-y}M_xNa_yO_{2-\delta}$. *(M = Sb, Nb) Line* y = 0.333x *shown as a guide to the eye.*

Local structure techniques are necessary in order to fully understand how the pentavalent ions are incorporated and where they sit within the fluorite lattice. This includes pair distribution function analysis from neutron total scattering; Nb EXAFS and H, Na and Nb NMR. All of these analyses are currently underway in collaboration with co-workers.

The thermal and redox behaviours of these materials are presented in Chapter 5.

3.8 References

(1) Kaneko, H.; Taku, S.; Naganuma, Y.; Ishihara, T.; Hasegawa, N.; Tamaura, Y. *J. Sol. Energy Eng. Trans.-ASME* **2010**, *132*, 021202.
(2) Le Gal, A.; Abanades, S. *J. Phys. Chem. C* **2012**, *116*, 13516.
(3) Pecharsky, V.; Zavalij, P. *Fundamentals of Powder Diffraction and Structural Characterization of Materials, Second Edition:*; Springer, 2009.
(4) Shannon, R. D. *Acta Crystallogr. Sect. A* **1976**, *32*, 751.
(5) Modeshia, D. R.; Darton, R. J.; Ashbrook, S. E.; Walton, R. I. *Chem. Commun.* **2009**, 68.
(6) Li, X.; Zang, J. *J. Phys. Chem. C* **2009**, *113*, 19411.
(7) Nolan, M. *Chem. Phys. Lett.* **2010**, *492*, 115.
(8) Chang, E. K.; Blumenthal, R. N. *J. Solid State Chem.* **1988**, *72*, 330.
(9) Mogensen, M.; Sammes, N. M.; Tompsett, G. A. *Solid State Ion.* **2000**, *129*, 63.
(10) Bevan, D. J. M.; Greis, O.; Strahle, J. *Acta Crystallogr. Sect. A* **1980**, *36*, 889.
(11) Willis, B. T. M. *Nature* **1963**, *197*, 755.
(12) Willis, B. T. M. *Acta Crystallogr. Sect. A* **1978**, *34*, 88.
(13) Garrido, F.; Hannon, A. C.; Ibberson, R. M.; Nowicki, L.; Willis, B. T. M. *Inorg. Chem.* **2006**, *45*, 8408.
(14) Desgranges, L.; Baldinozzi, G.; Siméone, D.; Fischer, H. E. *Inorg. Chem.* **2011**, *50*, 6146.
(15) Horlait, D.; Claparede, L.; Clavier, N.; Szenknect, S.; Dacheux, N.; Ravaux, J.; Podor, R. *Inorg. Chem.* **2011**, *50*, 7150.
(16) Li, G.; Smith, R. L.; Inomata, H. *J. Am. Chem. Soc.* **2001**, *123*, 11091.
(17) Mineshige, A.; Taji, T.; Muroi, Y.; Kobune, M.; Fujii, S.; Nishi, N.; Inaba, M.; Ogumi, Z. *Solid State Ion.* **2000**, *135*, 481.
(18) Li, L.; Chen, F.; Lu, J. Q.; Luo, M. F. *J. Phys. Chem. A* **2011**, *115*, 7972.
(19) Greenwood, N. N.; Earnshaw, A. *Chemistry of the Elements*; 2nd ed.; Butterworth–Heinemann, 1997.
(20) Wright, C. S.; Walton, R. I.; Thompsett, D.; Fisher, J.; Ashbrook, S. E. *Adv. Mater.* **2007**, *19*, 4500.
(21) Modeshia, D. R.; Wright, C. S.; Payne, J. L.; Sankar, G.; Fiddy, S. G.; Walton, R. I. *J. Phys. Chem. C* **2007**, *111*, 14035.
(22) Sardar, K.; Playford, H. Y.; Darton, R. J.; Barney, E. R.; Hannon, A. C.; Tompsett, D.; Fisher, J.; Kashtiban, R. J.; Sloan, J.; Ramos, S.; Cibin, G.; Walton, R. I. *Chem. Mater.* **2010**, *22*, 6191.
(23) Nowak, I.; Ziolek, M. *Chem. Rev.* **1999**, *99*, 3603.
(24) Sears, V. F. *Neutron News* **1992**, *3*, 29

Chapter 4: Hydrothermal Synthesis and Characterisation of Platinum Group Metal-Doped Cerium Oxides

4.1 Introduction

In this chapter an investigation of the synthesis and characterisation of fluorite cerium dioxide doped with platinum group metals[1] (PGMs), Pd and Pt, is reported. A detailed study of $Ce_{1-x}Pd_xO_{2-\delta}$ using a number of techniques has been undertaken in order to prove true doping and to determine the local environment of the Pd.

Highly dispersed PGM on high surface area CeO_2 (and doped CeO_2) is an integral part of three-way catalytic convertors for automobile exhausts[2-8] and water-gas shift reactors.[6,8,9] According to Seshadri and coworkers, the most atom efficient method of dispersing platinum group metal could be to substitute single ions into the nanoparticles of the oxide lattice.[10] Some research has already been carried out in on PGM-substituted CeO_2 (see Chapter 1), though only one report of hydrothermal preparation (where PGM = Ru) exists.[11] There is no consensus on how the Pd is incorporated into the structure. EXAFS studies[12,13] suggest a distorted six-coordinate environment, though the accuracy of this is questionable: the model that was fitted to the data contains 3.1 Å Pd – Pd correlations, though how these distances arise are not explained. Furthermore, their fitting to PdO EXAFS spectrum contains unfeasibly short Pd – Pd correlations (2.7 Å) which are not described by the crystal structure. Recently a model was suggested Scanlon *et al.*[14] from computational studies includes Pd(II) in its preferred square-planar coordination, whilst maintaining the average fluorite structure. This model is compared to Pd EXAFS data collected from hydrothermally synthesised $Ce_{1-x}Pd_xO_{2-\delta}$ (x = 0.05, 0.10, 0.20).

The catalytic properties and thermal stability of the oxides is explored in Chapter 5.

4.2 Palladium-Doped Ceria

4.2.1 Synthesis

$Ce_{1-x}Pd_xO_{2-\delta}$ (nominally $0.05 \leq x \leq 0.25$ in increments of $x = 0.05$) was prepared by a hydrothermal reaction at 240 °C. $CeCl_3 \cdot 7H_2O$ and $PdCl_2$ were mixed in a $(1 - x):x$ molar ratio; respectively; to give a total of 6 mmol of metal ions. To this 2 ml of cold H_2O was added, yielding a solution, to which 2 ml of H_2O_2 (37% aqueous solution) was added. This mixture was stirred for 15 minutes before 8 ml of 7.5 mol dm^{-3} NaOH was added dropwise with effervescence. The red-brown gel was stirred for a further 10-15 minutes before being sealed in a Teflon-lined steel autoclave and heated in a fan oven to 240 °C for 24 hours. The autoclave was cooled to room temperature before filtration and washing with copious amounts of boiling water. The resulting brown solids were dried in an oven at 80 °C overnight and ground in a pestle and mortar to give fine powders.

4.2.2 Powder XRD

Powder XRD patterns of $Ce_{1-x}Pd_xO_{2-\delta}$ ($0.05 \leq x \leq 0.25$) can all be indexed to a fluorite unit cell, space group $Fm\bar{3}m$ (Figure 4. 1). The mean crystallite size; derived from the peak shape term *Lx* using the Scherrer equation;[15] decreases from 30 nm to 11 nm with increasing Pd content (Table 4. 1). When the intended x was 0.30, reflections attributed to PdO (palladinite[16] space group $P4_2/mmc$) were observed and a slight decrease in lattice parameter was observed.

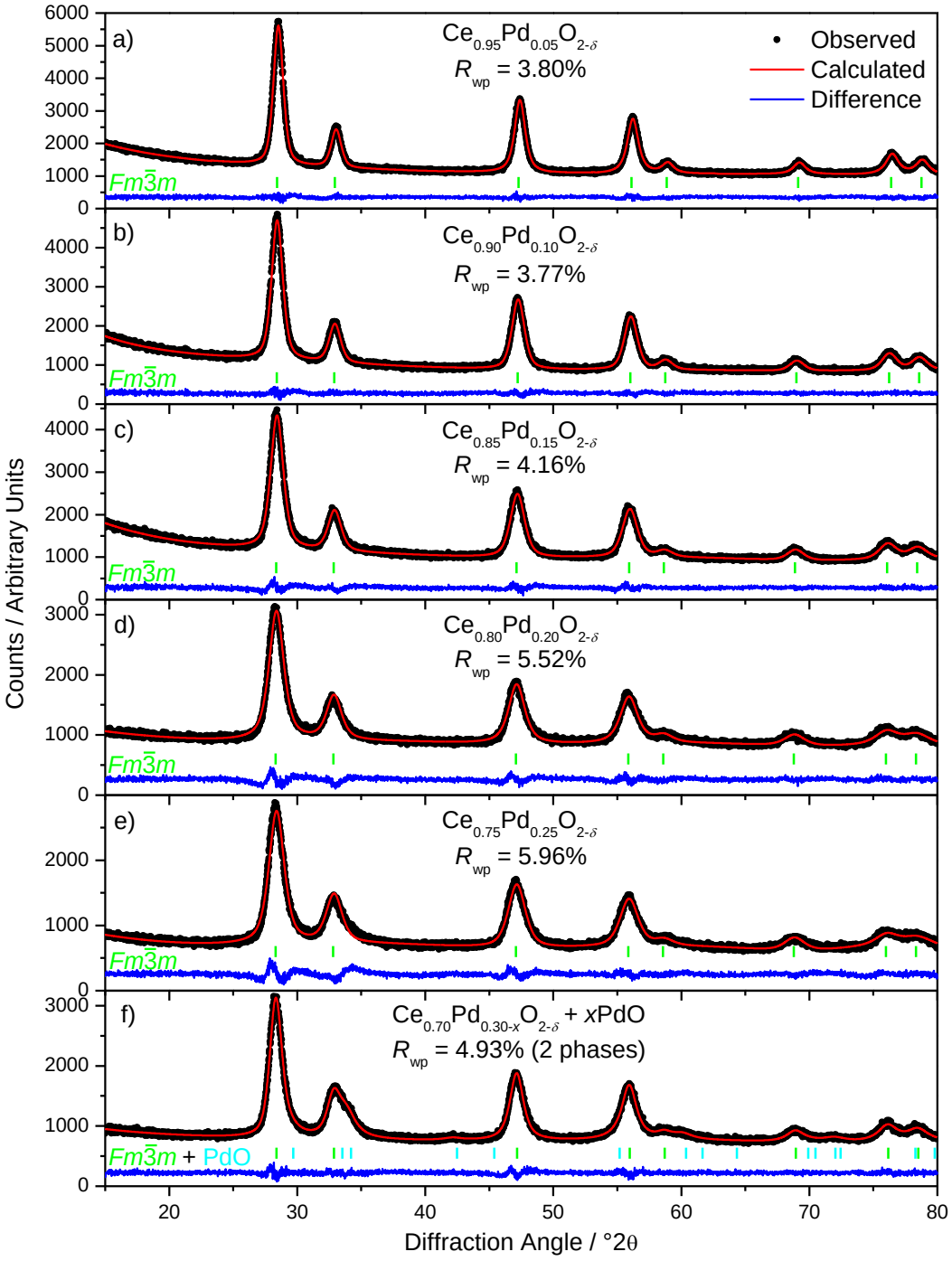

*Figure 4. 1 Le Bail fits to powder XRD data (λ = 1.54056 Å) of $Ce_{1-x}Pd_xO_{2-\delta}$ ($0.05 \leq x \leq 0.25$, a – e; respectively) made hydrothermally, using a fluorite phase. f) a two phase (fluorite and PdO) Le Bail fit to powder XRD data of $Ce_{0.70}Pd_{0.30-x}O_{2-\delta}$ and x*PdO.

*Table 4. 1 Results of Le Bail fitting to powder XRD data of $Ce_{1-x}Pd_xO_{2-\delta}$ ($0.03 \leq x \leq 0.30$) using monochromatic Cu $K\alpha_1$ radiation. *When the intended value of* x *was 0.30, some PdO was formed.*

x	*a* / Å	Scherrer Average Crystallite Size / nm	R_{wp}, %
0.05	5.4276(2)	30.0(4)	3.80
0.10	5.4402(3)	17.2(1)	3.77
0.15	5.4483(4)	13.7(1)	4.16
0.20	5.4543(6)	11.9(1)	5.52
0.25	5.4539(6)	10.6(1)	5.96
0.30*	5.4443(4)	-	4.93*

Up to $x = 0.15$, there is a linear lattice parameter increase consistent with previous reports of solution method synthesised $Ce_{1-x}Pd_xO_{2-\delta}$ (Figure 4. 2).[17] The expansion of the unit cell is not necessarily expected; Pd^{2+} is likely to be square planar in the CeO_2 lattice[14] and the ionic radius of square planar Pd^{2+} is 0.64 Å – two thirds of the ionic radius of the eight-coordinate Ce^{4+} (0.97 Å).[18] One explanation for this is that the Pd^{2+} is unlikely to occupy an eight-coordinate site and is instead sitting on an interstitial position, expanding the unit cell. Scanlon *et al.*[14] proposed and simulated the energy of a model in which Pd^{2+} is shifted by one quarter of the unit cell in one direction (1.2 – 1.3 Å), so as to adopt square planar geometry (Figure 4. 3a). Substituted into a fluorite with the literature CeO_2 lattice parameter (5.41165 Å) this would create a Pd – O bond length of 1.9133 Å (Figure 4. 3b), significantly smaller than the Pd – O bond length in other palladates such as PdO (2.0106 Å),[16] $La_2Pd_2O_5$ (2.0511 – 2.0734 Å)[19] or La_4PdO_7 (2.0131 – 2.0602 Å).[19] Pd^{2+} in this square planar environment would thus force the oxygen lattice in the fluorite structure further apart to give a physically realistic Pd – O distance. A Pd – O bond length of 1.983(14) Å (derived from Pd K-edge EXAFS of $Ce_{0.9}Pd_{0.1}O_{2-\delta}$, see Section 4.2.4) causes an expansion of ~0.1 Å in the PdO_4 plane (Figure 4. 3c). This would explain the increased unit cell parameter. To balance the charge, oxide vacancies must occur,

and are likely to be localised on the under-coordinated oxygen site created by the square-planar Pd.

The lattice parameter when $x = 0$ is slightly larger than the NIST value for CeO_2. This could be caused by a range of factors. There is the possibility of some Na inclusion into the lattice (see Chapter 3). Also, in the nanocrystalline regime, CeO_2 has been demonstrated to exhibit lattice expansion, caused by increased surface energy and surface Ce reduction.[20-22] Misch *et al.*[23] report an increased lattice parameter of as made $Ce_{1-x}Pd_xO_{2-\delta}$ ($0 \leq x \leq 0.10$) compared to the same samples after calcination (Figure 4. 2), possibly caused by a small amount of Ce^{3+} in the as made samples, which are oxidised by calcination.

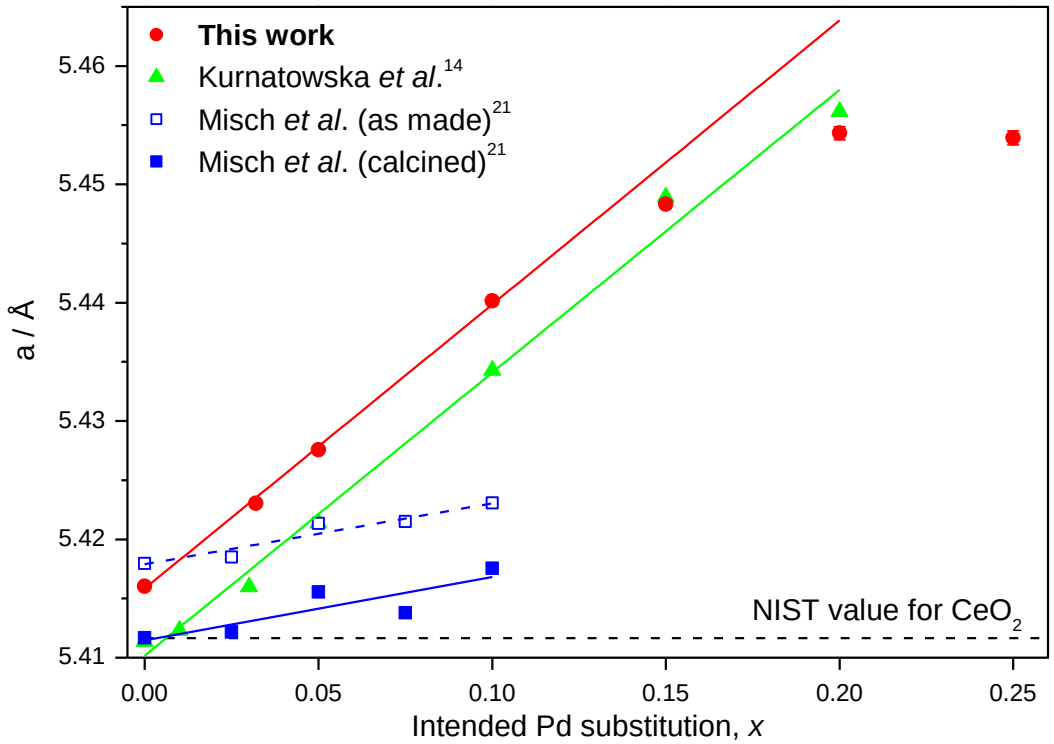

Figure 4. 2 Refined lattice parameter, a, *as a function of* x *in* $Ce_{1-x}Pd_xO_{2-\delta}$. *Linear fit to* $0 \leq x \leq 0.10$ *has been extrapolated up to* $x = 0.20$. *Lattice parameters for* $Ce_{1-x}Pd_xO_{2-\delta}$ *reported by Kurnatowska* et al.[14] *and Misch* et al.[21] *included for comparison.*

Having more than one Pd atom per unit cell (of the four metal atoms) would create unphysically short Pd – Pd distances, suggesting a maximum value of *x* of 0.25 from this model. There is no sign of extra Bragg peaks in the powder XRD, suggesting no ordering of the Pd atoms.

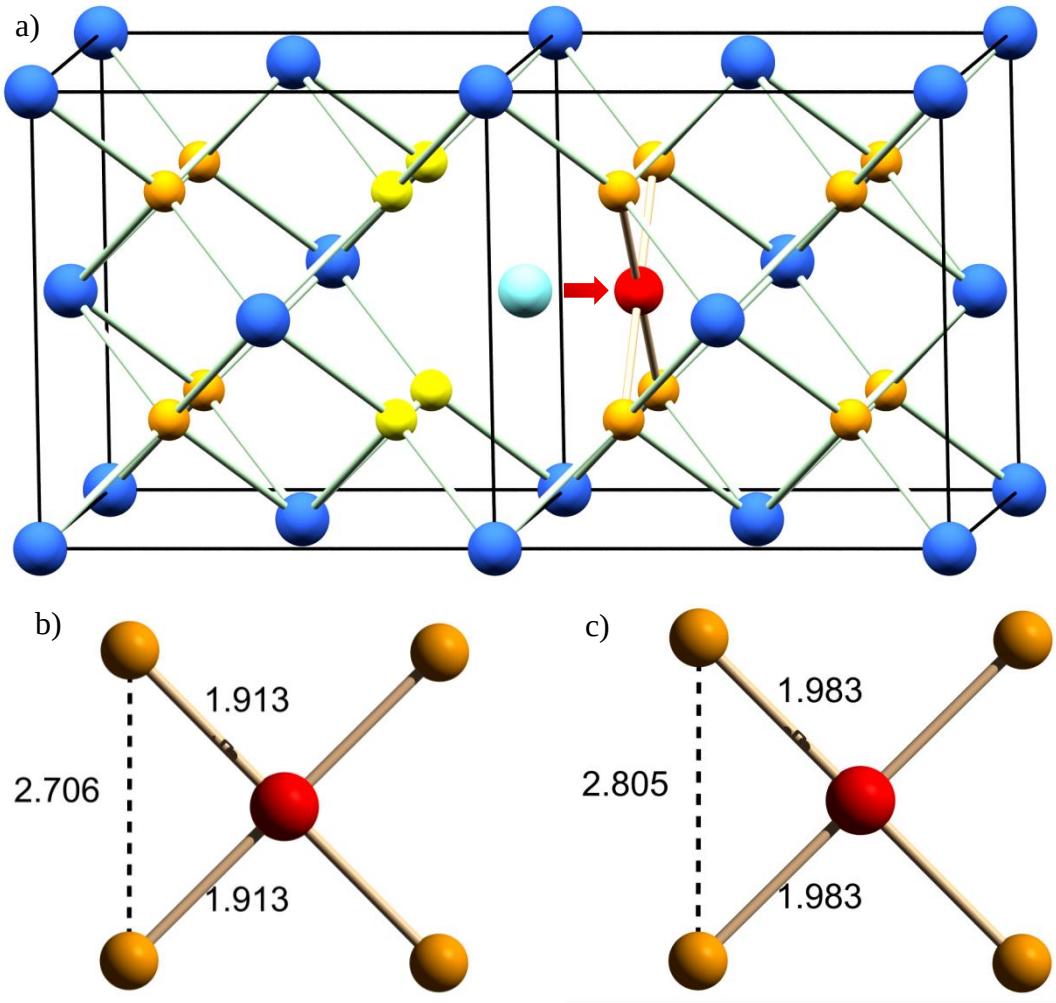

Figure 4. 3a) CeO_2 lattice with one Ce^{4+} ion substituted for a Pd^{2+} ion. Pd^{2+} is shown in red, Ce^{4+} in dark blue and O^{2-} in orange. The vacant Ce (4a) site is shown in light blue and the resulting under-coordinated O^{2-} are shown in yellow. This under-coordinated site is 75% occupied to achieve charge-balance. Adapted from Scanlon et al.[14] *b) O – O distance and resulting Pd – O bond length in a PdO_4 plane in undistorted CeO_2. This bond length is too short. b) Pd – O bond length and resulting O – O distance in a distorted PdO_4 plane to accommodate a Pd^{2+} ion. Distances are in Å.*

4.2.3 Further Characterisation

The presence of some surface water can be inferred by the presence of a broad O – H stretch visible by IR spectroscopy of $Ce_{1-x}Pd_xO_{2-\delta}$ (Figure 4. 4a). CeO_2 has several peaks below 2000 cm^{-1}, all of which are also visible in $Ce_{1-x}Pd_xO_{2-\delta}$ (x = 0.05, 0.10, 0.20), indicating no secondary phases are present.

TGA of $Ce_{0.90}Pd_{0.10}O_{2-\delta}$ and $Ce_{0.80}Pd_{0.20}O_{2-\delta}$ up to 1000 °C (Figure 4. 4b) shows that they both lose significantly more mass than CeO_2. All three begin to lose mass rapidly as soon as heated up to 130 °C, as adsorbed water is removed from the surface of the oxides. After this the rate of mass loss decreases more slowly. By 750 °C the mass of CeO_2 stops decreasing at 96.9% of its original mass, whilst $Ce_{0.90}Pd_{0.10}O_{2-\delta}$ and $Ce_{0.80}Pd_{0.20}O_{2-\delta}$ both continue to lose mass above 900 °C. At 1000 °C $Ce_{0.90}Pd_{0.10}O_{2-\delta}$ and $Ce_{0.80}Pd_{0.20}O_{2-\delta}$ are 94.4% and 93.5% of their original mass; respectively. This difference can be explained by the reduction of Pd^{2+} to Pd metal which would account for 1.0% and 2.0% mass loss in $Ce_{0.90}Pd_{0.10}O_{2-\delta}$ and $Ce_{0.80}Pd_{0.20}O_{2-\delta}$; respectively (see in situ powder XRD, Chapter 5).

ICP-OES elemental analysis shows the actual ratio of Ce:Pd in the products is very close to the intended ratio (Table 4. 2). There is an insignificant amount of Na present compared to when it is co-doped with a pentavalent ion in CeO_2 (Chapter 3), which can be assumed to be surface species not removed by washing with boiling

Table 4. 2 ICP-OES measured metal content by mass of $Ce_{1-x}Pd_xO_{2-\delta}$ with calculated formula assuming remaining mass is oxide.

Intended *x*	Ce / %	Pd / %	Na / %	Calculated Formula
0.05	72.5(3)	2.85(30)	0.18(30)	$Ce_{0.94(3)}Pd_{0.049(6)}Na_{0.01(2)}O_{2.8(1)}$
0.20	65.4(3)	12.6(3)	0.09(30)	$Ce_{0.79(3)}Pd_{0.200(8)}Na_{0.01(2)}O_{2.3(1)}$

water. No Na-substitution is expected, since doping of an ion with an oxidation state of less than +4 is not necessary to balance the charge, as is the case in the pentavalent ion-substituted ceria presented in Chapter 3.

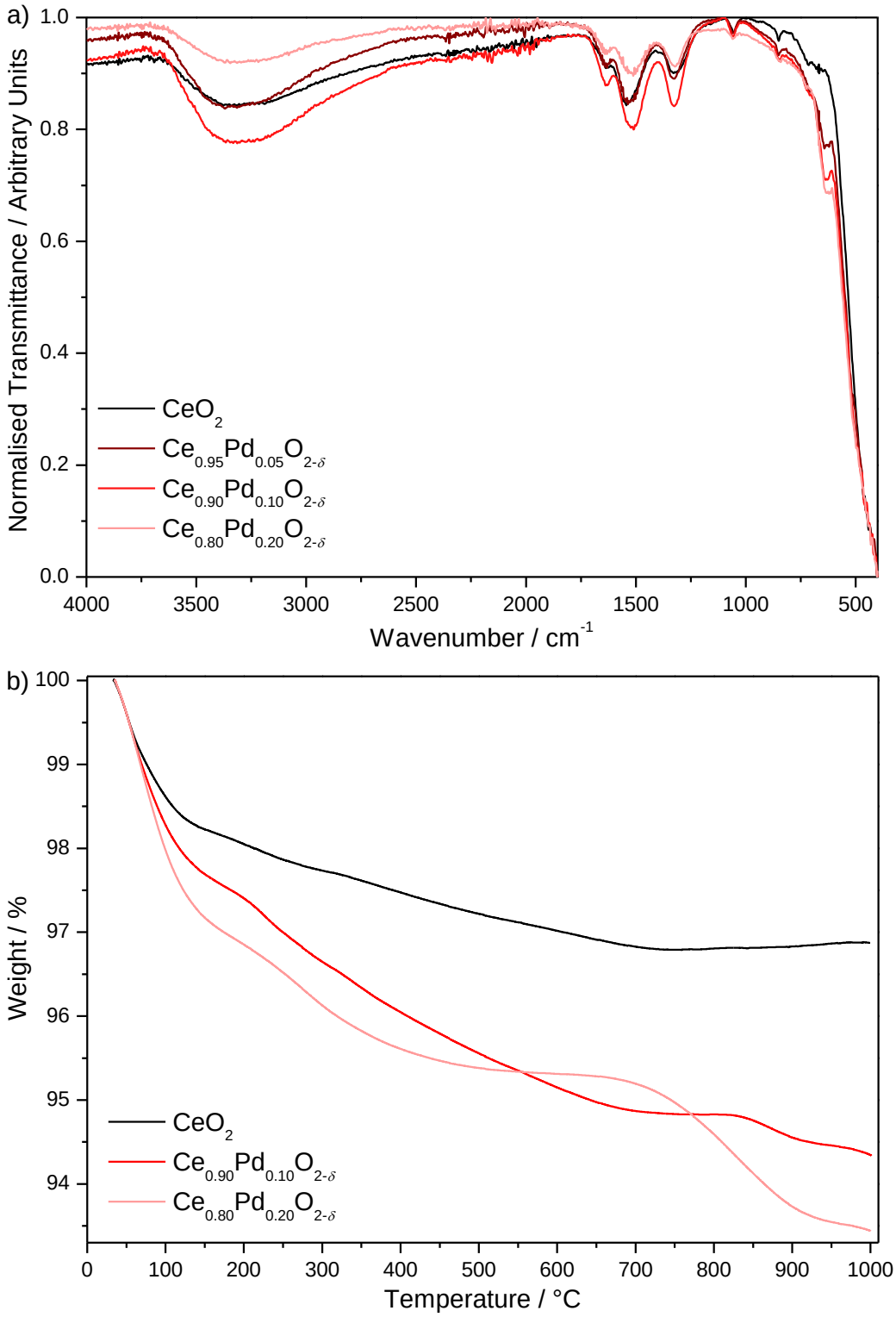

Figure 4. 4a) FTIR spectra and b) TGA of $Ce_{1-x}Pd_xO_{2-\delta}$ ($0 \leq x \leq 0.20$) prepared hydrothermally.

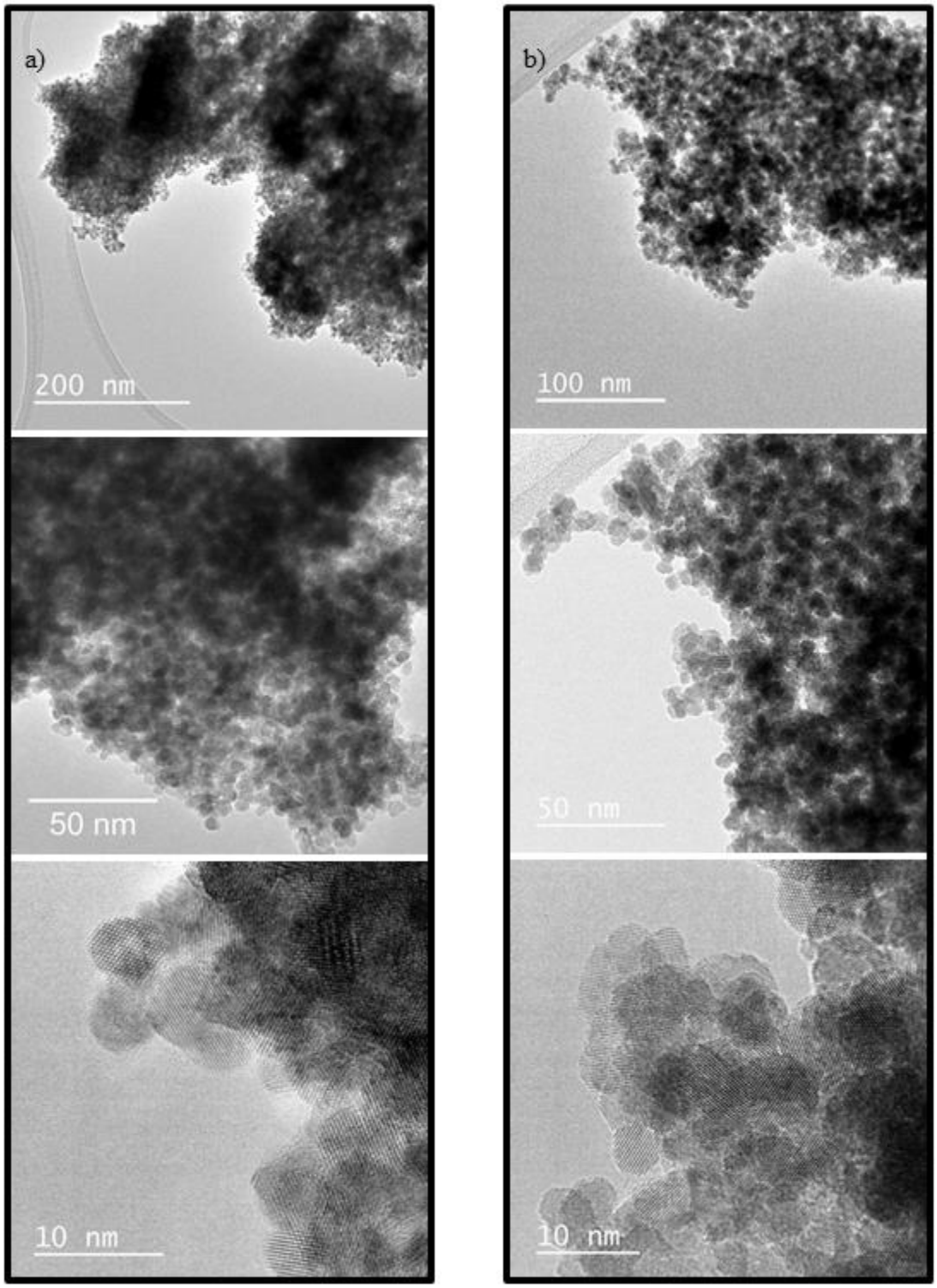

Figure 4. 5 High resolution transmission electron micrographs of a) $Ce_{0.90}Pd_{0.10}O_{2-\delta}$ b) $Ce_{0.80}Pd_{0.20}O_{2-\delta}$ each at three different magnifications.

TEM images of $Ce_{0.90}Pd_{0.10}O_{2-\delta}$ (Figure 4. 5a) and $Ce_{0.80}Pd_{0.20}O_{2-\delta}$ (Figure 4. 5b) show that they are both composed of aggregated highly uniform nanocrystals. In $Ce_{0.90}Pd_{0.10}O_{2-\delta}$ the crystallite diameters are 5 – 8 nm, whilst the crystallites of

$Ce_{0.80}Pd_{0.20}O_{2-\delta}$ tend to be 3 – 6 nm. EDX (Table 4. 3) at multiple areas of the sample shows that the measured Pd:Ce ratio is consistent with the intended value and is homogeneously distributed, ruling out the possibilities of Pd rich (or deficient) zones, or the presence of amorphous PdO. Energy filtered TEM of $Ce_{0.80}Pd_{0.20}O_{2-\delta}$ (Figure 4. 6) shows that the Ce and Pd are evenly distributed throughout the sample.

Table 4. 3 Measured values of x *from EDX elemental analysis (from high resolution TEM) of four different areas of* $Ce_{0.90}Pd_{0.10}O_{2-\delta}$ *and* $Ce_{0.80}Pd_{0.20}O_{2-\delta}$.

Intended *x*	Area 1 *x*	Area 2 *x*	Area 3 *x*	Area 4 *x*	Average *x*	Standard Deviation
0.10	0.116	0.121	0.107	0.097	0.110	0.011
0.20	0.190	0.166	0.183	0.185	0.181	0.011

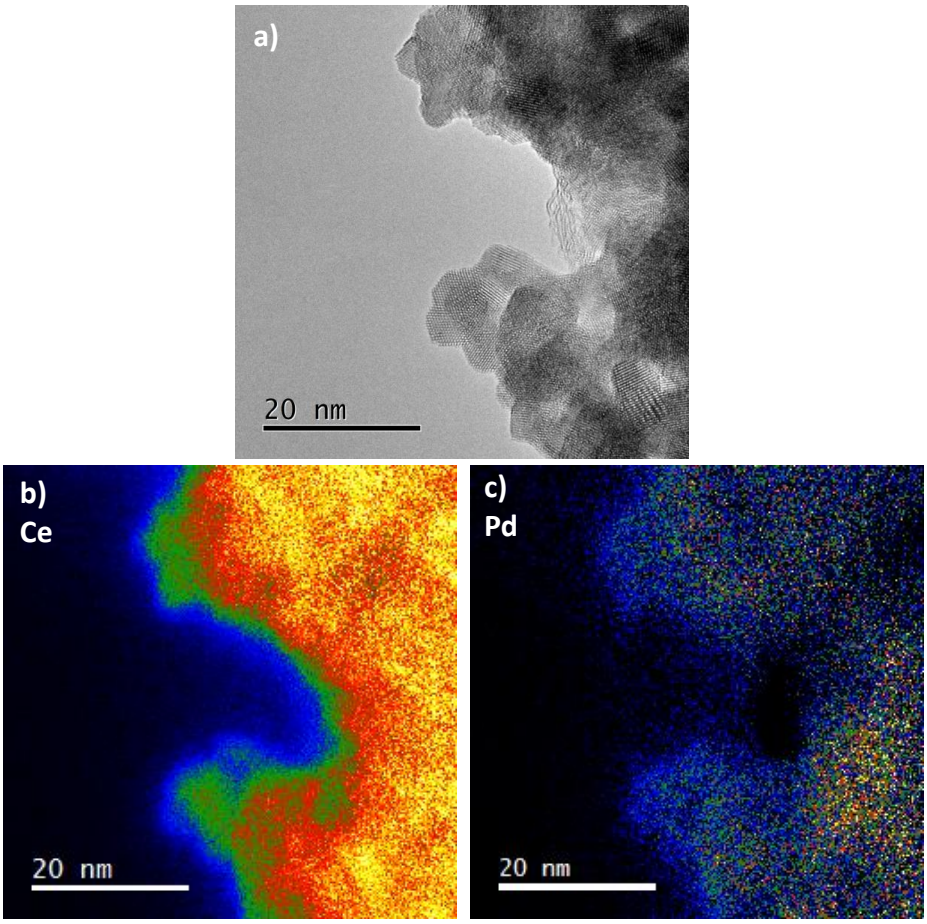

Figure 4. 6a) Transmission electron micrograph of $Ce_{0.80}Pd_{0.20}O_{2-\delta}$*: a) as made b, c) elemental maps of the same area showing concentration of Ce and Pd, respectively.*

4.2.4 X-ray Absorption Spectroscopy

X-ray absorption spectra at the Ce L_{III}- and Pd K-edges were collected on beamline B18,[24] at Diamond Light Source (U.K.) in transmission mode. Samples were first diluted with polyethylene powder to give an appropriate amount of target metal[25] and pressed into pellets approximately 1 mm thick. XANES spectra were collected at room temperature, whilst Pd K-edge EXAFS data were collected on samples cooled to 77 K in a liquid N_2 cryostat. Spectra were normalised using ATHENA,[26] and Pd K-edge EXAFS were fitted using ARTEMIS.[26] Edge positions were defined as the energy at which absorption = 0.5.

4.2.4.1 Ce L_{III}-Edge XANES

Ce L_{III}-edge XANES of $Ce_{1-x}Pd_xO_{2-\delta}$ are shown in Figure 4. 7. The position of the absorption edge is exactly the same (within the detection limits) as that of a Ce^{4+}

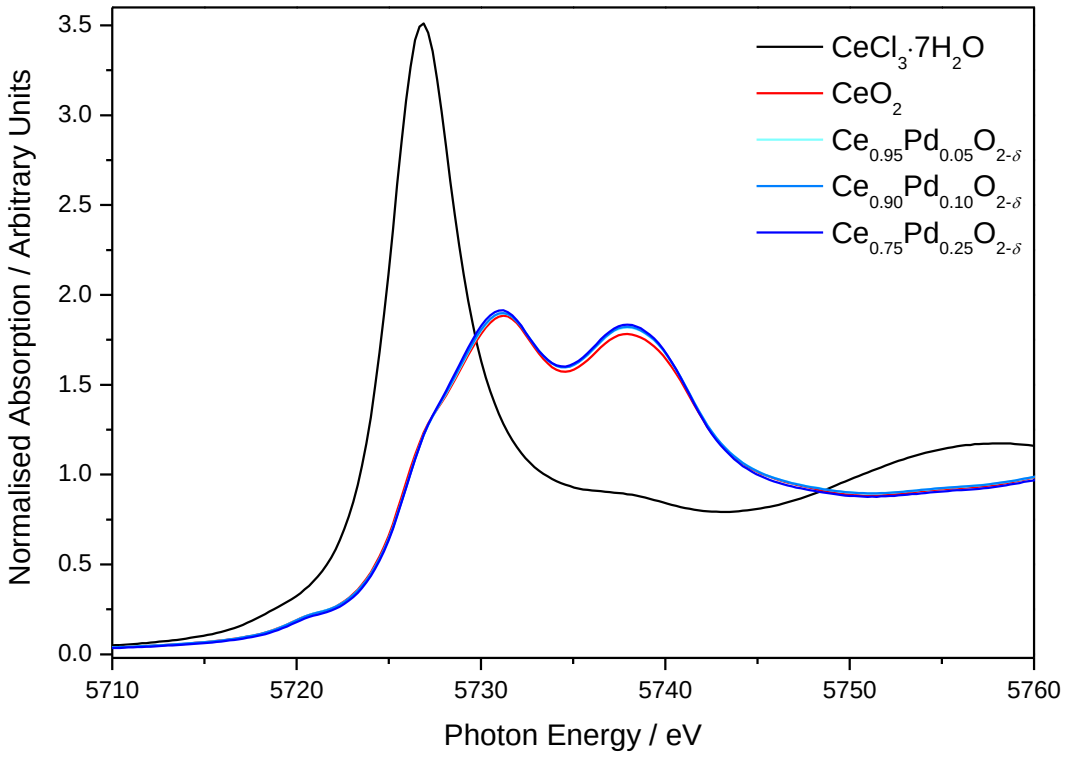

Figure 4. 7 Ce L_{III}-edge XANES spectra of $Ce_{1-x}Pd_xO_{2-\delta}$ (x = 0.05, 0.10, 0.25) compared to Ce^{3+} ($CeCl_3 \cdot 7H_2O$, Sigma-Aldrich) and Ce^{4+} (CeO_2, Sigma-Aldrich) references.

reference (CeO_2, Sigma-Aldrich), with no indication of any Ce reduction. This is expected since no Ce reduction is required to balance the charge. The near edge region of all of the doped materials consists of a double peak, characteristic of the Ce^{4+} ion,[27,28] and attributed to two different transitions from the core 2*p* level; to either the 5*d* or 4*f* levels.[27] There is very little difference in the spectra with increasing Pd content. However this is expected since the majority of the Ce atoms will be in a largely unchanged environment: at x = 0.25 only one quarter of the nearest metal neighbours will be Pd, and furthermore Pd^{2+} has only 10 fewer electrons than Ce^{4+}; and XANES is not very sensitive to next nearest neighbours.

4.2.4.2 Pd K-Edge XANES

Pd K-edge XANES (Figure 4. 8) shows that the Pd K-edge in $Ce_{1-x}Pd_xO_{2-\delta}$ is higher in energy than in PdO. This is not necessarily due to an increased average Pd oxidation state, since the Pd K-edge is known to be particularly sensitive to local environment as well as oxidation state.[29] A Pd oxidation state of greater than +2 is highly unlikely; Pd(III) and Pd(IV) oxides are exceedingly rare, typically require preparations utilising extreme oxygen pressures and the Pd readily reduces back to the +2 oxidation state.[30,31]

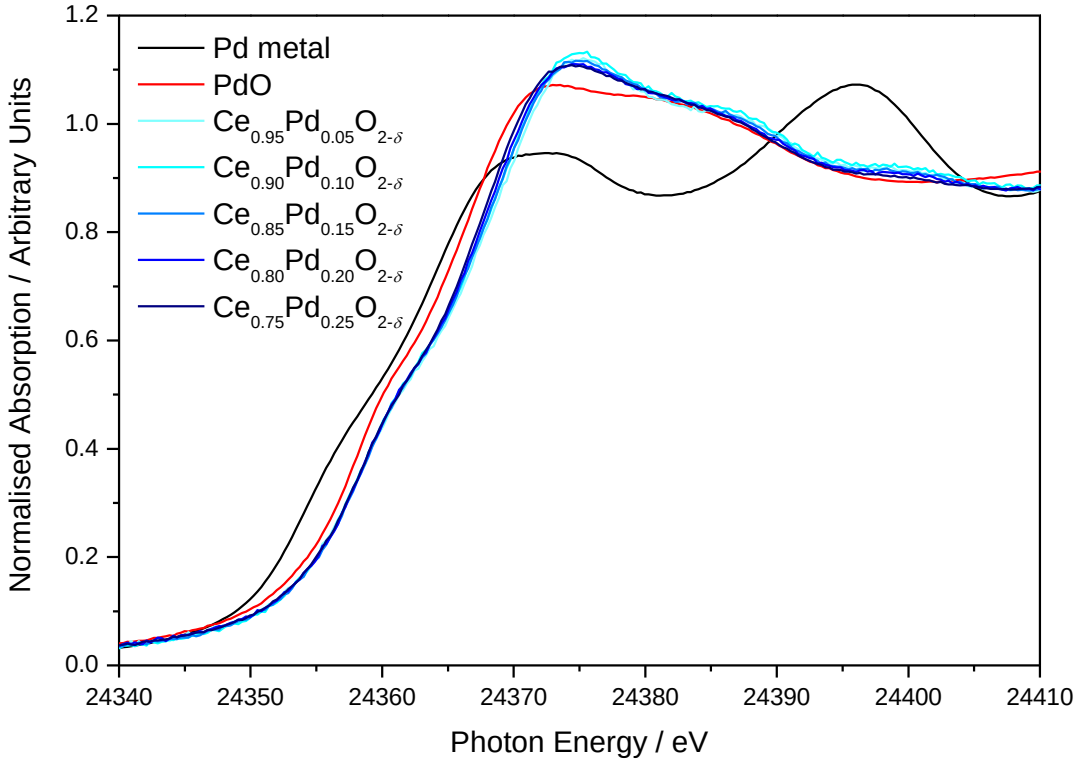

Figure 4. 8 Pd K-edge XANES spectra of $Ce_{1-x}Pd_xO_{2-\delta}$ (x = 0.05, 0.10, 0.15, 0.20, 0.25) compared to Pd metal foil (B18 reference) and Pd^{2+} (PdO, Sigma-Aldrich) references.

4.2.4.3 Pd K-edge EXAFS

Pd K-edge EXAFS spectra and Fourier transforms of PdO, $Ce_{0.95}Pd_{0.05}O_{2-\delta}$, $Ce_{0.90}Pd_{0.10}O_{2-\delta}$ and $Ce_{0.80}Pd_{0.20}O_{2-\delta}$ (Figure 4. 9) show that the Pd environment in the doped fluorites is significantly different to that of PdO. There is a visible evolution of the spectra with increasing Pd substitution, with the $Ce_{0.80}Pd_{0.20}O_{2-\delta}$ spectrum looking most like that of PdO, suggesting that the Pd environment becomes more PdO-like as *x* increases.

The EXAFS spectrum of PdO over the range 3 – 12.5 $Å^{-1}$ can be fitted to the crystal structure[32] (Table 4. 4, Figure 4. 10). However, fitting this same model to the spectra of $Ce_{1-x}Pd_xO_{2-\delta}$ yields poor fits with incorrect distances and small or negative σ^2 values (Table 4. 5), eliminating the possibility of Pd existing solely as amorphous PdO.

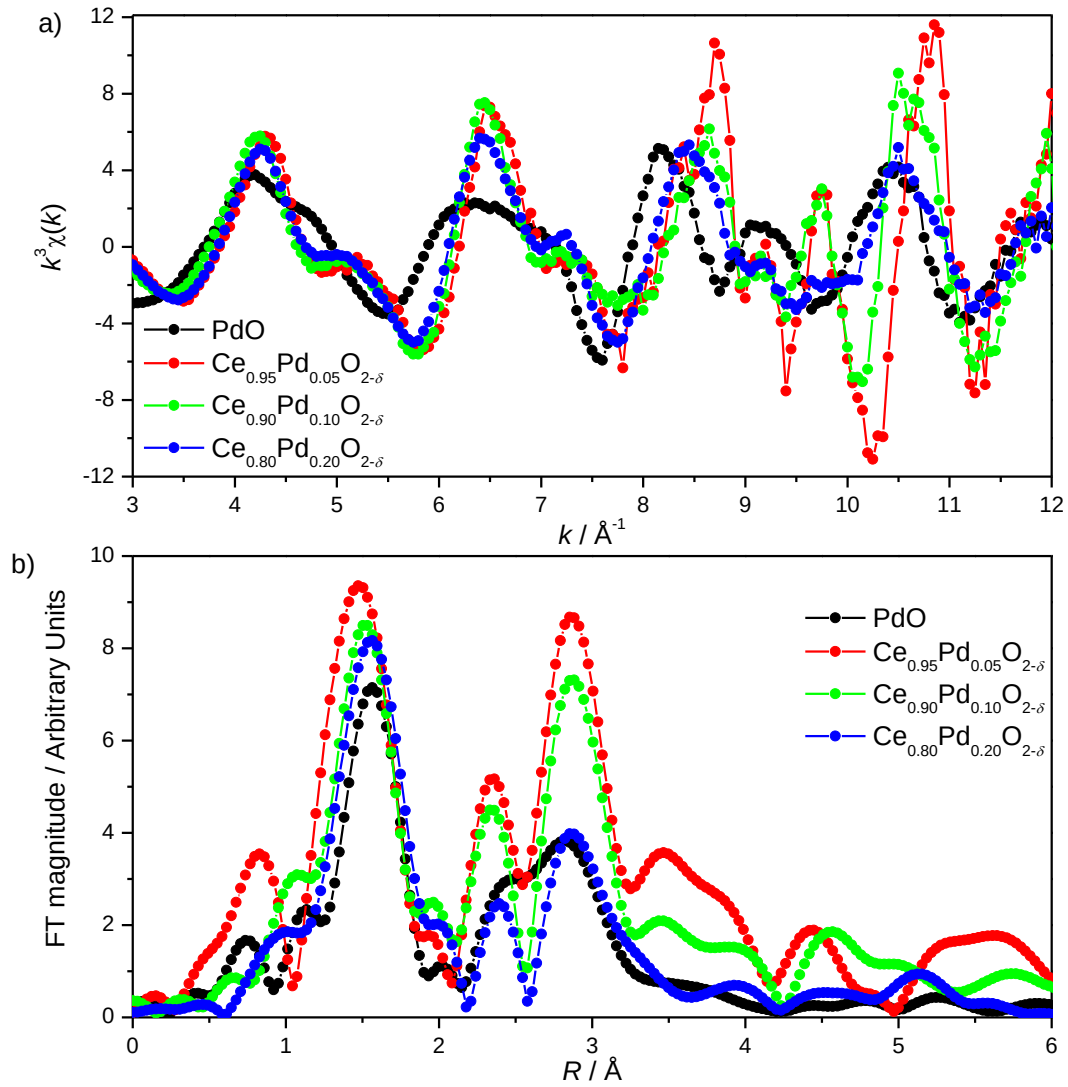

Figure 4. 9a) Overlaid Pd K-edge k^3*-weighted EXAFS spectra and b) overlaid Fourier transforms (not phase-shift corrected) of PdO and* $Ce_{1-x}Pd_xO_{2-\delta}$ (x = *0.05, 0.10, 0.20).*

Table 4. 4 Pd K-edge EXAFS fitting results for PdO. S_0^2 *= 0.826,* E_0 *= 1.052 eV,* R*-factor = 0.0312.*

Shell	Coordination Number	R_{cryst} / Å	R / Å	σ^2 / Å^2
O	4	2.018	2.035(10)	0.002(1)
Pd	4	3.030	3.055(12)	0.008(1)
Pd	8	3.420	3.482(48)	0.016(5)
O	8	3.640	3.888(80)	0.010(12)
O	4	4.275	4.319(82)	0.004(8)
Pd	4	4.285	4.285(257)	0.023(40)

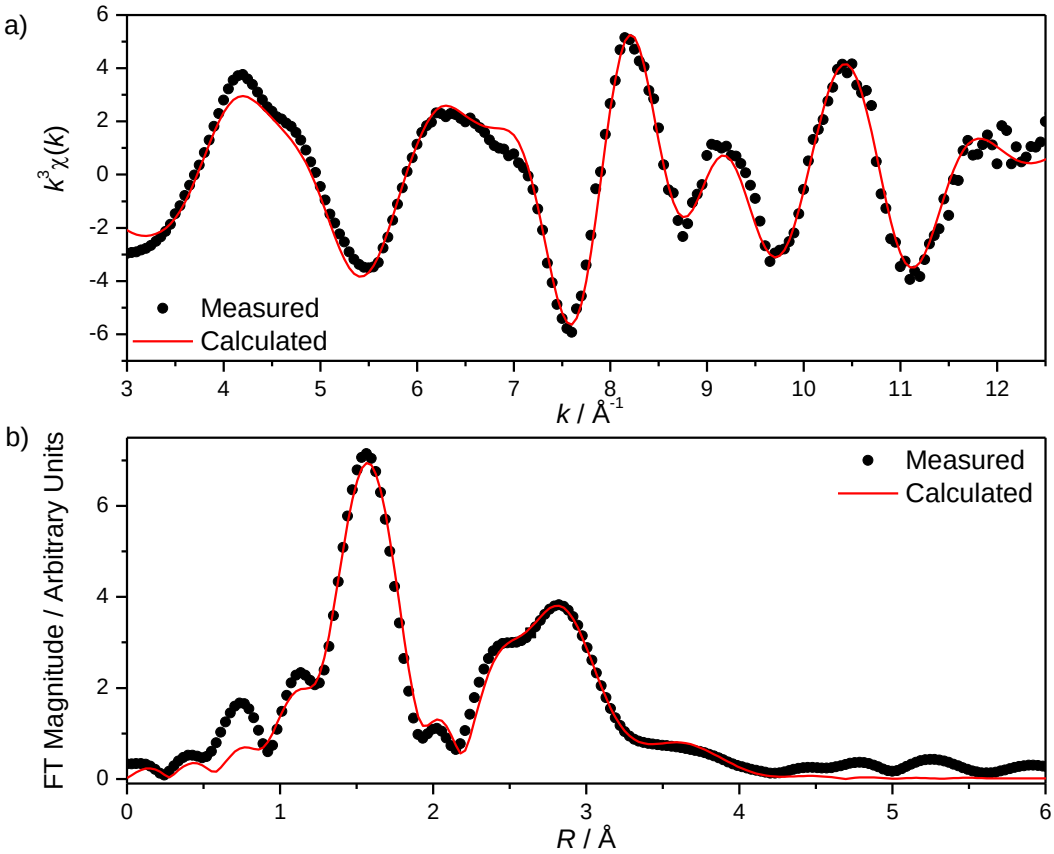

Figure 4. 10a) k^3*-weighted Pd EXAFS spectrum and b) the Fourier transform of PdO. Measured data are shown by points with best fit shown by line.*

Table 4. 5 Pd K-edge EXAFS fitting results for $Ce_{0.90}Pd_{0.10}O_{2-\delta}$ *(*S_0^2 *= 0.739,* E_0 *= -7.953 eV,* R*-factor = 0.0529) and* $Ce_{0.80}Pd_{0.20}O_{2-\delta}$ *(*S_0^2 *= 0.858,* E_0 *= -0.779 eV,* R*-factor = 0.0811) using crystalline PdO model. Figures in bold are large deviations from expected values or unphysical values.*

Shell	Coordination Number	R_{cryst} / Å	$Ce_{0.90}Pd_{0.10}O_{2-\delta}$		$Ce_{0.80}Pd_{0.20}O_{2-\delta}$	
			R / Å	σ^2 / Å^2	R / Å	σ^2 / Å^2
O	4	2.018	1.981(14)	0.0010(18)	2.005(12)	0.002(1)
Pd	4	3.030	**3.389(62)**	0.0032(76)	**2.900(128)**	0.026(21)
Pd	8	3.420	**3.779(449)**	0.0339(80)	**3.332(26)**	0.012(2)
O	8	3.640	3.393(41)	**-0.0057(38)**	**4.110(70)**	**0.001(6)**
O	4	4.275	**4.590(73)**	**-0.0050(53)**	**3.929(42)**	**-0.003(3)**
Pd	4	4.285	4.251(62)	0.0036(54)	**4.185(61)**	0.007(6)

A model where Pd is substituted into ceria, but rather than perfectly occupying the Ce site it is shifted to sit at the centre of a plane of O atoms in a square-planar environment (Figure 4. 3); was instead considered. An initial model with no expansion of the unit cell was used (although powder XRD suggests this is not the case). Fitting of this model to the spectra of $Ce_{0.95}Pd_{0.05}O_{2-\delta}$ and $Ce_{0.90}Pd_{0.10}O_{2-\delta}$ gives increased correlation distances (Table 4. 6), in accordance with the powder XRD. This also gives a Pd – O bond lengths that are physically reasonable.

In both cases three shells of atoms were sufficient to obtain a good fit to the data. Adding subsequent shells gave no improvement on the fit and caused the closer shells to have physically unreasonable values, suggesting a degree of disorder on this length scale. The fit to $Ce_{0.95}Pd_{0.05}O_{2-\delta}$ has a comparatively large *R*-factor, though this is caused by the reduced signal-to-noise ratio, particularly evident at high *k* (Figure 4. 11).

Table 4. 6 Pd K-edge EXAFS fitting results for $Ce_{0.95}Pd_{0.05}O_{2-\delta}$ (S_0^2 = 0.909, E_0 = -7.56 eV, R-*factor = 0.179) and $Ce_{0.90}Pd_{0.10}O_{2-\delta}$ (S_0^2 = 0.829, E_0 = -7.836 eV,* R-*factor = 0.0876) using model in Figure 4. 3*

Shell	Coordination Number	$R_{expected}$ / Å	$Ce_{0.95}Pd_{0.05}O_{2-\delta}$		$Ce_{0.90}Pd_{0.10}O_{2-\delta}$	
			R / Å	σ^2 / Å^2	*R* / Å	σ^2 / Å^2
O	4	1.91	1.963(26)	0.0022(37)	1.983(14)	0.0017(19)
Ce	4	3.03	3.158(30	0.0034(27)	3.191(38)	0.0044(21)
O	7	3.31	3.305(114)	0.0045(16)	3.352(58)	0.0011(80)

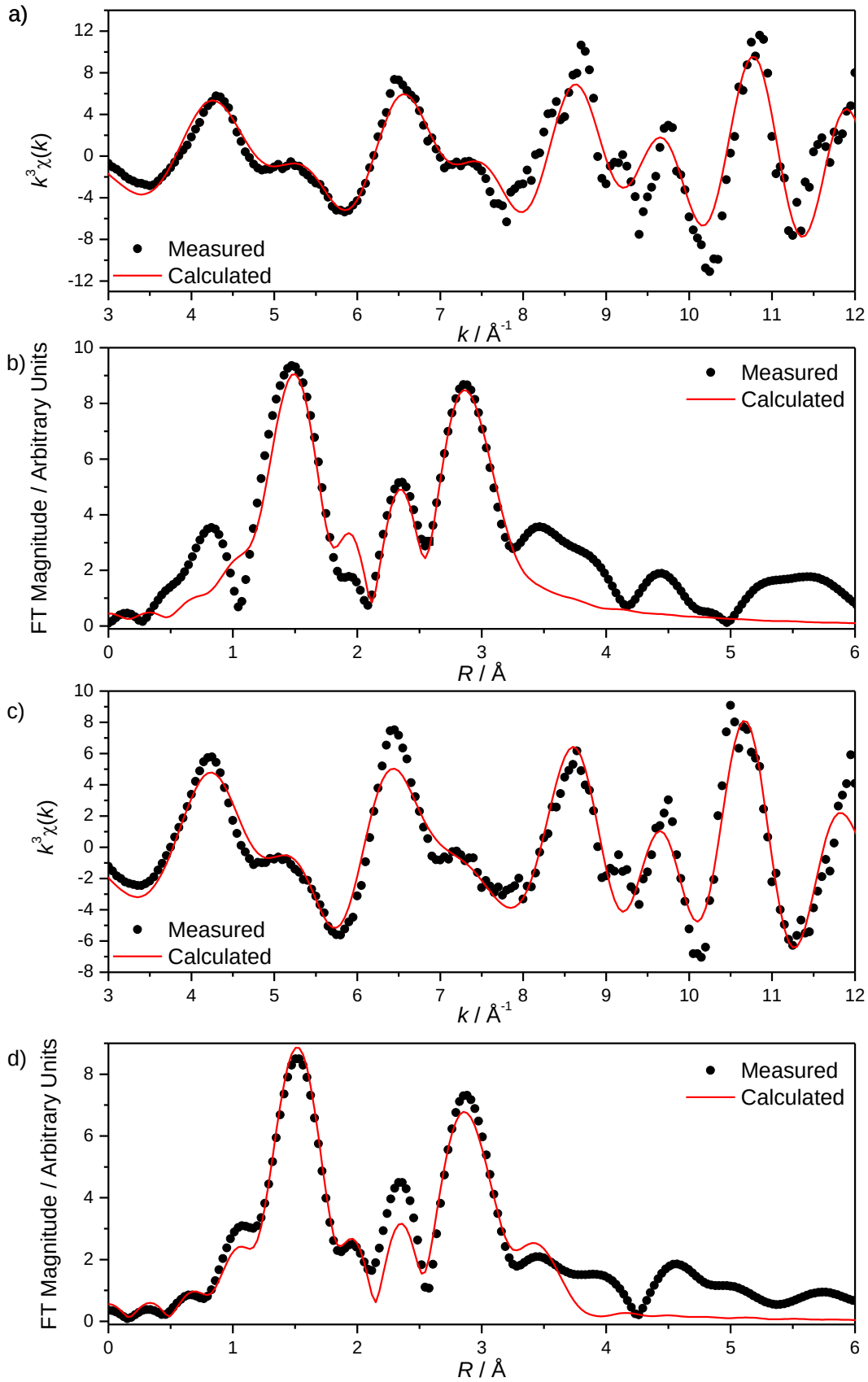

Figure 4. 11a) k^3*-weighted Pd EXAFS spectrum and b) the Fourier transform of* $Ce_{0.95}Pd_{0.05}O_{2-\delta}$*. c)* k^3*-weighted Pd EXAFS spectrum and d) the Fourier transform of* $Ce_{0.90}Pd_{0.10}O_{2-\delta}$ *Measured data are shown by points with best fit shown by line.*

The EXAFS signal of $Ce_{0.80}Pd_{0.20}O_{2-\delta}$ cannot be satisfactorily fit by this model however. Powder XRD shows that at high Pd content ($x > 0.25$) an impurity of PdO forms (Figure 4. 1f). Also, at values of x between 0.15 and 0.25 the lattice parameter increase is no longer linear as a function of x (Figure 4. 2), so it is conceivable that a small amount of PdO – undetectable by powder XRD – begins to form as a second phase at $x = 0.20$. The two phase EXAFS model is difficult to fit since Pd – Pd in PdO and Pd – Ce in the doped model are both close to 3 Å. Therefore, some parameters had to be fixed in order to obtain a satisfactory fit – S_0^2 was fixed at 0.826, the value found for PdO (and very close to the value for the doped model) and the Debye-Waller factor for the Ce shell was fixed at 0.0044 (found for the doped model) and the value for the second O shell at 0.001. The proportion of Pd present as PdO was estimated by fitting the lattice parameter of the fluorite to the extrapolated linear fit (fitted over the region $0 \leq x \leq 0.10$) to give a "true" value of x of 0.17. This means that approximately 15% of the Pd is present as PdO and 85% is found in $Ce_{0.83}Pd_{0.17}O_{2-\delta}$. Fitting this model to the EXAFS spectrum of "$Ce_{0.80}Pd_{0.20}O_{2-\delta}$" gives a satisfactory fit (Figure 4. 12, Table 4. 7).

Table 4. 7 Pd K-edge EXAFS fitting results for $Ce_{0.80}Pd_{0.20}O_{2-\delta}$ ($S_0^2 = 0.826$, $E_0 = -0.617$ eV, R-factor = 0.0295) comprising two phases: 0.03PdO and $Ce_{0.83}Pd_{0.17}O_{2-\delta}$ based on model in Figure 4. 3

Phase	Shell	Coordination Number	$R_{expected}$ / Å	R / Å	σ^2 / Å^2
PdO and fluorite	O	4	1.91	2.018(9)	0.0019(6)
PdO	Pd	0.6	3.03	3.130(78)	0.0003(22)
Fluorite	Ce	3.4	3.03	3.192(44)	0.0044
Fluorite	O	5.95	3.31	3.554(45)	0.0010
PdO	Pd	1.2	3.42	3.503(47)	0.0042(66)

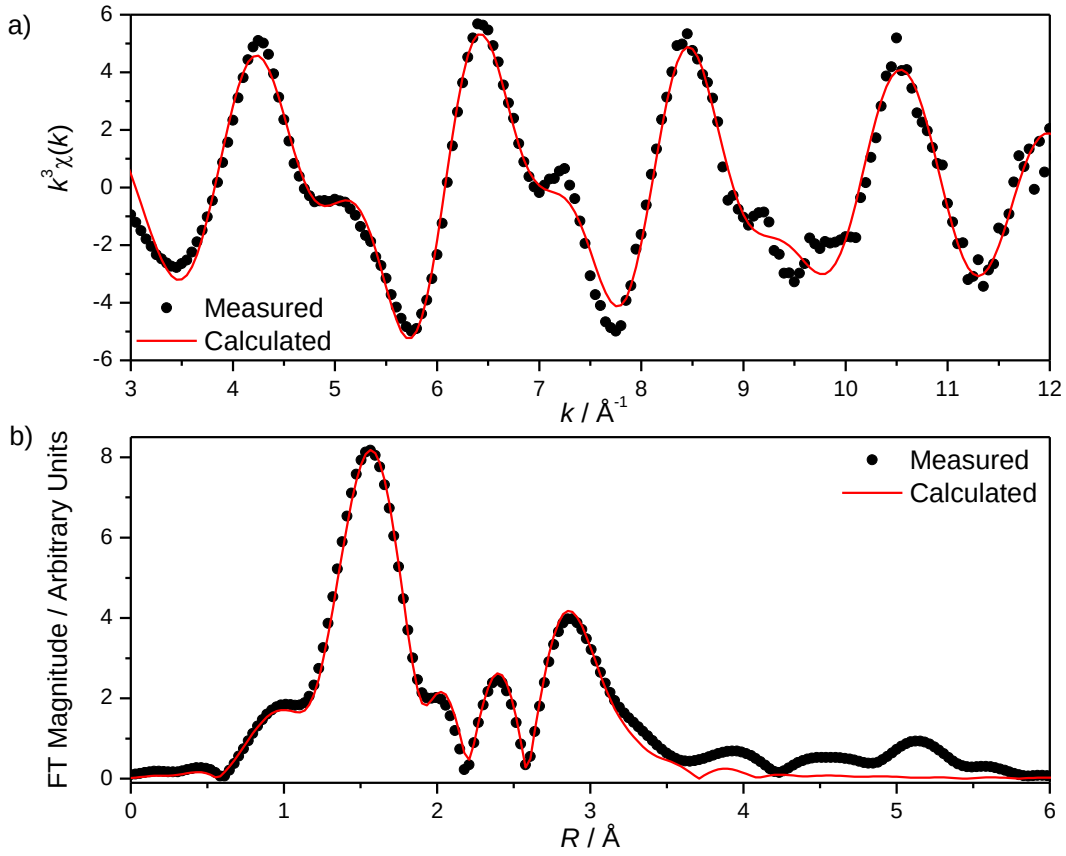

Figure 4. 12a) k^3*-weighted Pd EXAFS spectrum and b) the Fourier transform of "*$Ce_{0.80}Pd_{0.20}O_{2-\delta}$*" with a two-phase (fluorite and PdO) fit. Measured data are shown by points with best fit shown by line.*

4.3 Platinum-Doped Ceria

4.3.1 Synthesis

$Ce_{1-x}Pt_xO_{2-\delta}$ (nominally $0.05 \leq x \leq 0.30$ in increments of $x = 0.05$) was prepared by a hydrothermal reaction at 240 °C. $CeCl_3 \cdot 7H_2O$ and $H_2Pt(OH)_6$ were mixed in a $(1 - x):x$ molar ratio; respectively; to give a total of 6 mmol of metal ions. To this 2 ml of cold H_2O was added, yielding a solution, to which 2 ml of H_2O_2 (37% aqueous solution) was added. This mixture was stirred for 15 minutes before 8 ml of 7.5 mol dm^{-3} NaOH was added dropwise with effervescence. The red-brown gel was stirred for a further 10-15 minutes before being sealed in a Teflon-lined autoclave and heated to 240 °C for 24 hours. The autoclave was cooled to room temperature before filtration and washing with copious amounts of boiling water. The resulting golden yellow solids were dried in an oven at 80 °C overnight and ground in a pestle and mortar to give a fine powder.

4.3.2 Powder XRD

Powder XRD patterns of $Ce_{1-x}Pt_xO_{2-\delta}$ ($0.05 \leq x \leq 0.30$) can all be indexed to a fluorite unit cell, space group $Fm\bar{3}m$ (Figure 4. 13) with no other crystalline phases detected. The lattice parameter of the fluorite decreases linearly as a function of x

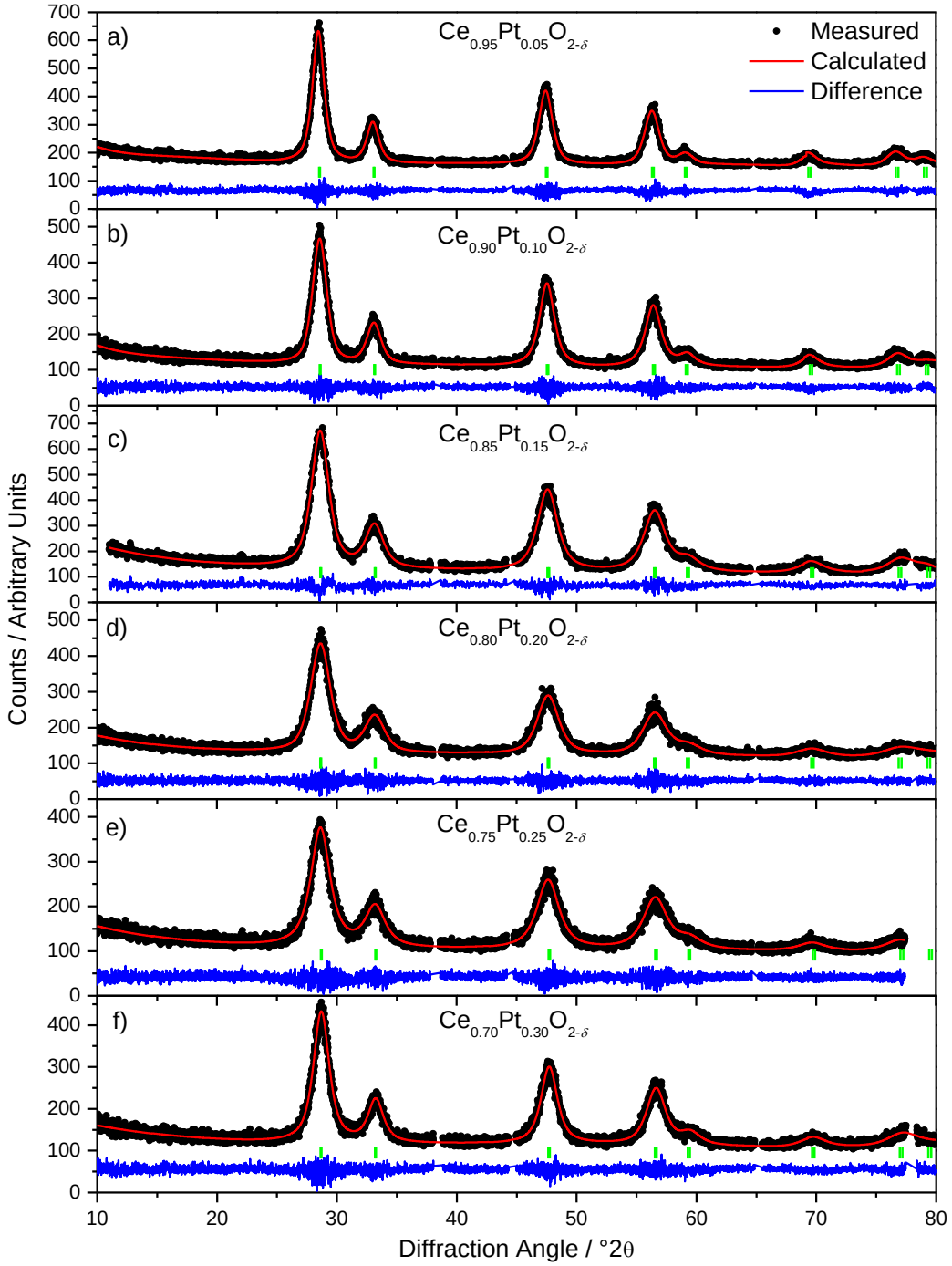

Figure 4. 13 Le Bail fits to powder XRD (Cu $K\alpha_{1,2}$ data of $Ce_{1-x}Pt_xO_{2-\delta}$ ($0.05 \leq x \leq 0.30$) made hydrothermally.

(Figure 4. 14). The lattice contraction can be explained by Pt(IV) sitting in an octahedral environment with the metal sitting slightly off the Ce site, since six-coordinate Pt^{4+} has an ionic radius of 0.63 Å, which is significantly smaller than eight-coordinate Ce^{4+} (0.97 Å).[18] Since the dopant is isovalent, there is no need for oxide vacancies to balance the charge.

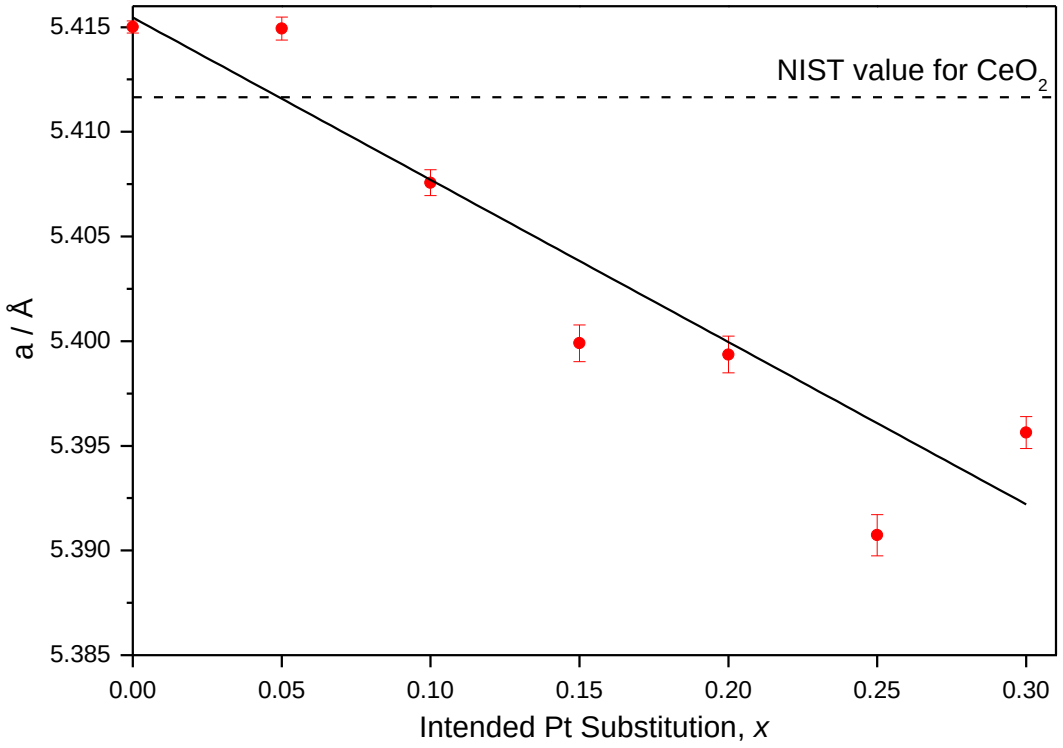

Figure 4. 14 Refined lattice parameter, a, *as a function of* x *in* $Ce_{1-x}Pt_xO_{2-\delta}$ *with linear fit. Lattice parameter for* CeO_2 *reported by NIST included for comparison.*

4.3.3 Further Characterisation

IR spectra of hydrothermally prepared $Ce_{1-x}Pt_xO_{2-\delta}$ (x = 0.10, 0.20, Figure 4. 15a) contain all the same features as CeO_2 prepared in the same way though the O – H stretch at ~3300 cm^{-1} and several other peaks between 700 – 2000 cm^{-1} become comparatively weaker as Pt content increases.

TGA in air of the same materials (Figure 4. 15b) shows a mass loss almost immediately up to 400 °C, which increases as a function of x, suggesting either that substitution with Pt also increases the amount of surface H_2O; that Pt^{4+} begins to reduce to Pt metal; or a combination of these effects. At 800 °C and 750 °C (in $Ce_{0.90}Pt_{0.10}O_{2-\delta}$ and $Ce_{0.80}Pt_{0.20}O_{2-\delta}$, respectively) there are large, sharp mass losses of 0.8% and 1.3%, respectively. These can be related to loss of approximately 9 mol% and 15 mol% of the oxygen in the fluorite which can be attributed to reduction of Pt species, though it is unclear whether this is Pt^{4+} being reduced to Pt^{2+}; or Pt^{2+} being reduced to Pt metal – if Pt^{4+} reduction has already occurred at lower temperatures.

ICP-OES elemental analysis of $Ce_{0.95}Pt_{0.05}O_{2-\delta}$ and $Ce_{0.80}Pt_{0.20}O_{2-\delta}$ (Table 4. 8) shows that the measured amount of Pt is lower than was used in the synthesis, suggesting that some of the Pt remains in solution and is washed away. Like $Ce_{1-x}Pd_xO_{2-\delta}$, $Ce_{1-x}Pt_xO_{2-\delta}$ oxides contain very little Na, which can be ascribed to a surface layer and considerably more oxide than expected from the nominal formula, which can be explained by surface water.

Table 4. 8 ICP-OES measured metal content by mass of $Ce_{1-x}Pt_xO_{2-\delta}$ with calculated formula assuming remaining mass is oxide.

Intended *x*	Ce / %	Pt / %	Na / %	Calculated Formula
0.05	69.4(3)	4.97(30)	0.17(3)	$Ce_{0.94(3)}Pt_{0.047(4)}Na_{0.01(2)}O_{3.0(1)}$
0.20	58.1(3)	14.7(3)	0.15(3)	$Ce_{0.83(3)}Pt_{0.151(7)}Na_{0.01(2)}O_{3.4(2)}$

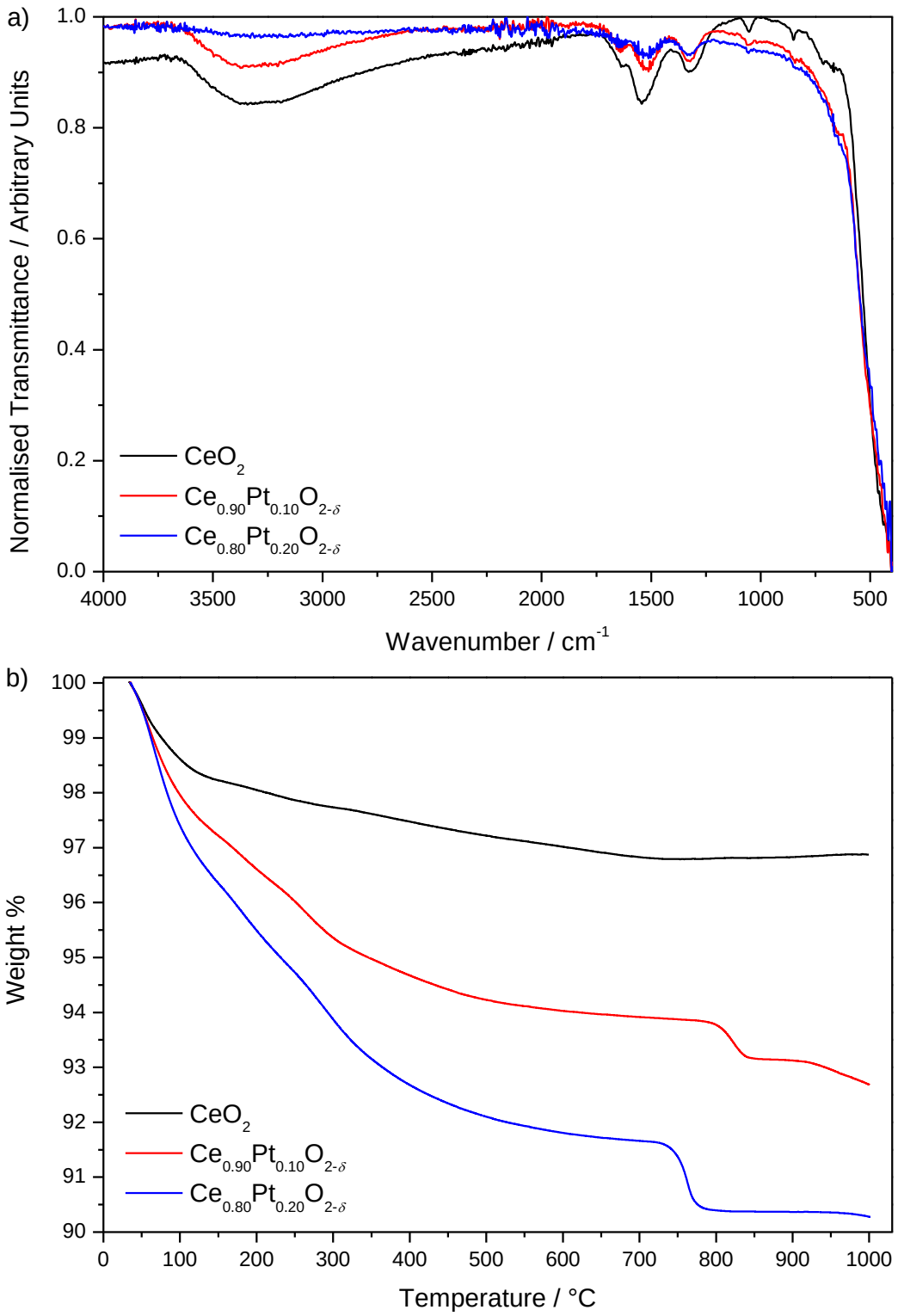

Figure 4. 15a) FTIR spectra and b) TGA up to 1000 °C of $Ce_{1-x}Pt_xO_{2-\delta}$ ($0 \leq x \leq 0.20$) prepared hydrothermally.

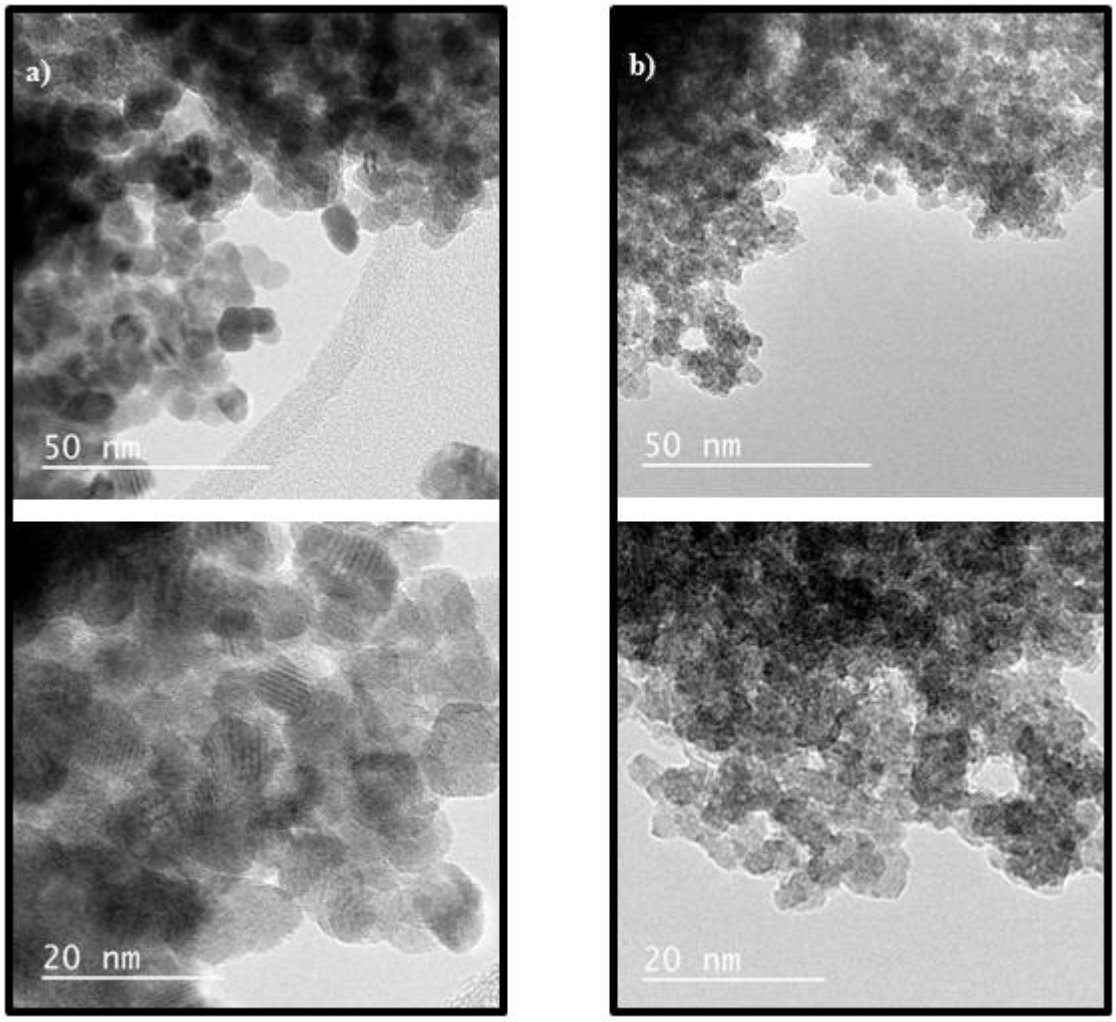

Figure 4. 16 High resolution transmission electron micrographs of a) $Ce_{0.90}Pt_{0.10}O_{2-\delta}$ b) $Ce_{0.80}Pt_{0.20}O_{2-\delta}$.

TEM images of $Ce_{0.90}Pt_{0.10}O_{2-\delta}$ and $Ce_{0.80}Pt_{0.20}O_{2-\delta}$ (Figure 4. 16a and b, respectively) show they are both composed of uniform nanocrystallites. Crystallites of $Ce_{0.90}Pt_{0.10}O_{2-\delta}$ are sized between 5 – 8 nm, whilst $Ce_{0.80}Pt_{0.20}O_{2-\delta}$ crystals are

Table 4. 9 Measured values of x *from EDX elemental analysis (from high resolution TEM) of four different areas of $Ce_{0.90}Pt_{0.10}O_{2-\delta}$ and $Ce_{0.80}Pt_{0.20}O_{2-\delta}$.*

Intended *x*	Area 1 *x*	Area 2 *x*	Area 3 *x*	Area 4 *x*	Average *x*	Standard Deviation
0.10	0.091	0.092	0.088	0.095	0.091	0.003
0.20	0.170	0.172	0.174	-	0.172	0.002

considerably smaller, ranging from 2 to 5 nm. EDX (Table 4. 9) at multiple areas of the sample shows that the measured Pt:Ce ratio is consistent with the intended value and is homogeneously distributed, ruling out the possibilities of Pt rich (or deficient) zones or ceria mixed with a secondary Pt containing phase.

4.3.4 X-ray Absorption Spectroscopy

X-ray absorption spectra at the Ce and Pt L_{III}-edges were collected on beamline B18,[24] at Diamond Light Source (U.K.) in transmission mode. Samples were first diluted with polyethylene powder to give an appropriate amount of target metal[25] and pressed into pellets approximately 1 mm thick. XANES spectra were collected at room temperature. Spectra were normalised using ATHENA.[26] Edge positions were defined as the energy at which absorption = 0.5.

4.3.4.1 Ce L_{III}-Edge XANES

Figure 4. 17 shows the XANES spectra of the Ce L_{III}-edge of $Ce_{1-x}Pt_xO_{2-\delta}$ (x = 0.10, 0.15, 0.20) together with reference compounds; $CeCl_3 \cdot 7H_2O$ (Ce^{3+}) and CeO_2 (Ce^{4+}). The spectra of all the doped oxides have a Ce L_{III}-edge very similar to that of CeO_2, suggesting that the Ce is all in the +4 oxidation state.

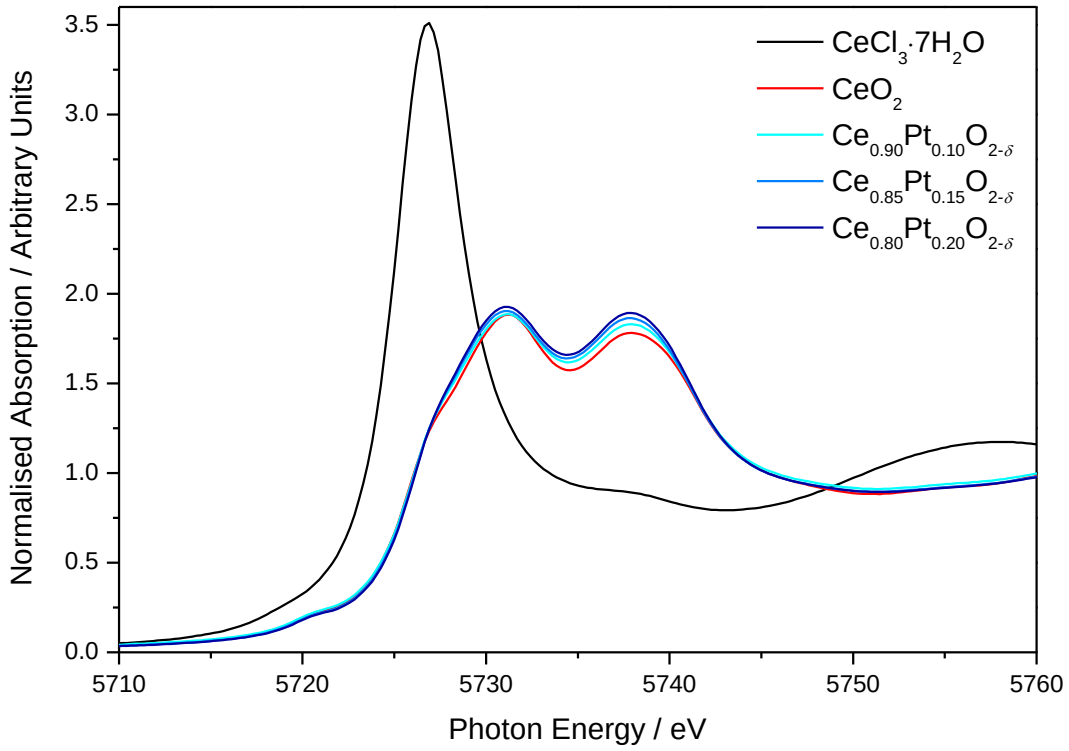

Figure 4. 17 Ce L_{III}-edge XANES spectra of $Ce_{1-x}Pt_xO_{2-\delta}$ (x = 0.10, 0.15, 0.20) compared to Ce^{3+} ($CeCl_3 \cdot 7H_2O$, Sigma-Aldrich) and Ce^{4+} (CeO_2, Sigma-Aldrich) references.

4.3.4.2 Pt L_{III}-Edge XANES

XANES spectra of the Pt L_{III}-edge of $Ce_{1-x}Pt_xO_{2-\delta}$ (x = 0.10, 0.15, 0.20) together with reference compounds; $PtCl_2$ (Pt^{2+}, Sigma-Aldrich) and $H_2[Pt(OH)_6]$ (Pt^{4+}, Johnson Matthey Catalysts) are shown in Figure 4. 18. The position of the Pt L_{III}-edge in the Pt-doped cerium oxides coincides with that of the Pt^{4+} reference, suggesting that the Pt exists as Pt^{4+} in the oxides, meaning that no oxide vacancies are required in order to accommodate Pt into the ceria lattice.

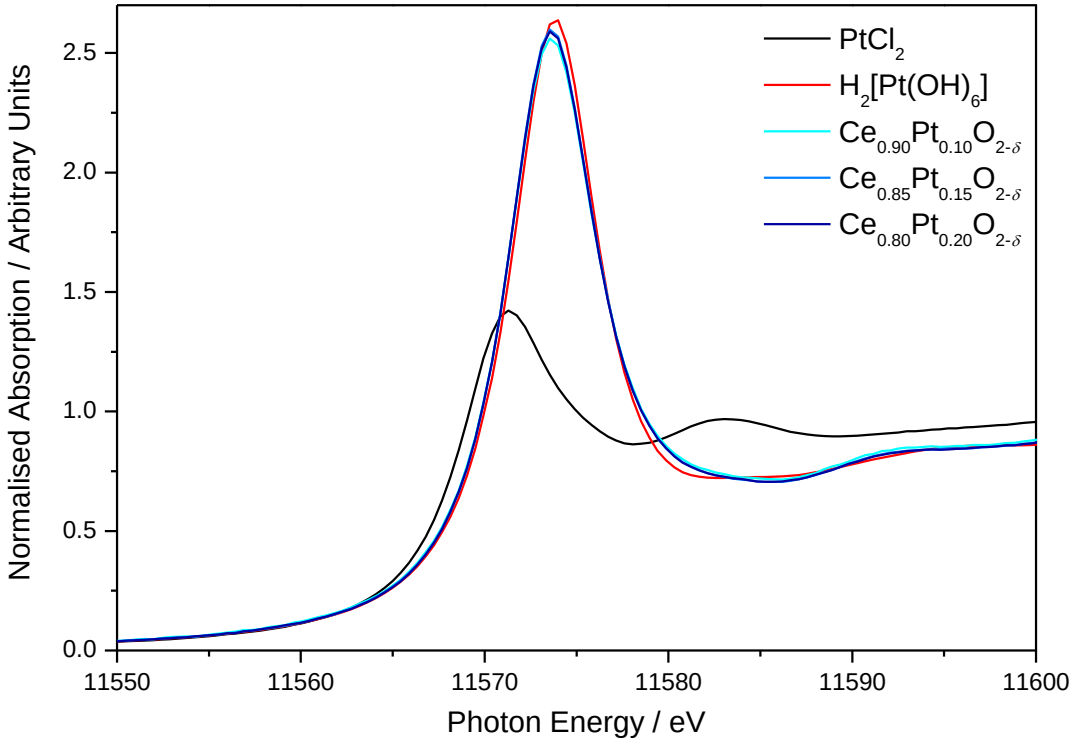

Figure 4. 18 Pt L_{III}-edge XANES spectra of $Ce_{1-x}Pt_xO_{2-\delta}$ (x =0.10, 0.15, 0.20) compared to $PtCl_2$ and $H_2[Pt(OH)_6]$ references.

4.3.4.3 Pt L_{III}-edge EXAFS

Pt L_{III}-edge EXAFS spectra of $Ce_{0.90}Pt_{0.10}O_{2-\delta}$, $Ce_{0.85}Pd_{0.15}O_{2-\delta}$ and $Ce_{0.80}Pt_{0.20}O_{2-\delta}$ (Figure 4. 19) are much more similar to the spectrum of $H_2[Pt(OH)_6]$; the Pt precursor consisting of isolated $[Pt^{4+}O_6]$ octahedra;[33] than to that of PtO_2. This has two potential explanations: that the Pt is substituted into ceria and distorts the

structure so as to sit in an octahedral environment with either highly disordered Ce atoms or no Ce atoms within 5 Å; or the materials consist of a mixture of un-substituted CeO_2 and amorphous $H_2[Pt(OH)_6]$. These possibilities were initially dismissed based on evidence from powder XRD and IR spectroscopy. Although heating $H_2[Pt(OH)_6]$ hydrothermally at 240 °C for 24 hours yields no reaction (the solid product is $H_2[Pt(OH)_6]$); no indication of $H_2[Pt(OH)_6]$ could be seen by XRD in the mixed Ce – Pt oxides (Figure 4. 13) and the refined lattice parameter decreases as a function of *x*. Furthermore, IR spectra of the oxides show that the absorbance of the O – H stretch at ~3400 cm^{-1} (Figure 4. 15a) decreases with increasing Pt content suggesting that the hydroxide content is not increasing.

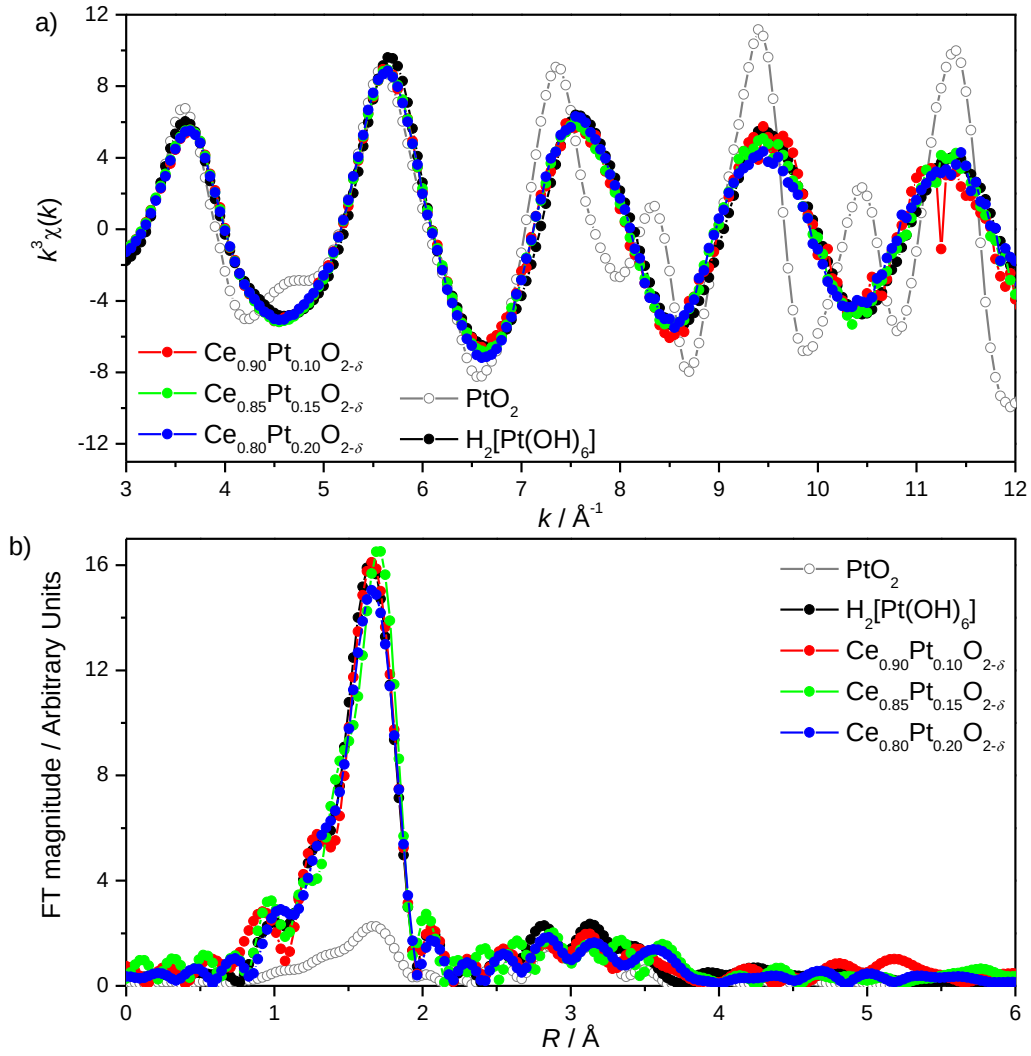

Figure 4. 19a)Overlaid Pt L_{III}-edge k^3-weighted EXAFS spectra and b) overlaid Fourier transforms (not phase-shift corrected) of PtO_2, $H_2[Pt(OH)_6]$ and $Ce_{1-x}Pt_xO_{2-\delta}$ (x = 0.10, 0.15, 0.20).

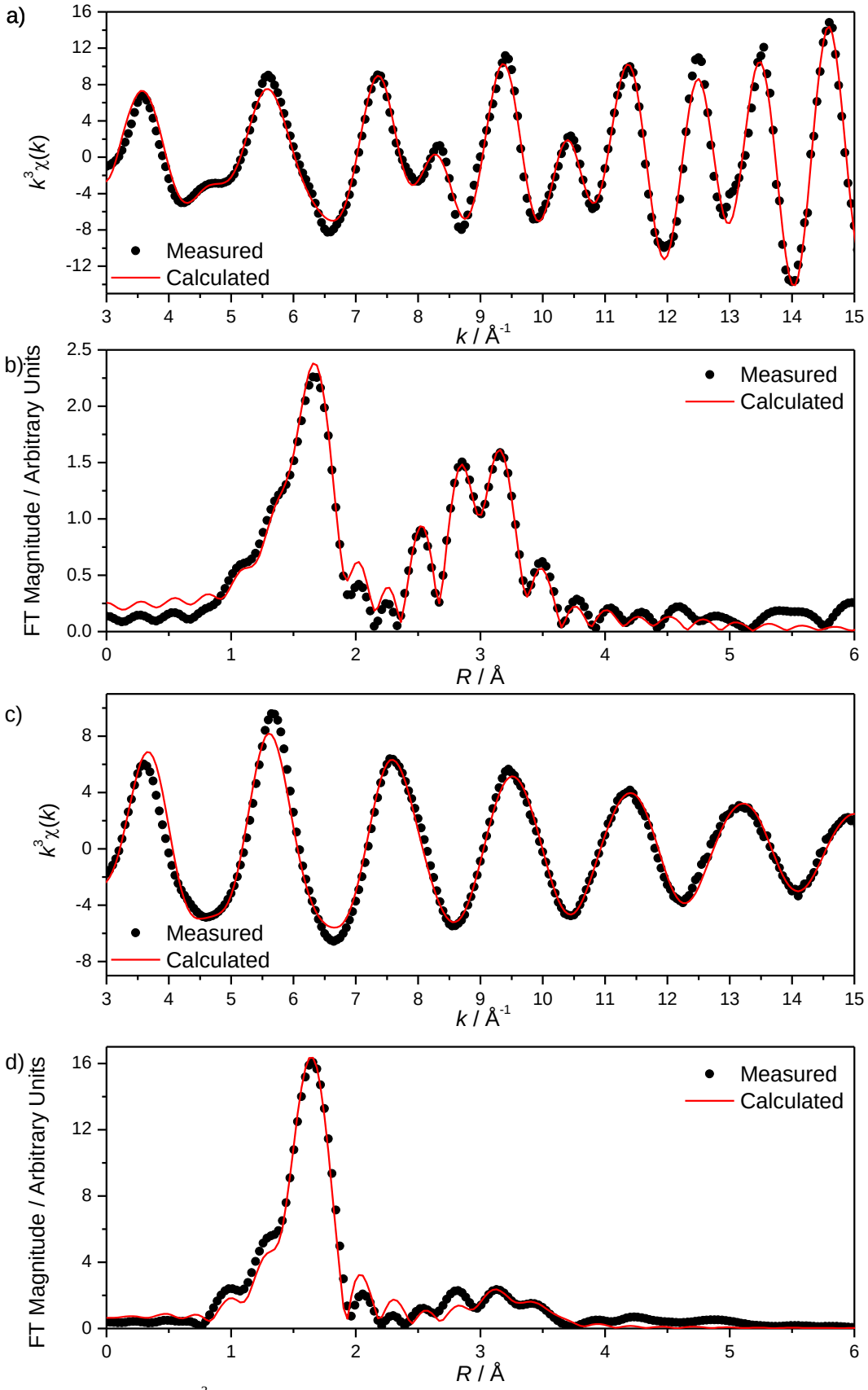

Figure 4. 20a) Fitted k^3*-weighted Pt EXAFS spectrum and b) the Fourier transform of* PtO_2*. c) Fitted* k^3*-weighted Pt EXAFS spectrum and d) the Fourier transform of* $H_2[Pt(OH)_6]$*. Measured data are shown by points with best fit shown by line.*

The crystallographic structures of α-PtO_2[34] and $H_2[Pt(OH)_6]$[33] can be fitted the respective k^3-weighted Pt L_{III}-edge EXAFS spectra of references over the range 3 – 15 $Å^{-1}$ (Table 4. 11, Table 4. 10, Figure 4. 20).

Table 4. 11 Pt L_{III}-edge EXAFS fitting results for PtO_2, S_0^2 = 0.833, E_0 = 10.116 eV, R-*factor = 0.0443.*

Shell	Coordination Number	R_{cryst} / Å	R / Å	σ^2 / $Å^2$
O	2 4	2.0700 2.0702	2.021(8)	0.0025(8)
Pt	6	3.1000	3.104(5)	0.0027(5)
O	2 4	3.5975 3.5976	3.614(97)	0.0039(88)
O	4 2	3.7276 3.7278	3.756(112)	0.0034(83)
Pt	2	4.1610	4.340(85)	0.0077(77)

Table 4. 10 Pt L_{III}-edge EXAFS fitting results for $H_2[Pt(OH)_6]$, S_0^2 = 0.794, E_0 = 7.955 eV, R-*factor = 0.0432.*

Shell	Coordination Number	R_{cryst} / Å	R / Å	σ^2 / $Å^2$
O	2 2 2	2.059 2.073 2.105	1.990(4)	0.0023(4)
O	2 2 2 2	3.795 3.801 3.805 3.823	3.605(33)	0.0081(46)
O	2 2 2 2	4.153 4.173 4.183 4.217	3.770(37)	0.0081(52)

Using the $H_2[Pt(OH)_6]$ crystal structure[33] as a model, Pt EXAFS spectra of $Ce_{1-x}Pt_xO_{2-\delta}$ (x = 0.10, 0.15, 0.20) can be fitted satisfactorily, with no evidence for any Pt – Pt or Pt – Ce correlations (Table 4. 12, Figure 4. 21).

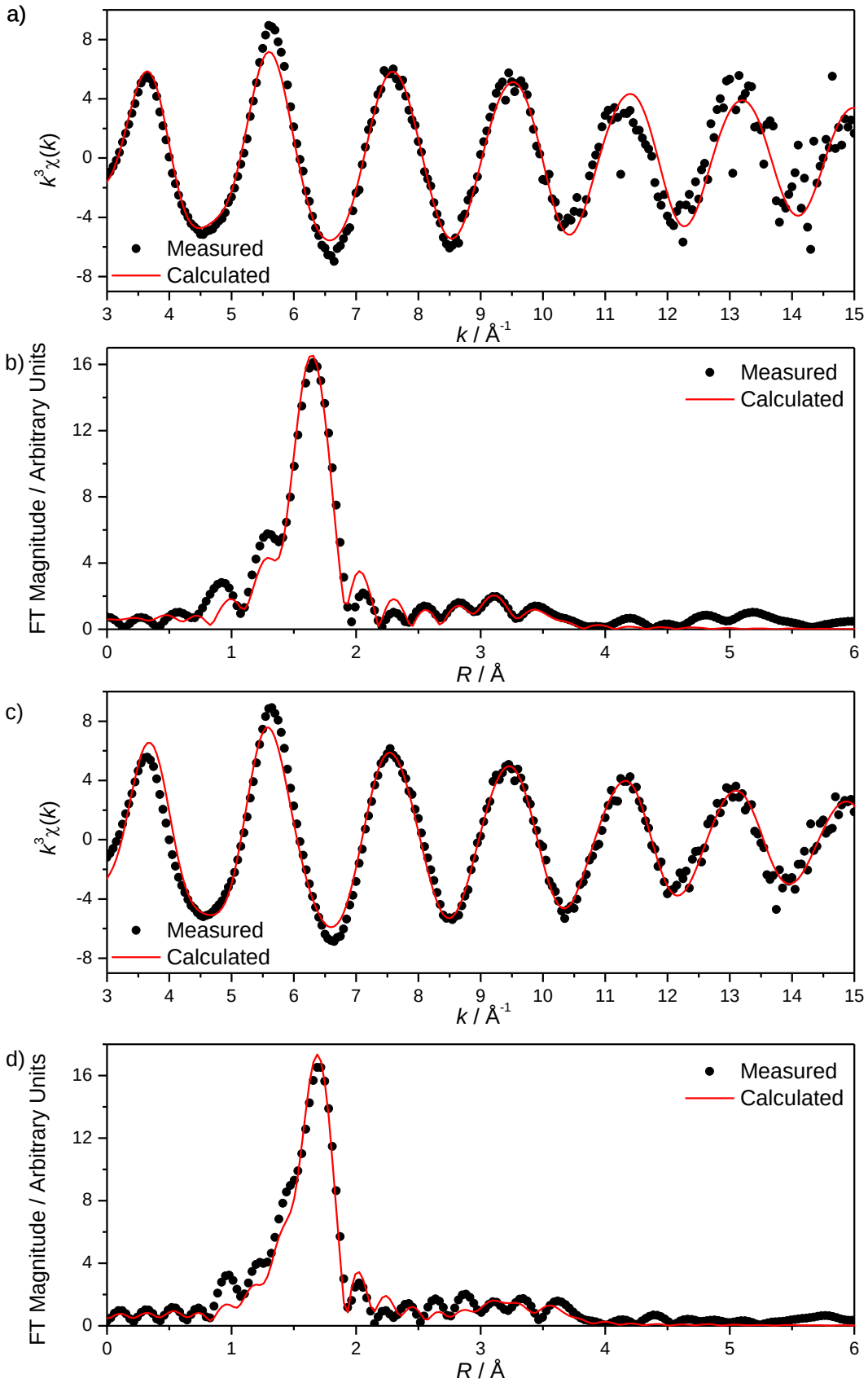
a)
$k^3\chi(k)$
Measured
Calculated
k / Å^{-1}
b)
FT Magnitude / Arbitrary Units
Measured
Calculated
R / Å
c)
$k^3\chi(k)$
Measured
Calculated
k / Å^{-1}
d)
FT Magnitude / Arbitrary Units
Measured
Calculated
R / Å

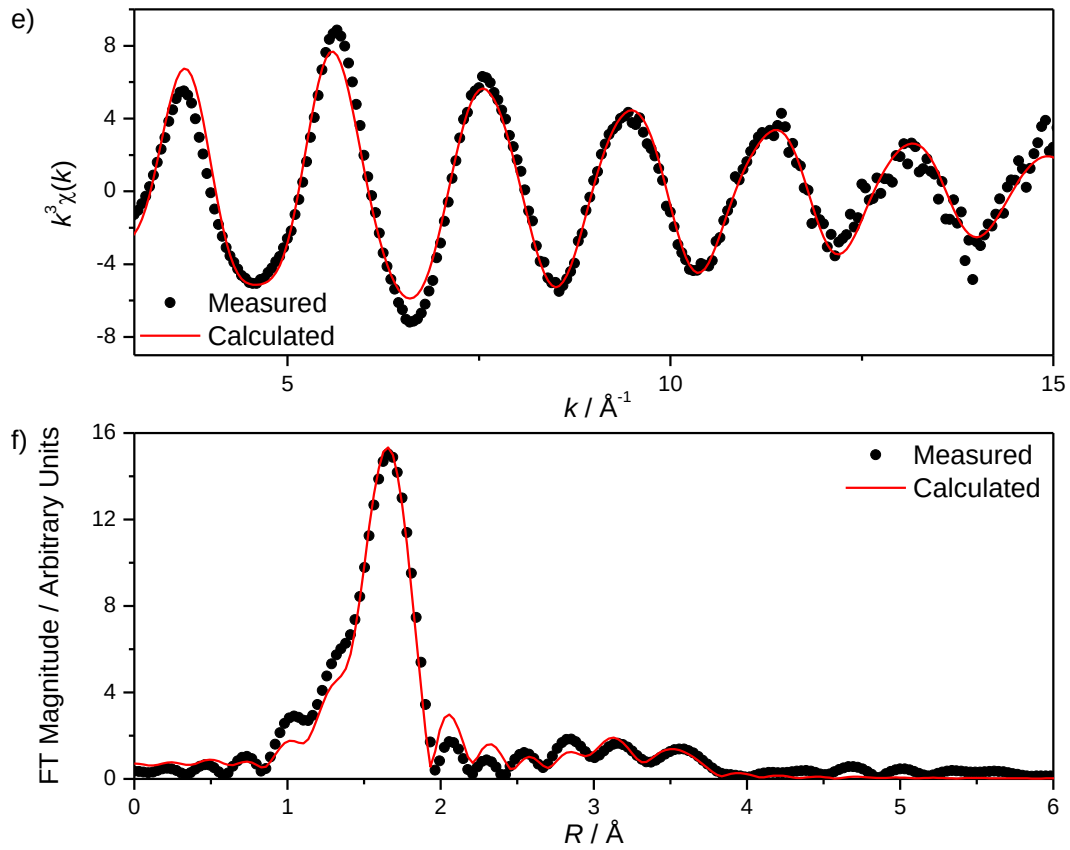

Figure 4. 21a) k^3*-weighted Pt EXAFS spectrum and b) the Fourier transform of* $Ce_{0.95}Pt_{0.10}O_{2-\delta}$*. c)* k^3*-weighted Pd EXAFS spectrum and d) the Fourier transform of* $Ce_{0.85}Pt_{0.15}O_{2-\delta}$*. e)* k^3*-weighted Pt EXAFS spectrum and f) the Fourier transform of* $Ce_{0.80}Pt_{0.20}O_{2-\delta}$*. Measured data are shown by points with best fit shown by line.*

Table 4. 12 Pt L_{III}*-edge EXAFS fitting results for* $Ce_{0.90}Pt_{0.10}O_{2-\delta}$ *(*S_0^2 *= 0.762,* E_0 *= 8.339 eV,* R*-factor = 0.0604),* $Ce_{0.85}Pt_{0.15}O_{2-\delta}$ *(*S_0^2 *= 0.771,* E_0 *= 9.988 eV,* R*-factor = 0.0601) and* $Ce_{0.80}Pt_{0.20}O_{2-\delta}$ *(*S_0^2 *= 0.817,* E_0 *= 8.633 eV,* R*-factor = 0.0497) using* $H_2[Pt(OH)_6]$[31] *as a starting model.*

Shell	Coordination Number	$R_{average}$ / Å	$Ce_{0.90}Pt_{0.10}O_{2-\delta}$		$Ce_{0.85}Pt_{0.15}O_{2-\delta}$		$Ce_{0.80}Pt_{0.20}O_{2-\delta}$	
			R / Å	σ^2 / Å^2	R / Å	σ^2 / Å^2	R / Å	σ^2 / Å^2
O	6	2.08	1.998 (66)	0.0021 (7)	2.008 (5)	0.0023 (4)	2.001 (5)	0.0029 (6)
O	8	3.81	3.593 (59)	0.0086 (69)	3.686 (39)	0.0086 (46)	3.614 (38)	0.0088 (43)
O	8	4.18	3.789 (62)	0.0079 (70)	3.873 (35)	0.0031 (28)	3.818 (39)	0.0078 (43)

4.4 Conclusions

$Ce_{1-x}Pd_xO_{2-\delta}$ has been prepared for the first time by hydrothermal synthesis from $CeCl_3 \cdot 7H_2O$ and $PdCl_2$.

High resolution powder XRD data of $Ce_{1-x}Pd_xO_{2-\delta}$ where $x \leq 0.25$ can be fitted to single, nanocrystalline fluorite phase, with an increasing lattice parameter as a function of *x*, in a similar manner to $Ce_{1-x}Pd_xO_{2-\delta}$ made by a coprecipitation technique.[17] The lattice expansion is explained by Pd EXAFS, which shows that over a range of values of *x* the Pd is in a square planar environment best fitted to a model similar to that proposed by Scanlon *et al.*[14] where the substituted Ce site is vacant, with the dopant Pd ion shifted to sit in an oxide plane, consistent with the preference of Pd^{2+} for square-planar geometry. Earlier EXAFS studies on $Ce_{1-x}Pd_xO_{2-\delta}$ (where *x* = 0.01, 0.05) struggled to de-convolute the signals of the mixed oxide from the Pd metal impurity present in their samples and did not explore the possibility of dopant Pd not occupying on the 4*a* Ce site.[12,13] Furthermore, the analyses of PdO by Baidya[12] and Priolkar[13] includes a Pd – Pd correlation at ~2.7 Å, which is not present in the crystal structure of the oxide. It is unclear whether this error influenced their analysis of the doped fluorites they report. Other reports of $Ce_{1-x}Pd_xO_{2-\delta}$ preparation report a much smaller lattice expansion[23,35] or; for small values of *x*; even a lattice contraction.[13,36-38] These reports all contain high temperature synthetic routes, and could possibly contain $Pd^{3+/4+}$ species in an octahedral geometry sitting closer to the 'ideal' 4*a* site.

Powder XRD of $Ce_{1-x}Pt_xO_{2-\delta}$ ($0.05 \leq x \leq 0.30$) shows that a nanocrystalline fluorite is the only crystalline phase present, and the lattice parameter decreases slightly as a function of *x*. Compositional analyses (ICP-OES and EDX) show that the Ce:Pt ratio

in the products is close to the ratio in the preparation. However, the possibility of an amorphous Pt oxide or hydroxide cannot be excluded. Pt XANES suggests that the Pt is in the +4 oxidation state, which is consistent with the slight decrease in the lattice parameter of the substituted fluorite, if it is indeed substituted. This slight decrease in lattice parameter has been observed in Pt-substituted cerium oxides made by solution combustion though $x = 0.05$ is the highest degree of substitution achieved by this route, and the highest level previously reported. Pt EXAFS suggests that the Pt is in an environment almost identical to that in the Pt precursor; $H_2[Pt(OH)_6]$; indicating that rather than a single phase fluorite the materials could possibly consist of a mixture of nanocrystalline CeO_2 and well dispersed, amorphous $H_2[Pt(OH)_6]$, though why the lattice parameter of the CeO_2 would decrease in this scenario is unclear.

In the next chapter the thermal and redox behaviour of these materials will be considered.

4.5 References

(1) Greenwood, N. N.; Earnshaw, A. *Chemistry of the Elements*; 2nd ed.; Butterworth–Heinemann, 1997.
(2) Bell, A. T. *Science* **2003**, *299*, 1688.
(3) Di Monte, R.; Kaspar, J. *Top. Catal.* **2004**, *28*, 47.
(4) Di Monte, R.; Kaspar, J. *J. Mater. Chem.* **2005**, *15*, 633.
(5) Fornasiero, P.; Balducci, G.; Kaspar, J.; Meriani, S.; Di Monte, R.; Graziani, M. *Catal. Today* **1996**, *29*, 47.
(6) Gorte, R. J. *AlChE J.* **2010**, *56*, 1126.
(7) Kaspar, J.; Fornasiero, P.; Graziani, M. *Catal. Today* **1999**, *50*, 285.
(8) Trovarelli, A. *Catal. Rev.-Sci. Eng.* **1996**, *38*, 439.
(9) Hilaire, S.; Wang, X.; Luo, T.; Gorte, R. J.; Wagner, J. *Appl. Catal. A-Gen.* **2001**, *215*, 271.
(10) Kurzman, J. A.; Misch, L. M.; Seshadri, R. *Dalton Trans.* **2013**, *42*, 14653.
(11) Singh, P.; Hegde, M. S. *Chem. Mater.* **2009**, *21*, 3337.
(12) Baidya, T.; Priolkar, K. R.; Sarode, P. R.; Hegde, M. S.; Asakura, K.; Tateno, G.; Koike, Y. *J. Chem. Phys.* **2008**, *128*, 124711.
(13) Priolkar, K. R.; Bera, P.; Sarode, P. R.; Hegde, M. S.; Emura, S.; Kumashiro, R.; Lalla, N. P. *Chem. Mater.* **2002**, *14*, 2120.
(14) Scanlon, D. O.; Morgan, B. J.; Watson, G. W. *Phys. Chem. Chem. Phys.* **2011**, *13*, 4279.
(15) Larson, A. C.; Van Dreele, R. B. *Los Alamos National Laboratory Report LAUR* **1994**, 86.
(16) Moore, W. J.; Pauling, L. *J. Am. Chem. Soc.* **1941**, *63*, 1392.
(17) Kurnatowska, M.; Kepinski, L.; Mista, W. *Appl. Catal., B* **2012**, *117–118*, 135.
(18) Shannon, R. D. *Acta Crystallogr. Sect. A* **1976**, *32*, 751.
(19) Attfield, J. P. *Acta Crystallogr. Sect. B* **1988**, *44*, 563.
(20) Hailstone, R. K.; DiFrancesco, A. G.; Leong, J. G.; Allston, T. D.; Reed, K. J. *J. Phys. Chem. C* **2009**, *113*, 15155.
(21) Tsunekawa, S.; Ishikawa, K.; Li, Z. Q.; Kawazoe, Y.; Kasuya, A. *Phys. Rev. Lett.* **2000**, *85*, 3440.
(22) Tsunekawa, S.; Sivamohan, R.; Ito, S.; Kasuya, A.; Fukuda, T. *Nanostruct. Mater.* **1999**, *11*, 141.
(23) Misch, L. M.; Kurzman, J. A.; Derk, A. R.; Kim, Y.-I.; Seshadri, R.; Metiu, H.; McFarland, E. W.; Stucky, G. D. *Chem. Mater.* **2011**, *23*, 5432.
(24) Dent, A. J.; Cibin, G.; Ramos, S.; Smith, A. D.; Scott, S. M.; Varandas, L.; Pearson, M. R.; Krumpa, N. A.; Jones, C. P.; Robbins, P. E. *J. Phys. Conf. Ser.* **2009**, *190*, 012039.
(25) Bunker, G. *Introduction to XAFS: A Practical Guide to X-ray Absorption Fine Structure Spectroscopy*; Cambridge University Press, 2010.
(26) Ravel, B.; Newville, M. *J. Synchrotron Rad.* **2005**, *12*, 537.
(27) Modeshia, D. R.; Wright, C. S.; Payne, J. L.; Sankar, G.; Fiddy, S. G.; Walton, R. I. *J. Phys. Chem. C* **2007**, *111*, 14035.
(28) Sardar, K.; Playford, H. Y.; Darton, R. J.; Barney, E. R.; Hannon, A. C.; Tompsett, D.; Fisher, J.; Kashtiban, R. J.; Sloan, J.; Ramos, S.; Cibin, G.; Walton, R. I. *Chem. Mater.* **2010**, *22*, 6191.
(29) Kim, S.-J.; Lemaux, S.; Demazeau, G.; Kim, J.-Y.; Choy, J.-H. *J. Mater. Chem.* **2002**, *12*, 995.

(30) Demazeau, G.; Omeran, I.; Pouchard, M.; Hagenmuller, P. *Mater. Res. Bull.* **1976**, *11*, 1449.
(31) Kim, S.-J.; Lemaux, S.; Demazeau, G.; Kim, J.-Y.; Choy, J.-H. *J. Am. Chem. Soc.* **2001**, *123*, 10413.
(32) Waser, J.; Levy, H. A.; Peterson, S. W. *Acta Crystallogr.* **1953**, *6*, 661.
(33) Scott, H. *Acta Crystallogr. Sect. B* **1979**, *35*, 3014.
(34) Hoekstra Henry, R.; Siegel, S.; Gallagher Francis, X. In *Platinum Group Metals and Compounds*; American Chemical Society: 1971; Vol. 98, p 39.
(35) Singh, P.; Hegde, M. S. *Cryst. Growth Des.* **2010**, *10*, 2995.
(36) Baidya, T.; Dutta, G.; Hegde, M. S.; Waghmare, U. V. *Dalton Trans.* **2009**, 455.
(37) Meng, L.; Jia, A.-P.; Lu, J.-Q.; Luo, L.-F.; Huang, W.-X.; Luo, M.-F. *J. Phys. Chem. C* **2011**, *115*, 19789.
(38) Wang, B.; Weng, D.; Wu, X.; Fan, J. *Catal. Today* **2010**, *153*, 111.

Chapter 5: Redox Properties of Doped Cerium Oxides

5.1 Introduction

In this chapter the redox properties and behaviour of the doped cerium oxides whose synthesis was described in chapters 3 and 4 is examined. The redox tests were carried out at Johnson Matthey Technology Centre (JMTC, Sonning Common, Reading, UK) whilst *in situ* characterisation was carried out at the University of Warwick.

Although pentavalent ion-doped ceria samples made in NaOH contain an appreciable amount of Na (see Chapter 3) in this chapter their structural formulae are simplified to $Ce_{1-x}M_xO_{2+\delta}$ for clarity.

5.2 Catalytic Properties of Cerium Dioxide

The TPR of commercially available CeO_2 samples were recorded. Highly crystalline, low surface area (LSA) CeO_2 (99.9%, Sigma-Aldrich) and high surface area (HSA) CeO_2 (26.1% H_2O, Rhodia) were compared (Figure 5. 1). Surface areas are shown in Table 5. 1. HSA CeO_2 has a significantly larger low temperature (below 500 °C) H_2 uptake (attributed to reduction close to the surface[1-4]) compared to the LSA CeO_2, and the total reduction (up to 950 °C) of HSA CeO_2 is approximately twice that of LSA CeO_2 (Table 5. 1). A small negative peak (where the measured H_2 uptake is 0) in the TPR profile of HSA CeO_2 at approximately 600 °C is attributed to desorption of surface species not adsorbed by the H_2O trap, such as a small amount of NH_3 or occluded nitrate arising from the synthesis. The presence of a secondary smaller, low temperature reduction peak (at 300 °C) in the profile of HSA CeO_2 can be observed. This can be attributed to the presence of surface-capping oxide species which can be easily reduced.[1,2]

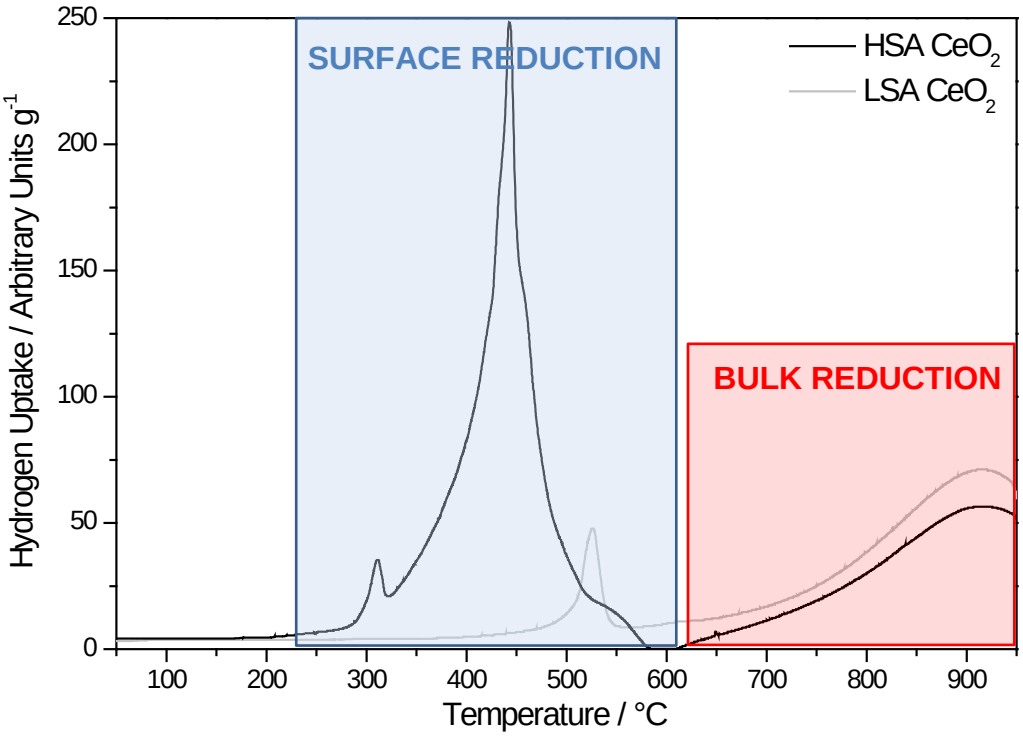

Figure 5. 1 TPR profiles of commercially available high and low surface area CeO_2.

The TPR profiles of CeO_2 prepared by a hydrothermal route at 240 °C using NaOH or NH_4OH are shown in Figure 5. 2. With a maximum at around 300 °C, CeO_2 made using NaOH exhibits a lower temperature reduction peak than commercial CeO_2 or CeO_2 prepared hydrothermally using NH_4OH despite having a lower surface area. After firing to 500 °C in air the TPR profile has an even lower temperature maximum as low as 230 °C, with an onset at just over 100 °C, whilst the temperature of the high temperature peak remains unchanged. This suggests that though the low temperature reduction is not merely due to desorption of volatile species present in the synthesis such as chloride, the surface of the hydrothermal CeO_2 made in NaOH is appreciably altered by firing to 500 °C. Reduction at very low temperatures has also been observed in $Ce_{1-x}Zr_xO_{2-\delta}$ phases hydrothermally prepared using NaOH,[5] where the presence of Na in the structure was shown to have a beneficial effect on the catalytic properties, possibly due to higher levels of oxide defects.

Like HSA CeO_2, both hydrothermally prepared CeO_2 samples exhibit a negative reduction peak attributed to loss of surface species at higher temperatures. Calcination in air at 500 °C does not remove these surface species since their TPR profiles both exhibit negative peaks similar to their un-calcined counterparts. CeO_2 made in NH_4OH (both before and after calcination) has a large desorption at around 600 °C, thought to be NH_3. CeO_2 made in NaOH has a small desorption at 680 °C which is unexplained. These desorptions will reduce the H_2 consumption values (Table 5. 1) obtained by analysis of TPR profiles.

The textural properties of CeO_2 and doped-CeO_2 (such as surface area and porosity) have been widely shown to have a huge effect on catalytic activity.[2,4,6] Unsurprisingly, whilst the degree of high temperature, bulk reduction of CeO_2 is largely independent of surface area, the degree of low temperature, surface Ce^{4+}

reduction increases with increasing surface area: the data for samples studied here are plotted in Figure 5. 3.

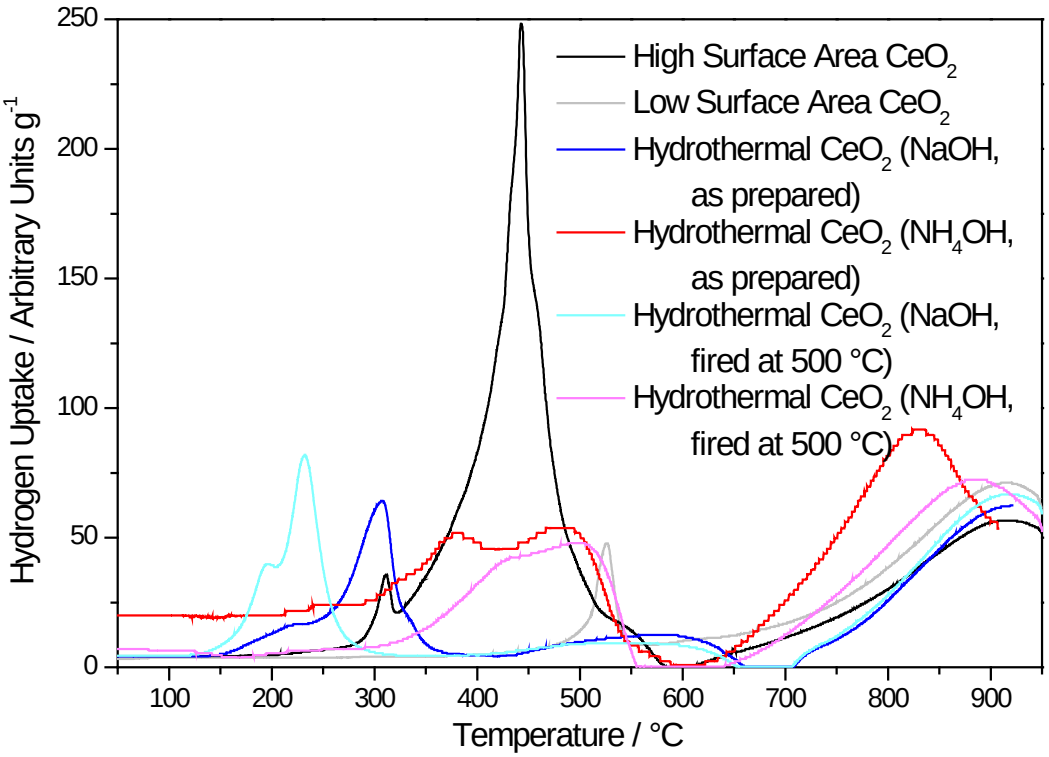

Figure 5. 2 TPR profiles of CeO_2 prepared hydrothermally using different bases as prepared and after firing at 500 °C compared to commercial CeO_2.

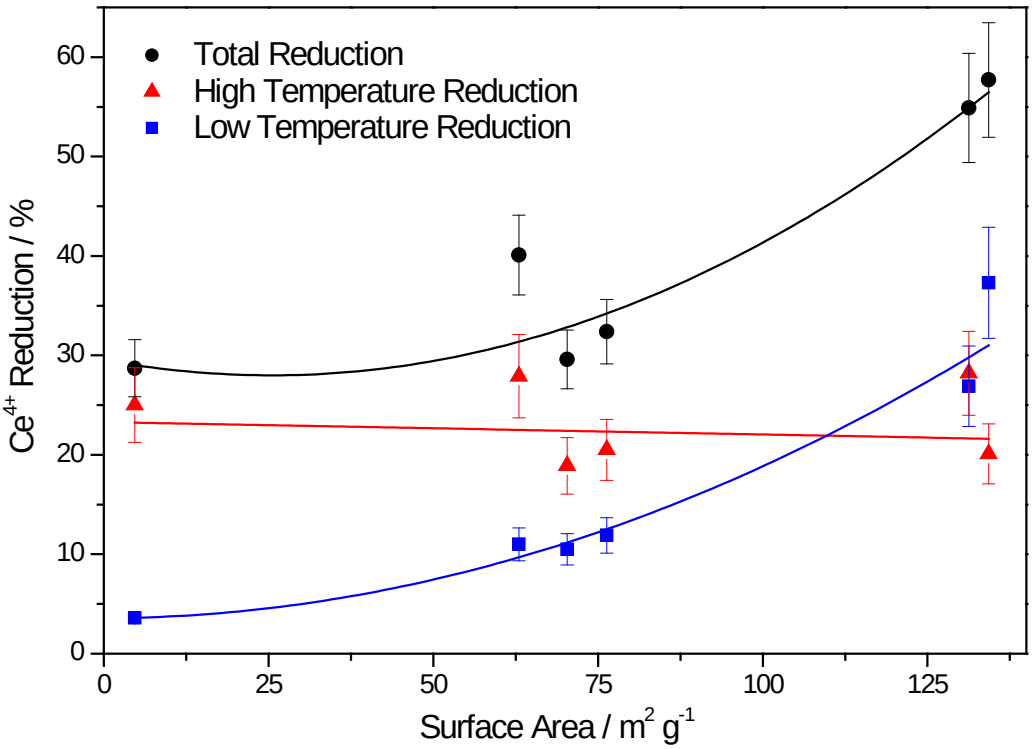

Figure 5. 3 Degree of Ce^{4+} reduction in CeO_2 samples as a function of their surface area, using data from Table 5.1.

CeO_2 Sample	S_{BET} / $m^2\ g^{-1}$	H oxidised / mmol g^{-1}			Ce^{4+} reduced / %			$T_{L\,max}$ / °C	$T_{H\,max}$ / °C
		Total	T_L	T_H	Total	T_L	T_H		
HSA (Commercial)	134.3(7)	3.35	2.17	1.17	57.7	37.3	20.1	440	920
LSA (Commercial)	4.70(1)	1.67	0.21	1.45	28.7	3.6	25.0	525	920
Hydrothermal (NaOH, as made)	70.3(3)	1.72	0.61	1.10	29.6	10.5	18.9	310	920
Hydrothermal (NH_4OH, as made)	131.3(4)	3.19	1.56	1.64	54.9	26.9	28.2	480	830
Hydrothermal (NaOH, fired)	63.0(2)	2.33	0.64	1.62	40.1	11.0	27.9	230	920
Hydrothermal (NH_4OH, fired)	76.3(3)	1.88	0.69	1.19	32.4	11.9	20.5	500	880

Table 5. 1 BET Surface areas (S_{BET}) and summary of results from TPR of CeO_2 synthesised by various routes. T_L *and* T_H *correspond to low and high temperature domains, respectively.* $T_{L\,max}$ *and* $T_{H\,max}$ *are the temperatures at which the low and high temperature domain maxima of* H_2 *uptake occur, respectively.*

5.3 Catalytic Properties of Pentavalent Ion-Doped Ceria

TPR measurement and *in situ* powder XRD were the main characterisation techniques implemented to assess the catalytic properties of CeO_2 doped with pentavalent ions (Sb, Nb, Ta and V). In order to evaluate the performance of the catalysts under conditions more comparable to those in a real application, such as three-way catalysts, where the oxygen-fuel mixture changes rapidly, dynamic OSC data have been collected. Whereas TPR gives a measure of the absolute oxygen storage capacity, this gives a measure of the *dynamic oxygen storage capacity*,[7-9] namely the oxygen that can be quickly removed from or absorbed by the material. $Ce_{1-x}Nb_xO_{2+\delta}$ ($0 \leq x \leq 0.30$) made in both NaOH and NH_4OH was chosen as a representative oxide to study the dynamic OSC.

5.3.1 Antimony-Doped Ceria

Heating in H_2 to temperatures beyond 550 °C was not performed due to the possibility of releasing toxic Sb (a volatile solid with a melting point of 631 °C) or even SbH_3, a highly poisonous gas.[10] The TPR profiles (up to 550 °C) of the lowest Sb-doped CeO_2 oxides, *i.e.* $Ce_{0.95}Sb_{0.05}O_{2+\delta}$, made in NaOH and NH_4OH (using $SbCl_5$ as a precursor) both show a very large H_2 uptake at 425-430 °C (Figure 5. 4), which is attributed to Sb(V) reduction.

Powder XRD of $Ce_{1-x}Sb_xO_{2+\delta}$ (x = 0.10, 0.30) after being heated in a tube furnace in a 5% H_2 in N_2 environment at 500 °C for 1 hour (Figure 5. 5) reveal in each case the presence of Sb metal and fluorite with a lattice parameter close to that of CeO_2

(Table 5. 3), suggesting that $Ce_{1-x}Sb_xO_{2+\delta}$ oxides phase separate much like previously reported $Ce_{1-x}Bi_xO_{2-0.5x}$.[11]

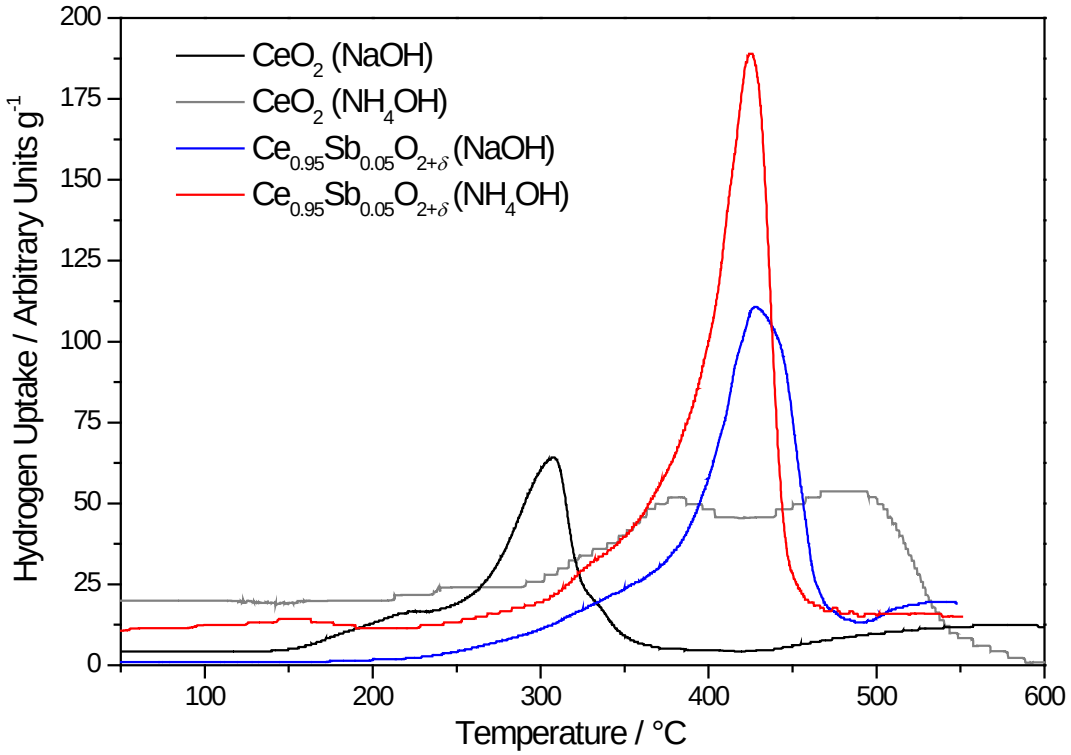

Figure 5. 4 TPR profiles of $Ce_{0.95}Sb_{0.05}O_{2+\delta}$ prepared hydrothermally using NaOH and NH_4OH.

The reduction of the Sb(V) in $Ce_{0.95}Sb_{0.05}O_{2+\delta}$ to Sb metal should consume approximately 1.46 mmol of H atoms per gram of sample, roughly the integrated area of both TPR profiles suggesting that little Ce(IV) reduction takes place (Table 5. 2). This is further implied by the absence of any visible secondary reduction peaks in the TPR profile, suggesting that the presence of Sb hinders CeO_2 reduction.

Table 5. 2 Summary of results from TPR of $Ce_{0.95}Sb_{0.05}O_{2.025}$ prepared hydrothermally in NaOH and NH_4OH. T_{max} is the temperature at which the maximum of H_2 uptake occurs.

Sb-Doped CeO_2 Sample	H oxidised / mmol g^{-1}	Ce^{4+} reduced / %	T_{max} / °C
$Ce_{0.95}Sb_{0.05}O_{2+\delta}$ (NaOH)	1.23	N/A	428
$Ce_{0.95}Sb_{0.05}O_{2+\delta}$ (NH_4OH)	1.43	N/A	425

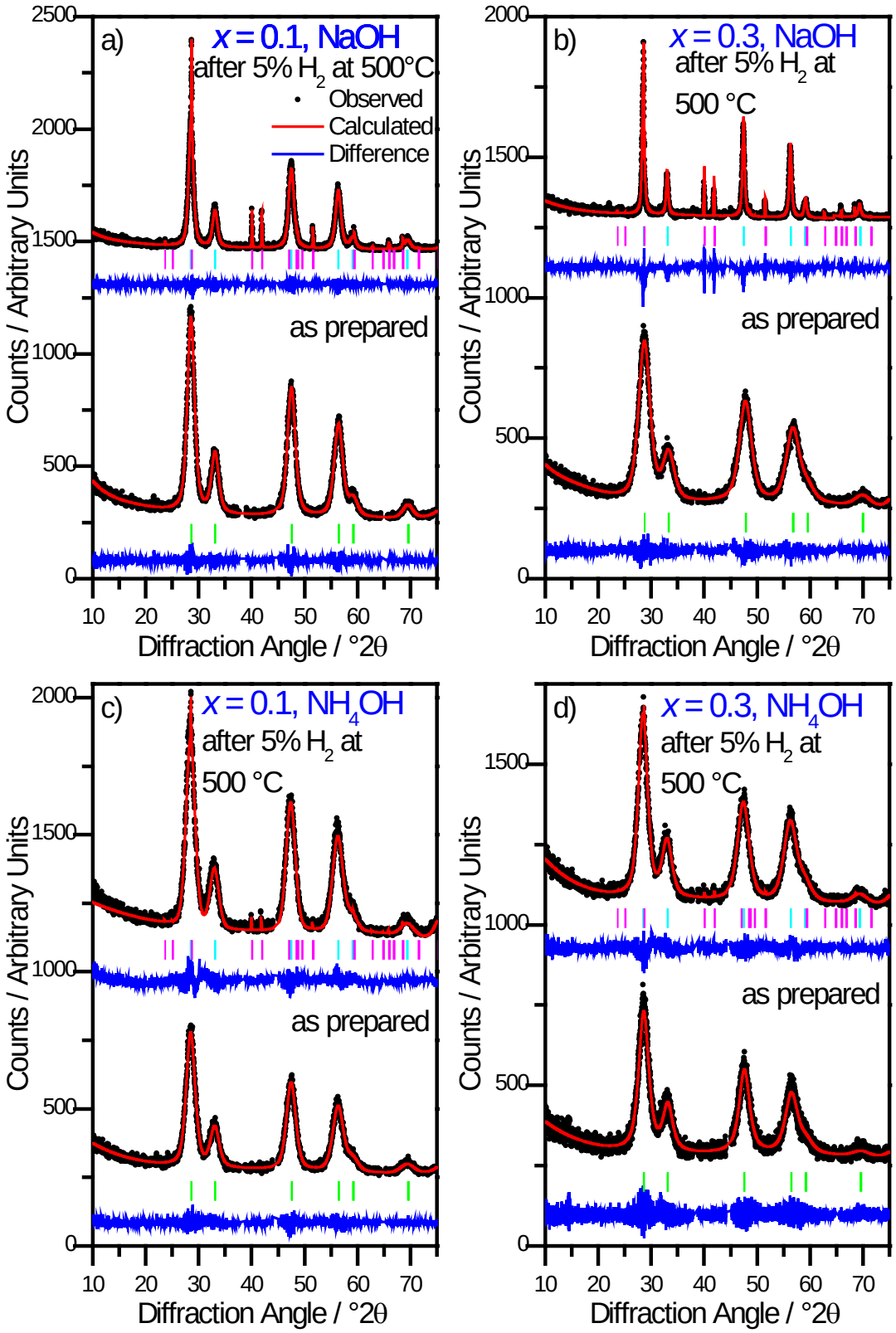

Figure 5. 5 Le Bail fits to powder XRD data of $Ce_{0.9}Sb_{0.1}O_{2+\delta}$ and $Ce_{0.7}Sb_{0.3}O_{2+\delta}$ made in NaOH and NH_4OH before and after heating in 5% H_2 in N_2 at 500 °C. Reflections due to Al sample holder at 38°, 44° and 65° excluded. Green tick marks correspond to the Sb-doped fluorite CeO_2 peak positions whilst light blue and magenta tick marks correspond to fluorite CeO_2 and α-Sb metal (entry 161492, ICSD), respectively

Table 5. 3 Lattice parameter of fluorite phase ($Ce_{1-x}Sb_xO_{2+\delta}$ or CeO_2) before and after heating in H_2 at 500 °C.

x	**Base**	*a*, as made / Å	*a*, heated in H_2 at 500 °C / Å
0.10	**NaOH**	5.4061(6)	5.4161(4)
0.30		5.377(1)	5.4130(3)
0.10	**NH_4OH**	5.4107(9)	5.4230(9)
0.30		5.399(1)	5.416(1)

5.3.2 Niobium-Doped Ceria

5.3.2.1 Temperature-Programmed Reduction

Figure 5. 6a shows the TPR profiles of $Ce_{1-x}Nb_xO_{2+\delta}$ ($0 \leq x \leq 0.35$) made in NaOH. When prepared using NaOH, the maximum temperature of the low temperature uptake of $Ce_{1-x}Nb_xO_{2+\delta}$ ($x \geq 0.05$) is approximately constant between 525 and 555 °C (Table 5. 4), significantly higher than the temperature of the low temperature peak of the CeO_2 made in NaOH. For low values of x (0.05 – 0.15, 0.25) the low temperature feature consists of a pair of peaks, whereas oxides containing more Nb have a single, broad low temperature peak. The reason for this is unclear; Nb reduction is unlikely at such low temperatures, and the TPR profiles of Nb_2O_5 and NbO_2 (Figure 5. 7, collected by John Kilmartin, JMTC) show little reduction takes place at low temperature. Furthermore it cannot be satisfactorily attributed to the presence of a mixture of phases, since when x = 0.35 phase separation has begun to occur (see Chapter 3); and the TPR of this mixed phase sample consists of one broad peak (Figure 5. 6).

The total hydrogen uptake increases even whilst the Ce content of the oxides decreases (*i.e.* increasing x), resulting in a drastic increase in % Ce^{4+} reduction as a function of x (Figure 5. 8). This trend continues when x = 0.35, which contains some $NaNbO_3$ as an impurity. It can also be seen that the increase in Ce^{4+} reduction is occurring entirely at low temperature, with the proportion of high temperature reduction decreasing slightly as Nb content increases. This can be attributed to the increase in surface area as Nb content increases (Table 5. 4).

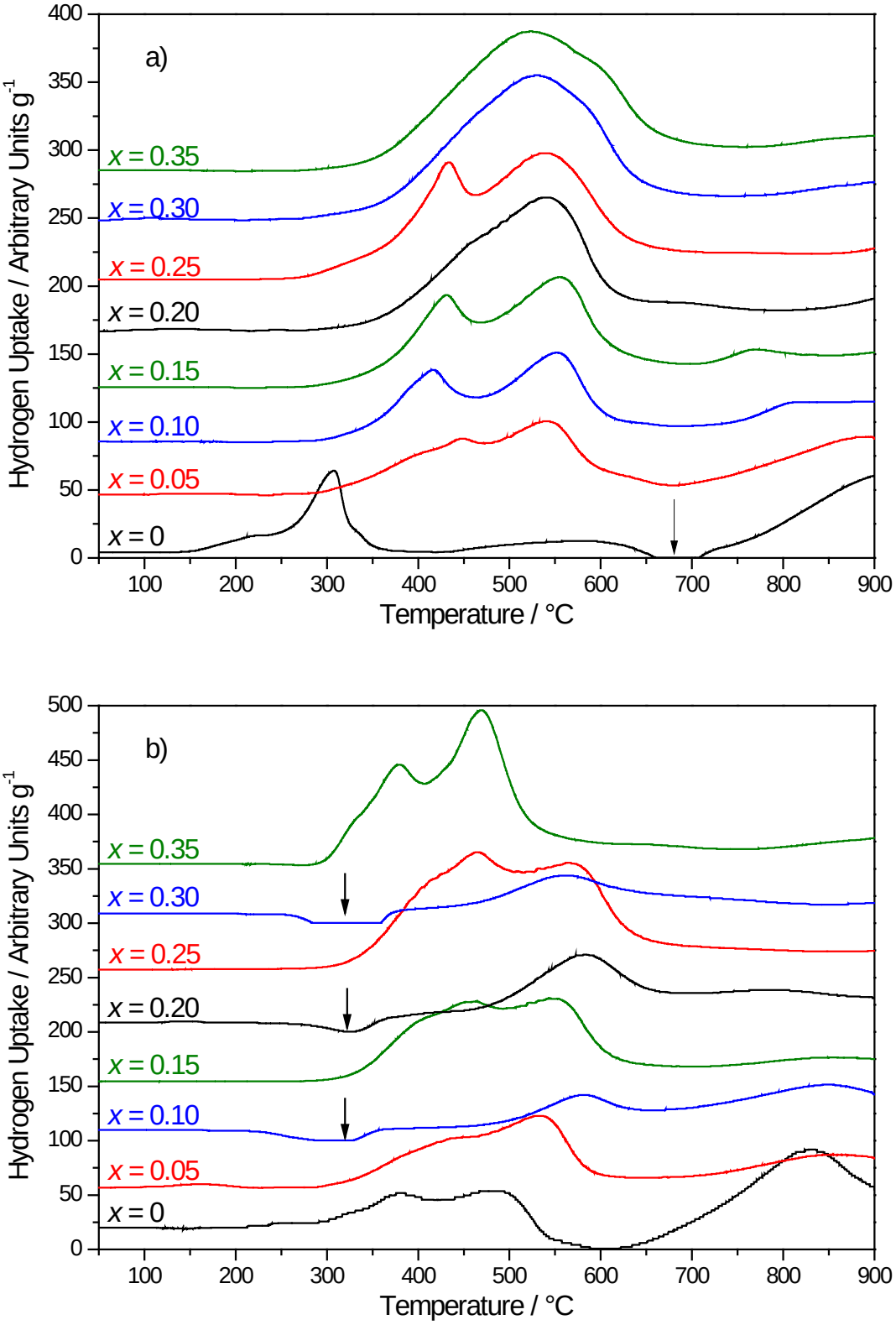

Figure 5. 6 TPR profiles of as prepared $Ce_{1-x}Nb_xO_{2+\delta}$ $(0 \leq x \leq 0.35)$ *made in a) NaOH and b)* NH_4OH. *Each profile is offset for clarity. Arrows show effect of desorption on profile.*

$Ce_{1-x}Nb_xO_{2+\delta}$		S_{BET} /	H oxidised / mmol g^{-1}			Ce^{4+} reduced / %			$T_{L\,max}$ / °C	$T_{H\,max}$ / °C
x	Base	$m^2\,g^{-1}$	Total	T_L	T_H	Total	T_L	T_H		
0.05	**NaOH**	122.0(5)	1.99	1.25	0.74	35.7	22.4	13.3	540	≥900
0.10	**NaOH**	128.0(6)	2.70	1.90	0.80	50.5	35.5	15.0	550	≥900
0.15	**NaOH**	-	2.61	1.86	0.75	51.0	36.4	14.6	555	≥900
0.20	**NaOH**	183.1(7)	2.68	2.10	0.58	55.1	43.2	11.9	540	≥900
0.25	**NaOH**	231.4(8)	3.01	2.37	0.64	65.1	51.2	13.9	540	≥900
0.30	**NaOH**	226.9(8)	3.04	2.59	0.45	69.5	59.4	10.2	530	≥900
0.35	**NaOH**	-	3.25	2.64	0.59	79.1	64.4	14.5	525	≥900
0.05	**NH_4OH**	133.7(6)	1.98	1.35	0.63	35.5	24.2	11.3	530	890
0.10	**NH_4OH**	145.9(1)	2.03	0.83	1.20	37.9	15.5	22.3	585	845
0.15	**NH_4OH**	-	2.81	2.10	0.70	54.9	41.1	13.6	460	860
0.20	**NH_4OH**	107.4(1)	1.87	1.12	0.74	38.4	23.0	15.2	585	795
0.25	**NH_4OH**	166.1(5)	3.51	2.91	0.60	76.0	63.0	13.0	465	≥900
0.30	**NH_4OH**	167.9(5)	1.55	0.95	0.61	35.6	21.7	13.9	565	890
0.35	**NH_4OH**	-	3.21	2.44	0.77	78.3	59.6	18.7	470	≥900
0.30*	**NaOH**	150.2(9)	3.61	2.94	0.67	82.5	67.3	15.2	530	≥900
0.30*	**NH_4OH**	74.1(2)	2.75	2.40	0.35	63.1	55.0	8.1	490	≥900

Table 5. 4 BET Surface areas (S_{BET}) and summary of results from TPR of as prepared $Ce_{1-x}Nb_xO_{2+\delta}$ synthesised hydrothermally in NaOH and NH_4OH. T_L *and* T_H *correspond to low and high temperature domains, respectively.* $T_{L\,max}$ *and* $T_{H\,max}$ *are the temperatures at which the low and high temperature domain maxima of H_2 uptake occur, respectively. Also included are data from $Ce_{0.7}Nb_{0.3}O_{2+\delta}$ made hydrothermally in NaOH and NH_4OH and subsequently fired in air at 500 °C, marked by an asterisk. Some BET surface areas not recorded.*

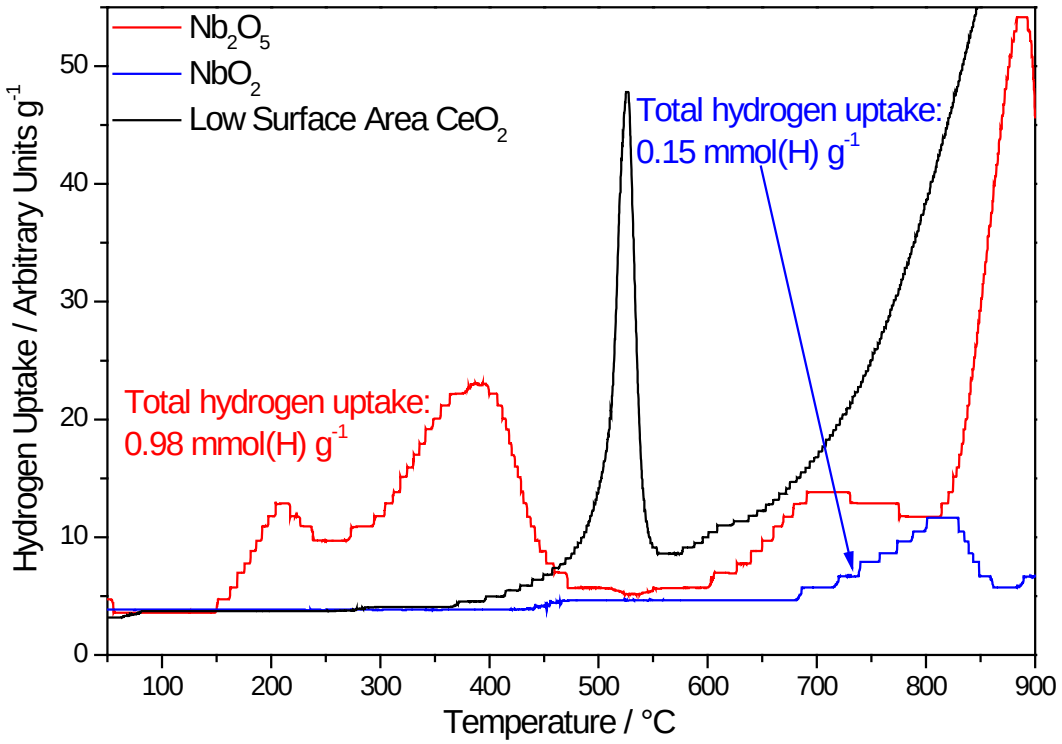

Figure 5. 7 TPR profiles of Nb_2O_5 and NbO_2 with low surface area CeO_2 for comparison.

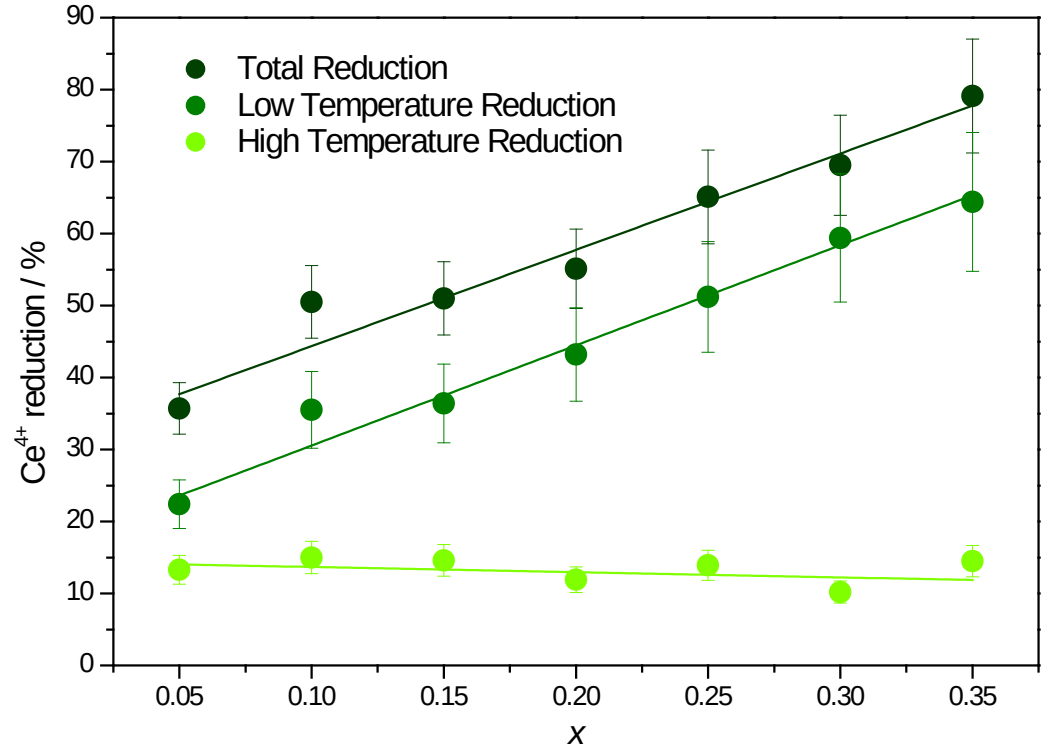

Figure 5. 8 Degree of Ce^{4+} reduction in $Ce_{1-x}Nb_xO_{2+\delta}$ made in NaOH as a function of x*, assuming only Ce is reduced.*

The TPR profiles of the as made $Ce_{1-x}Nb_xO_{2+\delta}$ made in NH_4OH have desorptions at 325 °C, which makes interpretation difficult (Figure 5. 6b), resulting in little

correlation between measured H_2 uptake and *x*. The desorptions are likely to be NH_3 or HCl; the presence of which is inferred from a small N – H stretching feature observed by IR spectroscopy at 3200 cm^{-1} (Figure 5. 9). Firing of the sample in air at 500 °C causes the N – H stretch to disappear, suggesting it is responsible for the desorption visible in the TPR profiles. TPR of $Ce_{0.70}Nb_{0.30}O_{2+\delta}$ made in NH_4OH and subsequently fired at 500 °C shows no sign of low temperature desorption (Figure 5. 10) and despite the reduction in surface area, the measured H_2 uptake is much higher (Table 5. 4).

Although the low temperature H_2 uptake of $Ce_{0.70}Nb_{0.30}O_{2+\delta}$ made in NaOH has a slightly higher onset when fired at 500 °C, the total consumption per gram is approximately 20% higher. An increased uptake after firing at 500 °C can also be

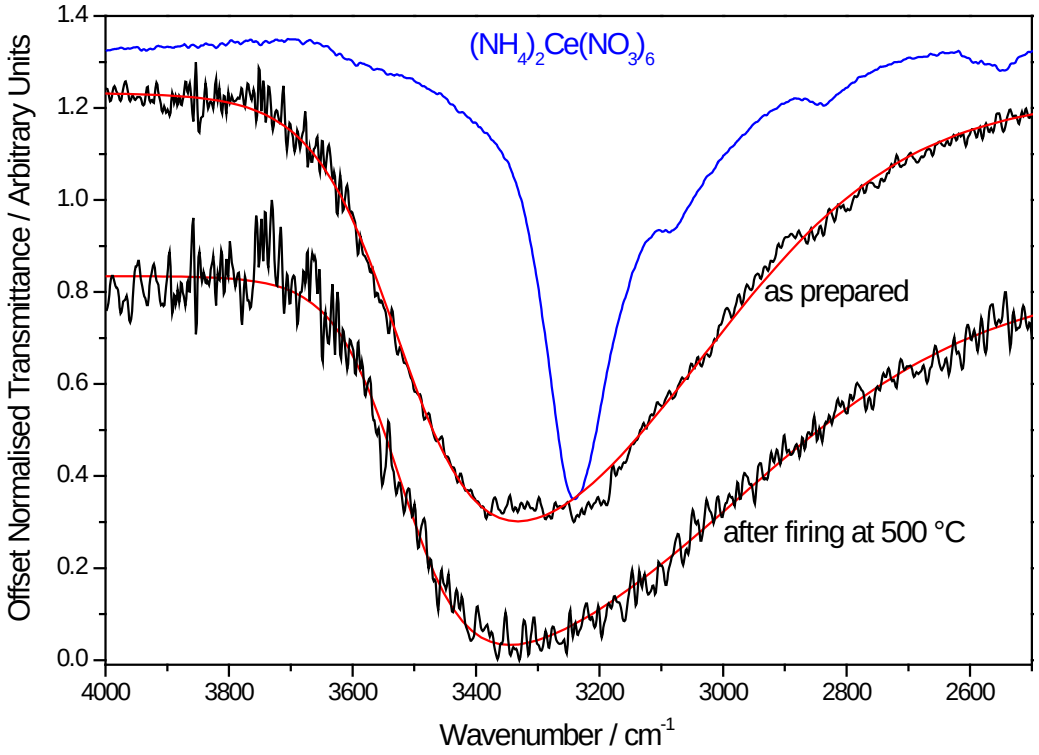

Figure 5. 9 Normalised IR spectra of $Ce_{0.70}Nb_{0.30}O_{2+\delta}$ made in NH_4OH before (offset by 0.3 units for clarity) and after heating at 500 °C. Red lines are asymmetric double sigmoidal fits of O – H stretching to data (in black). IR spectrum of $(NH_4)_2Ce(NO_3)_6$ shown in blue (offset by 0.35 units).

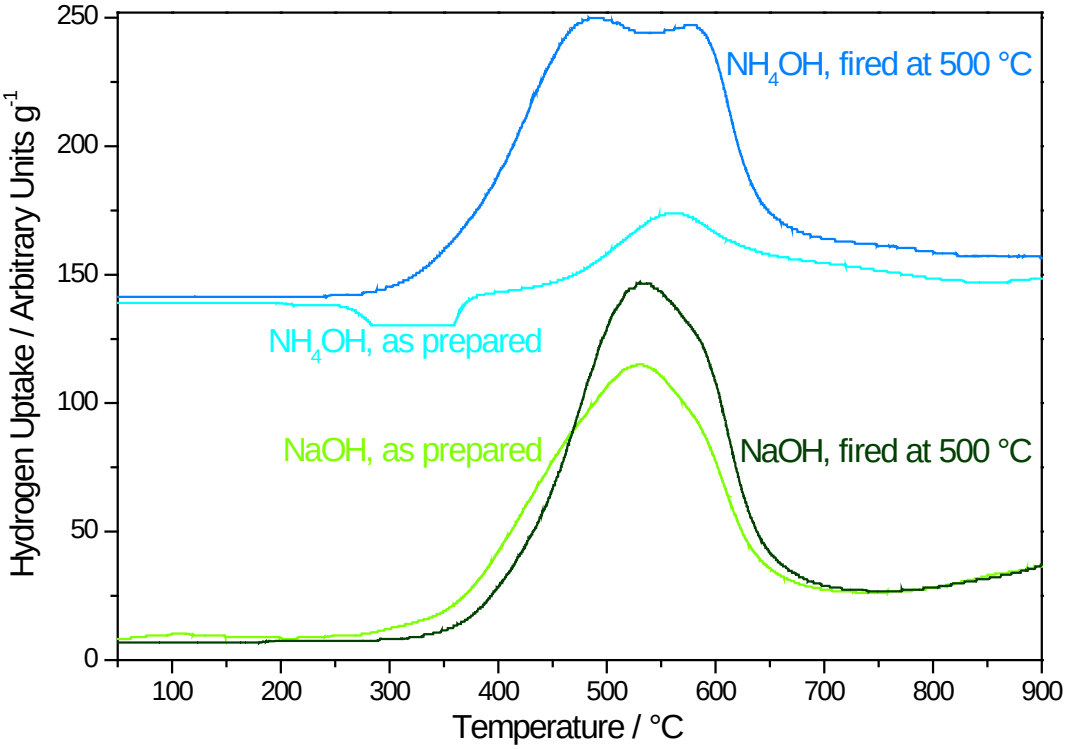

Figure 5. 10 TPR profiles of $Ce_{0.70}Nb_{0.30}O_{2+\delta}$ made in NaOH and NH_4OH before and after firing in air at 500 °C. TPR profiles of $Ce_{0.70}Nb_{0.30}O_{2+\delta}$ made in NH_4OH offset by 130 units.

observed in CeO_2 made in NaOH (Figure 5. 2). In both of these oxides made in NaOH, firing increases the amount of H_2 consumption associated with reduction of Ce^{4+} at the surface (*i.e.* low temperature), even as the surface area reduces. A similar phenomenon has been observed in $Ce_{0.5}Zr_{0.5}O_2$, where repeated high temperature redox cycling reduces the temperature of the low temperature hydrogen uptake.[6,12] However, this could possibly be explained by the formation of the pyrochlore $Ce^{III}_2Zr^{IV}_2O_7$.

5.3.2.2 *In situ* Powder X-ray Diffraction

In situ powder X-ray diffraction of $Ce_{0.75}Nb_{0.25}O_{2+\delta}$ was used to assess its structural stability upon heating in oxidising (air) and reducing (5% H_2 in N_2) atmospheres up to 800 °C.

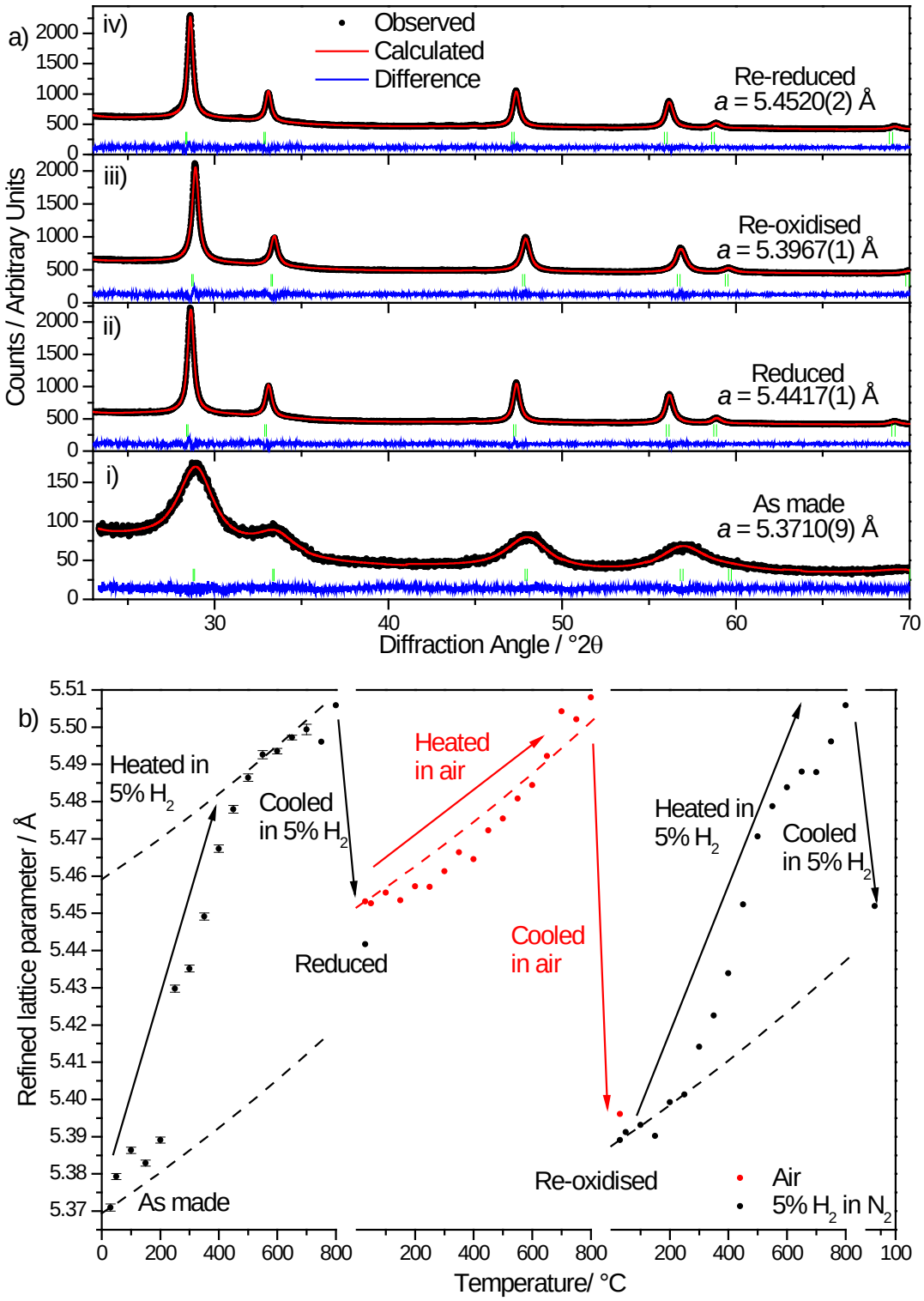

Figure 5. 11a) Le Bail fits to room temperature (30 °C) powder XRD patterns of $Ce_{0.75}Nb_{0.25}O_{2+\delta}$ *made in NaOH i) as made, ii) after heating to 800 °C in 5%* H_2*, iii) after subsequent heating in air to 800 °C and iv) after subsequent heating in 5%* H_2 *for a second time. b) Lattice parameters of the same material from Le Bail fitting of* in situ *powder XRD heating experiments. Dashed lines show calculated thermal expansion of a fluorite, using the thermal expansion coefficient of* CeO_2*. Where no error bars are shown the errors are smaller than the data points.*

Powder XRD patterns of $Ce_{0.75}Nb_{0.25}O_{2+\delta}$ made in NaOH after heating in H_2 and air at 800 °C (Figure 5. 11a) show that no phase separation or formation of secondary phases such as $CeNbO_4$ occurs; though the peaks are significantly sharper, suggesting significant annealing of the oxide. When heating under H_2, the lattice parameter, *a*, increased sharply at 250 °C (Figure 5. 11b), coinciding with the onset of H_2 consumption observed in TPR. This is caused by reduction of Ce(IV) to Ce(III), which is considerably larger (eight-coordinate Ce(III) is 1.143 Å, compared to 0.97 Å for Ce(IV)[13]). This rapid increase in lattice parameter from 250 °C far exceeds thermal lattice expansion, which can be calculated as a function of temperature using the formula derived for oxides adopting the fluorite structure by Taylor,[14] Equation 5. 1:

$$a' = (1 + x_1 T + x_2 T^2) a$$

Equation 5. 1 Lattice parameter, a', for the fluorite structure as a function of temperature, T, in °C; where x_1 and x_2 are coefficients with units $°C^{-1}$ and $°C^{-2}$, respectively; and a is the lattice parameter at 0 °C.

For x_1 and x_2 the coefficients of pure CeO_2 (9.73 $°C^{-1}$ and 2.23 $°C^{-2}$, respectively) were used, and the lattice parameter at 0 °C, *a*, was chosen so that the calculated *a'* at 30 °C was the same as the measured value at that temperature. These are shown as dashed lined in Figure 5. 11b. At 550 – 600 °C the rate of lattice expansion slows to be approximately equal to thermal expansion, suggesting Ce(IV) reduction slows, coinciding with the lowering of H_2 consumption in the TPR of $Ce_{0.75}Nb_{0.25}O_{2+\delta}$.

After cooling to 30 °C (whilst still under H_2) the resulting lattice parameter was considerably larger than in the as made $Ce_{0.75}Nb_{0.25}O_{2+\delta}$, suggesting some Ce(III) remains. Upon heating in air, the lattice parameter increase is initially smaller than would be expected purely from thermal expansion. This can be explained by the re-

oxidation of Ce(III) and resulting contraction of the unit cell. However, by around 650 °C the lattice expansion has again exceeded the value expected from thermal expansion alone. This can be explained again by the slight reduction of Ce(IV), which has been observed in CeO_2 at elevated temperatures.[15]

When cooled in air the lattice parameter of $Ce_{0.75}Nb_{0.25}O_{2+\delta}$ decreases to a value smaller than that of hydrothermally prepared CeO_2, though it is slightly larger than that of the as made oxide. This suggests incomplete re-oxidation of Ce(III) upon heating at 800 °C in air. Subsequent heating under 5% H_2 causes the lattice parameter to closely follow the thermal expansion curve up to 250 °C, suggesting little Ce(IV) reduction below 300 °C in a similar manner to the as made $Ce_{0.75}Nb_{0.25}O_{2+\delta}$. Above 300 °C the lattice parameter increases sharply as Ce(IV) reduction commences. However the lattice expansion slows at around 650 – 700 °C, and the lattice parameter is smaller than at the same temperature when first heated under H_2. At around 750 °C the lattice expansion again increases sharply. This can be attributed to the increased particle size caused by annealing of the sample during previous heating. The much larger particle size means that a larger proportion of the Ce is confined to the bulk of the sample and less low temperature reduction takes place, whilst a considerably larger 'bulk' reduction occurs at 750 – 800 °C.

When heated in H_2, *in situ* powder XRD of $Ce_{0.75}Nb_{0.25}O_{2+\delta}$ made in NH_4OH (Figure 5. 12a, i – iii) shows that at approximately 850 °C $CeNbO_4$ begins to form. Subsequent heating in air to 900 °C does not cause the reformation of the phase-pure fluorite (Figure 5. 12a, iv). Up to 150 °C the refined lattice parameter is indicative of little Ce^{4+} reduction (Figure 5. 12b), since it is very close to the value calculated from thermal expansion alone (Equation 5. 1). From 200 °C the presence of some Ce^{3+} causes the lattice to expand rapidly, which corresponds to the onset of a H_2

consumption peak in TPR (Figure 5. 6b). Above 550 °C the rate of lattice expansion decreases to a value consistent with thermal expansion, which is approximately the temperature the H_2 consumption seen by TPR begins to decrease. The total lattice expansion at 800 °C seen is smaller than the expansion seen in $Ce_{0.75}Nb_{0.25}O_{2+\delta}$ made in NaOH (Figure 5. 11b). This suggests that the presence of Na in the structure allows a significantly larger lattice expansion, whilst also helping to stabilise the structure and prevent formation of $CeNbO_4$.

Whilst the *in situ* data suggest that $Ce_{1-x}Nb_xO_{2+\delta}$ made in NH_4OH may readily decompose at elevated temperatures in H_2, the oxides made in NaOH have proven very robust. Despite significant annealing, a second reduction cycle shows a similar lattice expansion, suggesting it is still highly reducible.

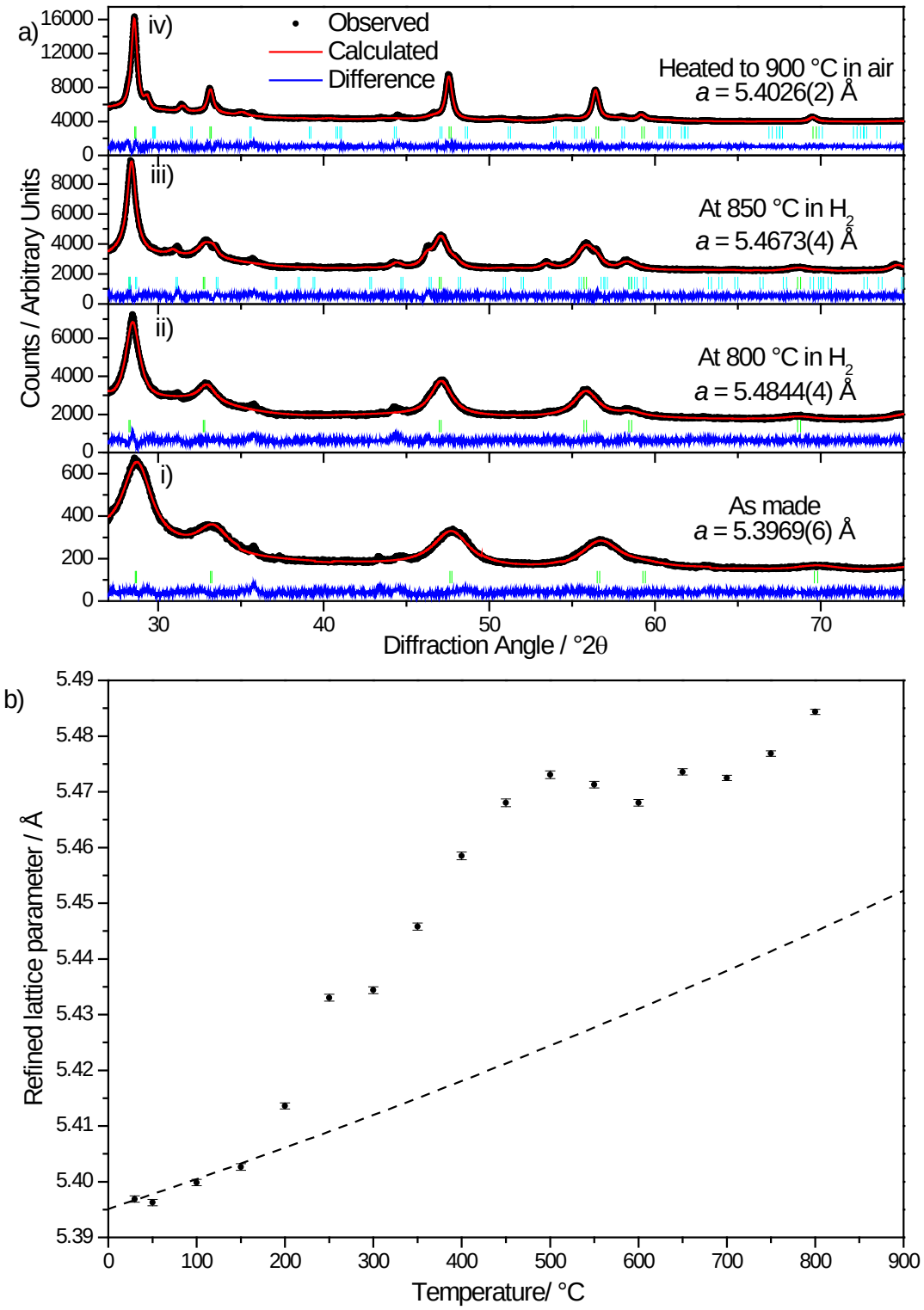

Figure 5. 12a) Le Bail fits to powder XRD patterns of $Ce_{0.75}Nb_{0.25}O_{2+\delta}$ made in NH_4OH i) as made at room temperature, ii) at 800 °C in 5% H_2, iii) at 850 °C in 5% H_2, iv) at room temperature after subsequent heating in air. Green and blue tickmarks show positions of fluorite and tetragonal $CeNbO_4$ peaks, respectively. b) Lattice parameters of the same material from Le Bail fitting of in situ *powder XRD heating in 5% H_2. Dashed line shows calculated thermal expansion of a fluorite, using the thermal expansion coefficient of CeO_2.*

5.3.2.3 Dynamic Oxygen Storage Capacity Measurements

Figure 5. 13 shows the measured CO concentration in the gas stream over one CO 250 s pulse after it has passed over various 0.5 wt% Rh/$Ce_{1-x}Nb_xO_{2+\delta}$ catalysts at temperatures from 150 to 600 °C. The breakthrough times of all oxides increases as temperature increases. CeO_2 made in NaOH or NH_4OH loaded with 0.5 wt% Rh both show little CO oxidation, even at 500 – 600 °C. The inclusion of Nb markedly increases the breakthrough time in $Ce_{1-x}Nb_xO_{2+\delta}$ made in both NaOH and NH_4OH.

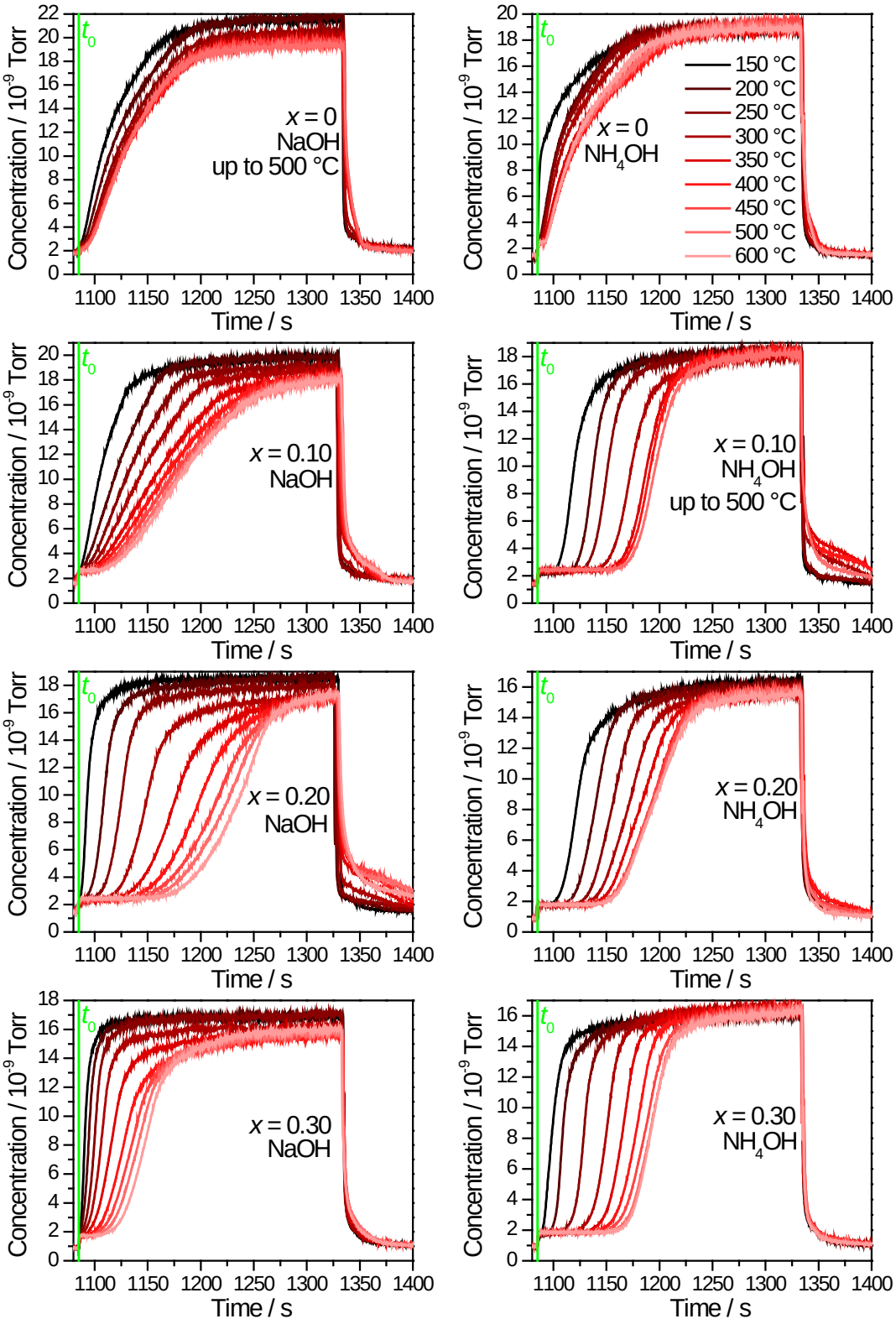

Figure 5. 13 CO concentration measured by mass spectrometry after passing over $Ce_{1-x}Nb_xO_{2+\delta}$ *(x = 0.00 – 0.30) coated with 0.5 wt% Rh by IWI and fired at 500 °C. Data from 150 °C to 600 °C (unless otherwise stated) shown.* CO_2 *and* O_2 *mass spectrometry traces omitted for clarity.*

In addition to the dynamic OSC information provided from the CO breakthrough time, the CO concentration plots also show that $Ce_{1-x}Nb_xO_{2+\delta}$ materials continue releasing oxygen slowly after the CO has begun to break through, by the slower increase in measured CO concentration. This is particularly evident for $Ce_{1-x}Nb_xO_{2+\delta}$ made in NaOH at elevated temperatures, where even after 250 s the CO concentration at 600 °C is not constant.

Compared to $Ce_{1-x}Nb_xO_{2+\delta}$, CeO_2 whether made in NaOH or NH_4OH has a poor dynamic OSC (Figure 5. 14). Neither undoped samples exhibit any OSC below 250 °C and release less than 50 $\mu mol_{[O]}\ g^{-1}$ at 600 °C. The inclusion of Nb into CeO_2 greatly improves the dynamic OSC regardless of whether it is made in NaOH or NH_4OH. Of the $Ce_{1-x}Nb_xO_{2+\delta}$ made in NaOH, $Ce_{0.80}Nb_{0.20}O_{2+\delta}$ has the highest

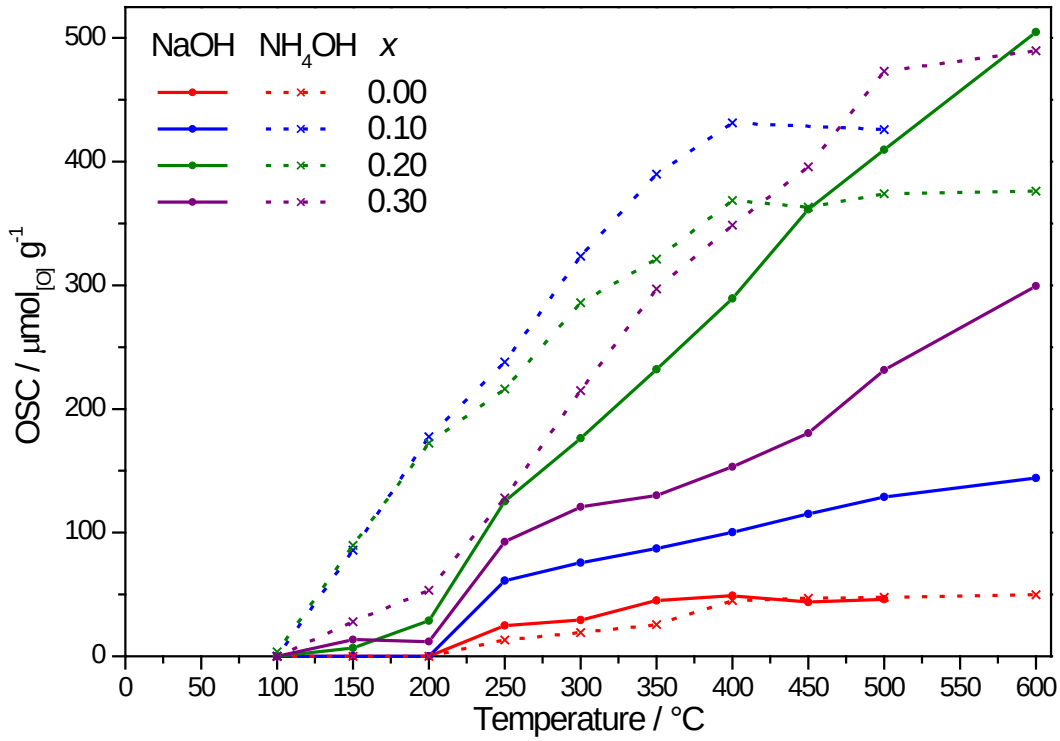

Figure 5. 14 Dynamic OSC per gram as a function of temperature for $Ce_{1-x}Nb_xO_{2+\delta}$ (x = 0, 0.10, 0.20, 0.30, made in either NaOH or NH_4OH) coated with 0.5 wt% Rh. Solid lines show OSC of oxides made in NaOH and dashed lines show OSC of oxides made in NH_4OH.

dynamic OSC of 500 $\mu mol_{[O]}$ g^{-1} at 600 °C. $Ce_{0.80}Nb_{0.20}O_{2+\delta}$ and $Ce_{0.70}Nb_{0.30}O_{2+\delta}$ both start to release oxygen at 150 °C and the amount of oxygen released has not plateaued by 600 °C in either case. $Ce_{0.90}Nb_{0.10}O_{2+\delta}$ made in NaOH has a higher dynamic OSC than CeO_2, though it is considerably worse than $Ce_{0.80}Nb_{0.20}O_{2+\delta}$ or $Ce_{0.70}Nb_{0.30}O_{2+\delta}$.

$Ce_{1-x}Nb_xO_{2+\delta}$ materials (where x = 0.10, 0.20 and 0.30) made in NH_4OH have considerably better dynamic OSC per gram at low temperatures, compared with the same samples made in NaOH. They all begin releasing oxygen at around 150 °C, and between 200 – 400 °C they release significantly more than their counterparts made in NaOH. However, beyond approximately 400 °C the amount of oxygen released remains virtually constant at 350 – 475 $\mu mol_{[O]}$ g^{-1}, suggesting that the Ce-Nb oxides made in NH_4OH reach their maximum dynamic OSC at lower temperature than those made in NaOH.

Table 5. 5 BET surface areas of $Ce_{1-x}Nb_xO_{2+\delta}$ (x = 0 – 0.30) made in NaOH and NH_4OH before and after loading with 0.5 wt% Rh and firing at 500°C.

$Ce_{1-x}Nb_xO_{2+\delta}$		S_{BET} / m^2 g^{-1}	
x	**Base**	As made	Coated with 0.5 wt% Rh and fired at 500 °C
0	**NaOH**	70.3(3)	65.5(3)
0.10	**NaOH**	128.0(6)	99.8(4)
0.20	**NaOH**	183.1(7)	146(1)
0.30	**NaOH**	226.9(8)	134.0(8)
0	**NH_4OH**	131.3(4)	58.4(4)
0.10	**NH_4OH**	145.9(1)	67.6(2)
0.20	**NH_4OH**	107.4(1)	108.7(4)
0.30	**NH_4OH**	167.9(5)	73.4(2)

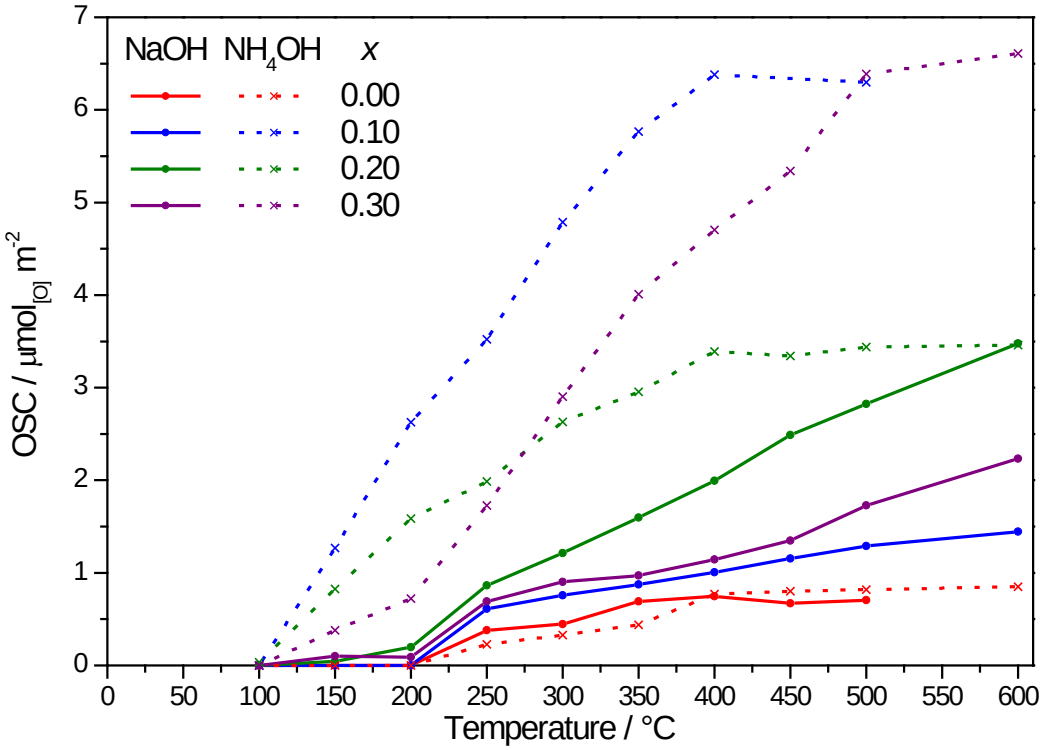

Figure 5. 15 Dynamic OSC per square metre as a function of temperature for $Ce_{1-x}Nb_xO_{2+\delta}$ (x = 0.00, 0.10, 0.20, 0.30, made in either NaOH or NH_4OH) coated with 0.5 wt% Rh. Solid lines show OSC of oxides made in NaOH and dashed lines show OSC of oxides made in NH_4OH.

Since surface oxide is more mobile than oxide in the bulk of CeO_2,[16] particularly when acting as a support for Rh,[16,17] surface area has a crucial role in determining dynamic OSC. Using the BET surface area of all eight $Ce_{1-x}Nb_xO_{2+\delta}$ (with 0.5 wt% Rh supported) after firing at 500 °C (Table 5. 5), the effect of surface area can be normalised (Figure 5. 15). This shows that now the $Ce_{1-x}Nb_xO_{2+\delta}$ made in NaOH all perform similarly. All of the Ce-Nb oxides made in NH_4OH have higher OSC (per m^2) than their NaOH counterparts. When x = 0.10 and 0.30 the OSC is highest, plateauing at 6.3 – 6.6 $\mu mol_{[O]}\ m^{-2}$.

5.3.3 Tantalum-Doped Ceria

5.3.3.1 Temperature-Programmed Reduction

Each TPR profile of $Ce_{1-x}Ta_xO_{2+\delta}$ ($0 \leq x \leq 0.25$) made in NaOH (Figure 5. 16a) shows two peaks in the low temperature domain (≤ 600 °C). Integration of the profiles shows that the low temperature hydrogen consumption per unit mass of the oxides increases with increasing Ta content (Table 5. 6), even as the Ce^{4+} content decreases. This leads to a linear increase in the proportion of Ce^{4+} reduced (Figure 5. 17a). The high temperature domain shows a broad, small hydrogen uptake which has remains approximately constant. $Ce_{0.75}Ta_{0.25}O_{2+\delta}$ has a much larger than expected hydrogen consumption, which leads to almost complete (95%, ±10%) Ce^{4+} reduction by 900 °C, assuming no Ta reduction.

Unlike $Ce_{1-x}Nb_xO_{2+\delta}$ oxides made in NH_4OH, $Ce_{1-x}Ta_xO_{2+\delta}$ oxides show no signs of NH_3 desorption, meaning the TPR profiles (Figure 5. 16b) can be used to quantitatively assess the hydrogen uptake. TPR profiles of $Ce_{1-x}Ta_xO_{2+\delta}$ ($0 \leq x \leq 0.25$) made in NH_4OH show two low temperature peaks, similar to the analogues made in NaOH, and increasing low temperature hydrogen uptake (Table 5. 6), even though the surface area remains approximately constant. The degree of low temperature Ce^{4+} reduction increases linearly with Ta content (Figure 5. 17b) leading to 74% (±7%) Ce^{4+} reduction in $Ce_{0.75}Ta_{0.25}O_{2+\delta}$.

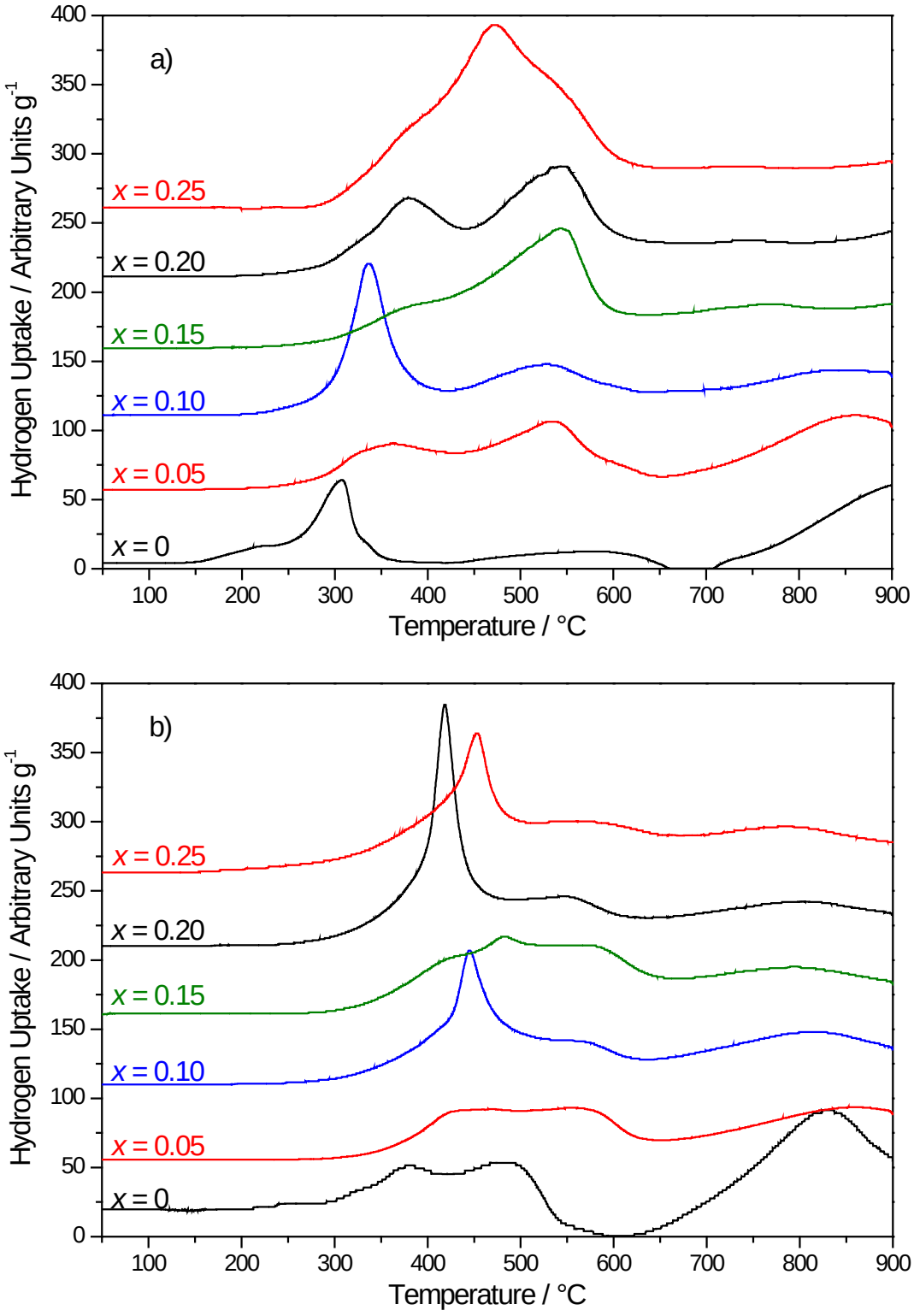

Figure 5. 16 TPR profiles of as prepared $Ce_{1-x}Ta_xO_{2+\delta}$ ($0 \leq x \leq 0.25$) made in a) NaOH and b) NH_4OH. Each profile is offset for clarity.

$Ce_{1-x}Ta_xO_{2+\delta}$		S_{BET} /	H oxidised / mmol g^{-1}			Ce^{4+} reduced / %			$T_{L\,max}$ / °C	$T_{H\,max}$ / °C
x	Base	$m^2\,g^{-1}$	Total	T_L	T_H	Total	T_L	T_H		
0.05	**NaOH**	-	2.35	1.32	1.03	43.2	24.3	18.9	535	855
0.10	**NaOH**	-	2.41	1.55	0.87	47.4	30.5	17.1	335	855
0.15	**NaOH**	-	2.67	1.75	0.93	56.4	36.9	19.6	545	≥ 900
0.20	**NaOH**	-	2.70	1.92	0.77	61.4	43.7	17.5	540	≥ 900
0.25	**NaOH**	-	3.87	2.81	1.07	95.1	69.1	26.3	470	≥ 900
0.05	**NH_4OH**	74.9(2)	2.00	1.03	0.97	36.7	18.9	17.8	450	855
0.10	**NH_4OH**	83.9(2)	2.34	1.34	1.00	46.0	26.4	19.7	445	815
0.15	**NH_4OH**	71.8(1)	2.44	1.56	0.88	51.5	32.9	18.6	480	795
0.20	**NH_4OH**	86.2(2)	2.83	1.74	1.09	64.3	39.6	24.8	420	800
0.25	**NH_4OH**	91.7(2)	2.99	2.07	0.92	73.5	50.9	22.6	450	785

Table 5. 6 BET Surface areas (S_{BET}) and summary of results from TPR of as prepared $Ce_{1-x}Ta_xO_{2+\delta}$ synthesised hydrothermally in NaOH and NH_4OH. T_L *and* T_H *correspond to low and high temperature domains, respectively.* $T_{L\,max}$ *and* $T_{H\,max}$ *are the temperatures at which the low and high temperature domain maxima of H_2 uptake occur, respectively.*

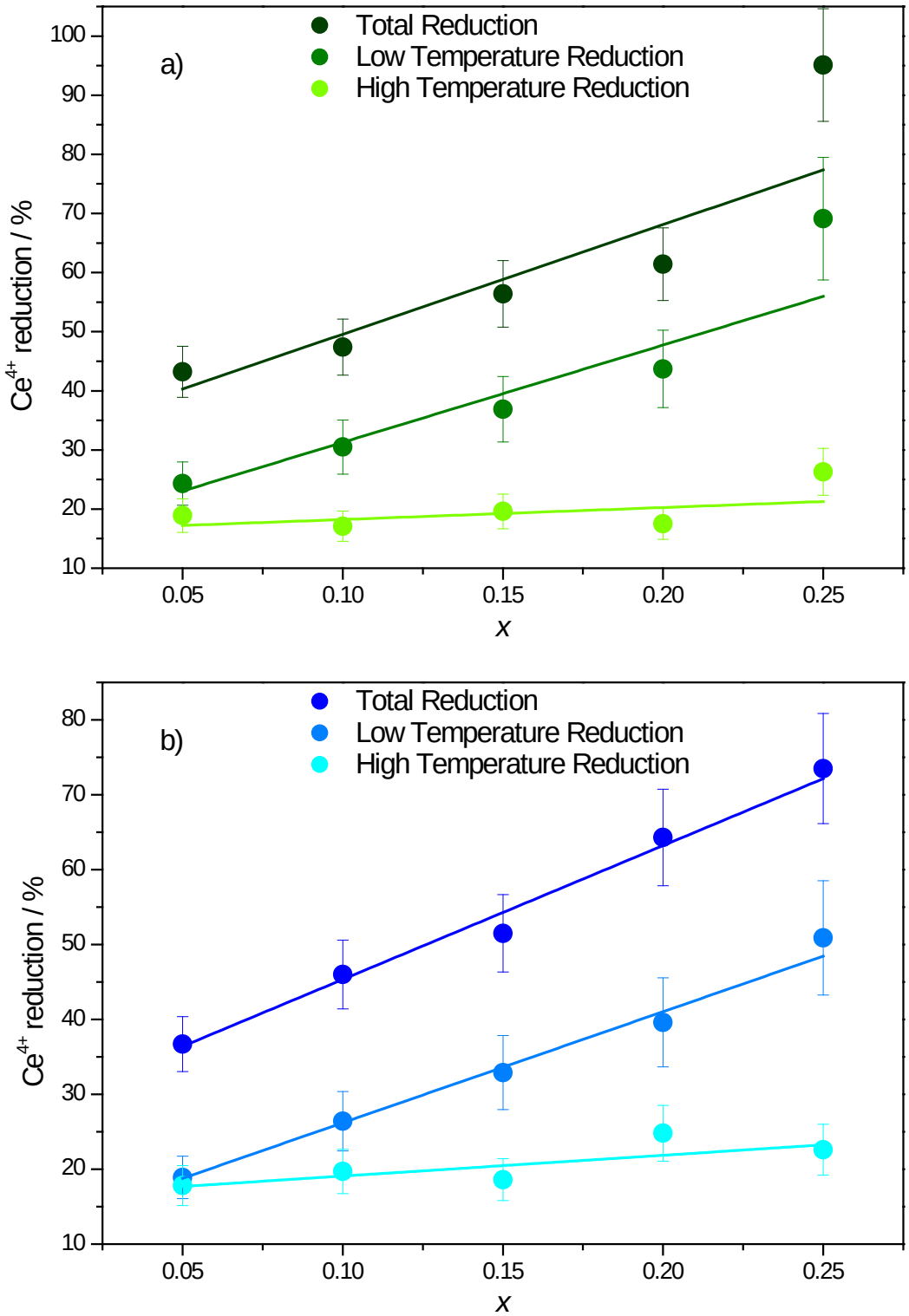

Figure 5. 17 Degree of Ce^{4+} reduction in $Ce_{1-x}Ta_xO_{2+\delta}$ made in a) NaOH and b) NH_4OH; as a function of x.

5.4 Reducibility of Precious Metal-Doped Ceria

5.4.1 Precious metals supported on CeO_2 and $Ce_{1-x}M_xO_{2-\delta}$

A small amount (< 1%) of platinum group metal (PGM) dispersed on the surface of ceria and doped ceria is widely known to greatly enhance the reducibility of ceria at low temperature.[16,18-22] This has been attributed to the catalysis of dissociation of H_2, at the surface of these metals Figure 5. 18. The dissociated H atoms then spill over onto the cerium oxide, where they are oxidised to form H_2O.[1] Figure 5. 19 shows the TPR profile of 5 wt% Pd supported on HSA CeO_2. A massive, sharp H_2 uptake at 85 °C suggests reduction of 40% of the Ce^{4+} present whilst subsequent uptakes at 320 °C and 850 °C are caused by the reduction of a further 25% and 30% of the Ce^{4+} present, leading to almost complete reduction of the CeO_2.

In order to fully exploit this effect in a cost efficient way, both the PGM particles' surface – volume ratio and the PGM – ceria interactions should be maximised. Whilst many preparative techniques can approach atomic PGM dispersion on the surface of supports, strong PGM metal – metal interactions mean that sintering readily occurs at elevated temperatures to give low surface area PGM.[23] A possible solution to this is doping of the PGM into nanocrystalline CeO_2,[24] achieving

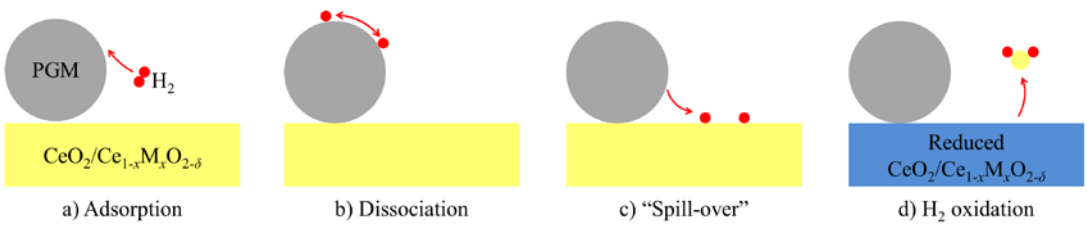

Figure 5. 18 Scheme showing a) the adsorption of a H_2 molecule onto the surface of a PGM particle. b) The dissociation of the H_2 molecule into H atoms. c) The H atoms then move onto the surface of the ceria-based support. d) the H atoms then readily form water on reaction with surface oxide, leaving the ceria-based support reduced. Adapted from Rao et al.[2]

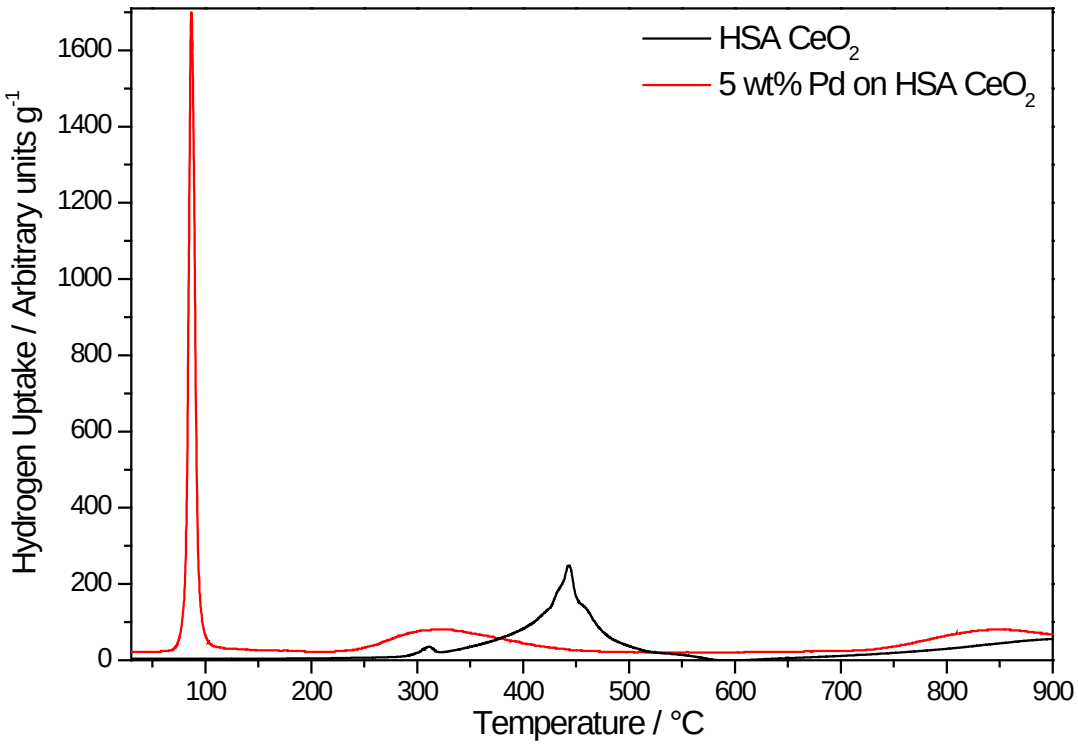

Figure 5. 19 TPR profile of HSA CeO_2 coated with 5 wt% Pd by IWI (donated by Noelia Cortes Felix, JMTC). TPR profile of HSA CeO_2 is also shown for comparison.

complete atomic dispersion and a strong PGM – ceria interaction, whilst being bound in the oxide structure prevents PGM sintering from taking place. In light of this, the catalytic properties of hydrothermally prepared $Ce_{1-x}Pd_xO_{2-\delta}$ and $Ce_{1-x}Pt_xO_{2-\delta}$, where isolated PGM ions are dispersed in the CeO_2 structure (Chapter 4) were investigated.

5.4.2 Palladium-Doped Ceria

5.4.2.1 Temperature-Programmed Reduction

TPR profiles of $Ce_{1-x}Pd_xO_{2-\delta}$ ($0 \leq x \leq 0.30$) up to 300 °C (Figure 5. 20a) show in each case (except $x = 0.30$, where phase separation has occurred) the presence of a large, sharp, low temperature peak, which cannot be solely attributed to the reduction of Pd^{2+} to Pd metal (Table 5. 7). For $Ce_{0.95}Pd_{0.05}O_{2-\delta}$ (~3.1 wt% Pd) this peak is at 172 °C, almost 100 °C higher than in 5 wt% Pd supported on CeO_2 (Figure 5. 19), demonstrating a difference between the two materials. The temperature of the low temperature peak decreases and the amount of hydrogen oxidised increases with increasing x up to $Ce_{0.75}Pd_{0.25}O_{2-\delta}$. Up to $Ce_{0.80}Pd_{0.20}O_{2-\delta}$ the increase in degree of Ce^{4+} reduction is linear (Figure 5. 20b), this may reflect the increasing proportion of Ce in close proximity to Pd^{2+} in the doped oxide which can be easily reduced.

After subtracting the H_2 required to reduce Pd^{2+} to Pd^0, TPR suggests that only approximately 10% of the Ce^{4+} in "$Ce_{0.70}Pd_{0.30}O_{2-\delta}$" is reduced. This material consists of $Ce_{0.70}Pd_{0.30-y}O_{2-\delta}$ and yPdO (detected by powder XRD, Chapter 4) in the

x	T_{PGM} / °C	H oxidised / mmol g^{-1}	Ce^{4+} reduced / %
0.05	172	1.36	13.8
0.10	120	2.23	19.2
0.15	96	3.13	25.3
0.20	73	4.08	32.7
0.25	65	4.37	26.3
0.30	48	4.24	9.5

Table 5. 7 Summary of results from TPR of as prepared $Ce_{1-x}Pd_xO_{2-\delta}$ ($0 \leq x \leq 0.30$). $T_{PGM\ max}$ *is the temperature of the low temperature peak. The extent of* Ce^{4+} *reduction assumes complete* Pd^{2+} *reduction.*

sample as made, and as there is only one (relatively broad) reduction peak in the TPR (at 48 °C), it suggests that the Pd^{2+} in both oxides are simultaneously reduced. The degree of Ce^{4+} reduction in $Ce_{0.75}Pd_{0.25}O_{2-\delta}$ is also lower than expected,

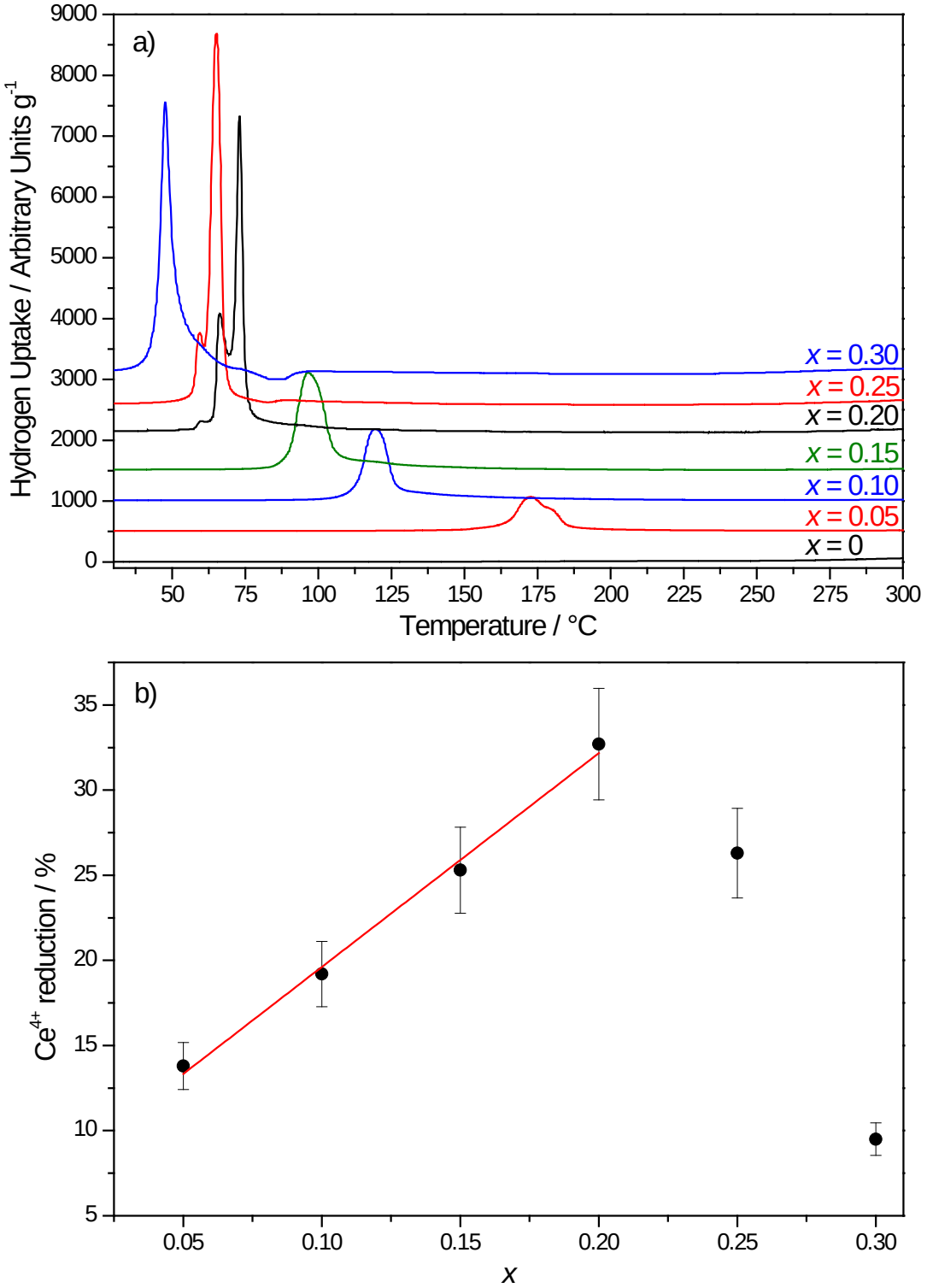

Figure 5. 20a) TPR profiles of as prepared $Ce_{1-x}Pd_xO_{2-\delta}$ ($0 \leq x \leq 0.30$). Each profile is offset for clarity. b) Degree of Ce^{4+} reduction as a function of x *with a line of best fit, $0.05 \leq x \leq 0.20$.*

compared to $Ce_{1-x}Pd_xO_{2-\delta}$ ($x \leq 0.20$), suggesting that very large amounts of Pd lead to less low temperature Ce^{4+} reduction, possibly due to high distortion and a high degree of oxide deficiency already present in the fluorite.

Sequential TPR profiles of $Ce_{0.95}Pd_{0.05}O_{2-\delta}$ with intermediate re-oxidations (by heating in 10% O_2 in He to 700 °C) are shown in Figure 5. 21. Re-oxidation at 300 °C leads to no subsequent reduction. TPRs after re-oxidation (*i.e.* TPRs 2 – 4) show a smaller amount of H oxidised compared to the as made $Ce_{0.95}Pd_{0.05}O_{2-\delta}$ (1.14 – 1.18 versus 1.36; respectively) and the temperature of this peak decreases to 120 – 175 °C. This could be due to the formation of Pd metal, which has been shown to occur in $Ce_{1-x}Pd_xO_{2-\delta}$ under reducing conditions.[25,26]

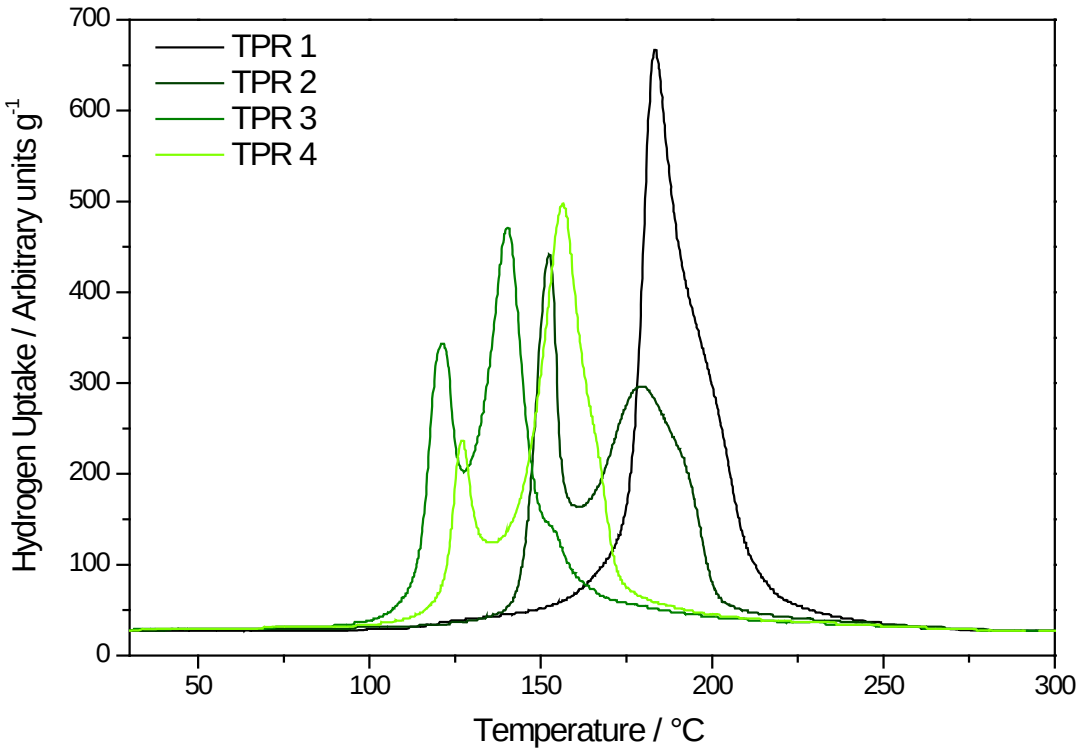

Figure 5. 21 Sequential TPR profiles of $Ce_{0.95}Pd_{0.05}O_{2-\delta}$, with intermediate re-oxidations at 700 °C.

5.4.2.2 *In situ* Powder X-Ray Diffraction

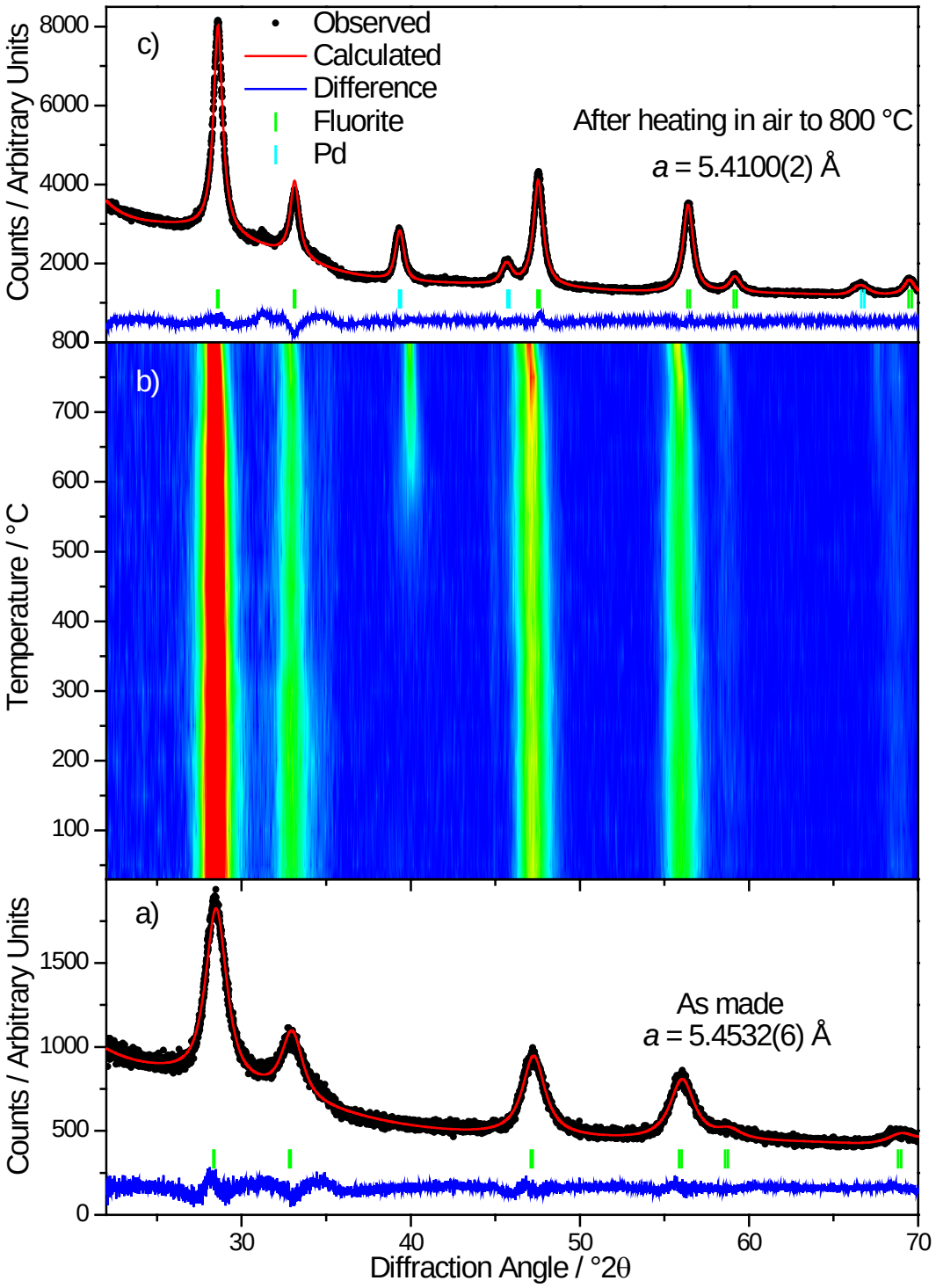

Figure 5. 22a) Le Bail fit to room temperature (30 °C) powder XRD data of $Ce_{0.80}Pd_{0.20}O_{2-\delta}$ as made. b) 2D contour plot of in situ *powder XRD in air up to 800 °C showing $Ce_{0.80}Pd_{0.20}O_{2-\delta}$ phase separating into CeO_2 and Pd metal, beginning at 350 °C. c) Le Bail fit to room temperature (30 °C) powder XRD data of $Ce_{0.80}Pd_{0.20}O_{2-\delta}$ after heating to 800 °C.*

Reflections attributed to Pd metal can be seen by *in situ* powder X-ray diffraction data of $Ce_{0.80}Pd_{0.20}O_{2-\delta}$ in air at temperatures as low as 350 °C (Figure 5. 22), suggesting phase separation at temperatures at or below this temperature. In contrast, Kurnatowska *et al.*[26] and Misch *et al.*[25] report stability up to 700 °C in air of $Ce_{1-x}Pd_xO_{2-\delta}$ ($x \leq 0.30$). The lattice parameter thermal expansion (Figure 5. 23) is significantly smaller (up to 800 °C) than would be expected for a fluorite (Equation 5. 1), and at certain stages decreases slightly, caused by a return to undoped CeO_2. After heating to 800 °C in air and cooling back to room temperature the lattice parameter is 5.4100(2) Å, significantly smaller than in the as made material, and close to the literature value of the lattice parameter of CeO_2 (5.41165 Å, NIST).

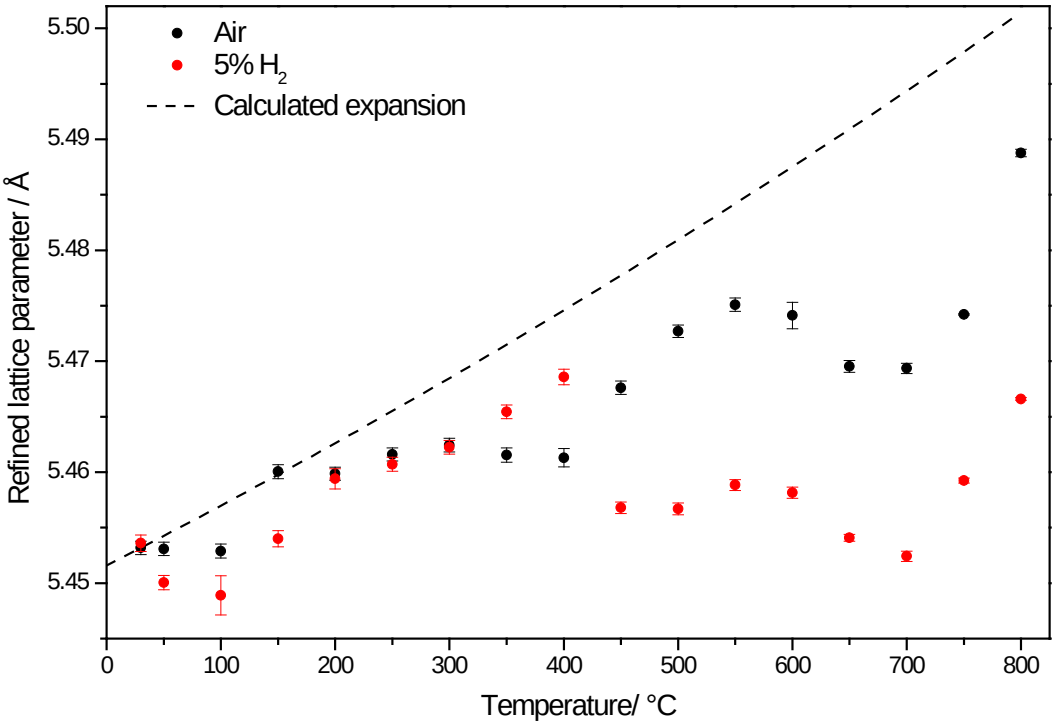

Figure 5. 23 Lattice parameters of $Ce_{0.80}Pd_{0.20}O_{2-\delta}$ from Le Bail fitting of in situ *powder XRD heating in air and 5% H_2 in N_2. Dashed line shows calculated thermal expansion of a fluorite structure, using the thermal expansion coefficient of CeO_2.*

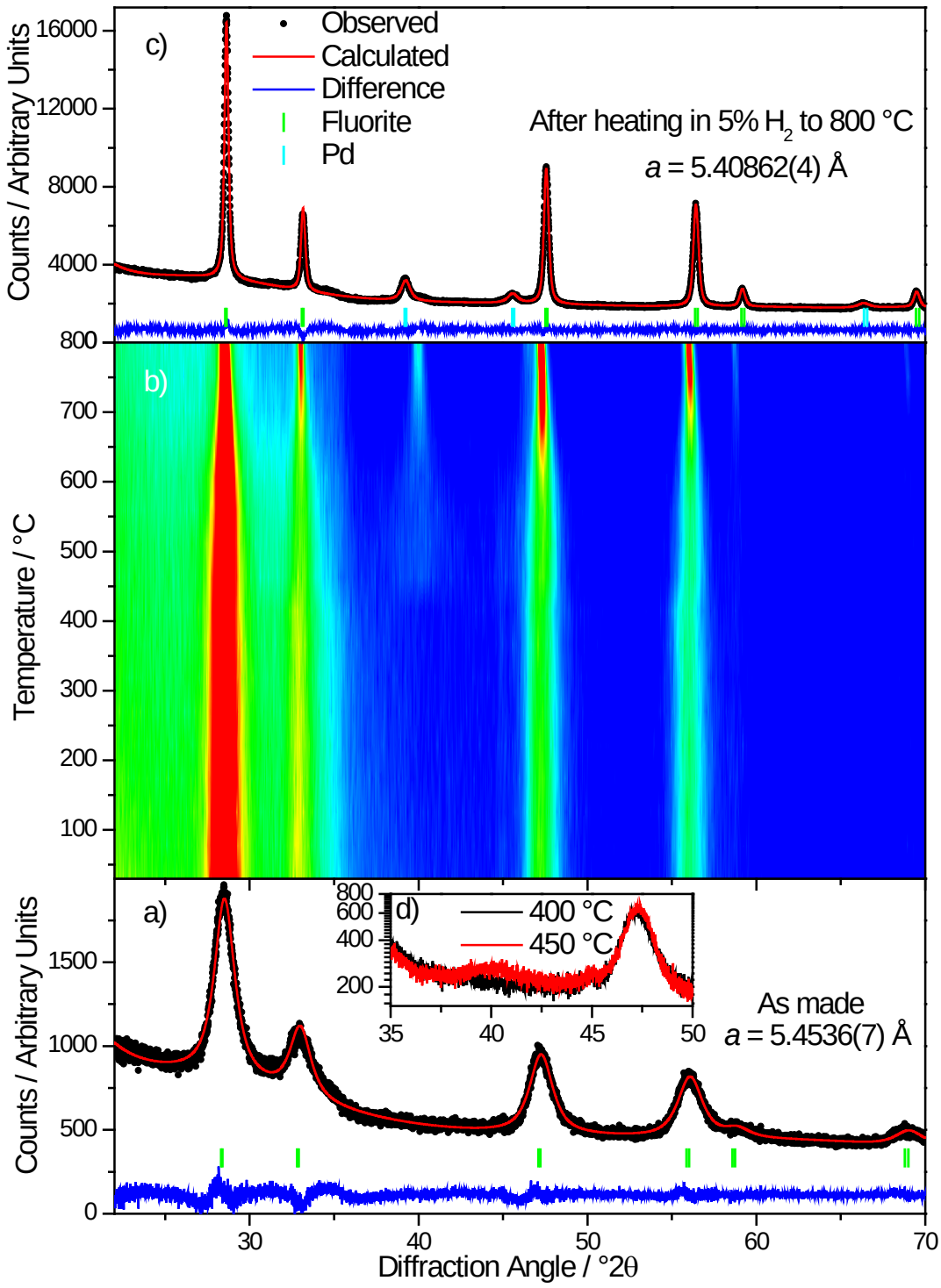

Figure 5. 24a) Le Bail fit to room temperature (30 °C) powder XRD data of $Ce_{0.80}Pd_{0.20}O_{2-\delta}$ *as made. b) 2D contour plot of* in situ *powder XRD in 5%* H_2 *up to 800 °C showing* $Ce_{0.80}Pd_{0.20}O_{2-\delta}$ *phase separating into* CeO_2 *and Pd metal. c) Le Bail fit to room temperature (30 °C) powder XRD data of* $Ce_{0.80}Pd_{0.20}O_{2-\delta}$ *after heating to 800 °C. d) Diffraction patterns before (400 °C) and after (450 °C) Pd metal crystallisation zoomed to show the Pd (111) reflection.*

Surprisingly, *in situ* powder XRD in 5% H_2 in N_2 of the same material does not show Pd diffraction peaks until 450 °C (Figure 5. 24). It is likely that whilst phase separation coincides with the reduction seen in TPR (73 °C), the Pd metal is well dispersed on the CeO_2 surface or is amorphous until 450 °C. It should also be noted that Pd metal readily reacts at atmospheric pressure to give metastable PdH_x ($x < 1$),[10] where H sits in interstitial sites in the Pd lattice. It is difficult to differentiate this from Pd by XRD, particularly at non-ambient temperatures where lattice expansion is an issue.

Despite being heated in H_2, lattice parameters extracted from *in situ* powder XRD suggests very little Ce reduction occurs (Figure 5. 23), since the lattice expansion is smaller in H_2 than in air, and upon cooling to room temperature (whilst still in a H_2 environment) the lattice parameter is 5.40862(4) Å, approximately equal to the literature value of CeO_2.

TEM of $Ce_{0.80}Pd_{0.20}O_{2-\delta}$ before and after heating in H_2 (Figure 5. 25a, d) was collected by Reza J. Kashtiban (Department of Physics, University of Warwick) show the particle size is much larger after heating, from approximately 5 nm in the as made oxide to over 50 nm in diameter after heating. Energy filtered maps of Ce (Figure 5. 25b) and Pd (Figure 5. 25c) concentration in the as made oxide shows in both cases a uniform distribution through the specimen, whilst after heating there are crystallites of high Ce concentration, with the same areas showing little Pd fluorescence; and *vice versa*; demonstrating the separation of the two phases. It can also be seen that the Pd metal particles are significantly larger than the CeO_2 crystallites

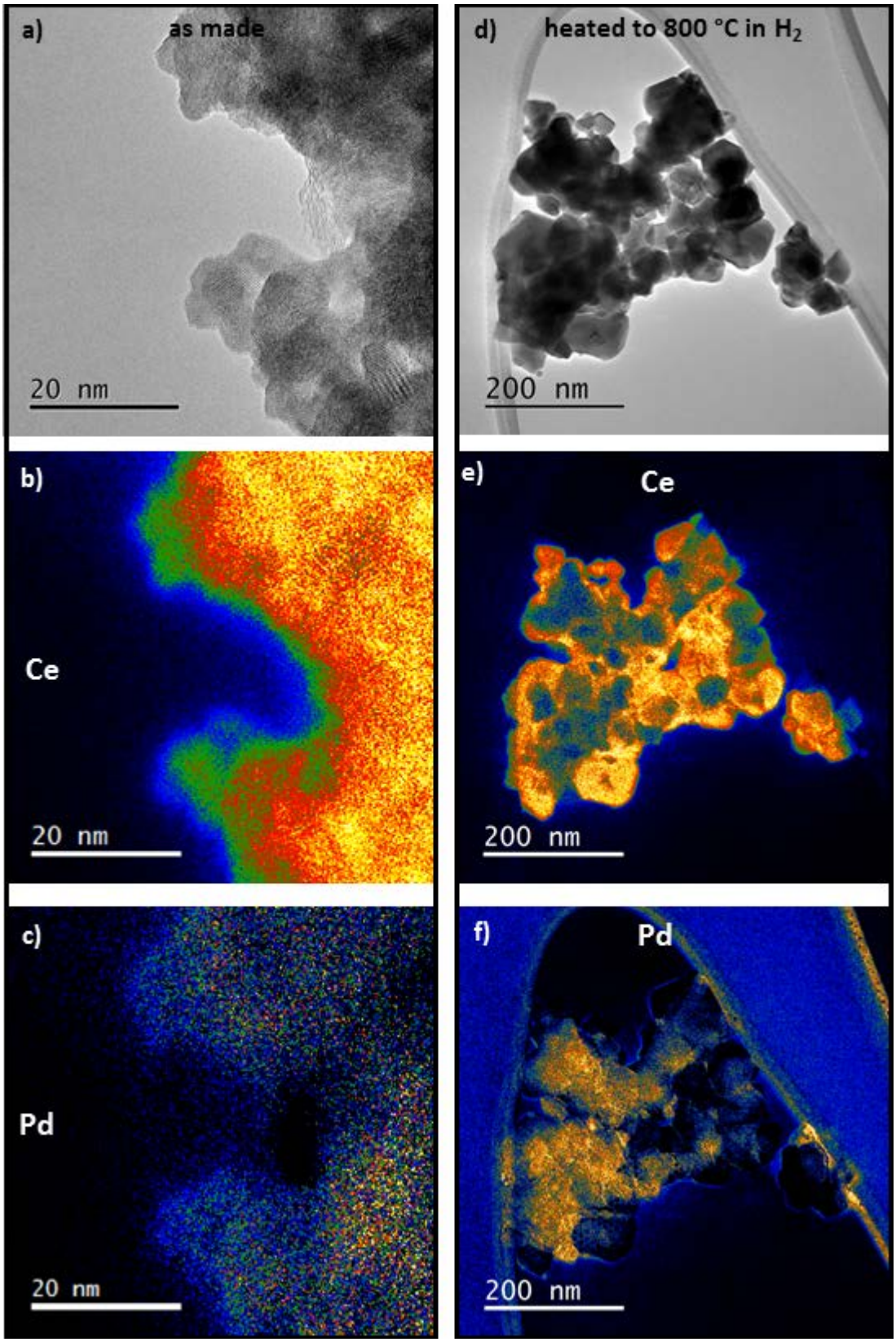

Figure 5. 25 a) Transmission electron micrograph of $Ce_{0.80}Pd_{0.20}O_{2-\delta}$: a) as made b, c) elemental maps of the same area showing concentration of Ce and Pd, respectively. d) after heating in H_2 to 800 °C e, f) elemental maps of the same area showing concentration of Ce and Pd, respectively.

5.4.3 Platinum-Doped Ceria

TPR profiles of $Ce_{1-x}Pt_xO_{2-\delta}$ ($0 \leq x \leq 0.25$) up to 300 °C (Figure 5. 26) show a sharp reduction peak at 120 – 150 °C associated with Pt^{4+} reduction. The temperature of the peak decreases slightly with increasing Pt content and the amount of H_2 oxidised increases, though the amount of Ce^{4+} reduced slowly decreases (Table 5. 8). When $x = 0.25$ the hydrogen consumption suggests that not quite all of the Pt^{4+} has been reduced to Pt metal (~90%), due to the high proportion of Pt^{4+} in the bulk of the CeO_2.

A second TPR (with an intermediate re-oxidation in 5% O_2 in He at 700 °C) of $Ce_{0.95}Pt_{0.05}O_{2-\delta}$ (Figure 5. 27) shows a slightly increased temperature of reduction and a decrease in the amount of hydrogen oxidised (1.52 mmol g^{-1}). This can be explained by Pt metal not being re-oxidised in 5% O_2 at 700 °C.

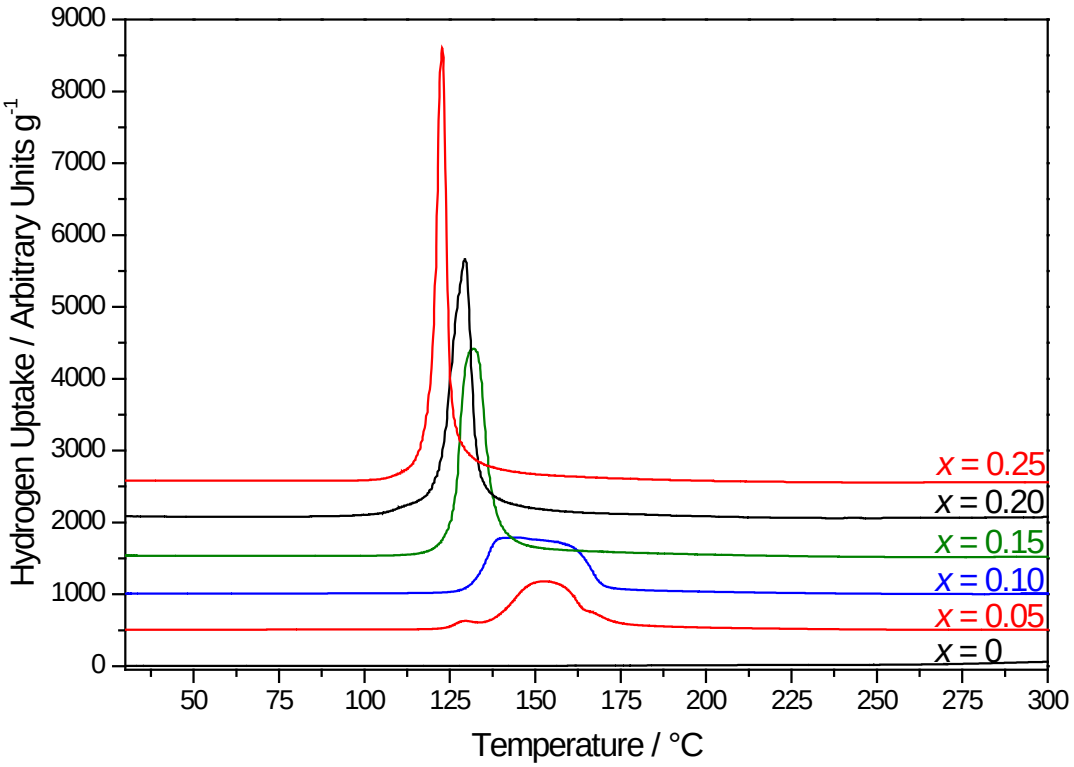

Figure 5. 26 TPR profiles of as prepared $Ce_{1-x}Pt_xO_{2-\delta}$ ($0 \leq x \leq 0.25$). Each profile is offset for clarity.

x	T_{PGM} / °C	H oxidised / mmol g^{-1}	Ce^{4+} reduced / %
0.05	153	2.25	20.4
0.10	149	3.11	16.9
0.15	132	4.13	17.0
0.20	129	4.77	9.2
0.25	122	4.88	0

Table 5. 8 Summary of results from TPR of as prepared $Ce_{1-x}Pt_xO_{2-\delta}$ *(*$0 \leq x \leq 0.30$*).* $T_{PGM\ max}$ *is the temperature of the low temperature peak. The extent of* Ce^{4+} *reduction assumes complete* Pt^{4+} *reduction.*

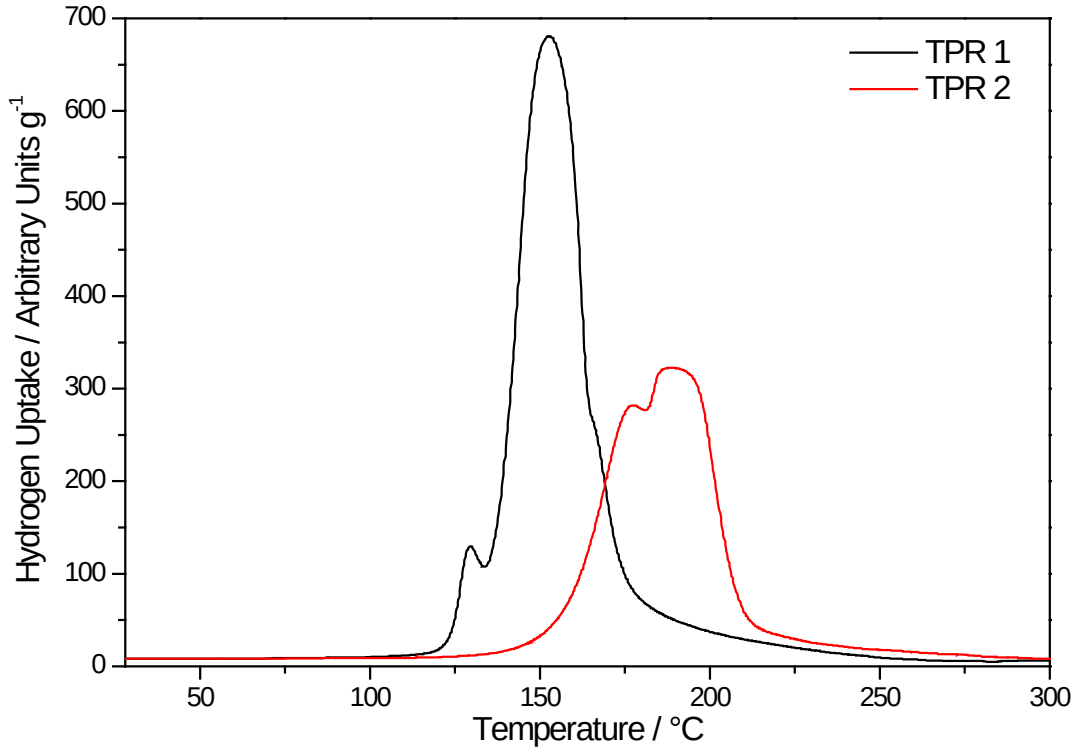

Figure 5. 27 Sequential TPR profiles of $Ce_{0.95}Pt_{0.05}O_{2-\delta}$*, with an intermediate re-oxidation at 700 °C.*

5.5 Conclusions

In this chapter the redox properties of hydrothermally prepared pentavalent ion- and precious metal-doped cerium dioxide have been explored by TPR, *in situ* powder XRD and dynamic oxygen storage capacity measurement.

Whilst fluorite oxides of the form $Ce_{1-x}Sb_xO_{2+\delta}$ can be prepared, TPR of $Ce_{0.95}Sb_{0.05}O_{2+\delta}$ made in both NaOH and NH_4OH shows that Sb^{5+} is reduced at 425 °C causing phase separation to Sb metal and CeO_2, rendering it an unsuitable candidate for catalytic applications and no further testing was carried out.

H_2-TPR shows $Ce_{1-x}Nb_xO_{2+\delta}$ made in NaOH displayed increasing H_2 consumption as a function of *x*, particularly in the low temperature region attributed to surface reduction, which constitutes the majority of the total reduction. This is unlikely to be caused by Nb(V) reduction and therefore is attributed to the reduction of Ce. The increased surface reduction could be correlated to the increase in surface area, as is observed in CeO_2. When $Ce_{1-x}Nb_xO_{2+\delta}$ is prepared using NH_4OH as the base the H_2-TPR profiles are complicated by the desorption of NH_3 which superimposes a negative peak on the profile. Firing in air at 500 °C removes all surface NH_3 and TPR of fired $Ce_{0.70}Nb_{0.30}O_{2+\delta}$ shows it has a large H_2 consumption at low temperature, like the oxides made in NaOH. *In situ* powder XRD of $Ce_{0.75}Nb_{0.25}O_{2+\delta}$ made in NH_4OH suggests that it is unstable in reducing conditions as $CeNbO_4$ is formed. On the other hand, when made in NaOH $Ce_{0.75}Nb_{0.25}O_{2+\delta}$ appears to be stable and remains a single, fluorite phase after several cycles heating in both reducing and oxidising environments. Furthermore, dynamic OSC measurements of $Ce_{1-x}Nb_xO_{2+\delta}$ prepared hydrothermally and loaded with 0.5 wt% Rh show that the presence of Nb and Na significantly improve the reducibility of Ce^{4+}, compared to

CeO_2. TPR profiles of $Ce_{1-x}Ta_xO_{2+\delta}$ show similar reduction behaviour to $Ce_{1-x}Nb_xO_{2+\delta}$, though profiles of oxides made using NH_4OH show no sign of NH_3 desorption.

TPR profiles of $Ce_{1-x}PGM_xO_{2-\delta}$ (PGM = Pt, Pd) show low temperature hydrogen oxidation peaks common of precious metal containing cerium oxides. The temperature of this oxidation decreases with increasing *x*, as does the amount of hydrogen oxidised, though this can mainly be attributed to reduction of the precious metal and the degree of Ce^{4+} reduction increases very little, or indeed decreases. *In situ* powder XRD and TEM before and after reduction of $Ce_{0.80}Pd_{0.20}O_{2-\delta}$ show separation into CeO_2 and large crystallites of Pd metal.

Future work includes *in situ* XAFS or XANES under simulated TPR conditions of the pentavalent ion-doped ceria in order to determine if the pentavalent ion itself is reduced, and a more detailed study of the dynamic oxygen storage properties of these oxides.

5.6 Summary

In chapters 3, 4 and 5 the synthesis, structure, stability and redox properties of several substituted cerium(IV) oxides has been presented.

For the first time substantial amounts of pentavalent ions Sb^{5+}, Nb^{5+} and Ta^{5+} have been shown to be incorporated into the cerium dioxide fluorite structure by hydrothermal synthesis. Based on elemental analysis, lattice parameters, Raman spectroscopy and X-ray absorption spectroscopy it was shown that the co-substitution of Na (when present in the hydrothermal reaction solution) is the mechanism by which this occurs. The existing theory by which pentavalent incorporation would occur (Ce^{3+} formation) has been disproven by Ce L_{III}-edge XANES. Neutron PDF analysis of $Ce_{1-x}Nb_xO_{2+\delta}$ made in NaOH is underway in order to determine the local environment of the Nb^{5+} in the structure. However, it is unclear how this substitution occurs when NH_4OH is used instead of NaOH in the hydrothermal synthesis. The possible explanations for this are the presence of NH_4^+ or H^+ in the structure, or the presence of excess oxide in the structure. ^1H NMR and analysis of neutron PDF data of $Ce_{1-x}Nb_xO_{2+\delta}$ made in NH_4OH are ongoing in order to both determine which of these models is more plausible and how the Nb^{5+} is coordinated within the structure. The $Ce_{1-x}Sb_xO_{2+\delta}$ with even small amounts of Sb^{5+} were found to be unstable upon heating in both air and dilute H_2, separating into Sb metal and CeO_2. $Ce_{1-x}Nb_xO_{2+\delta}$ made in NH_4OH shows good oxygen storage capacity and reducibility, though *in situ* XRD suggests that $CeNbO_4$ is irreversibly formed in reducing conditions, meaning that they have limited cycling capability. However, $Ce_{1-x}Nb_xO_{2+\delta}$ made in NaOH was shown to be stable after repeatedly being heated to 800 °C in both reducing and oxidising environments, and also exhibits excellent oxygen storage capacity.

In addition, the incorporation of Pd^{2+} and Pt^{4+} into the CeO_2 fluorite has been demonstrated by hydrothermal synthesis for the first time. Pt-substituted CeO_2 has previously only been reported up to 10% Pt substitution, though by a hydrothermal route $Ce_{1-x}Pt_xO_{2-\delta}$ ($0 \leq x \leq 0.30$) was prepared. A decrease in lattice parameter of the fluorite was observed, consistent with the smaller ionic radius of octahedral Pt^{4+}. Pt L_{III}-edge X-ray absorption spectroscopy confirmed that the Pt exists in the +4 oxidation state, and that the Pt ions exist in an octahedral environment. $Ce_{1-x}Pd_xO_{2-\delta}$ ($0 \leq x \leq 0.25$) was hydrothermally prepared as a single fluorite phase. A similar degree of Pd incorporation was prepared by a sol-gel technique,[26] though high temperature methods have only succeeded in obtaining values of x up to 0.10.[25] For the first time Pd K-edge EXAFS has shown that the Pd exists in a square planar environment within the fluorite cell. At high levels of Pd substitution, Pd was found to be present as an impurity, suggesting that the limit of substitution is around 15%. Upon heating in either air or hydrogen Pd metal was extruded at low temperatures, suggesting that the oxides are unstable.

5.7 References

(1) Ranga Rao, G. *Bull. Mater. Sci.* **1999**, *22*, 89.
(2) Ranga Rao, G.; Mishra, B. G. *Bull. Catal. Soc. India* **2003**, *2*, 122.
(3) Perrichon, V.; Laachir, A.; Bergeret, G.; Frety, R.; Tournayan, L.; Touret, O. *J. Chem. Soc., Faraday Trans.* **1994**, *90*, 773.
(4) Giordano, F.; Trovarelli, A.; de Leitenburg, C.; Giona, M. *J. Catal.* **2000**, *193*, 273.
(5) Wright, C. S.; Walton, R. I.; Thompsett, D.; Fisher, J.; Ashbrook, S. E. *Adv. Mater.* **2007**, *19*, 4500.
(6) Di Monte, R.; Kaspar, J. *J. Mater. Chem.* **2005**, *15*, 633.
(7) Boaro, M.; de Leitenburg, C.; Dolcetti, G.; Trovarelli, A. *J. Catal.* **2000**, *193*, 338.
(8) Descorme, C.; Taha, R.; Mouaddib-Moral, N.; Duprez, D. *Appl. Catal., A* **2002**, *223*, 287.
(9) Meiqing, S.; Xinquan, W.; Yuan, A.; Duan, W.; Minwei, Z.; Jun, W. *J. Rare Earth.* **2007**, *25*, 48.
(10) Greenwood, N. N.; Earnshaw, A. *Chemistry of the Elements*; 2nd ed.; Butterworth–Heinemann, 1997.
(11) Sardar, K.; Playford, H. Y.; Darton, R. J.; Barney, E. R.; Hannon, A. C.; Tompsett, D.; Fisher, J.; Kashtiban, R. J.; Sloan, J.; Ramos, S.; Cibin, G.; Walton, R. I. *Chem. Mater.* **2010**, *22*, 6191.
(12) Balducci, G.; Fornasiero, P.; Di Monte, R.; Kaspar, J.; Meriani, S.; Graziani, M. *Catal. Lett.* **1995**, *33*, 193.
(13) Shannon, R. D. *Acta Crystallogr. Sect. A* **1976**, *32*, 751.
(14) Taylor, D. *Trans. J. Brit. Ceram. Soc.* **1984**, *83*, 32.
(15) Ricken, M.; Nölting, J.; Riess, I. *J. Solid State Chem.* **1984**, *54*, 89.
(16) Martin, D.; Duprez, D. *J. Phys. Chem.* **1996**, *100*, 9429.
(17) Song, W.; Popa, C.; Jansen, A. P. J.; Hensen, E. J. M. *J. Phys. Chem. C* **2012**, *116*, 22904.
(18) Barrabés, N.; Föttinger, K.; Dafinov, A.; Medina, F.; Rupprechter, G.; Llorca, J.; Sueiras, J. E. *Appl. Catal., B* **2009**, *87*, 84.
(19) Di Monte, R.; Kaspar, J. *Top. Catal.* **2004**, *28*, 47.
(20) Fornasiero, P.; Di Monte, R.; Rao, G. R.; Kaspar, J.; Meriani, S.; Trovarelli, A.; Graziani, M. *J. Catal.* **1995**, *151*, 168.
(21) Kaspar, J.; Fornasiero, P.; Graziani, M. *Catal. Today* **1999**, *50*, 285.
(22) Liu, Y.; Hayakawa, T.; Ishii, T.; Kumagai, M.; Yasuda, H.; Suzuki, K.; Hamakawa, S.; Murata, K. *Appl. Catal., A* **2001**, *210*, 301.
(23) Hegde, M. S.; Madras, G.; Patil, K. C. *Acc. Chem. Res.* **2009**, *42*, 704.
(24) Kurzman, J. A.; Misch, L. M.; Seshadri, R. *Dalton Trans.* **2013**, *42*, 14653.
(25) Misch, L. M.; Kurzman, J. A.; Derk, A. R.; Kim, Y.-I.; Seshadri, R.; Metiu, H.; McFarland, E. W.; Stucky, G. D. *Chem. Mater.* **2011**, *23*, 5432.
(26) Kurnatowska, M.; Kepinski, L.; Mista, W. *Appl. Catal., B* **2012**, *117–118*, 135.

Chapter 6: Hydrothermal Synthesis and Characterisation of New Ruthenium(V) Oxides

6.1 Introduction

Though a range of alkaline earth metal – ruthenium oxides have been prepared, the majority of these contain Ru with an oxidation state of +4 (see Chapter 1). Ruthenium(V)-containing oxides commonly contain Ba – such as $Ba_5Ru_3O_{12}$[1] and $Ba_5Ru_2O_{11}$.[2] – This has been ascribed to the high electropositivity of Ba, which forces electron density onto oxygen leading to high levels of covalency in the Ru – O bonds.[3] This inductive effect is said to stabilise Ru in its higher oxidation states of +5 and even +6.[4]

Ruthenium oxides are of great interest for a variety of applications. They are considered candidates for electrocatalysts for the oxygen evolution reaction (OER),[5-7] and for heterogeneous methane oxidation.[8] However, the majority of research in this area has focused on Ru(IV) containing oxides, such as the rutile RuO_2[9] or the perovskites $ARuO_3$ (A = Ca, Sr, Ba).[10] Furthermore, the diverse and unusual magnetic properties of complex ruthenium oxides have been widely explored, and they show distinct differences to the oxides of the first row transition metals. For example, Sr_2RuO_4 is a rare example of a Cu-free high temperature superconductor[11] whilst $SrRuO_3$ is a ferromagnetic metallic conductor.[12,13]

Despite the wide range of alkaline earth ruthenates already in the literature (Chapter 1), reports of hydrothermal preparation of ruthenium oxides are very limited. Low temperature hydrothermal synthesis has been used to prepare the pyrochlore phases $(Na_{0.33}Ce_{0.67})Ru_2O_7$[14] and $M_2Ru_2O_7$ (M = Pr, Sm, Eu, Gd, Tb, Dy, Ho),[15] all of which contain Ru(IV). Renard *et al.*[16,17] and the group of Sato[18-20] have had success in preparing several new ruthenates by high temperature, high pressure ($T \geq 500$ °C, $P \geq 150$ MPa) hydrothermal synthesis, which often contain ruthenium with an

average oxidation state > 4. Of particular interest is the pyrochlore $Ca_2Ru_2O_7$ which contains Ru in the +5 oxidation state[18] and exhibits spin-glass behaviour.[21] Since the open nature of the pyrochlore structure leads to high oxide conductivity, and the lack of research into electrocatalysis using Ru(V), a low temperature route to preparing the alkaline earth ruthenium oxide pyrochlores was investigated with a view to testing their electrocatalytic properties. This led to the discovery of several new phases which are described in this chapter.

6.2 $Ca_{1.5}Ru_2O_7$

6.2.1 Synthesis

In a typical synthesis, $KRuO_4$ (1 mmol, Alfa Aesar, 98%) and CaO_2 (1 mmol, Sigma; 75%, remainder $Ca(OH)_2$) were added to 10 ml distilled water with stirring. The mixture was sealed in a 23 ml Teflon-lined steel autoclave and heated to 200 °C for 24 hours in a preheated fan oven. The autoclave was then cooled and the resulting precipitate was recovered by suction filtration. Washing at this stage with dilute HCl was necessary in order to remove a $Ca(OH)_2$ impurity.

Addition of excess CaO_2 did not change the composition of the pyrochlore, but instead led to formation of more $Ca(OH)_2$. Longer reactions (up to 1 month) did not yield any other crystalline phases, and the crystal morphology (size and shape) was unaffected. Reducing the reaction temperature to 125 °C causes a large proportion of ruthenium to stay in solution, as evidenced by the orange colour of the filtrate, but the solid product was $Ca_{1.5}Ru_2O_7$, albeit in a reduced yield. If the ruthenium source was changed to hydrated $RuCl_3$ then the product was less crystalline and contaminated with RuO_2.

6.2.2 Powder X-Ray Diffraction

High resolution powder XRD data (Figure 6. 1) could be indexed to a cubic pyrochlore phase, space group $Fd\bar{3}m$, a = 10.21367(9) Å, slightly larger than the lattice parameter reported for $Ca_2Ru_2O_7$ (a = 10.197 Å), the pyrochlore previously synthesised by high temperature hydrothermal synthesis.[18] The pyrochlore structure (Figure 6. 2) can be viewed as a tetrahedral three-dimensional network of corner-sharing RuO_6 octahedra with an interpenetrating network of anti-cristobalite A_2O channels.[22]

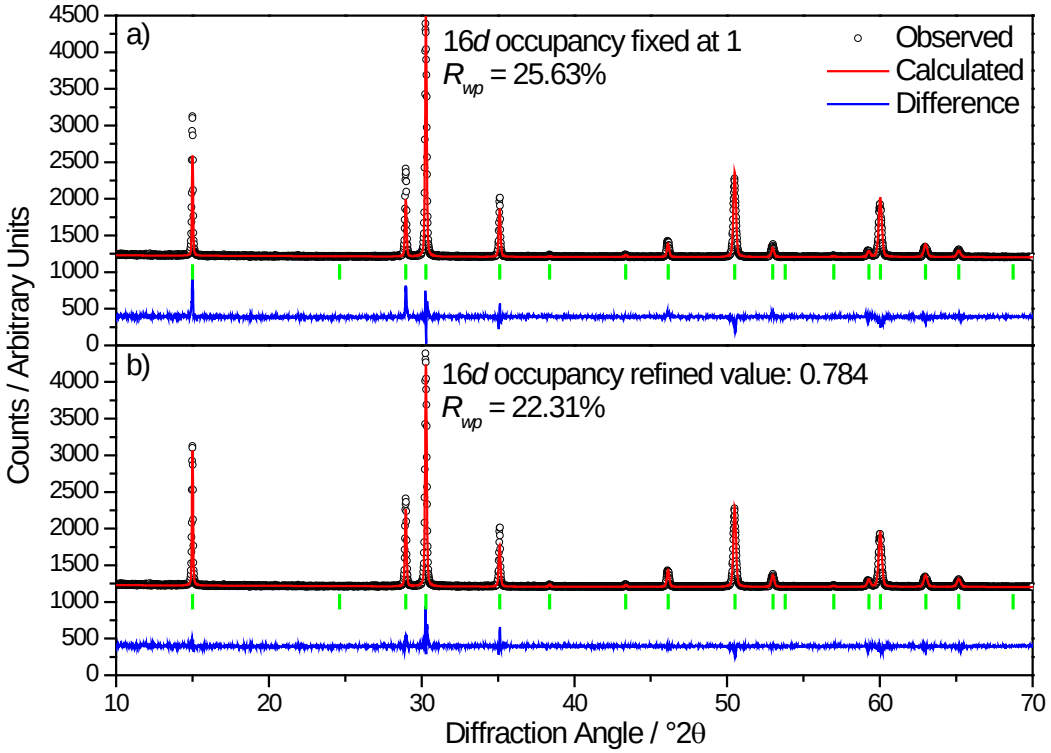

*Figure 6. 1 Rietveld refinements of structure of a Ca – Ru pyrochlore to high resolution powder XRD (λ = 1.5406 Å). a) with all occupancies fixed at 1 and ADPs fixed to a sensible value. b) the same fit with Ca occupancy on the 16*d *site allowed to refine.*

The powder XRD gives no indication of any other phases, and no appreciable Scherrer broadening, indicating a large crystallite size. A Rietveld refinement with occupancies fixed at 1 to give the stoichiometric pyrochlore $Ca_2Ru_2O_7$ yields an

unsatisfactory fit (Figure 6. 1a). However, allowing the occupancy of the Ca 16*d* site to refine causes it to decrease to 0.784 and the *R*-factor improves, from 25.6% to 22.3% (Table 6. 1). Upon allowing the occupancy of the other atoms to refine, their deviation from 1 is < 2% and the improvement to the *R*-factor is negligible.

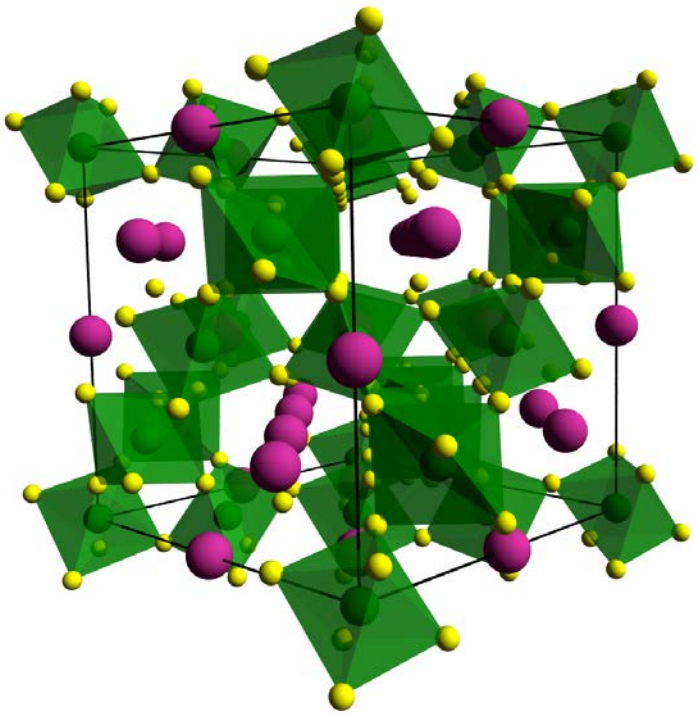

Figure 6. 2 The structure of $Ca_{1.5}Ru_2O_7$ pyrochlore. Corner-sharing RuO_6 octahedra (green) form a tetrahedral network, with channels of Ca (purple, 75% occupied) and O atoms (yellow).

Table 6. 1 Refined atomic coordinates and atomic displacement parameters (ADP) of $Ca_{1.5}Ru_2O_7$ to high resolution powder XRD data; Space group $Fd\bar{3}m$; a = *10.21367(9) Å;* χ^2 *= 2.0;* R_{wp} *= 22.3%;* R_p *= 15.3%.*

Atom	Wyckoff	*x*	*y*	*z*	Occupancy	ADP / Å^2
Ca	16*d*	0.5	0.5	0.5	0.787(5)	0.0025
Ru	16*c*	0	0	0	1	0.0025
O1	48*c*	0.32061(8)	0.125	0.125	1	0.0025
O2	8*b*	0.375	0.375	0.375	1	0.0025

Although the sample was being rotated, the possibility of textural effects (*i.e.* preferred orientation) cannot be excluded, and so the reduced occupancy of the Ca site cannot be confirmed by powder XRD alone. In addition the possibility of A-site water or a small oxygen defect cannot be tested using XRD, which is dominated by diffraction by the metal atoms. This will be explored further when the neutron diffraction results are described later (Section 6.2.4)

6.2.3 Further Characterisation

ICP-OES elemental analysis (Table 6. 2) suggests a Ca:Ru ratio of 0.83(4):1, confirming a significant deviation from the $A_2B_2O_7$ composition of the stoichiometric pyrochlore. Assuming that the remainder of the mass is oxide and that there is no Ru deficiency gives an empirical formula of $Ca_{1.66(8)}Ru_2O_{7.8(2)}$. This slight excess of oxide can be explained by surface water to give $Ca_{1.66(8)}Ru_2O_7 \cdot 0.8(2)H_2O$. Elemental analysis also confirms the absence of K in the solid, which is present in the hydrothermal reaction (from the $KRuO_4$ precursor).

Table 6. 2 Measured metal content by mass in the calcium ruthenate pyrochlore and elemental ratios.

Metal	Measured Metal Content / mass %	Atomic Ratio
Ru	51.5(3)	1
Ca	16.8(3)	0.83(4)
K	< 10 ppm	N/A

Scanning electron microscopy (SEM, Figure 6. 3) shows the material is composed of agglomerated, faceted octahedral crystallites, whilst EDX spectroscopy gives a similar metal ratio to that found by ICP-OES and over a range of areas shows no sign of compositional inhomogeneity.

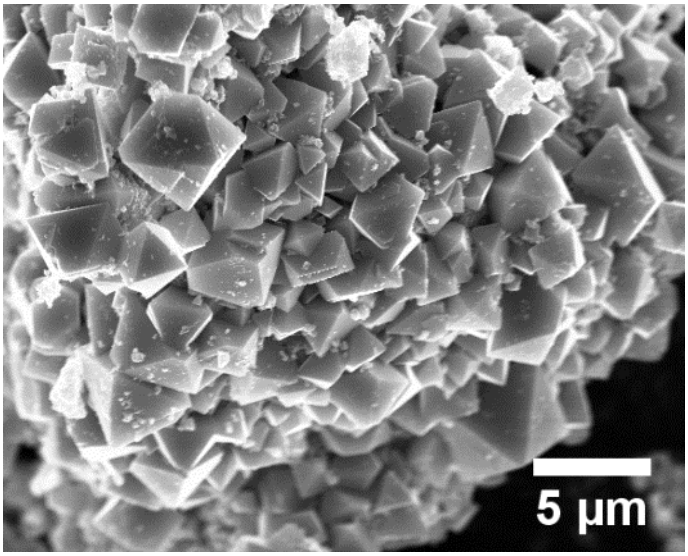

Figure 6. 3 SEM micrograph of $Ca_{1.5}Ru_2O_7$ octahedral crystals.

In situ powder XRD upon heating in air up to 900 °C (Figure 6. 4a) shows phase separation into a new pyrochlore (based on peak intensities) and RuO_2 at around 300 °C. Structural refinements using these *in situ* XRD data reveal that an increase in the *A*-site occupancy to 1 coincides with the appearance of RuO_2 (Figure 6. 4b, Table 6. 3), suggesting that the stoichiometric pyrochlore, $Ca_2Ru_2O_7$, forms by ejecting RuO_2 at around 300 °C. This is consistent with reports of preparation of the non-deficient pyrochlore by high-temperature, high-pressure hydrothermal synthesis.[18,21] Further heating eventually causes the collapse of this stoichiometric pyrochlore into the perovskite $CaRuO_3$ (space group *Pnma*) at round 750 °C.

Table 6. 3 Refined structural parameters of the Ca – Ru pyrochlore and phase ratios (in formula units) at selected temperatures using in situ *powder XRD, λ = Cu $K\alpha_{1,2}$ (1.5418 Å). N/R = not refined.*

***T* / °C**	O1 *x*	Ca Occupancy	*a* / Å	Pyrochlore:RuO_2	Perovskite:RuO_2
30	0.3258(2)	0.810(2)	10.21494(9)	N/R	N/R
550	0.3238(2)	1.025(2)	10.24789(5)	1.946(8)	N/R
900	N/R	N/R	N/R	N/R	3.82(3)

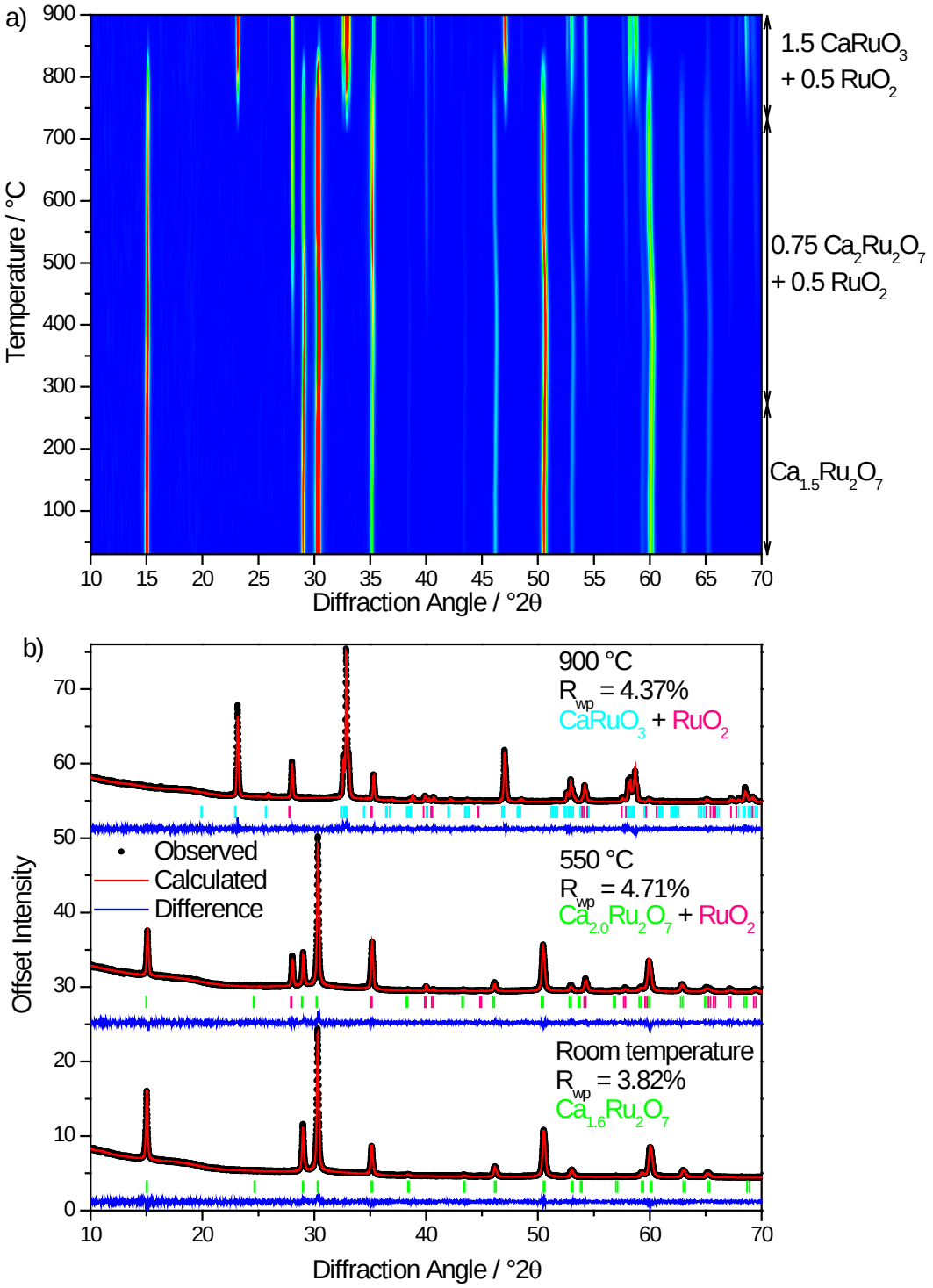

Figure 6. 4a) Contour plot of in situ *powder XRD patterns of* $Ca_{1.5}Ru_2O_7$*, with phase(s) present indicated on the right. b) Rietveld refinements of three representative* in situ *heating powder XRD patterns showing the thermal decomposition to* RuO_2 *and* $CaRuO_3$*. Thermal displacements parameters were fixed to values obtained from room temperature powder neutron diffraction experiments. The only site occupancy refined was that of the pyrochlore A-site.*

Infrared spectroscopy (Figure 6. 5a) shows no absorbance in the O – H stretching region (3200 – 3600 cm^{-1}), which would suggest little surface water and no structural hydroxide. However, thermogravimetric analysis (TGA, Figure 6. 5b) shows that the oxide begins to lose mass as soon as heating begins. At 1000 °C 9.7% mass loss has occurred, consistent with the mass of oxygen lost by the transformation to $CaRuO_3$ and RuO_2 (expected to be 6.4%), plus a small amount of surface water.

Ru K-edge XANES (Figure 6. 6a) was used to estimate the oxidation state of the Ru in the pyrochlore. The Ru edge position has been shown to have a linear relationship to oxidation state over the range +3 to +5.[23,24] By comparing the Ru edge position with that of reference compounds (see Chapter 2 for preparation details) with known Ru valence allows the Ru oxidation state to be estimated at +5.4 (Figure 6. 6b), in line with the composition proposed.

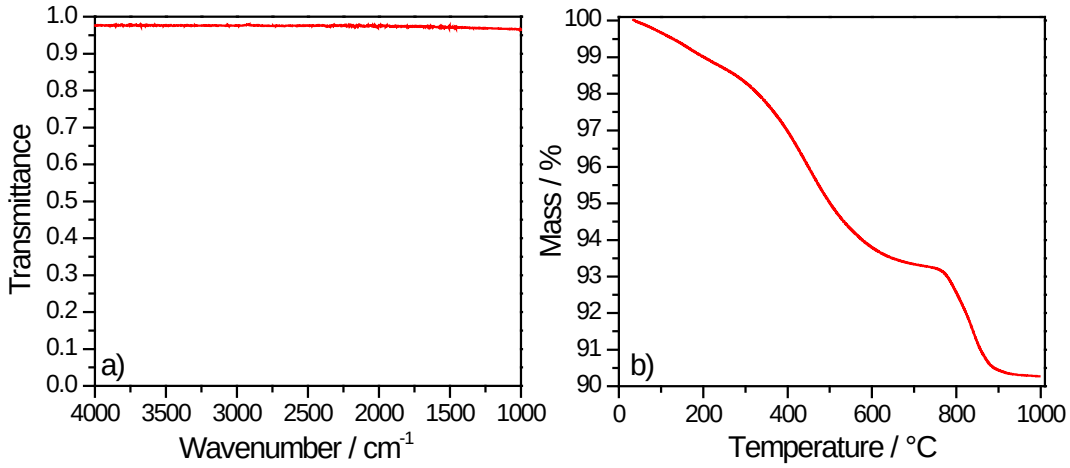

Figure 6. 5a) IR spectrum and b) TGA plot of $Ca_{1.5}Ru_2O_7$.

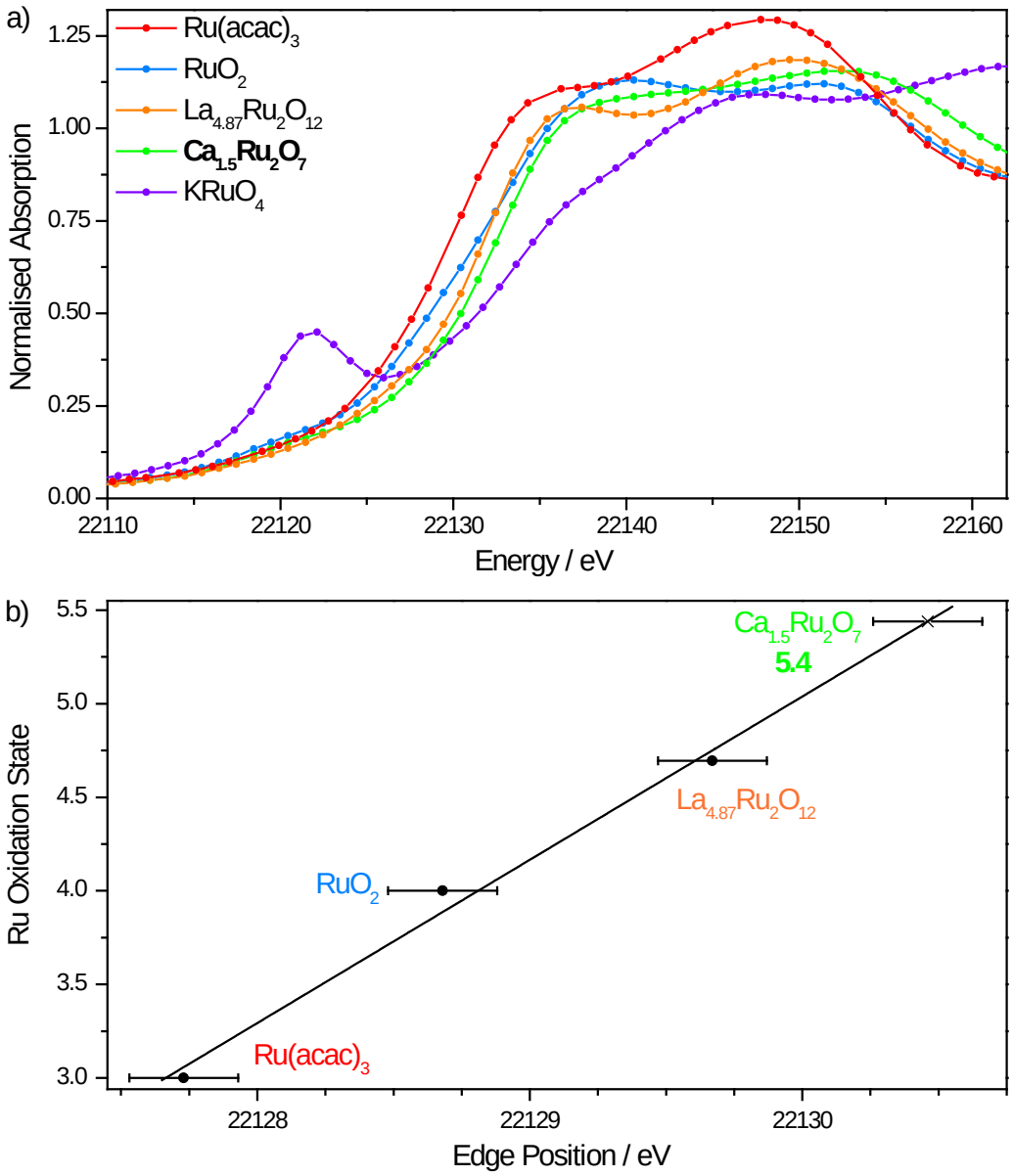

*Figure 6. 6a) Normalised Ru K-edge XANES spectra of $Ca_{1.5}Ru_2O_7$ and reference compounds with known Ru oxidation state ($[Ru^{III}(acac)_3]$, $Ru^{IV}O_2$, $La_{4.87}Ru^{4.7}{}_2O_{12}$ and $KRu^{VII}O_4$). b) A plot of edge position (defined as energy at which normalised absorption = 0.5) as a function of oxidation state, with a linear fit of reference compounds, which is used to estimate the Ru oxidation state in the pyrochlore. $KRuO_4$ is omitted as a reference due to the pre-edge 1*s-4d *feature at 22121 eV.*

6.2.4 Time-of-Flight Powder Neutron Diffraction

A Rietveld structural refinement of the *A*-site deficient calcium ruthenate pyrochlore was carried out using powder neutron diffraction data collected on GEM (ISIS, U.K.), Banks 3 and 5 (Figure 6. 7). The refined structure, Table 6. 4, gives good fits to the banks of data (R_{wp} = 2.20%, R_p = 2.15%), though there some discrepancy in the intensity of the (111) reflection (Bank 3, 16.2 ms). However, allowing the occupancies of all atoms to refine does not cause significant deviation from the given

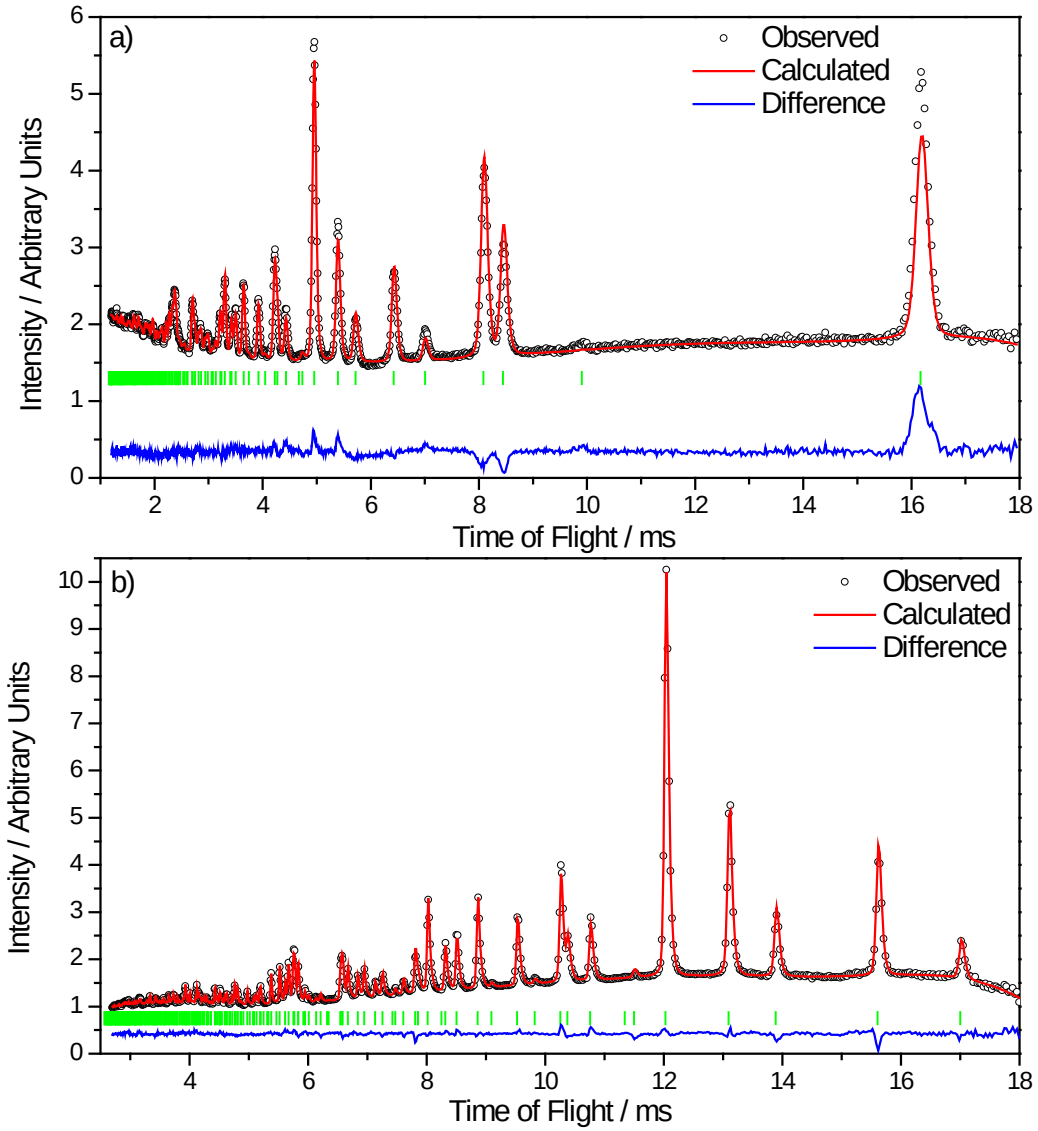

Figure 6. 7 Rietveld refinements of $Ca_{1.5}Ru_2O_7$ to room temperature powder neutron diffraction data. Tick marks denote positions of space group $Fd\bar{3}m$, a = *10.1997(1) Å. a) GEM Bank 3 (mean scattering angle 2θ = 34.96°), b) GEM Bank 5 (mean scattering angle 2θ = 94.30°).*

values, and gives only a slight improvement to the fit. A Fourier difference map was examined, and there was no sign of any structural hydrogen or oxygens in fluorite sites. This suggests that in order to achieve charge balance the Ru must have a mixed (V,VI) oxidation state. Using the Ru – O bond distance from this structure (1.94158(1) Å) allows the average Ru valence to be estimated using the bond valence sum equation:[25]

$$V_i = \sum_j e^{(R_{ij} - d_{ij})/0.37}$$

Equation 6. 1 Bond valence sum equation, where V_i *is the valence of an atom,* R_{ij} *is the bond valence parameter, a value derived empirically by analysis of bond lengths of compounds with well characterised atom valences and* d_{ij} *is the distance between atoms* i *and* j.

A bond valence parameter of 1.888 for Ru(V) in oxides, derived by Dussarrat *et al.*,[1] was used to give an estimated Ru oxidation state of +5.19. This oxidation state is close to the expected oxidation state of +5.5 in the chemical formula $Ca_{1.5}Ru_2O_7$, and the value obtained by Ru K-edge XANES.

Table 6. 4 Refined atomic coordinates and atomic displacement parameters (ADP) of $Ca_{1.5}Ru_2O_7$ *to neutron time of flight diffraction data (GEM banks 3 and 5); Space group* $Fd\bar{3}m$; a = *10.1997(1) Å;* χ^2 *= 5.2;* R_{wp} *= 2.20% (2.44% and 2.14% for respective banks);* R_p *= 2.15% (2.45% and 1.72% for respective banks).*

Atom	Wyckoff	*x*	*y*	*z*	Occupancy	ADP / Å^2
Ca	16*d*	0.5	0.5	0.5	0.75	0.0098(2)
Ru	16*c*	0	0	0	1	0.0106(5)
O1	48*c*	0.32061(8)	0.125	0.125	1	0.0129(1)
O2	8*b*	0.375	0.375	0.375	1	0.0209(6)

6.2.5 Magnetic Susceptibility Studies

Above 25 K the field cooled (FC) susceptibility, χ, of $Ca_{1.5}Ru_2O_7$ (Figure 6. 8a) can be fitted to a Curie-Weiss function with an added temperature independent term, χ_0:

$$\chi = \frac{C}{T - \theta} + \chi_0$$

Equation 6. 2 The Curie-Weiss law, where C *is the Curie constant,* T *is temperature and* θ *is the Weiss temperature.*

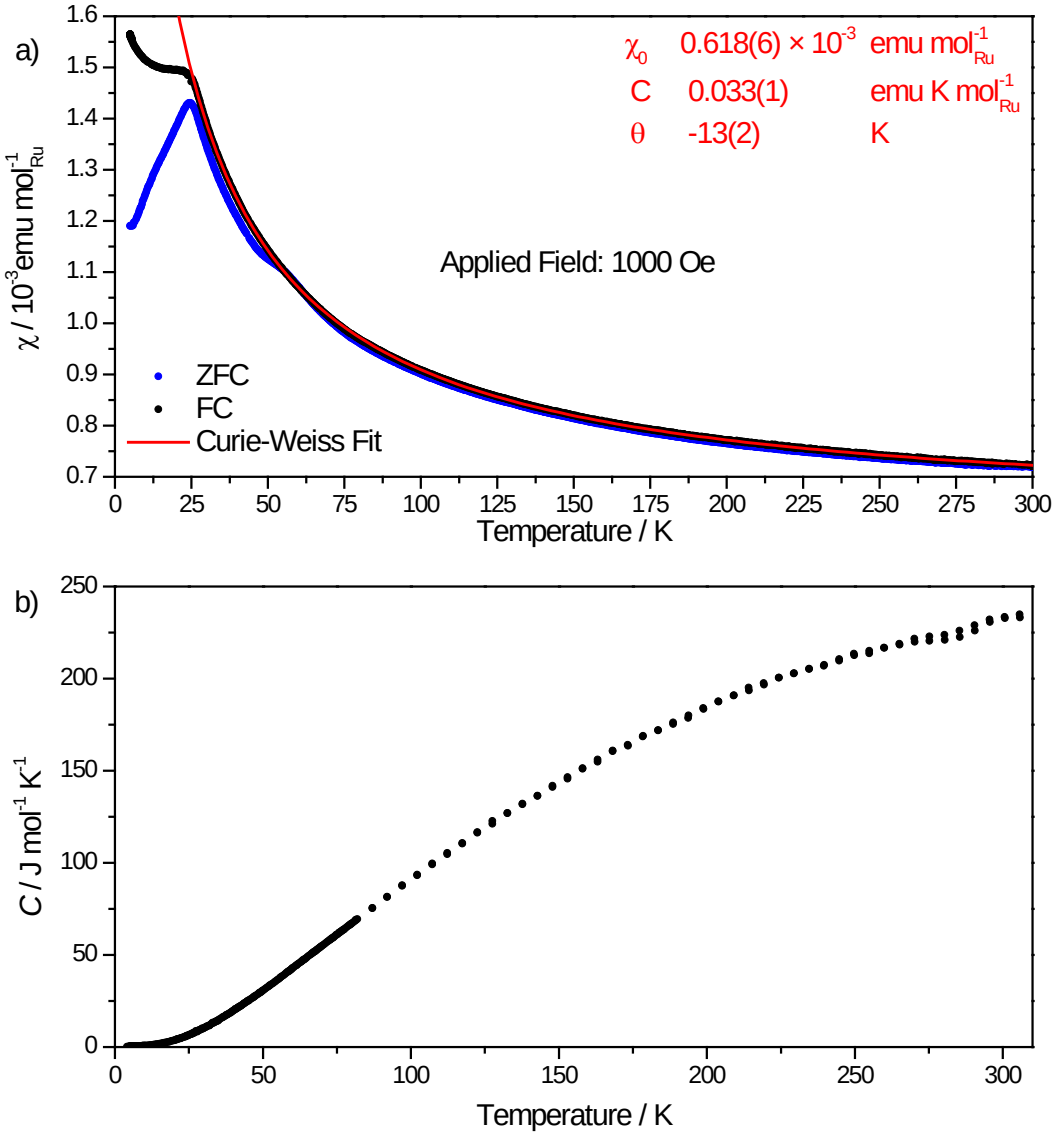

Figure 6. 8a) Field-cooled (FC) and zero field-cooled (ZFC) magnetic susceptibility as a function of temperature of $Ca_{1.5}Ru_2O_7$, with a Curie-Weiss-type fit to the FC data. b) Heat capacity measurement from 2 – 300 K of $Ca_{1.5}Ru_2O_7$, demonstrating the absence of any ordering transition. Two points were recorded at each temperature.

This fit yields a Weiss temperature of -13(2) K, indicative of antiferromagnetic correlations. The effective magnetic moment per Ru, μ_{eff}, can be calculated from the derived Curie constant using Curie's Law:

$$\mu_{\text{eff}}{}^2 = \frac{3k_{\text{B}}C}{N_{\text{A}}\mu_{\text{B}}{}^2}$$

Equation 6. 3. Curie's Law, where μ_B *is the Bohr magneton,* k_B *is the Boltzmann constant and* N_A *is Avagadro's constant.*

This gives a μ_{eff} of 0.36 μ_{B}, identical to the value reported for the pyrochlore $Ca_2Ru_2O_7$,[18] but an order of magnitude smaller than the spin only value for d^3 or d^2 ions, 3.87 and 2.83 μ_{B}, respectively. This is explored further in the Discussion (Section 6.6).

Below 25 K the FC susceptibility deviates from the Curie-Weiss law, becoming almost constant. Zero-field cooled (ZFC) susceptibility displays a sharp cusp at 25 K, deviating from both the Curie-Weiss law and the FC data. This is indicative of magnetic frustration of antiferromagnetic moments,[21] whereby some spins are unable to align with all their neighbours due to the crystal symmetry. This is a feature of magnetic pyrochlores,[26] where the tetrahedral network of *B*-site magnetic metal ions will always show frustration (Figure 6. 9).

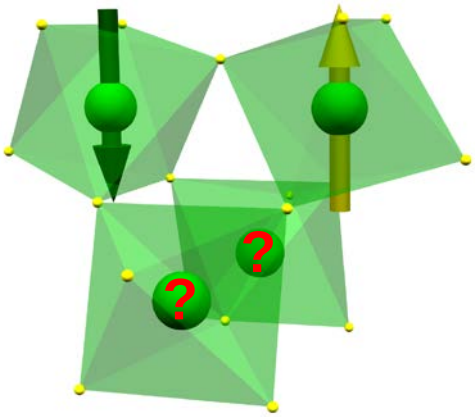

Figure 6. 9 The tetrahedral B-*site lattice of the pyrochlore structure. If two magnetic ions in a tetrahedron align antiferromagnetically it is impossible for the remaining two ions to minimise their interaction energy with all neighbours.*

The ZFC data also show an additional anomaly at 53 K, corresponding to the onset of hysteresis between the FC and ZFC data, indicative of possible spin glass behaviour. Heat capacity measurement (Figure 6. 8b) shows no anomalies over these temperatures, suggesting no magnetic ordering transition occurs.

6.3 $SrRu_2O_6$

6.3.1 Synthesis

In a typical synthesis, $KRuO_4$ (1 mmol, Alfa Aesar, 98%) and SrO_2 (0.5 mmol, Sigma; 98%) were added to 10 ml distilled water with stirring. The mixture was sealed in a 23 ml Teflon-lined steel autoclave and heated to 200 °C for 24 hours in a preheated fan oven. The autoclave was then cooled and the resulting precipitate was recovered by suction filtration. Washing at this stage with dilute HCl was necessary in order to remove a $Sr(OH)_2$ impurity.

Addition of excess SrO_2 did not change the composition of the oxide, but instead led to formation of more $Sr(OH)_2$. Longer reactions (up to 1 month) did not yield any

other crystalline phases, and the crystal morphology (size and shape) was unaffected. Reducing the reaction temperature to 125 °C causes a large proportion of ruthenium to stay in solution, as evidenced by the orange colour of the filtrate and the solid product was $SrRuO_4 \cdot H_2O$.

6.3.2 Powder X-ray Diffraction

The room temperature powder XRD pattern (Figure 6. 10) consists of reflections which can all be indexed to a primitive hexagonal unit cell, analogous to that of the $PbSb_2O_6$-type structure[27,28] (space group $P\bar{3}1m$, a = 5.20573(3) Å, c = 5.23454(7) Å). This structure consists of layers of edge-sharing RuO_6 octahedra interlayed with Sr^{2+} ions (Figure 6. 11). There was no indication of any other phases, and no appreciable Scherrer broadening, indicating a large crystallite size.

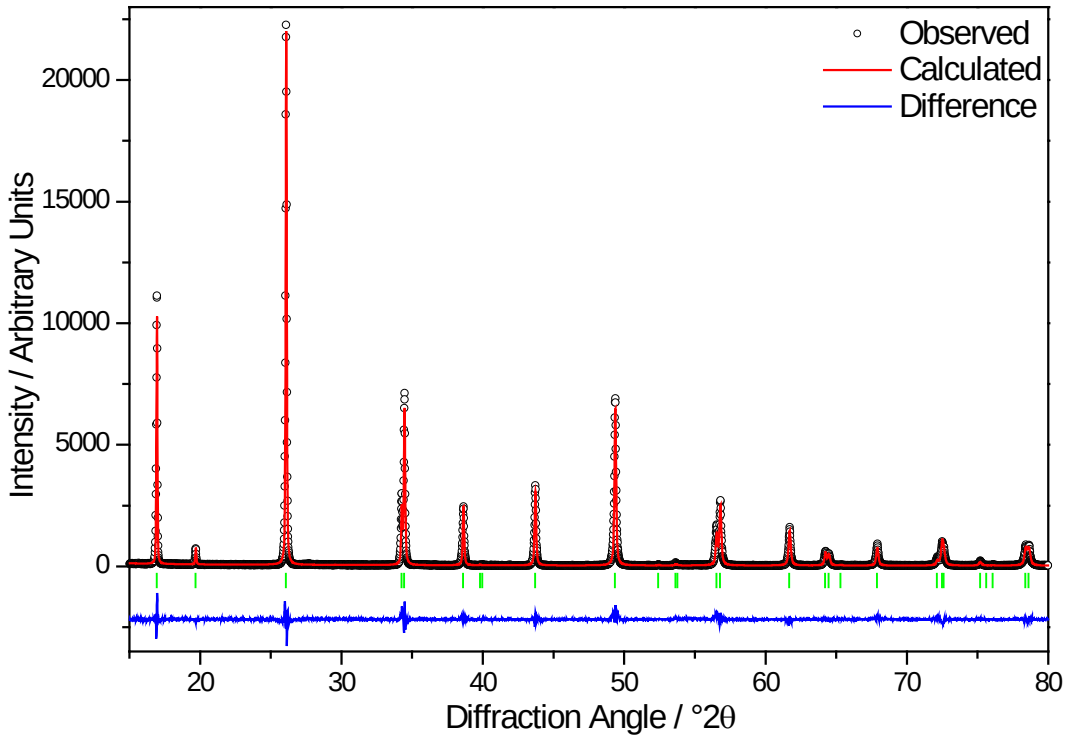

Figure 6. 10 Le Bail fit to high resolution powder XRD (λ = 1.5406 Å), space group P$\bar{3}$1m, a = *5.20573(3) Å,* c = *5.23454(7) Å.*

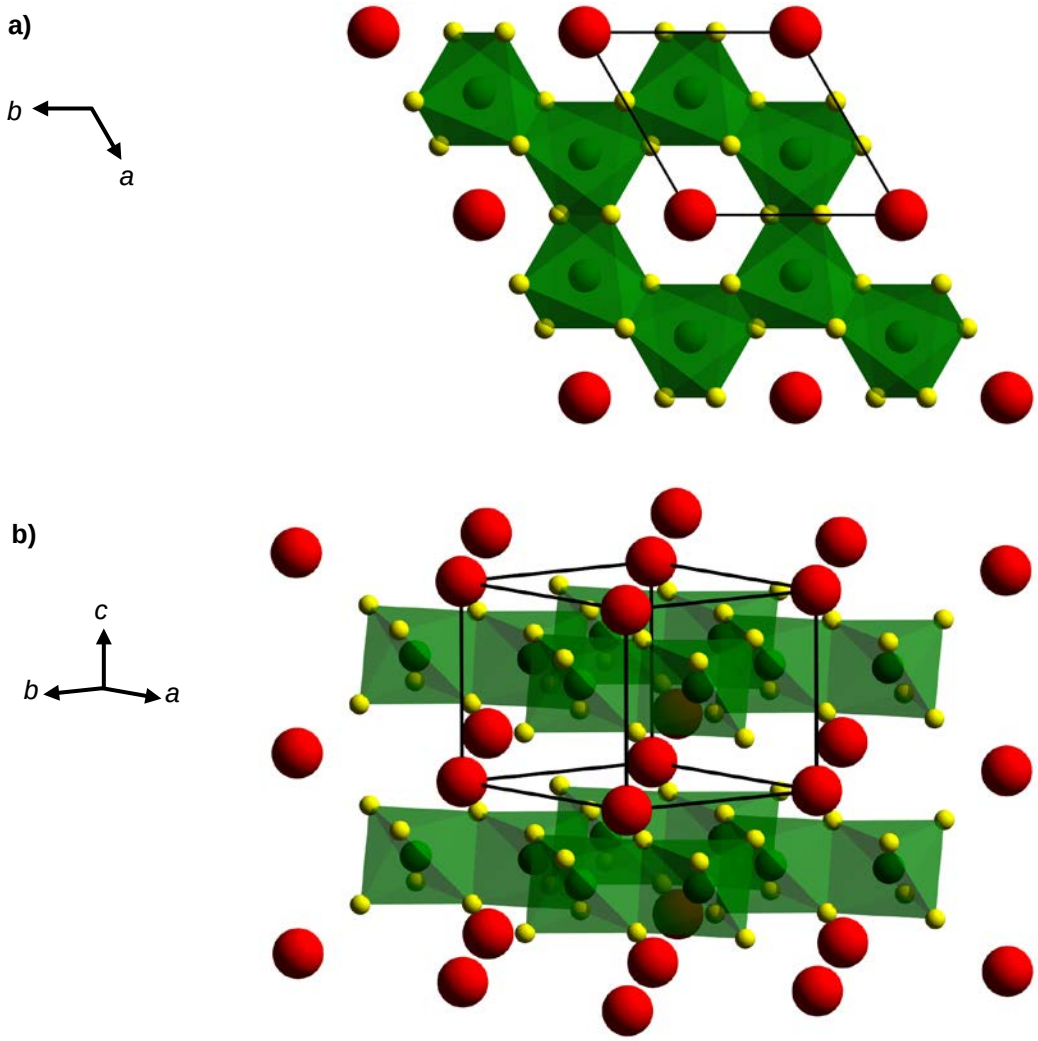

Figure 6. 11 $SrRu_2O_6$, a) as viewed in the ab *plane. b)a representation showing the layered structure with green RuO_6 octahedra (yellow O atoms) and red Sr atoms.*

6.3.3 Further Characterisation

ICP-OES elemental analysis (Table 6. 5) gives a Sr:Ru ratio of 0.467(6):1, consistent with the assigned formula of $SrRu_2O_6$. Furthermore there is no detectable K, proving it is not incorporated into the structure.

SEM (Figure 6. 12) shows that the oxide is made up of large (3 – 8 μm) hexagonal crystallites, whilst EDX spectroscopy gives a value comparable to that found by ICP-OES.

Table 6. 5 Measured metal content by mass in $SrRu_2O_6$ and elemental ratios.

Metal	Measured Metal Content / mass %	Atomic Ratio
Ru	54.6(3)	1
Sr	22.1(3)	0.467(6)
K	< 10 ppm	N/A

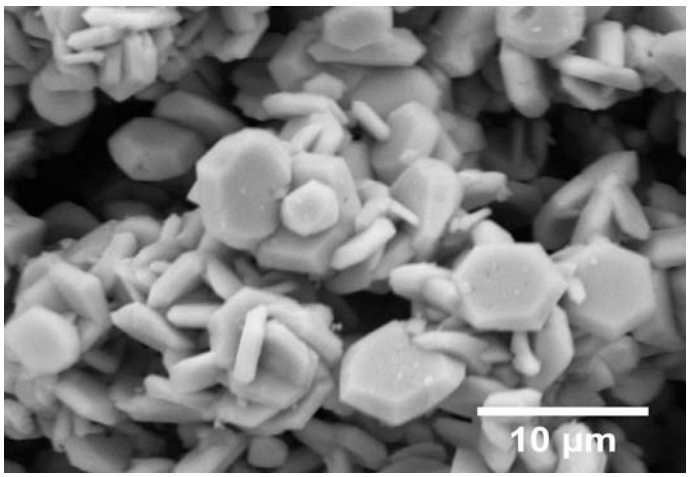

Figure 6. 12 SEM micrograph of hexagonal crystals of $SrRu_2O_6$.

In situ powder XRD up to 900 °C (Figure 6. 13a) shows that at around 450 °C peaks attributable to RuO_2 and $SrRuO_3$ begin to appear, though the $SrRu_2O_6$ peaks remain until 600 °C. Refinement of the lattice parameters, *a* and *c*, using data collected during both heating (up to the decomposition at 550 °C) and cooling (in a separate experiment, down to -253 °C) *in situ* shows that as a function of temperature, *c* can be approximated to a quadratic function, whilst there is very little change in *a* over the whole temperature range. This suggests that the edge-sharing RuO_6 octahedra form a rigid network, whilst the interlayer interactions are much more flexible.

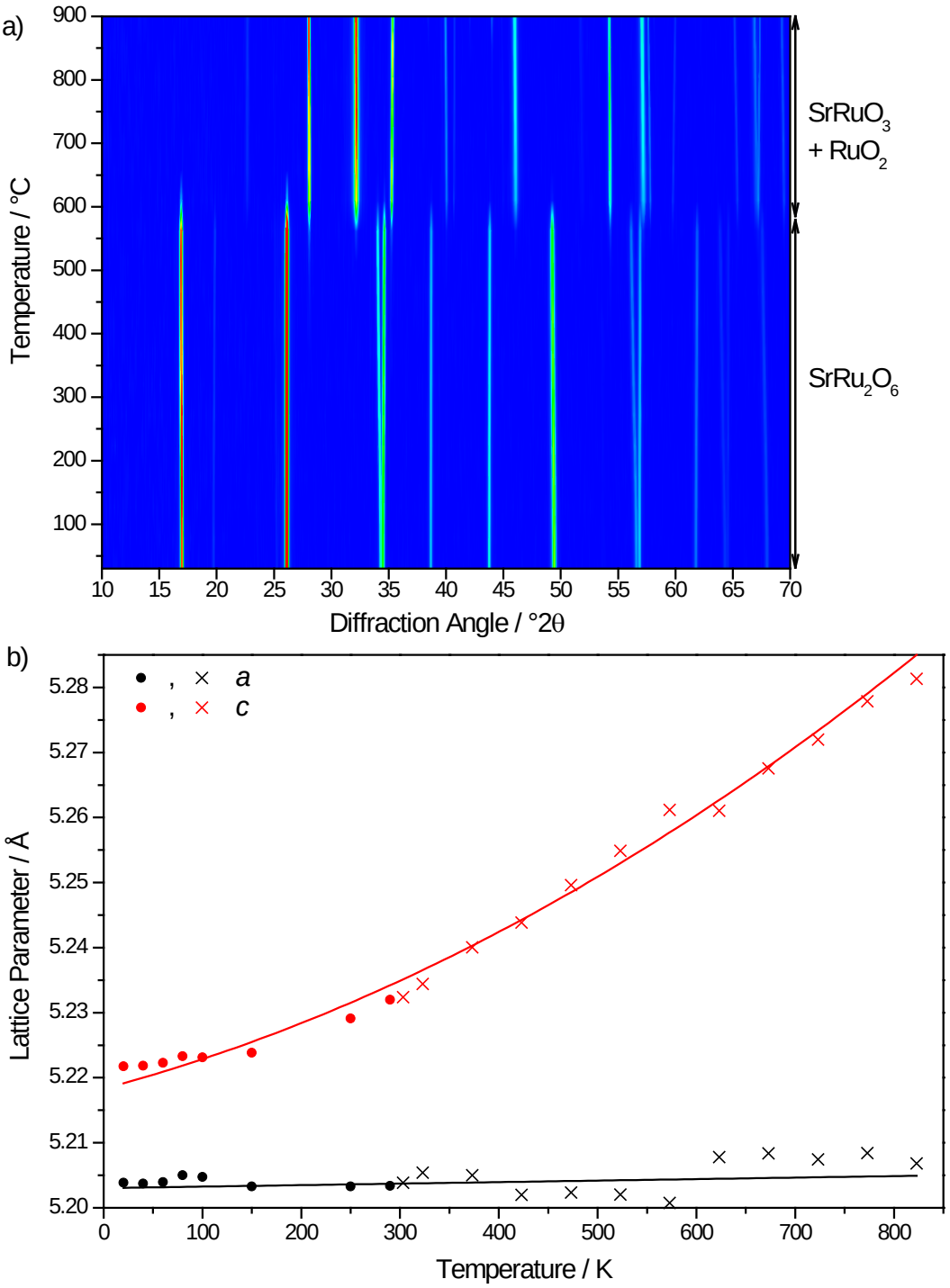

Figure 6. 13a) Contour plot of in situ *powder XRD patterns of $SrRu_2O_6$ from room temperature to 900 °C, with phase(s) present indicated on the right. b) Refined lattice parameters* a *and c as a function of temperature from 20 K (-253 °C) to 823 K (550 °C).* a *has a linear fit, whilst* c *has been fitted to a quadratic function. Different symbols (circles and dots) denote different (cooling and heating, respectively) experiments. Error bars are smaller than the data points.*

Although the $PbSb_2O_6$-type structure has been shown to accommodate hydroxide (for example in $CdTi_2O_4(OH)_2$[28]), the IR spectrum of $SrRu_2O_6$ (Figure 6. 14a) shows

no discernable O – H stretch in the range 3200 – 3600 cm^{-1}, suggesting that there is no structural hydroxide, and only a small amount of surface water. TGA (Figure 6. 14b) also confirms this, with only a tiny amount (< 1%) of mass loss before a sharp drop (~4% mass loss) at 640 °C, attributed to the loss of oxygen associated with the thermal decomposition into $SrRuO_3$ and RuO_2 seen by *in situ* powder XRD at 400 – 600 °C, which is expected to give a 4.2% mass loss.

Ru K-edge XANES data of $SrRu_2O_6$ were collected (Figure 6. 15a) on B18 (Diamond Light Source, U.K.). By comparing the Ru edge position with that of reference compounds with known Ru valence allows the Ru oxidation state to be estimated at +5.0 (Figure 6. 15b), identical to the value suggested by the formula.

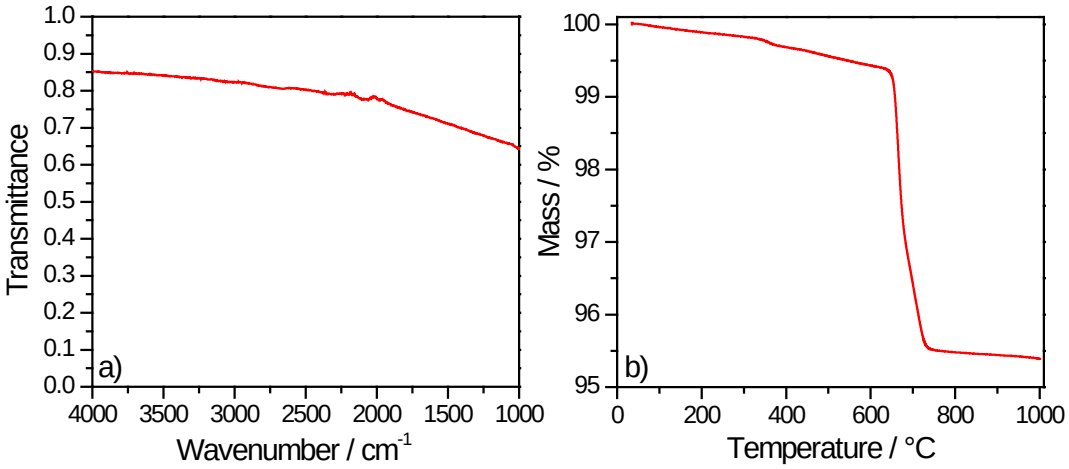

Figure 6. 14 a) IR spectrum and b) TGA plot of $SrRu_2O_6$.

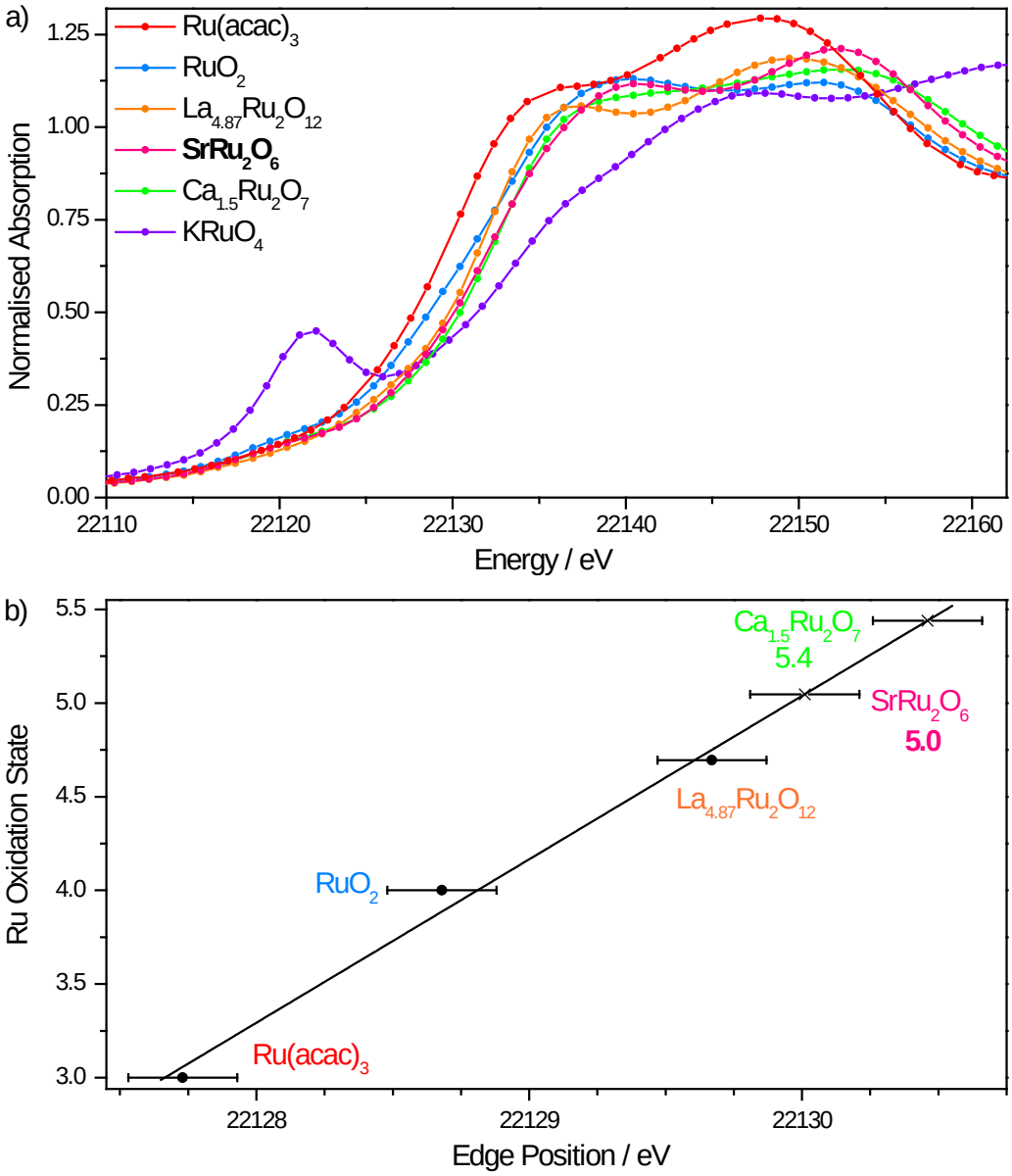

Figure 6. 15a) Normalised Ru K-edge XANES spectra of $SrRu_2O_6$ and reference compounds with known Ru oxidation state ($[Ru^{III}(acac)_3]$, $Ru^{IV}O_2$, $La_{4.87}Ru^{4.7}{}_2O_{12}$ and $KRu^{VII}O_4$). b) A plot of edge position (defined as energy at which normalised absorption = 0.5) as a function of oxidation state, with a linear fit of reference compounds, which is used to estimate the Ru oxidation state in the pyrochlore. $KRuO_4$ is omitted as a reference due to the pre-edge feature at 22121 eV. Spectrum and edge position of $Ca_{1.5}Ru_2O_7$ included for comparison.

6.3.4 Time-of-Flight Powder Neutron Diffraction

Time-of-flight powder neutron diffraction data collected on GEM, ISIS at room temperature (Figure 6. 16) contain reflections not present in the powder XRD pattern and which cannot be indexed to the $P\bar{3}1m$ space group. Instead these reflections can be attributed to magnetic scattering of an antiferromagnetic array of Ru(V) centres.

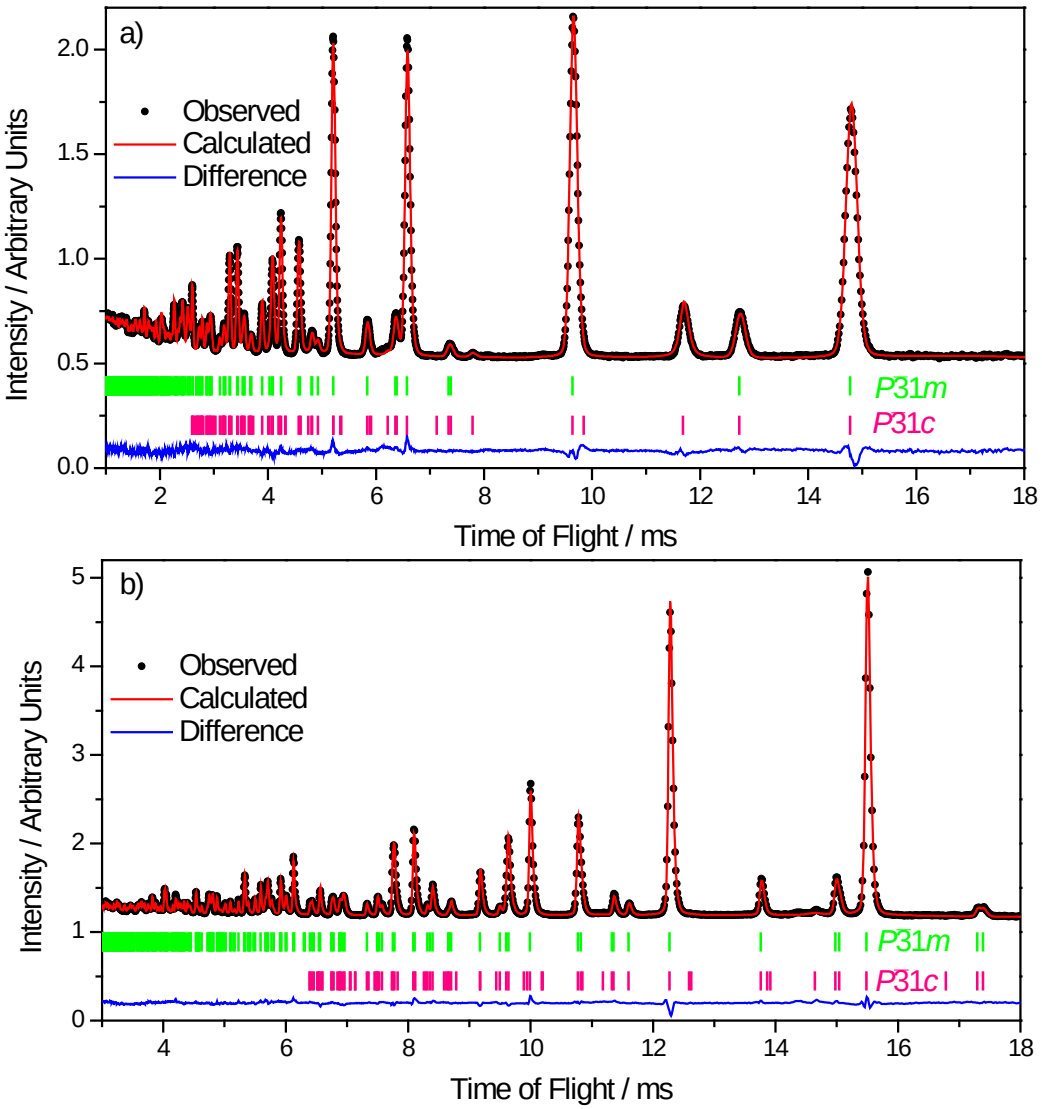

Figure 6. 16 Rietveld refinements of $SrRu_2O_6$ to room temperature powder neutron diffraction data. Tick marks denote peak positions of structural reflections ($P\bar{3}1m$, a = *5.20460(4) Å*, c = *5.23329(7) Å, green) and magnetic reflections* ($P\bar{3}1c$, a = *5.20460(4) Å*, c = *10.46658(14) Å, pink). a) GEM Bank 3 (mean scattering angle 2θ = 34.96°), b) GEM Bank 5 (mean scattering angle 2θ = 94.30°).*

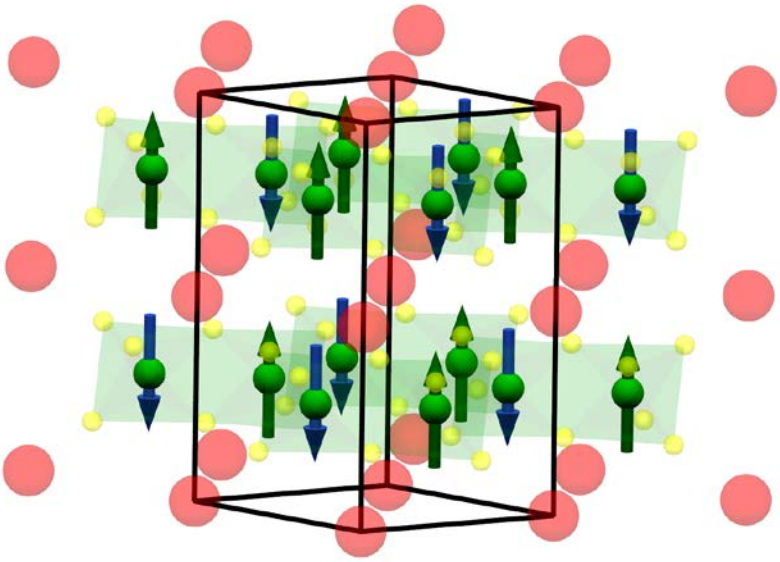

Figure 6. 17 Antiferromagnetic alignment of Ru(V) atoms (green) in $SrRu_2O_6$ with semi-transparent Sr (red) and O (yellow) atoms.

This arrangement can be indexed to a hexagonal unit cell with $a_{magnetic} = a_{structural}$ and $c_{magnetic} = 2c_{structural}$ (*i.e.* 10.46908(14) Å), in the space group $P\bar{3}1c$ with the Ru atoms antiferromagnetically coupled in both the *ab* plane and parallel to the *c*-axis (Figure 6. 17). The Ru(V) magnetic form factor derived by Parkinson *et al.*[29] was used. The magnetic moment is along the *c* direction, with a refined magnitude of 1.37(1) μ_B.

Using bond distances derived from the refined structure, the bond valence sum (Equation 6. 1) of each atom was calculated (Table 6. 6). Each atom has a calculated valence close to their expected values of +5, providing further evidence for the Ru oxidation state and absence of hydroxide in the crystal structure.

Table 6. 6 Refined atomic coordinates, ADPs and bond valence sums (BVS) of $SrRu_2O_6$ to neutron time of flight diffraction data (GEM banks 3 and 5). Space group P$\bar{3}1$m; a = *5.20460(4) Å,* c = *5.23329(7) Å, with a magnetic phase* P$\bar{3}1$c; a = *5.20460(4) Å,* c = *10.4666(1) Å,* χ^2 = *8.07;* R_{wp} = *4.63% (4.49% and 4.71% for respective banks);* R_p = *3.78% (3.84% and 3.72% for respective banks).*

Atom	Wyckoff	*x*	*y*	*z*	Occupancy	ADP / Å^2	BVS
Sr	1*a*	0	0	0	1	0.0088(2)	+2.07
Ru	2*d*	0.33333	0.66667	0.5	1	0.00474(8)	+5.17
O	6*k*	0.3787(1)	0	0.2977(1)	1	0.00760(6)	-2.07

6.3.5 Magnetic Susceptibility Studies

The magnetic susceptibility of $SrRu_2O_6$ from 350 – 5 K in 1000 Oe (Figure 6. 18) shows a very small Ru moment, with no clear ordering temperature except a very small increase on cooling from around 85 K. However, this increase in susceptibility (~0.3×10^{-3} emu mol_{Ru}^{-1}) can be explained by uncompensated spins, or due to an impurity of rutile RuO_2.[30] Although no RuO_2 was detected by diffraction, only approximately 1% (by mass) would be needed to cause this susceptibility change.

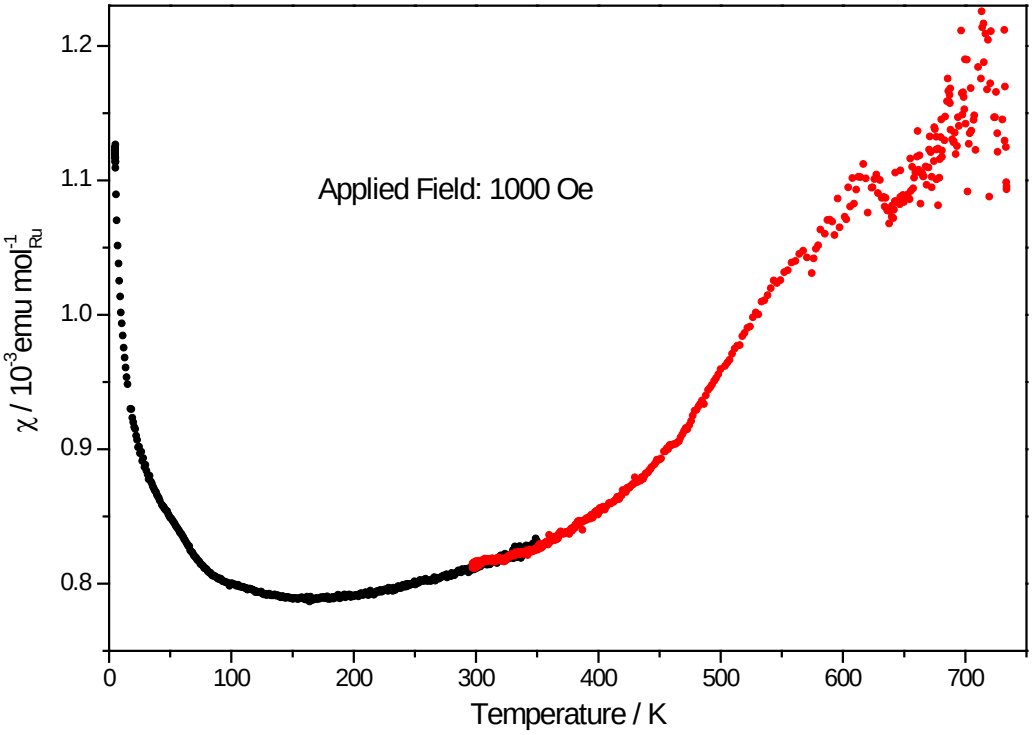

Figure 6. 18 Field-cooled magnetic susceptibility as a function of temperature of $SrRu_2O_6$. Data collected in two datasets, from 723 – 300 K (red) and from 350 – 5 K (black).

Because of the lack of ordering temperature between 350 K and room temperature, an *in situ* furnace was used in an attempt to ascertain the ordering temperature. A maximum temperature of 723 K (450 °C) was chosen, as it was just below the temperature at which RuO_2 reflections were observed by *in situ* powder XRD (Figure 6. 13a). The data are very noisy above 550 K, making determination of an

ordering temperature difficult, though a small jump in the susceptibility can be seen from 640 – 620 K.

6.3.6 *In Situ* Time-of-Flight Powder Neutron Diffraction

In situ powder neutron diffraction data were collected using WISH (ISIS, U.K.) from 5 to 623 K (-268 to 350 °C), in order to determine the magnetic ordering temperature of $SrRu_2O_6$. Rietveld refinement to the data at 5 K (Figure 6. 19a) shows the structure is similar to that found from room temperature diffraction collected on GEM (Table 6. 6), albeit with slightly different lattice parameters, as expected, and an increased Ru moment (1.425(10) μ_B). As the temperature is increased, the intensity of the purely magnetic reflections decrease until they disappear at 563 K (Figure 6. 19b, c).

Each pattern was fitted individually using initial parameters taken from the room temperature refinement of GEM data, which were then allowed to refine. The refined structural parameters obtained by Rietveld refinements to the *in situ* data as a function of temperature are shown in Figure 6. 20. From 5 to 500 K the Ru^{5+} moment decreases slightly, before rapidly decreasing to zero by 563 K. A Néel temperature of 563 K is therefore assigned.

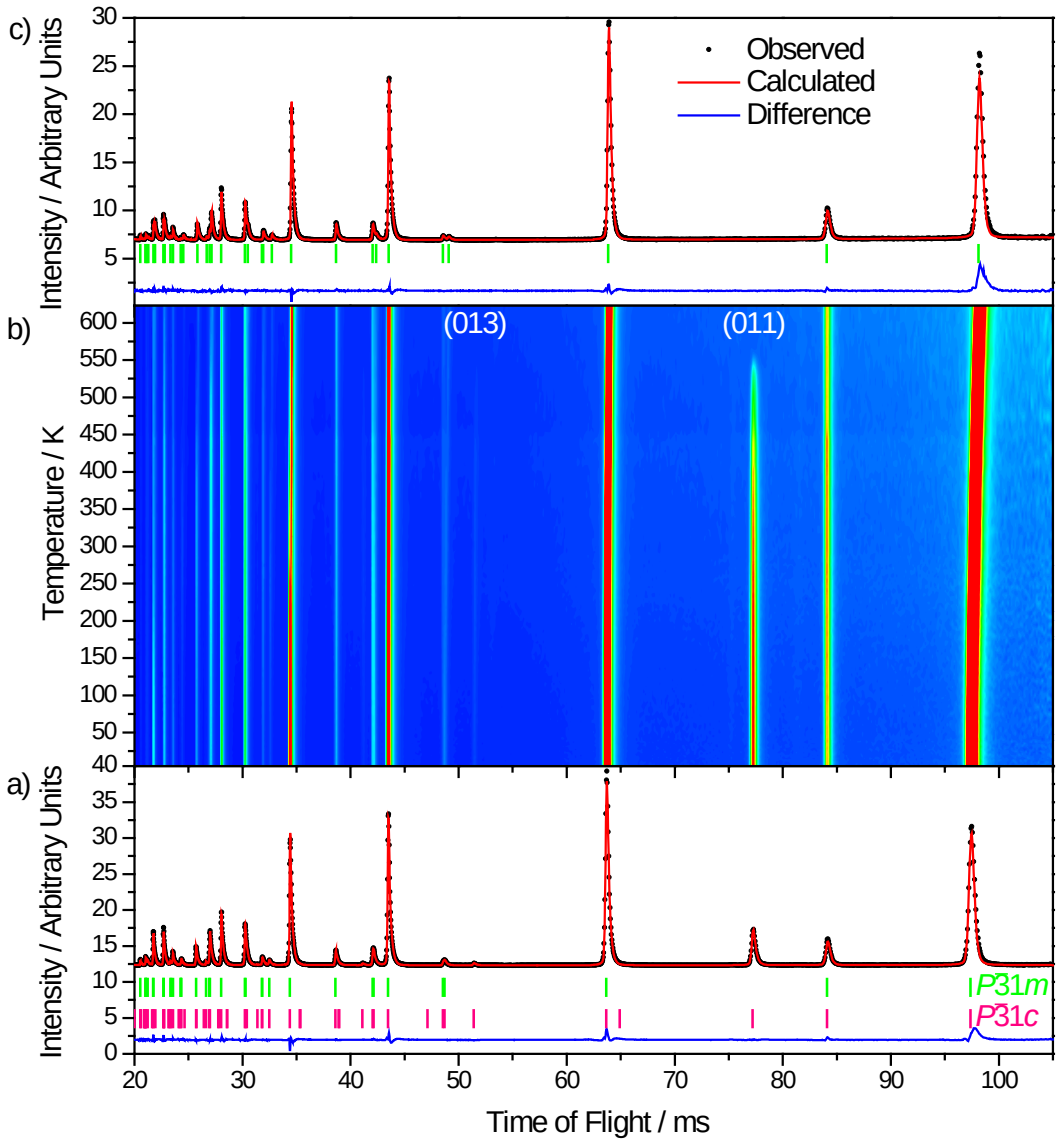

Figure 6. 19a) Rietveld fit to in situ *powder neutron diffraction data at 5 K of* $SrRu_2O_6$*, with structural reflection tick marks in green and magnetic reflection tick marks in pink. b) 2D contour plot of* in situ *powder neutron diffraction from 5 to 623 K showing the disappearance of magnetic reflections. The two strongest magnetic Miller indices ((011) and (013)) are labelled. c) Rietveld fit to* in situ *powder neutron diffraction data at 623 K, showing the absence of any magnetic reflections.*

In addition to the magnetic ordering temperature, the refinement data reveal anisotropic thermal expansion. Whilst the *c*-axis length displays a quadratic increase as a function of temperature (as observed by *in situ* powder XRD), the high resolution of WISH reveals that *a* actually displays a slight negative thermal expansion at low temperature, which could not be discerned from powder XRD.

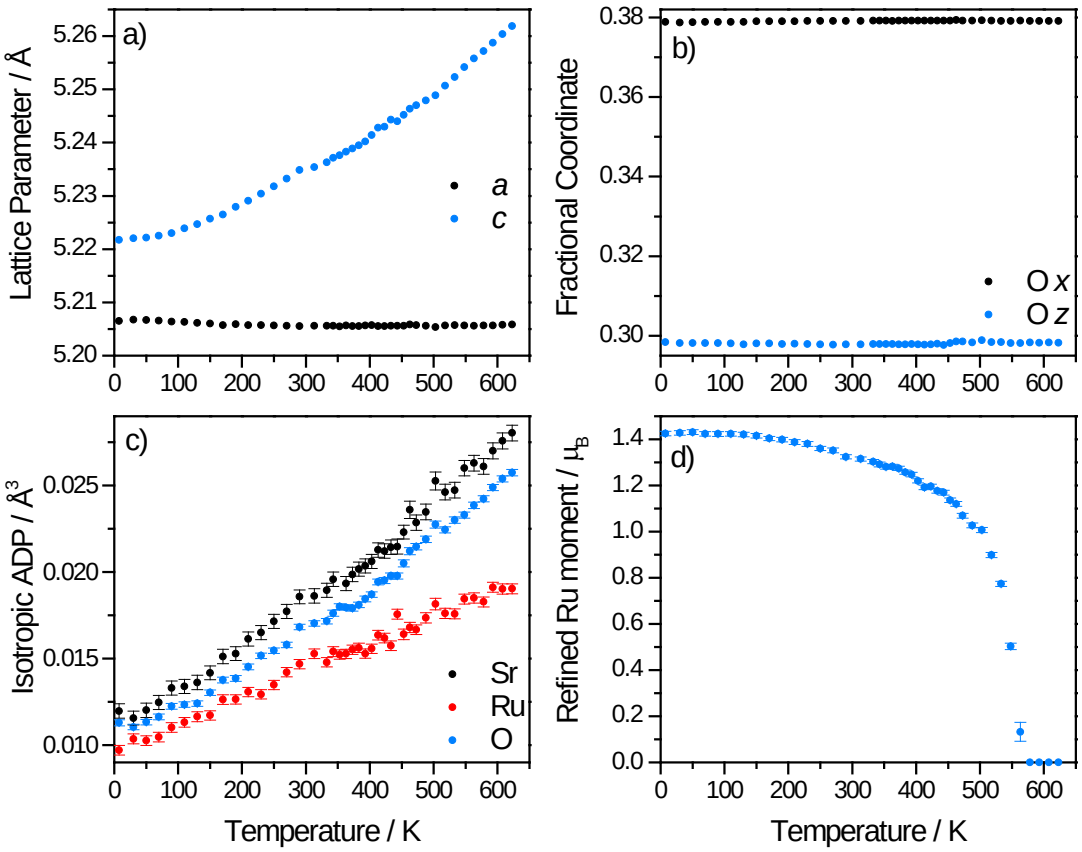

Figure 6. 20 Rietveld refined structural parameters of $SrRu_2O_6$ (a) lattice parameters a *and* c, *b) oxygen* x *and* z *coordinates, c) atomic displacement parameters and d) Ru moment) from* in situ *powder neutron diffraction, as a function of temperature.*

6.4 $Ba_2Ru_3O_9(OH)$

6.4.1 Synthesis

In a typical synthesis, $KRuO_4$ (1 mmol, Alfa Aesar, 98%) and BaO_2 (0.67 mmol, Sigma; 98%) were added to 10 ml distilled water with stirring. The mixture was sealed in a 23 ml Teflon-lined steel autoclaves and heated to 200 °C for 24 hours in a preheated fan oven. The autoclave was then cooled and the resulting precipitate was recovered by suction filtration. Washing at this stage with dilute HCl was necessary in order to remove any $Ba(OH)_2$ impurity.

Addition of excess BaO_2 causes the formation of an impurity of a second new phase, $Ba_4Ru_3O_{12}$ (See Section 6.5). Longer reactions (up to 1 month) did not yield any

other crystalline phases, and the crystal morphology (size and shape) was unaffected. Reducing the reaction temperature to 125 °C causes a large proportion of ruthenium to stay in solution, as evidenced by the orange colour of the filtrate and the solid product was $BaRuO_4 \cdot H_2O$.

6.4.2 Powder X-ray Diffraction

High-resolution laboratory powder XRD allowed the oxide to be indexed to a primitive orthorhombic unit cell, a = 12.1943(1) Å, b = 9.8783(1) Å, c = 7.05771(9) Å (Figure 6. 21). No structure with similar lattice parameters could be found on the ICSD, suggesting a new structure type. The peak shape shows no Scherrer broadening, suggesting a large particle size. However, crystals large enough for single crystal diffraction could not be prepared, meaning that structure solution from powder diffraction data was necessary.

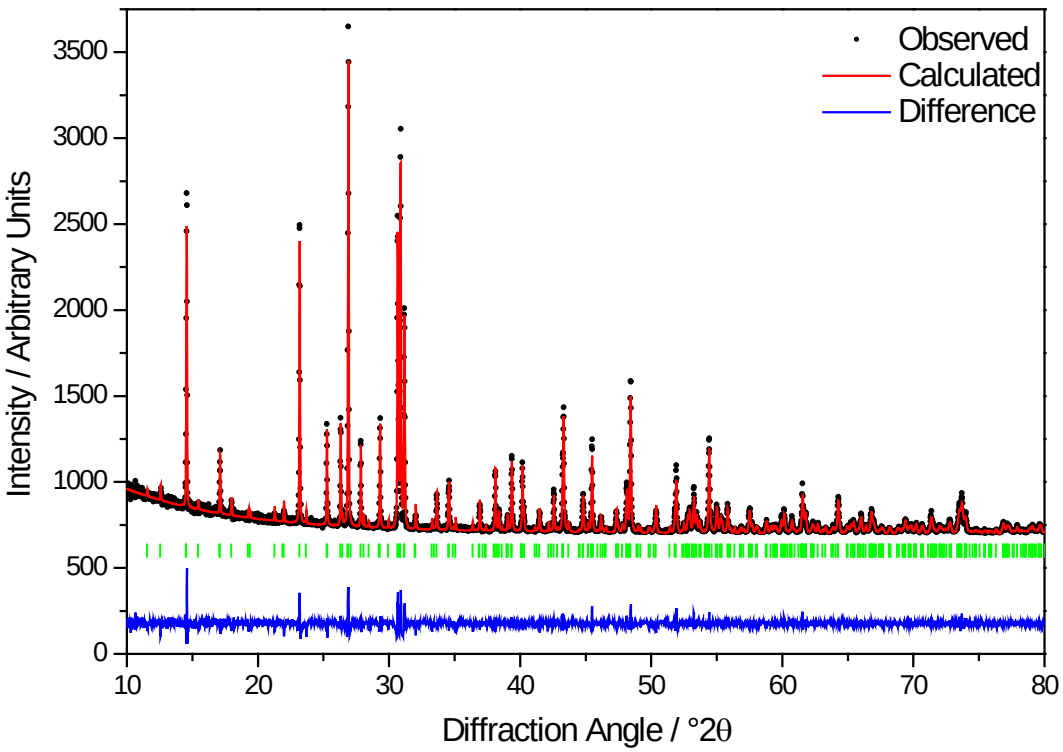

Figure 6. 21 Le Bail fit to high-resolution laboratory powder XRD data (λ = 1.5406 Å), space group P*222 (the lowest symmetry orthorhombic space group),* a = *12.1943(1) Å,* b = *9.8783(1) Å,* c = *7.05771(9) Å.*

6.4.3 Further Characterisation

ICP-OES elemental analysis (Table 6. 7) suggests a Ba:Ru ratio of 0.658(7):1, in accordance with the ratio of metals added in the hydrothermal reaction. As with the Ca and Sr materials, no appreciable amount of K was found to be present, suggesting that it stays in solution as a hydroxide by-product of the reaction. Assuming the remainder of the mass is oxide gives the initial structural formula of $Ba_{1.97(2)}Ru_3O_{9.9(3)}$.

Table 6. 7 Measured metal content by mass in $Ba_2Ru_3O_9(OH)$ and elemental ratios.

Metal	Measured Metal Content / mass %	Atomic Ratio
Ru	41.3(3)	1
Ba	36.9(3)	0.658(7)
K	< 10 ppm	N/A

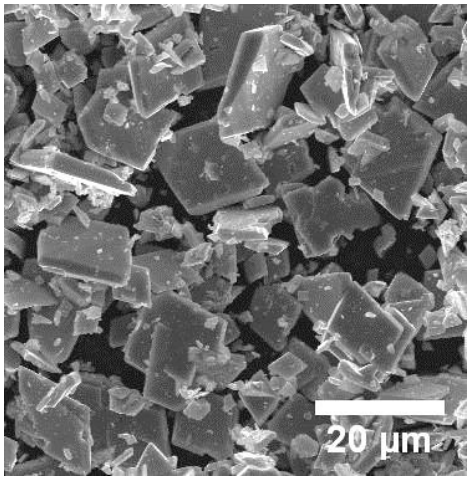

Figure 6. 22 SEM micrograph of rhombohedral plate-like crystals of $Ba_2Ru_3O_9(OH)$.

SEM (Figure 6. 22) shows the oxide consists of rhombohedral plates 10 – 15 µm across and 2 – 4 µm thick. EDX of several areas showed a Ba:Ru ratio similar to that found by ICP-OES throughout.

In situ powder XRD (Figure 6. 23) reveals that upon heating to 500 °C, the oxide decomposes to RuO_2 and the 4H perovskite $BaRuO_3$, previously only prepared by

high pressure, or at temperatures in excess of 1000 °C.[31] TGA data (Figure 6. 24b) shows very little change in the mass up to 400 °C, before a large (4%) drop in mass, which is consistent with the mass lost by the transformation from $Ba_2Ru_3O_{10}$ (assigned formula) to $BaRuO_3$ and RuO_2. IR spectroscopy (Figure 6. 24a) shows no sign of sign of O – H stretching.

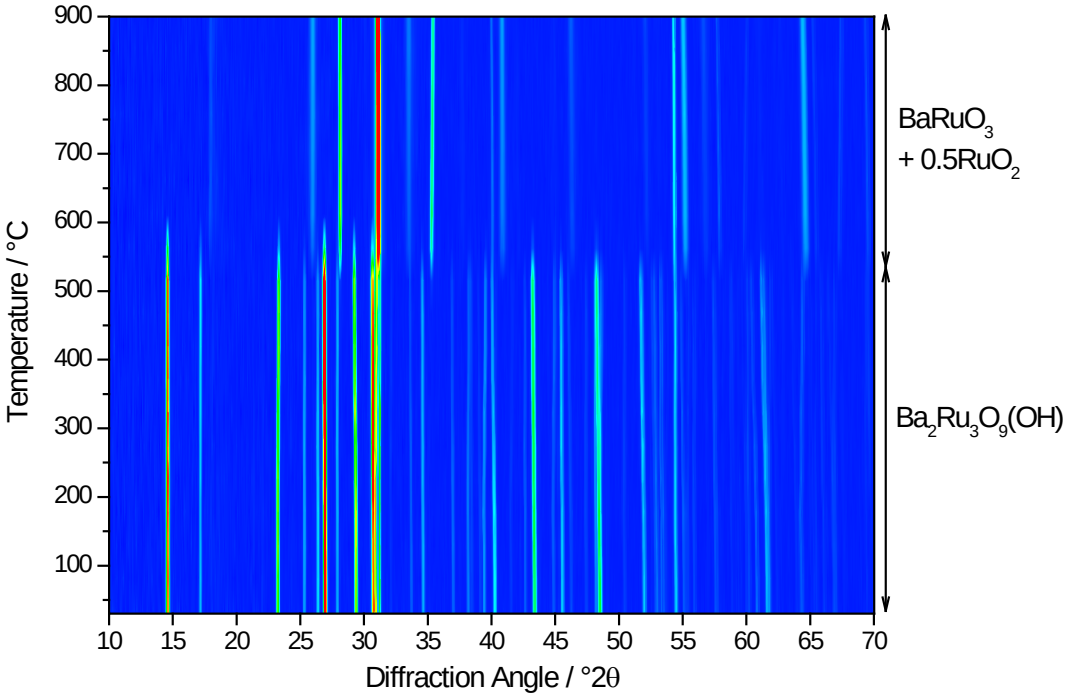

Figure 6. 23 Contour plot of in situ *powder XRD patterns of $Ba_2Ru_3O_9(OH)$ from room temperature to 900 °C, with phase(s) present indicated on the right.*

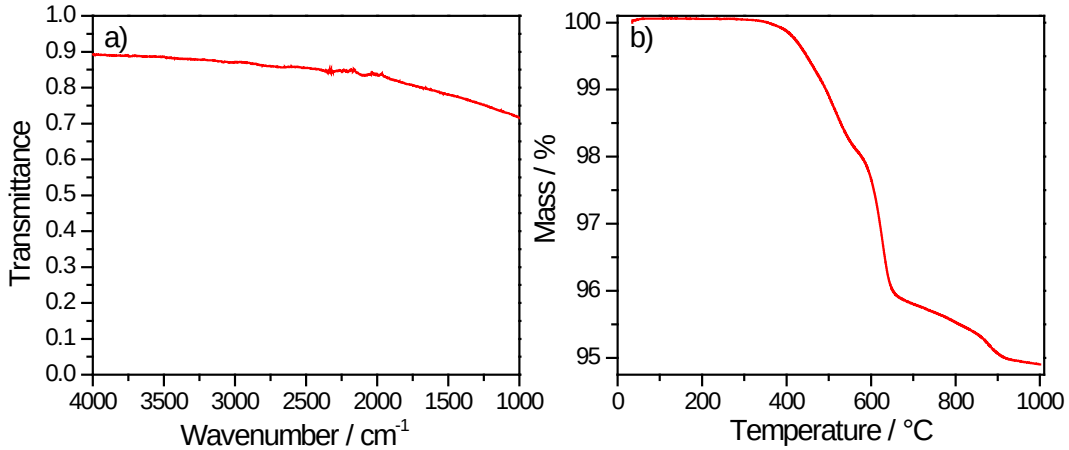

Figure 6. 24a) IR spectrum and b) TGA plot of $Ba_2Ru_3O_9(OH)$.

Ru K-edge XANES (B18, Diamond Light Source, U.K.; Figure 6. 25) shows that the oxide contains Ru in an oxidation state +4.9, slightly lower than would be expected

from the initially assigned formula of $Ba_2Ru_3O_{10}$, which suggests an average Ru oxidation state of +5.33.

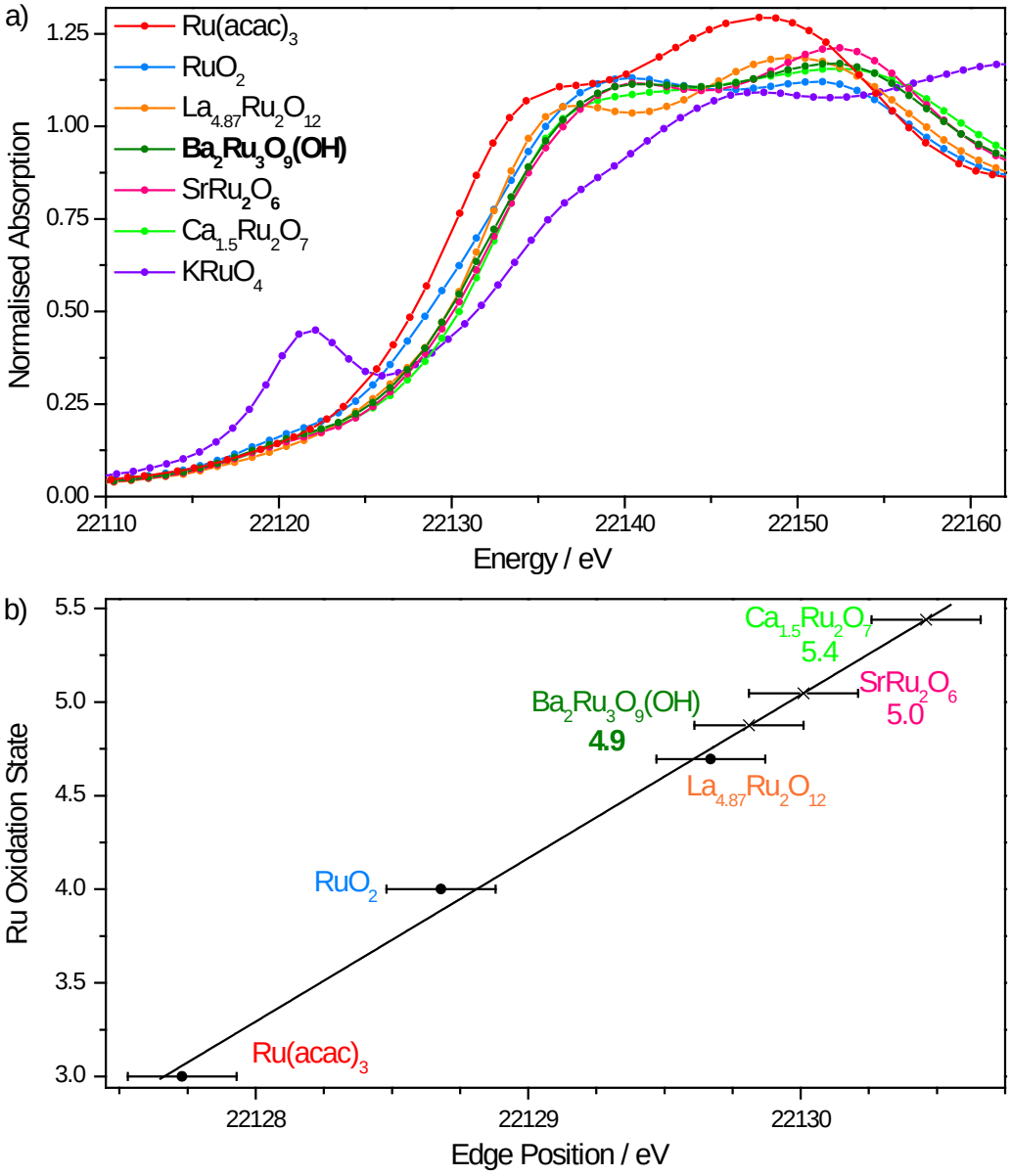

Figure 6. 25a) Normalised Ru K-edge XANES spectra of $Ba_2Ru_3O_9(OH)$ and reference compounds with known Ru oxidation state ($[Ru^{III}(acac)_3]$, $Ru^{IV}O_2$, $La_{4.87}Ru^{4.7}{}_2O_{12}$ and $KRu^{VII}O_4$). b) A plot of edge position (defined as energy at which normalised absorption = 0.5) as a function of oxidation state, with a linear fit of reference compounds, which is used to estimate the Ru oxidation state in the pyrochlore. $KRuO_4$ is omitted as a reference due to the pre-edge feature at 22121 eV. Spectra and edge positions of $Ca_{1.5}Ru_2O_7$ and $SrRu_2O_6$ are included for comparison.

6.4.4 *Ab Initio* Structure Determination from Powder Synchrotron X-ray and Neutron Diffraction

A density of 6.038(1) g cm^{-3} was found by pycnometry. The orthorhombic cell parameters found by powder XRD (Section 6.4.2) gives a cell volume of 850.17(2) $Å^3$. Using the formula weight of $Ba_2Ru_3O_{10}$ suggests a value of *Z* (the number of formula units per unit cell) of 4.19. A crude method proposed by Le Bail[32] for estimating the number of anions (in oxides and fluorides) – dividing the cell volume by 20 – also gives a *Z* of 4.25. Based on these estimations, *Z* was given a preliminary value of 4.

High-resolution powder synchrotron XRD (λ = 0.827154 Å) data was collected on Beamline I11 (Diamond Light Source, U.K., Figure 6. 26a). Close inspection of the low angle region of the diffraction pattern reveals the presence of very weak (100), (010) and (001) reflections (Figure 6. 26, inset). Only three orthorhombic space groups permit these reflections: *P*222, *Pmm*2 and *Pmmm*.

An initial structural model was developed using the software FOX,[33] implementing a Monte Carlo optimisation in direct-space (moving atoms in the cell and comparison of observed and calculated diffraction patterns). A 'parallel-tempering' temperature algorithm was used. Initial models containing only metal atoms were explored when fitting to the synchrotron XRD data, due to oxygen's comparatively weak X-ray form factor. No satisfactory model could be found by using any of the space groups without special reflection conditions. A 'symmetry-less' model (*i.e*. *P*1 space group) showed no signs of possessing an inversion centre (*i.e*. non-centrosymmetric) or mirror plane along any axis. The space group $P2_12_12_1$, consisting of three perpendicular two-one screw axes, was chosen, and the weak (100), (010) and (001)

reflections were assigned to a slight superstructure effect. Using this space group, an initial arrangement of metal atoms was found (Figure 6. 26b). The metal atom positions were then fixed, oxygen atoms were inserted into the model and allowed to

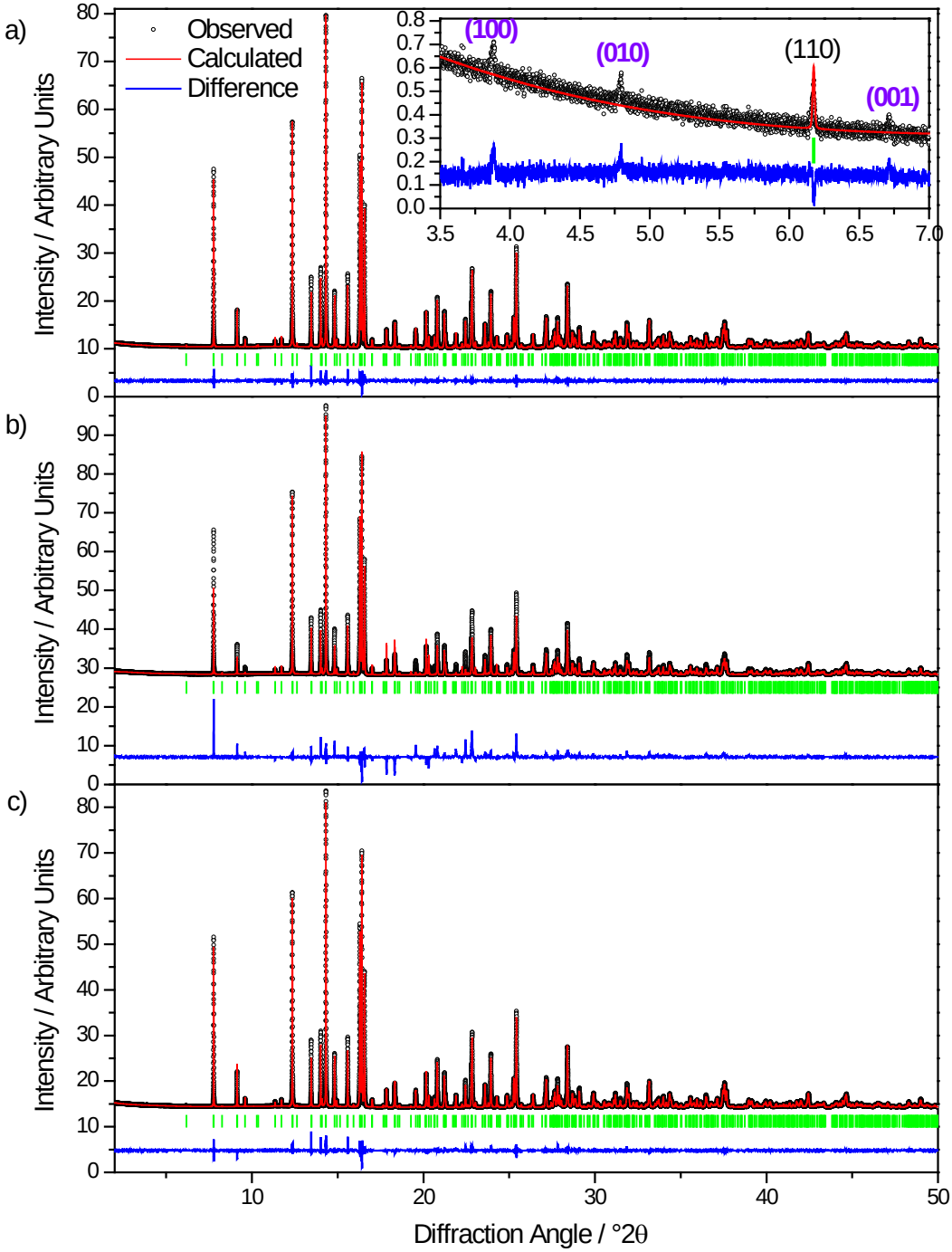

Figure 6. 26 Fits to powder synchrotron XRD (λ = 0.827154 Å) data of $Ba_2Ru_3O_9(OH)$. a) Le Bail fit to space group $P2_12_12_1$. Inset shows magnified low-angle region of the pattern with forbidden Miller indices labelled in purple. b) Initial fit using model containing only metal atoms. c) Final Rietveld fit to $Ba_2Ru_3O_9(OH)$.

move into a configuration best fitting to powder neutron time-of-flight diffraction data (GEM, ISIS, U.K.). From this initial configuration of atoms, a full Rietveld refinement was carried out, using both the powder synchrotron XRD and neutron diffraction data in GSAS.

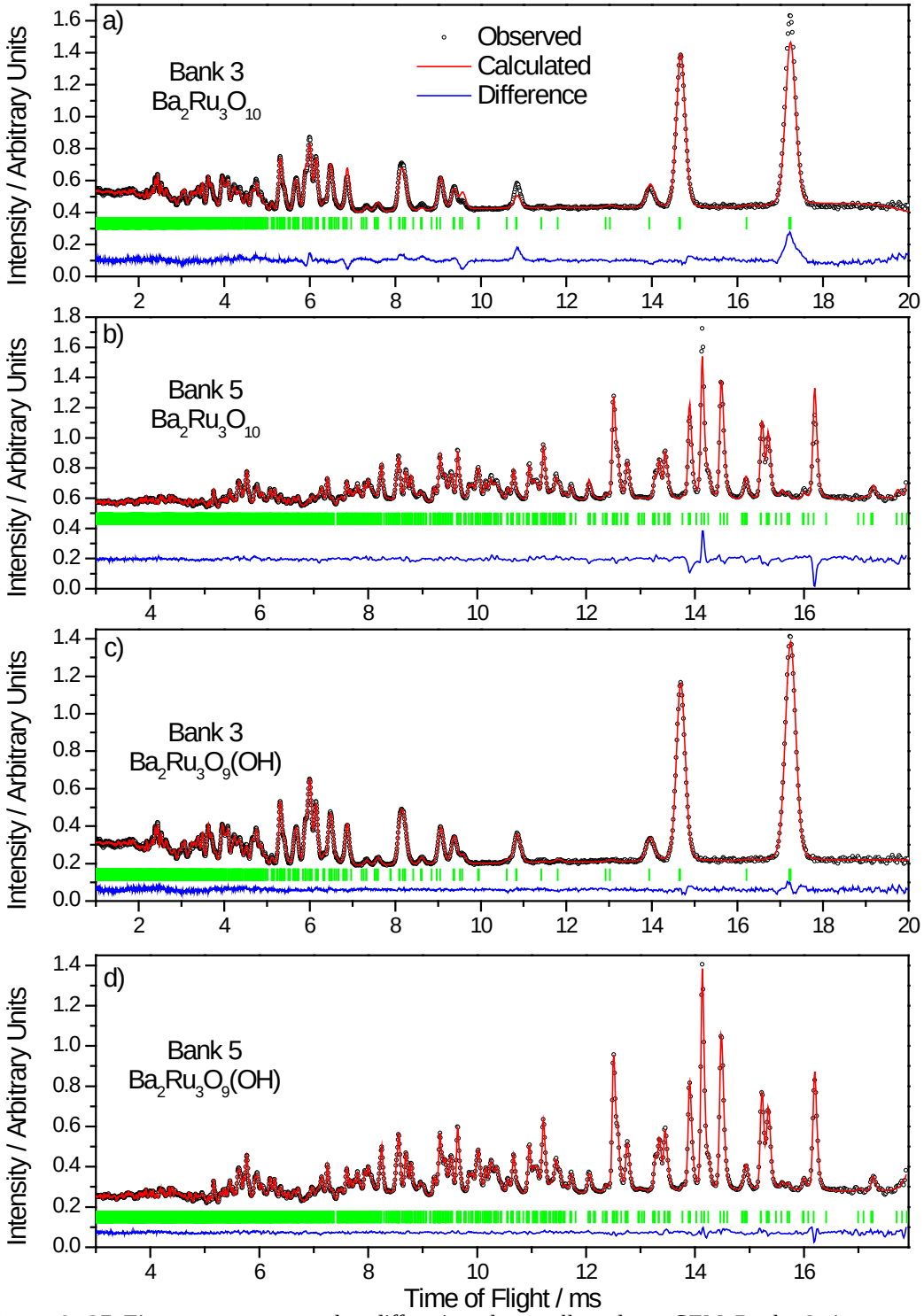

Figure 6. 27 Fits to neutron powder diffraction data collected on GEM Banks 3 (a, c; mean scattering angle 2θ = 34.96°) and 5 (b, d; mean scattering angle 2θ = 91.30°). a and b show the fits using the $Ba_2Ru_3O_{10}$ model, whilst c and d show fits using $Ba_2Ru_3O_9(OH)$.

Table 6. 8 Refined atomic coordinates, ADPs and bond valence sums (BVS) of $Ba_2Ru_3O_9OH$ to neutron time-of-flight diffraction data (GEM banks 3 and 5); Space group $P2_12_12_1$; a = *12.1967(1) Å,* b = *9.8791(1) Å,* c = *7.01616(1) Å;* χ^2 = *1.601;* R_{wp} = *1.80% (1.91% and 1.70% for respective banks);* R_p = *1.77% (1.89% and 1.59% for respective banks).*

Atom	Wyckoff	*x*	*y*	*z*	Occupancy	ADP / Å^2	BVS
Ba1	4*a*	0.3607(3)	0.0873(4)	0.9688(5)	1	0.0102(5)	+2.17
Ba2	4*a*	0.6400(3)	0.8874(3)	0.0253(4)	1	0.0063(4)	+2.54
Ru1	4*a*	0.0949(2)	0.2617(3)	0.3202(3)	1	0.0052(2)	+4.84
Ru2	4*a*	0.9073(2)	0.7544(3)	0.6816(4)	1	0.0082(2)	+5.18
Ru3	4*a*	-0.0029(4)	0.0099(4)	0.0018(7)	1	0.0044(2)	+5.10
O1	4*a*	0.0141(2)	0.0973(3)	0.2498(4)	1	0.0021(2)	-2.14
O2	4*a*	0.1447(2)	0.4418(3)	0.4088(4)	1	0.0017(2)	-2.01
O3	4*a*	0.4089(2)	0.6548(3)	0.5674(5)	1	0.0077(3)	-2.02
O4	4*a*	0.5543(3)	0.6535(3)	0.8794(4)	1	0.0075(3)	-2.06
O5	4*a*	0.2375(3)	0.1899(3)	0.2775(4)	1	0.0110(4)	-1.34
O6	4*a*	0.4473(3)	0.3216(3)	0.1179(4)	1	0.0068(3)	-2.13
O7	4*a*	0.1359(3)	0.0802(3)	0.9254(5)	1	0.0065(3)	-1.98
O8	4*a*	0.4071(2)	0.8191(3)	0.0735(5)	1	0.0093(4)	-2.25
O9	4*a*	0.0297(2)	0.4216(3)	0.7403(4)	1	0.0044(3)	-2.17
O10	4*a*	0.7506(3)	0.8058(3)	0.7088(4)	1	0.0078(3)	-2.23
H1	4*a*	0.2312(5)	0.6247(5)	0.3919(9)	1	0.022(1)	+0.98

Although a good fit to the powder XRD was obtained (Figure 6. 26c), there was some discrepancy between the calculated and observed powder neutron diffraction patterns (Figure 6. 27a, b). A manual search of the difference Fourier map showed an area of negative nuclear density 0.96 Å from an oxygen atom. This was attributed to an H atom. No O – H stretch was visible in the IR spectrum (3200 – 3600 cm^{-1}, Figure 6. 24a), which may be due to there only being one H per formula unit. Adding one H per formula unit (to give $Ba_2Ru_3O_9(OH)$) improves the fit to the neutron diffraction data (Figure 6. 27c, d). The presence of one H atom makes very little

difference to the powder XRD fit (due to the very small H X-ray form factor) and to the mass analysis (TGA, density). This assigned formula importantly gives an average Ru oxidation state of 5, consistent with the value observed by Ru K-edge XANES (Figure 6. 25).

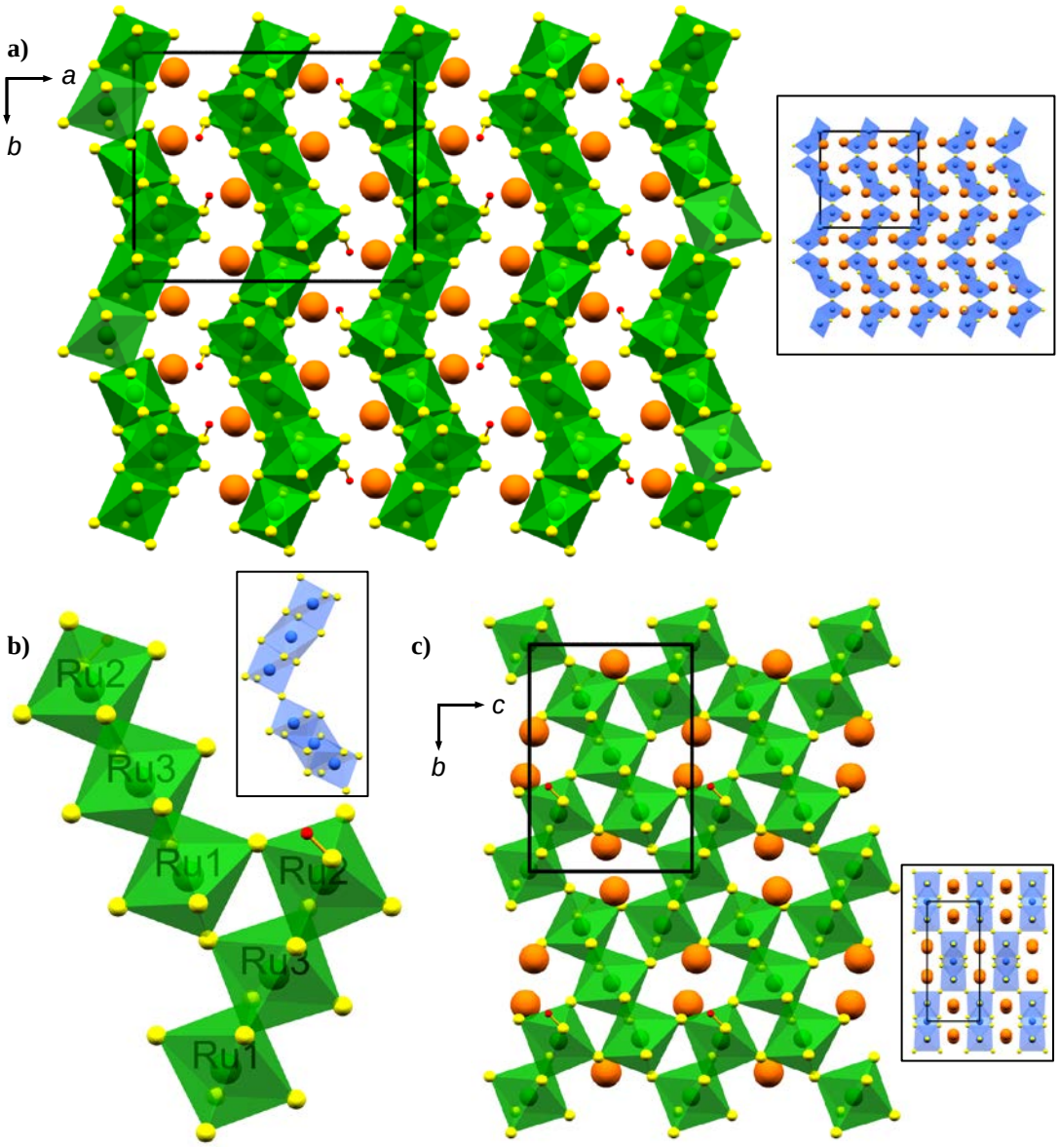

Figure 6. 28a) Structure of $Ba_2Ru_3O_9(OH)$ as viewed along the c-direction. b) Two quasi-trimeric units of RuO_6 octahedra showing "inter-trimer" edge-sharing and "intra-trimer" corner-sharing connectivity. c) One layer of RuO_6 octahedra, with the Ba and H atoms shown. Insets show the equivalent perspectives of $Ba_4Ru_3O_{10}$. RuO_6 octahedra shown in green (blue in insets), with yellow oxygen atoms, orange Ba atoms and red H.

The final structural model (Table 6. 8) can be viewed as "zig-zag" layers of RuO_6 octahedra with Ba and H ions projecting into the space between the layers (Figure 6. 28a). Each layer consists of units of three edge-sharing octahedra which are each corner-linked to neighbouring trimers at two points to create a corrugated two-dimensional network (Figure 6. 28b,c). In this sense, the structure can be compared to $Ba_4Ru_3O_{10}$, a Ru^{IV} containing oxide (Figure 6. 28 insets).[1,34] It also can be viewed as corrugated layers of composed of RuO_6 trimers which are corner-linked to each other. However, the trimers are composed of three *face*-sharing octahedra; and a trimer is connected to each neighbour by only one corner-linkage, generating chequerboard-type layers (as viewed along (010)).

As a means to assess the quality of the structural model the bond valence sum of each atom (Table 6. 8), and the O – Ru – O bond angles were calculated (Table 6. 9). For each atom the bond valence was close to expected values (within 15%), with the exception of the Ba2 and O5. The higher than expected Ba1 and Ba2 charges (+2.17 and +2.54, respectively) are caused by compression of the Ba sites, which has been previously reported in a range of perovskite oxides.[35,36] O5 had a bond valence sum of -1.34, significantly lower than expected. A neutron Fourier difference map did not give any indication for the presence of nearby H atom or other atoms nearby, and so the lower than expected valence has been attributed to structural constraints. The bond angles in RuO_6 octahedra (Table 6. 9) show a similar degree of distortion to other ruthenium oxides.[34,37,38]

Table 6. 9 O – Ru – O bond angles in $Ba_2Ru_3O_9(OH)$.

Atom 1	Atom 2	*Atom 3*	*Angle 2, 1, 3 / °*	Atom 1	Atom 2	*Atom 3*	*Angle 2, 1, 3 / °*
Ru1	O2	O3	85.24(16)	Ru2	O9	O10	97.98(16)
	O2	O8	94.67(16)		O6	O7	79.60(16)
	O2	O1	167.51(18)		O6	O3	87.77(15)
	O2	O5	96.01(16)		O6	O10	169.00(19)
	O2	O4	80.79(15)		O7	O3	93.37(16)
	O3	O8	177.79(19)		O7	O10	90.17(16)
	O3	O1	96.07(15)		O3	O10	88.84(15)
	O3	O5	91.95(16)	Ru3	O4	O2	83.84(19)
	O3	O4	89.59(15)		O4	O1	86.70(22)
	O8	O1	83.55(16)		O4	O7	96.07(23)
	O8	O5	90.25(16)		O4	O9	93.85(19)
	O8	O4	88.22(15)		O4	O6	177.02(29)
	O1	O5	96.36(16)		O2	O1	87.50(22)
	O1	O4	86.79(15)		O2	O7	177.43(30)
	O5	O4	176.32(19)		O2	O9	88.90(22)
Ru2	O8	O9	93.97(17)		O2	O6	99.00(23)
	O8	O6	93.64(17)		O1	O7	89.94(21)
	O8	O7	90.87(17)		O1	O9	176.27(30)
	O8	O3	175.72(20)		O1	O6	92.51(18)
	O8	O10	90.51(16)		O7	O9	93.67(24)
	O9	O6	91.90(17)		O7	O6	81.05(19)
	O9	O7	170.48(20)		O9	O6	87.12(23)
	O9	O3	81.93(16)				

6.4.5 Magnetic Susceptibility Studies

$Ba_2Ru_3O_9(OH)$ in a 100 Oe applied field (Figure 6. 29a) shows a large increase in χ at 70 K, indicative of a ferromagnetic transition. A Curie-Weiss fit (Equation 6. 2) in the paramagnetic region ($T \geq 150$ K, Figure 6. 29b) gives a Weiss temperature of 84(1) K, again suggesting ferromagnetic ordering of the Ru(V) moments. The moment per Ru atom, found using Curie's Law (Equation 6. 3), is 0.73 μ_B, which is significantly smaller than the spin-only value for an octahedral d^3 ion (3.87 μ_B).

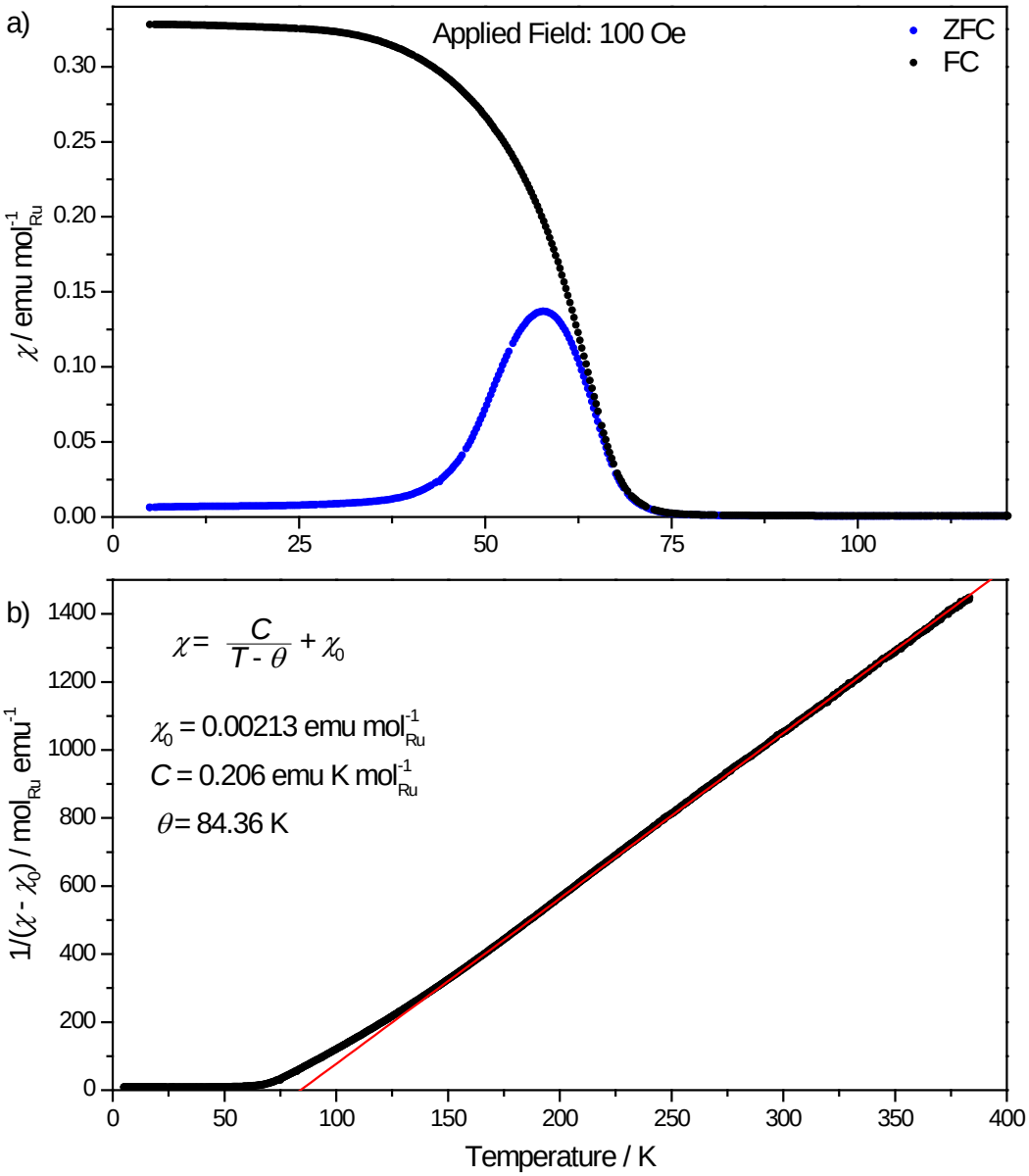

Figure 6. 29a) Field-cooled (FC) and zero field-cooled (ZFC) magnetic susceptibility as a function of temperature of $Ba_2Ru_3O_9(OH)$ in a 100 Oe applied field. b) A linear Curie-Weiss fit to inverse susceptibility (minus a temperature independent term) in paramagnetic region of $Ba_2Ru_3O_9(OH)$ as a function of temperature.

6.5 $Ba_4Ru_3O_{12}$

6.5.1 Synthesis

In a typical synthesis, $KRuO_4$ (1 mmol, Alfa Aesar, 98%) and an excess of BaO_2 (2 mmol, Sigma; 98%) were added to 10 ml distilled water with stirring. The mixture was sealed in a 23 ml Teflon-lined steel autoclave and heated to 200 °C for 24 hours in a preheated fan oven. The autoclave was then cooled and the resulting precipitate was recovered by suction filtration. Washing at this stage with dilute HCl was necessary in order to remove any $Ba(OH)_2$ impurity.

Adding the stoichiometric amount of BaO_2 (1.33 mmol) causes formation of $Ba_2Ru_3O_9(OH)$ as a minor phase. Longer reactions (up to 1 month) did not yield any other crystalline phases, and the crystal morphology (size and shape) was unaffected. Reducing the reaction temperature to 125 °C causes a large proportion of ruthenium to stay in solution, as evidenced by the orange colour of the filtrate and the solid product was $BaRuO_4 \cdot H_2O$.

6.5.2 Powder X-ray Diffraction

The HR-XRD pattern (λ = 1.5406 Å) was best indexed to a hexagonal unit cell, space group $P6_3mc$ with lattice parameters a = 5.7812(1) Å and c = 18.7876(6) Å (Figure 6. 30). These lengths are characteristic of an 8H hexagonal perovskite (Table 6. 10). A hexagonal perovskite consists of layers of close-packed [AO_3] units (where *A* is a large cation, Ba in this instance) stacked along the *c*-axis, with *B* atoms (typically small, highly charged cations, *i.e.* Ru^{5+}) occupying one third of the octahedral interstices.[39] Each layer can either stack in a 'hexagonal' (*h*) or 'cubic' (*c*) manner resulting in face-sharing or corner-sharing octahedra, leading to repeating

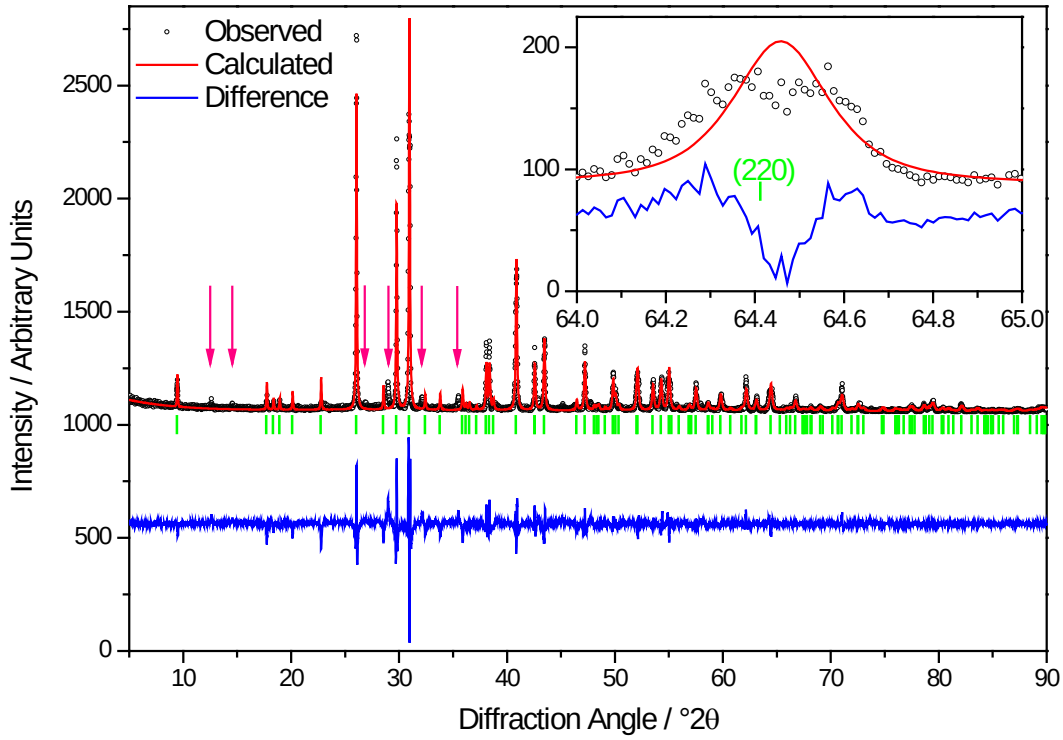

Figure 6. 30 Le Bail fit to high-resolution laboratory powder XRD data (λ = 1.5406 Å), space group P63mc, a = *5.7812(1) Å,* c = *18.7678(6) Å. Weak, additional peaks marked with an arrow are due to a small* $Ba_2Ru_3O_9(OH)$ *impurity. Inset shows magnified region around the (220) reflection.*

stacking sequences (Figure 6. 31). *B* cation vacancies are commonly required in order to achieve charge balance leading to empty octahedra, particularly when the number of layers > 6, leading to $A_xB_{x-\delta}O_{3x}$ stoichiometries.[36,40,41]

Although the expected and observed peak positions match well, the profiles could not be well matched in a Le Bail fit. At high diffraction angles, peaks appear to split, suggesting a lowering of symmetry, from hexagonal to monoclinic (Figure 6. 30, inset). This distortion has been noted in other ruthenium hexagonal perovskites,[16] but the very slight distortion in this case was difficult to index reliably using laboratory powder XRD data.

Table 6. 10 Ba – Ru hexagonal perovskite-type oxides.

Structure	*a* / Å	*c* / Å	Space Group	Reference
4H-perovskite	5.729(1)	9.500(1)	$P6_3/mmc$	Hong & Sleight[31]
6H-perovskite ($Ba_4Ru_3LiO_{12}$)	5.7828(1)	14.1917(4)	$P6_3/mmc$	Battle *et al.*[37]
8H-perovskite	**5.7812(1)**	**18.7876(6)**	$\boldsymbol{P6_3mc}$	**This work**
8H-perovskite ($Ba_4Ru_3NaO_{12}$)	5.8142(1)	19.2643(4)	$P6_3mc$	Battle *et al.*[37]
$Ba_5Ru_2O_{10}$	5.9470(5)	18.043(1)	$P6_3/mmc$	Dussarrat *et al.*[42]
9R-perovskite	5.75	21.60	$R\bar{3}m$	Donahue *et al.*[43]
10H-perovskite	5.756(2)	23.727(8)	$P6_3/mmc$	Ogawa & Sato[19]

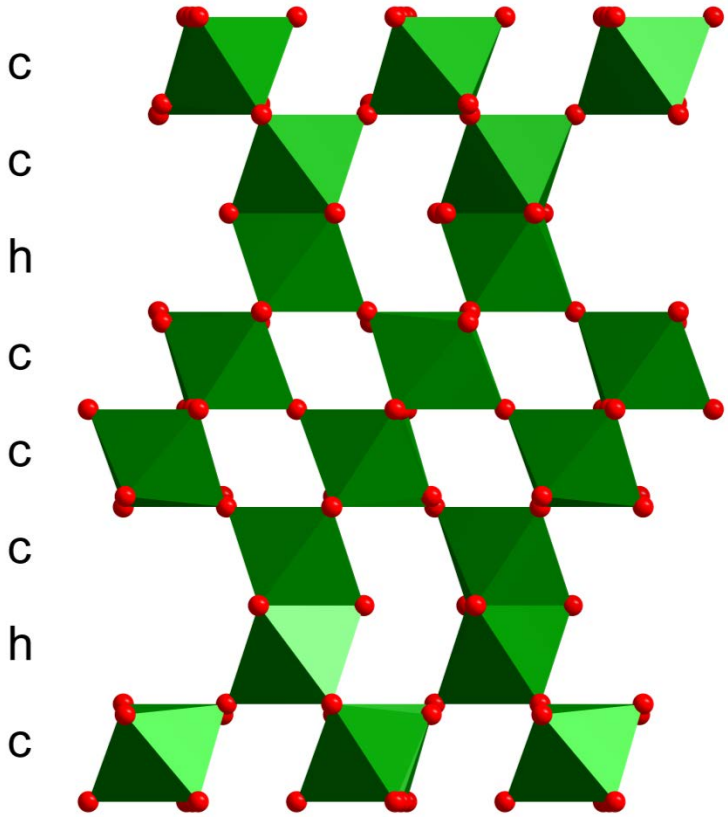

Figure 6. 31 Crystal structure of an 8H-perovskite ($Ba_8Ta_4Ti_3O_{24}$) with only octahedra shown for clarity. Letters c *and* h *denote cubic or hexagonal stacking, respectively.*

6.5.3 Further Characterisation

ICP-OES elemental analysis (Table 6. 11) gives a Ba:Ru ratio of 1.33(1):1, despite the large excess of Ba precursor added to the reaction mixture. No K was found to be present in the oxide. Assuming the remainder of the mass is oxygen gives a formula of $Ba_{3.99(5)}Ru_3O_{12.1(1)}$, leading to the assigned formula $Ba_4Ru_3O_{12}$, which contains Ru with an average oxidation state of +5.33.

Table 6. 11 Measured metal content by mass in $Ba_4Ru_3O_{12}$ and elemental ratios.

Metal	Measured Metal Content / mass %	Atomic Ratio
Ru	29.0(3)	1
Ba	52.4(3)	1.33(1)
K	< 10 ppm	N/A

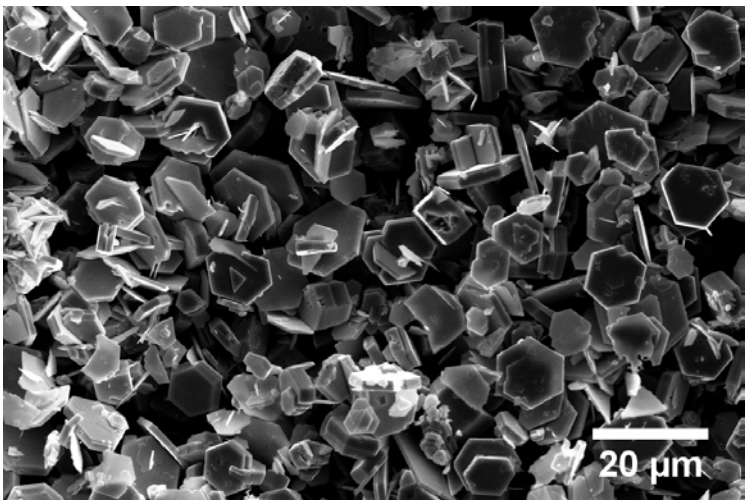

Figure 6. 32 SEM micrograph of hexagonal plate-like crystals of $Ba_4Ru_3O_{12}$.

SEM (Figure 6. 32) showed that the oxide is composed of hexagonal plate-like crystals, approximately 5 – 10 µm across and 1 – 2 µm tall. EDX elemental analysis of several areas showed that the Ba:Ru ratio was constant throughout the sample.

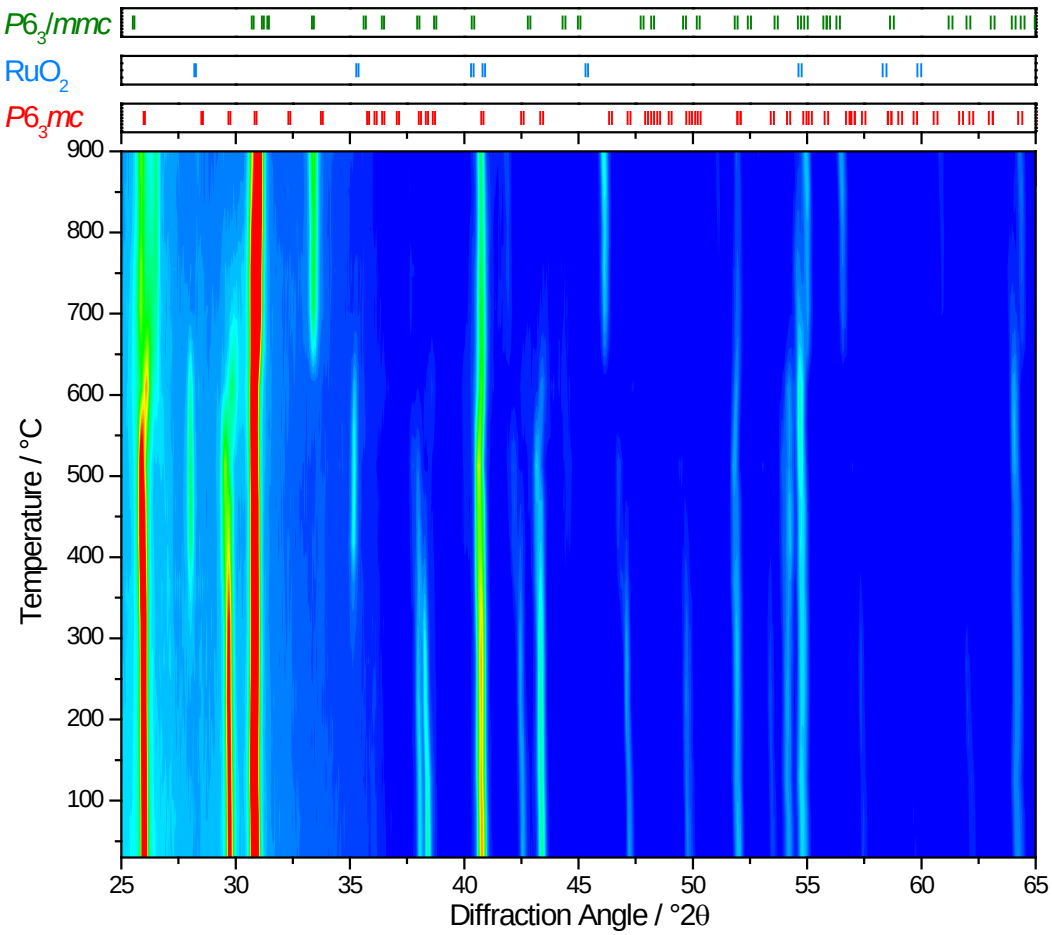

Figure 6. 33 Contour plot of in situ *powder XRD patterns of* $Ba_4Ru_3O_{12}$ *from room temperature to 900 °C, with tickmarks of present phases shown above.* $P6_3mc$ *corresponds to the initial* $Ba_4Ru_3O_{12}$ *phase and* P63/mmc *corresponds to a 6H-perovskite.*

In situ powder XRD (Figure 6. 33) shows that upon heating to 300 °C in air, RuO_2 begins to crystallise, though there is little visible change to the peaks of the 8H-perovskite. Further heating causes the diffraction peaks attributed to RuO_2 to then disappear at 700 °C and the transformation from the 8H to the known 6H perovskite. However, there is one peak at 46.2° which cannot be assigned to this model, and it is unclear what happens to the excess Ba.

TGA in N_2 (Figure 6. 34b) shows that $Ba_4Ru_3O_{12}$ begins to lose mass as soon as it is heated above room temperature in air. Since no structural change was observed at low temperature by *in situ* XRD, this has been attributed to the loss of surface water.

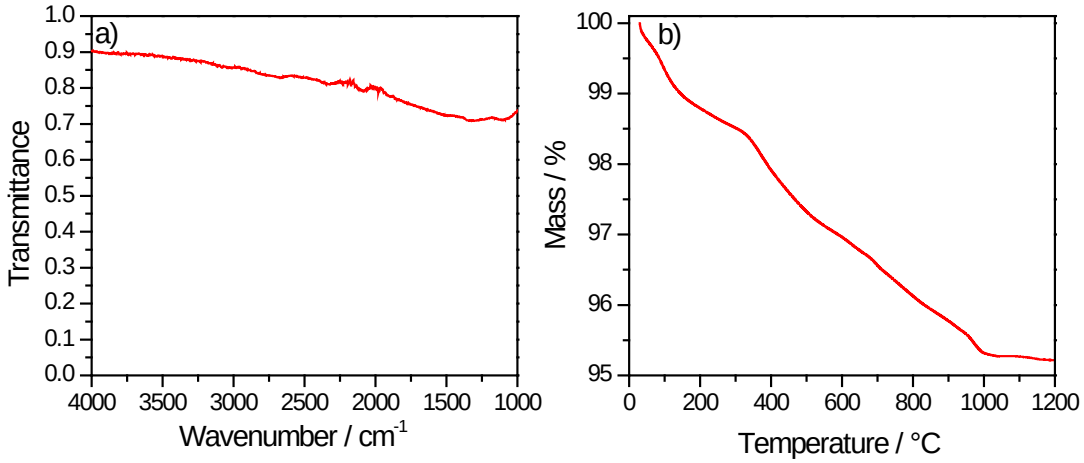

Figure 6. 34a) IR spectrum and b) TGA (in N_2) plot of $Ba_4Ru_3O_{12}$.

The mass loss caused by the loss of oxygen due to reduction of Ru^{5+} to Ru^{4+} is calculated to be 3.1%, consistent with the mass lost between 350 °C and 1000 °C. The IR spectrum (Figure 6. 34a) shows no sign of any O – H stretching at 3600 – 3200 cm^{-1}. Ru K-edge XANES suggests an average oxidation state very close to +5 (Figure 6. 35).

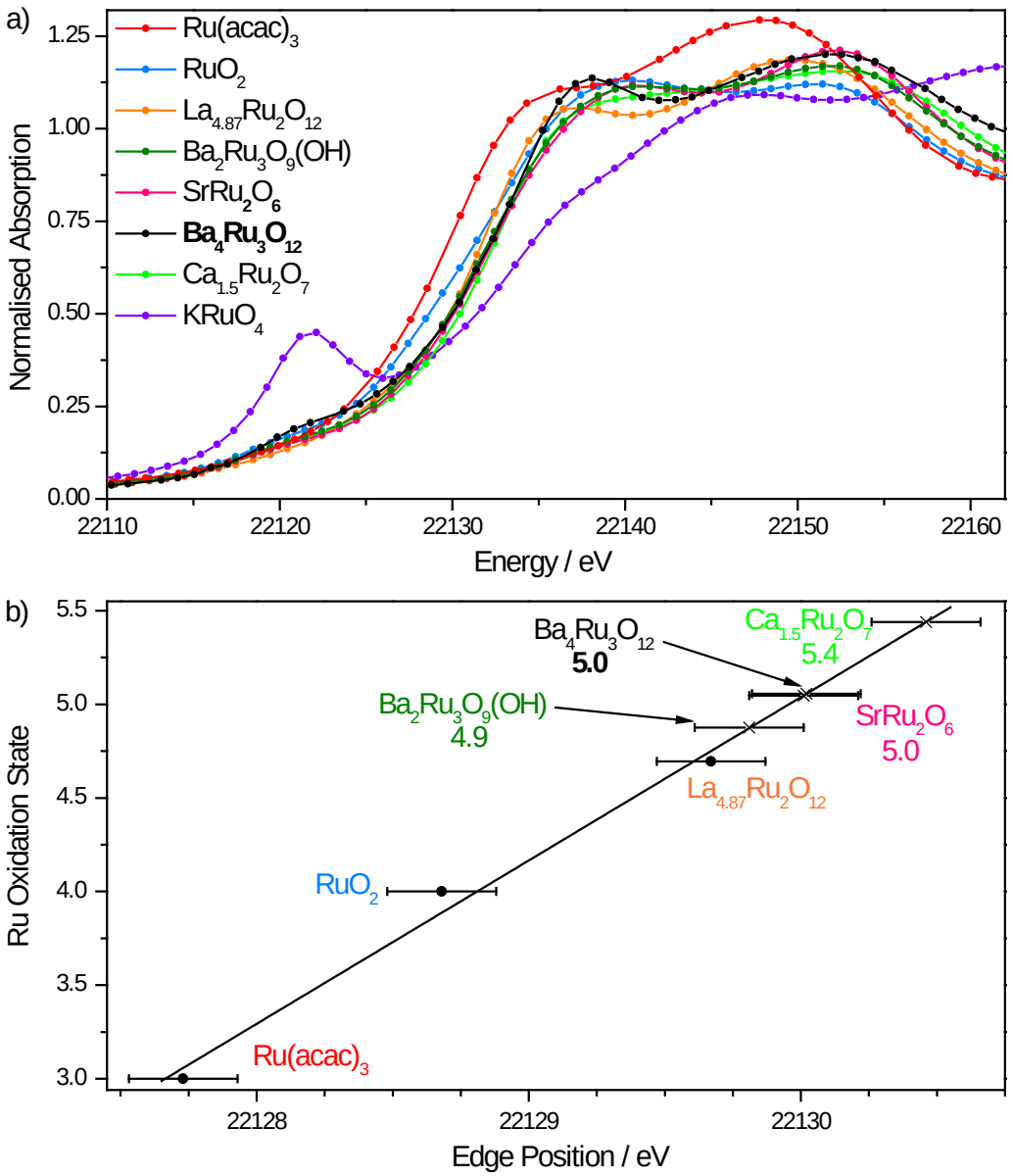

Figure 6. 35 Normalised Ru K-edge XANES spectra of $Ba_4Ru_3O_{12}$ and reference compounds with known Ru oxidation state ($[Ru^{III}(acac)_3]$, $Ru^{IV}O_2$, $La_{4.87}Ru^{4.7}{}_2O_{12}$ and $KRu^{VII}O_4$). b) A plot of edge position (defined as energy at which normalised absorption = 0.5) as a function of oxidation state, with a linear fit of reference compounds, which is used to estimate the Ru oxidation state in the pyrochlore. $KRuO_4$ is omitted as a reference due to the pre-edge feature at 22121 eV. Spectra and edge positions of $Ca_{1.5}Ru_2O_7$, $SrRu_2O_6$ and $Ba_2Ru_3O_9(OH)$ are included for comparison.

6.5.4 *Ab Initio* Structure Determination from Powder Synchrotron X-ray and Neutron Diffraction

Attempts to fit known the structures of 8H-pevovskites and related oxides – including the 8H perovskite prepared by hydrothermal synthesis $Sr_4Ru_{3.05}O_{12}$ (Figure 6. 37b)[17] – to both the X-ray diffraction pattern and neutron diffraction patterns were unsatisfactory, and so the program Fox[33] was used (using the same algorithms and parameters as were used to solve the structure of $Ba_2Ru_3O_9(OH)$, Section 6.4.4) to find a structural solution using powder neutron diffraction data collected on GEM (ISIS, U.K.). The initial model was then refined using GSAS. The structure solution provided by *ab initio* determination was determined in the space group $P6_3mc$ (Table 6. 12) using powder neutron diffraction data (Figure 6.

Table 6. 12 Refined atomic coordinates, ADPs and bond valence sums (BVS) of $Ba_4Ru_3O_{12}$ to neutron time-of-flight diffraction data (GEM banks 3 and 5); Space group $P6_3mc$; a = *5.7876(1) Å*, c = *18.7182(6) Å;* χ^2 *= 2.143;* R_{wp} *= 2.99% (2.65% and 3.21% for respective banks);* R_p *= 2.22% (1.93% and 2.57% for respective banks).*

Atom	Wyckoff	*x*	*y*	*z*	Occupancy	ADP / Å^2	BVS
Ba1	2*a*	0	0	0	1	0.002(1)	+2.36
Ba2	2*a*	0	0	0.246(1)	1	0.029(2)	+2.08
Ba3	2*b*	0.33333	0.66667	0.1302(4)	1	0.009(1)	+2.32
Ba4	2*b*	0.33333	0.66667	0.3739(7)	1	0.008(1)	+2.40
Ru1	2*b*	0.33333	0.66667	0.5639(4)	1	0.032(2)	+5.10
Ru2	2*b*	0.33333	0.66667	0.8077(3)	1	-0.003(1)	+4.52
Ru3	2*b*	0.33333	0.66667	0.9477(4)	1	0.029(2)	+4.63
O1	6*c*	0.5042(4)	0.0084(9)	0.2493(6)	1	0.0207(5)	-1.64
O2	6*c*	0.4984(7)	-0.003(1)	-0.0027(5)	1	0.0109(4)	-2.30
O3	6*c*	0.1747(4)	0.3494(9)	0.8748(2)	1	0.0111(4)	-1.98
O4	6*c*	0.1802(6)	0.360(1)	0.6183(2)	1	0.0256(7)	-1.87

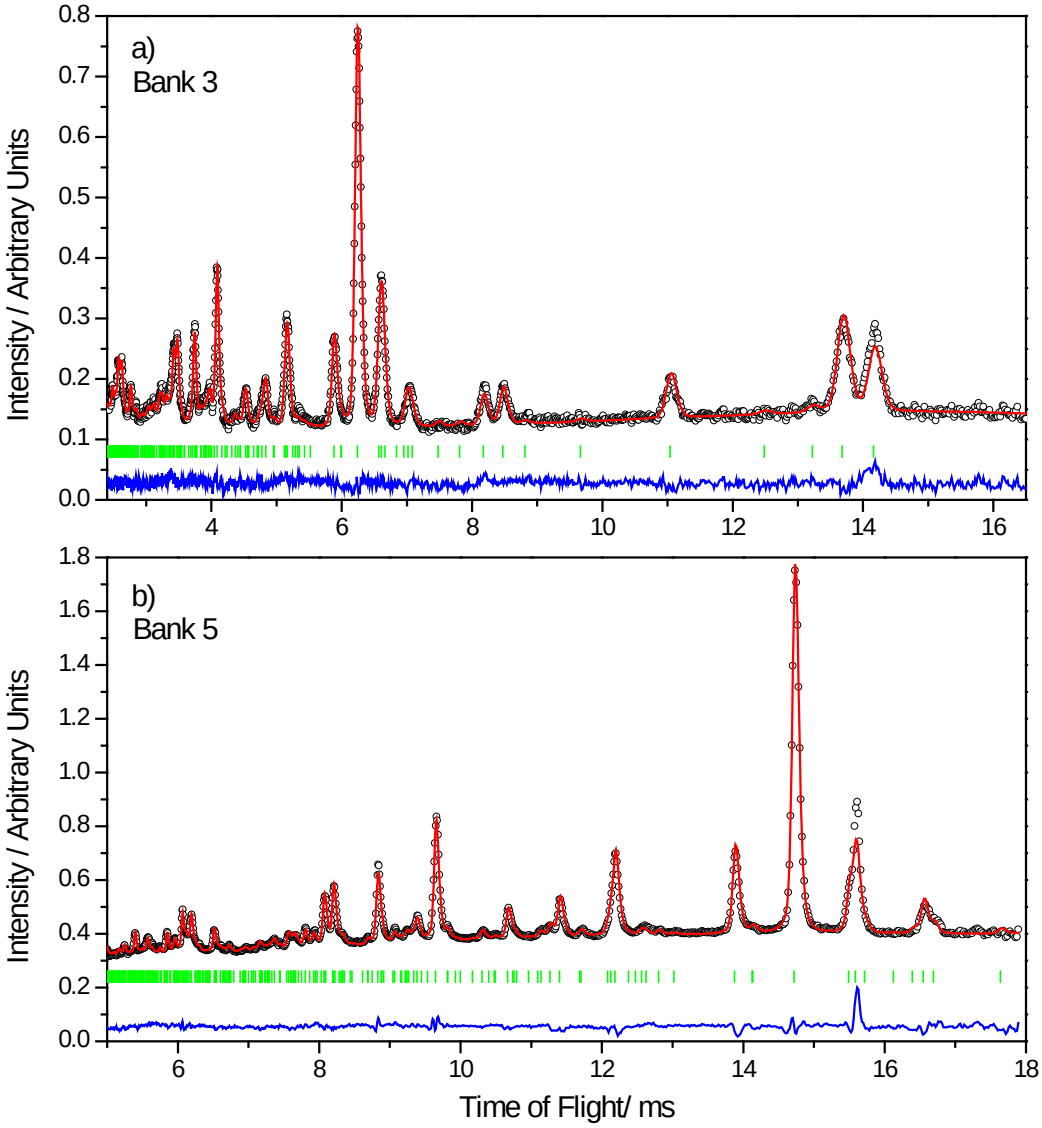

*Figure 6. 36 Rietveld refinements of $Ba_4Ru_3O_{12}$ to room temperature powder neutron diffraction data. Tick marks denote peak positions of reflections (*P63mc, a = *5.7876(1) Å,* c = *18.7182(6) Å,). a) GEM Bank 3 (mean scattering angle 2θ = 34.96°), b) GEM Bank 5 (mean scattering angle 2θ = 94.30°).*

36). The neutron diffraction data collected on GEM (ISIS) is significantly lower resolution than HR-XRD, and so the peak splitting observed by laboratory XRD (Figure 6. 30) is masked by a slightly broadened peak shape, even in the high angle detector banks (Figure 6. 36b).

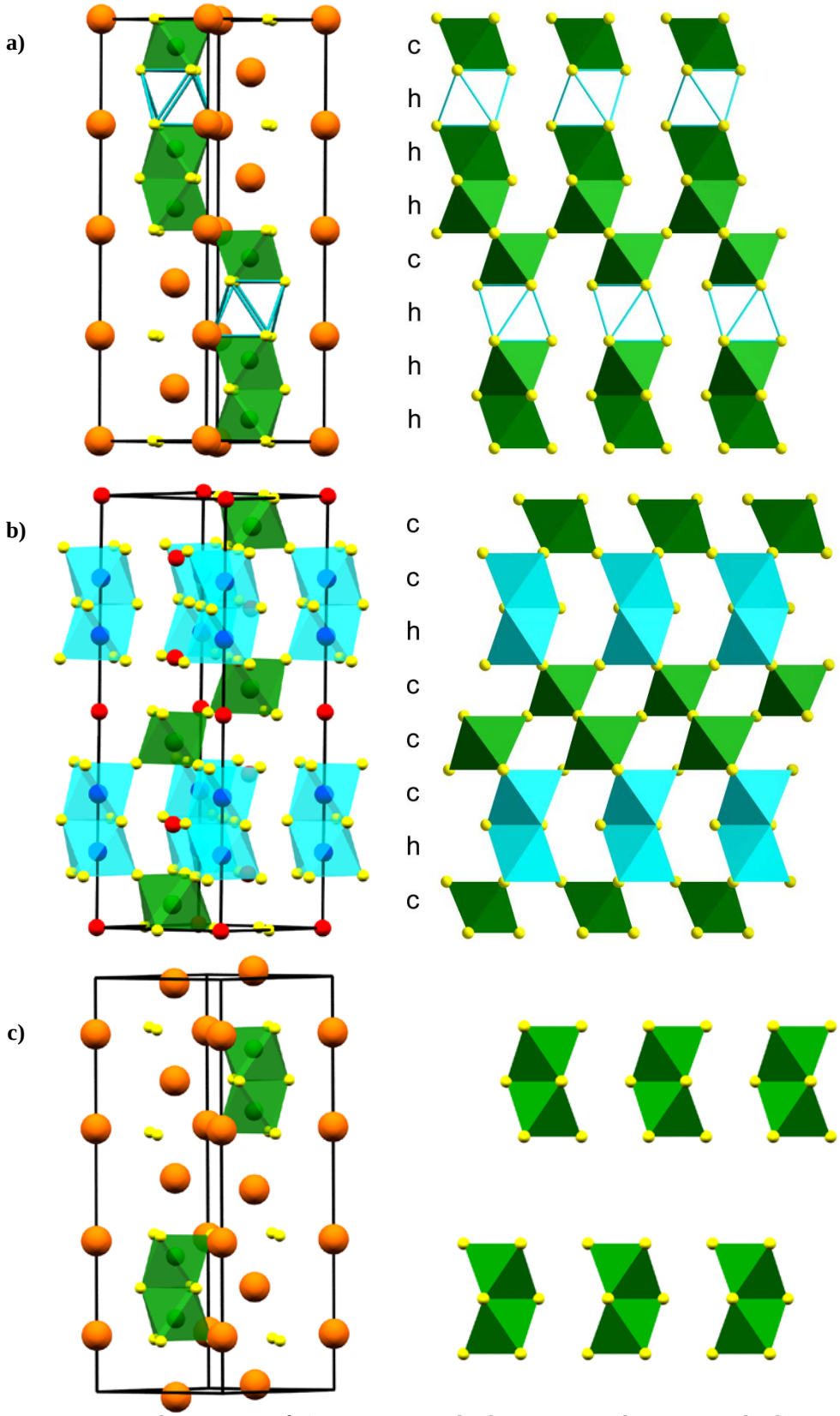

Figure 6. 37 Crystal structures of a) $Ba_4Ru_3O_{12}$ and other 8H perovskite-type oxides b) $Sr_4Ru_{3.05}O_{12}$ (an 8H-perovskite with partially filled Ru octahedra) and c) $Ba_5Ru_2O_{10}$. Ba atoms in orange, Sr atoms in red, oxygen atoms in yellow, filled RuO_6 polyhedra in green, partially occupied RuO_6 octahedra in blue. Vacant octahedra shown by blue frames.

Like other hexagonal perovskites the structure of $Ba_4Ru_3O_{12}$ consists of channels of metal atoms in the (0, 0, *z*), (⅓, ⅔, *z*) and (⅔, ⅓, *z*) columns, however in $Ba_4Ru_3O_{12}$ one of these columns (the (0, 0, *z*)) contains only Ba atoms (Figure 6. 37a). The stacking sequence $(chhh)_2$ is to the best of the author's knowledge unique and forms chains of four face-sharing octahedra, with one of those octahedra empty. The absence of a Ru atom in these octahedra makes the cell non-centrosymmetric, reducing the symmetry from $P6_3/mmc$ to $P6_3mc$. The oxide $Sr_4Ru_{3.05}O_{12}$[17] (Figure 6. 37b) has a similar composition and similar hexagonal cell lengths ($P6_3mc$; a = 5.566(4) Å; c = 18.186(5) Å) to this structural model. However, it adopts the stacking sequence common to most 8H perovskites ($(ccch)_2$) with two ~50% occupied face-sharing octahedra. The oxide $Ba_5Ru_2O_{10}$ (Figure 6. 37c)[42] can also be compared to $Ba_4Ru_3O_{12}$. They both contain Ba-only channels and face-sharing RuO_6 octahedra dimers, however, in $Ba_5Ru_2O_{10}$ these dimers are isolated and are surrounded by Ba atoms.

Bond valence sums (Equation 6. 1) of both Ba and O have values close to the expected oxidation states (+2 and -2, respectively), though again some compression of the Ba atoms coordination environments was observed and the oxygen atoms which form the vacant octahedra are under-coordinated (Table 6. 12). Ru1, Ru2 and Ru3 have bond valence sums of +5.10, +4.52 and +4.63 respectively, which are all reasonable close to +5 and are consistent with Nb(V) bond valences in the hexagonal perovskite $Ba_8CoNb_6O_{24}$.[36] The O – Ru – O bond angles (Table 6. 13) are consistant with regular octahedra with a similar degree of distortion to other ruthenium oxides.

Table 6. 13 O – Ru – O bond angles in $Ba_4Ru_3O_{12}$.

Atom 1	Atom 2	*Atom 3*	*Angle 2, 1, 3 / °*
Ru1	O4	O4	92.22(25)
	O4	O2	89.55(26)
	O4	O2	177.50(29)
	O2	O2	88.68(27)
Ru2	O1	O1	93.54(25)
	O1	O3	91.02(26)
	O1	O3	173.36(29)
	O3	O3	84.06(27)

Atom 1	Atom 2	*Atom 3*	*Angle 2, 1, 3 / °*
Ru3	O2	O2	96.96(36)
	O2	O3	89.60(33)
	O2	O3	170.12(40)
	O3	O3	83.03(31)

6.5.5 Magnetic Susceptibility Studies

The magnetic susceptibility FC $Ba_4Ru_3O_{12}$ was measured in a 1000 Oe external field (Figure 6. 38), and shows increasing χ with decreasing temperature. A Curie-Weiss fit (Equation 6. 2) in the paramagnetic region (T > 250 K) gives a Weiss temperature of -629.2(8) K, which indicates antiferromagnetic ordering of the Ru(V) moments; and a Curie constant of 1.22 emu K mol_{Ru}^{-1}. From this Curie constant the Ru μ_{eff} was calculated (Equation 6. 3), giving a value 3.13 μ_B. The average oxidation state of Ru in $Ba_4Ru_3O_{12}$ is +5.33, suggesting a mixture of d^2 and d^3 ions, which have spin only moments of 2.83 μ_B and 3.87 μ_B, respectively, and a value between these is expected.

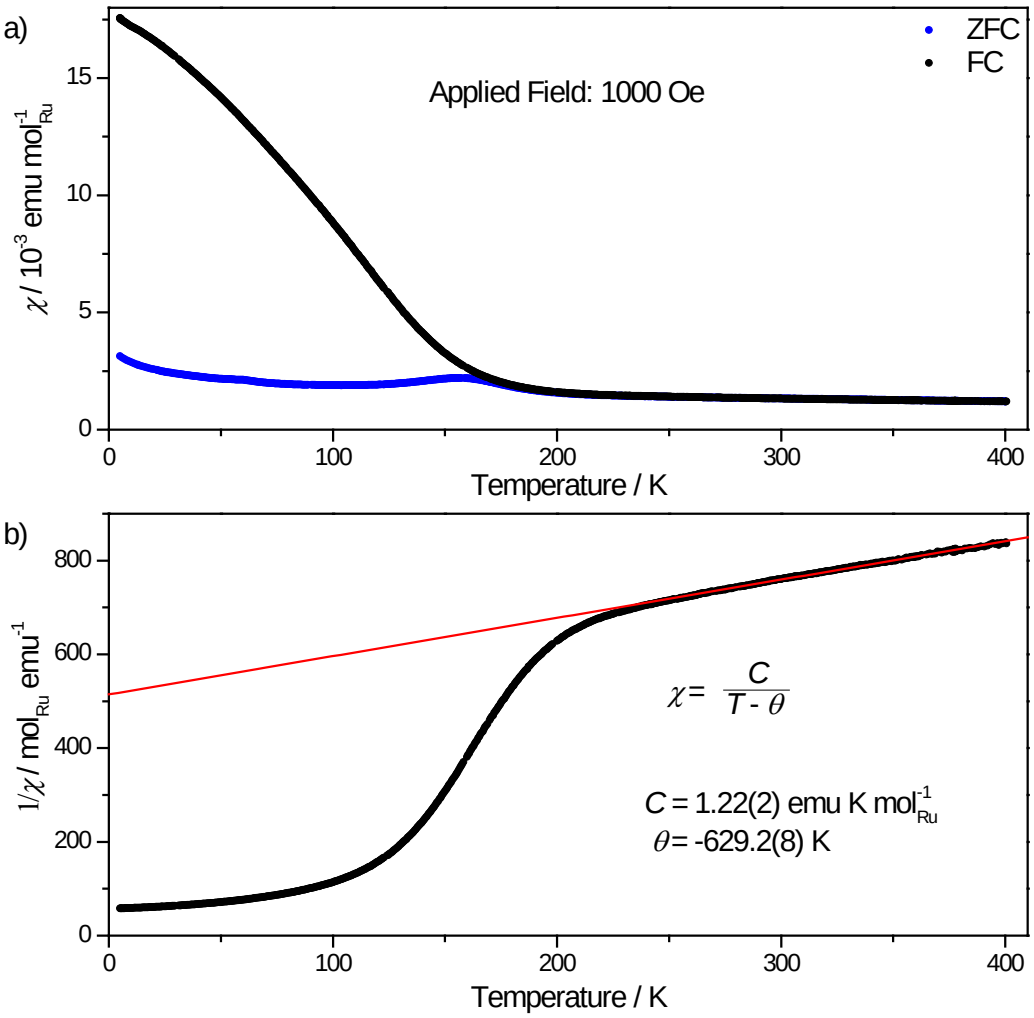

Figure 6. 38a) Field-cooled (FC) and zero field-cooled (ZFC) magnetic susceptibility as a function of temperature of $Ba_4Ru_3O_{12}$ in a 1000 Oe applied field. b) A linear Curie-Weiss fit to inverse susceptibility in paramagnetic region of $Ba_4Ru_3O_{12}$ as a function of temperature.

6.6 Discussion

The pyrochlore phase $Ca_{1.5}Ru_2O_7$ is unusual in its high level of *A*-site deficiency, though this is not unprecedented. Many pyrochlores are known to contain some degree of non-stoichiometry on the *A*-site, though it is often accompanied by oxide vacancies.[22,44] In the extreme case this can lead to compositions of the form $ABB'O_6$, such as $A(Mo^{VI}Sb^{V})O_6$ (*A* = Rb, Cs).[45] Although no H was detected by IR or difference Fourier mapping, a small degree of disordered H from structural OH or H_2O would have been difficult to detect. However, the oxidation state determined from XANES and bond valence sums was significantly higher than 5, which is consistent with this finding.

$SrRu_2O_6$ is a rare example of a magnetic $PbSb_2O_6$-type structure. Other examples contain transition metals on the 1*a* site, such as $PdAs_2O_6$;[46] or have first-row (3*d*) transition metals on the 2*d* site, as is the case in UM_2O_6 (*M* = Cr^{3+},[47,48] V^{3+},[47] Fe^{3+},[48] (Mn^{4+}/Ni^{2+})[48]). The only investigation of magnetic structure by neutron diffraction of any of these materials was on UCr_2O_6 at 4.2 K, where Cr^{3+} (a d^3 ion like Ru^{5+}) aligns antiferromagnetically in the *ab* plane with spins pointing into this plane and it is unclear as to whether any ordering in the *c*-direction occurs. This is unlike $SrRu_2O_6$ where the moments are perpendicular to the *ab* plane and order antiferromagnetically in both the *ab* plane and in the *c*-direction.

Particularly noteworthy is the extraordinarily high ordering temperature of the Ru^{5+} ions (Néel temperature: 563 K). The only 4*d* metal with a higher ordering temperature in an oxide found by a survey of the literature was Tc^{4+} in the perovskite $SrTcO_3$,[49] where a Néel temperature of 750 °C (1023 K) was observed. This

magnetic persistence was explained by electronic structure calculations as being due to the proximity of the part-filled t_{2g} shells to an itinerant-to-localised transition.[50]

The Ru effective moment in the oxides $Ca_{1.5}Ru_2O_7$, $SrRu_2O_6$ and $Ba_2Ru_3O_9(OH)$ was in each case (0.36 μ_B, 1.43 μ_B and 0.73 μ_B; respectively) significantly smaller than the spin-only values; this can be attributed to covalency in the Ru – O bonds[51] due to strong spin orbit coupling not seen in 3*d* metal oxides.[52] The low effective moment could also be a result of the failure of the Curie-Weiss law to adequately model the magnetic data, possibly due to electron delocalisation, or changing electron configuration as a function of temperature, as observed in 5*d* metal oxides.[53,54]

6.7 Conclusions

In this chapter the hydrothermal synthesis of four new alkaline earth ruthenium oxides has been presented:

- $Ca_{1.5}Ru_2O_7$, an *A*-site deficient pyrochlore;
- $SrRu_2O_6$, adopting a layered hexagonal structure analogous to that in $PbSb_2O_6$;
- $Ba_2Ru_3O_9(OH)$, adopting a previously unreported orthorhombic structure, containing puckered layers of corner and edge sharing RuO_6 octahedra separated by layers of Ba atoms.
- $Ba_4Ru_3O_{12}$, an 8H hexagonal perovskite containing a previously unreported stacking sequence and vacant octahedral sites.

All of these oxides were synthesised by permutations of a simple hydrothermal reaction of just two commercially available precursors with no additional mineraliser, and contain Ru in an oxidation state of ≥ 5.

All these oxides are metastable (as demonstrated by *in situ* powder XRD), which explains why none has been previously synthesised by solid-state synthesis or other high temperature routes.

In addition to studying the magnetic properties, these oxides were prepared with the intention of investigating their catalytic properties. An initial investigation at JMTC found that like most ruthenium oxides, they are unstable under acidic conditions, making them inappropriate for electrocatalysis under these conditions. However, the possibility of use for heterogeneous catalysis is currently being explored.

6.8 References

(1) Dussarrat, C.; Grasset, F.; Bontchev, R.; Darriet, J. *J. Alloys Compd.* **1996**, *233*, 15.
(2) Grasset, F.; Dussarrat, C.; Darriet, J. *J. Mater. Chem.* **1997**, *7*, 1911.
(3) Kurzman, J. A.; Misch, L. M.; Seshadri, R. *Dalton Trans.* **2013**, *42*, 14653.
(4) Stitzer, K. E.; Smith, M. D.; Gemmill, W. R.; zur Loye, H.-C. *J. Am. Chem. Soc.* **2002**, *124*, 13877.
(5) Park, S.; Shao, Y.; Liu, J.; Wang, Y. *Energy Environ. Sci.* **2012**, *5*, 9331.
(6) Zen, J. M.; Manoharan, R.; Goodenough, J. B. *J. Appl. Electrochem.* **1992**, *22*, 140.
(7) Abate, C.; Esposito, V.; Duncan, K.; Nino, J. C.; Gattia, D. M.; Wachsman, E. D.; Traversa, E. *J. Am. Ceram. Soc.* **2010**, *93*, 1970.
(8) Ashcroft, A. T.; Cheetham, A. K.; Foord, J. S.; Green, M. L. H.; Grey, C. P.; Murrell, A. J.; Vernon, P. D. F. *Nature* **1990**, *344*, 319.
(9) Over, H. *Chem. Rev.* **2012**, *112*, 3356.
(10) Atta, N. F.; Galal, A.; Ali, S. M. *Int. J. Electrochem. Sci.* **2012**, *7*, 725.
(11) Ishida, K.; Mukuda, H.; Kitaoka, Y.; Asayama, K.; Mao, Z. Q.; Mori, Y.; Maeno, Y. *Nature* **1998**, *396*, 658.
(12) Bouchard, R. J.; Gillson, J. L. *Mater. Res. Bull.* **1972**, *7*, 873.
(13) Longo, J. M.; Raccah, P. M.; Goodenough, J. B. *J. Appl. Phys.* **1968**, *39*, 1327.
(14) Darton, R. J.; Turner, S. S.; Sloan, J.; Lees, M. R.; Walton, R. I. *Cryst. Growth Des.* **2010**, *10*, 3819.
(15) Yao, L. R.; Wang, D.; Peng, W.; Hu, W. W.; Yuan, H. M.; Feng, S. H. *Sci. China-Chem.* **2011**, *54*, 941.
(16) Renard, C.; Daviero-Minaud, S.; Abraham, F. *J. Solid State Chem.* **1999**, *143*, 266.
(17) Renard, C.; Daviero-Minaud, S.; Huve, M.; Abraham, F. *J. Solid State Chem.* **1999**, *144*, 125.
(18) Munenaka, T.; Sato, H. *J. Phys. Soc. Jpn.* **2006**, *75*, 103801.
(19) Ogawa, T.; Sato, H. *J. Alloys Compd.* **2004**, *383*, 313.
(20) Sato, H.; Watanabe, T.; Yamaura, J.-I. *Solid State Commun.* **2004**, *131*, 707.
(21) Taniguchi, T.; Munenaka, T.; Sato, H. In *Highly Frustrated Magnetism 2008*; Journal of Physics: Conference Series: Braunschweig, Germany, 2009; Vol. 145, p 012017.
(22) Subramanian, M. A.; Aravamudan, G.; Subba Rao, G. V. *Prog. Solid State Chem.* **1983**, *15*, 55.
(23) Arčon, I.; Benčan, A.; Kodre, A.; Kosec, M. *X-Ray Spectrom.* **2007**, *36*, 301.
(24) Planas, N.; Vigara, L.; Cady, C.; Miró, P.; Huang, P.; Hammarström, L.; Styring, S.; Leidel, N.; Dau, H.; Haumann, M.; Gagliardi, L.; Cramer, C. J.; Llobet, A. *Inorg. Chem.* **2011**, *50*, 11134.
(25) Brese, N. E.; O'Keeffe, M. *Acta Crystallogr. Sect. B* **1991**, *47*, 192.
(26) Gardner, J. S.; Gingras, M. J. P.; Greedan, J. E. *Rev. Mod. Phys.* **2010**, *82*, 53.
(27) Deboer, B. G.; Young, R. A.; Sakthivel, A. *Acta Crystallogr. Sect. C* **1994**, *50*, 476.
(28) Kumada, N.; Takei, T.; Kinomura, N.; Wang, H.; Zhang, X.; Yan, H. *Mater. Res. Bull.* **2005**, *40*, 1166.

(29) Parkinson, N. G.; Hatton, P. D.; Howard, J. A. K.; Ritter, C.; Chien, F. Z.; Wu, M.-K. *J. Mater. Chem.* **2003**, *13*, 1468.
(30) Bolzan, A. A.; Fong, C.; Kennedy, B. J.; Howard, C. J. *Acta Crystallogr. Sect. B* **1997**, *53*, 373.
(31) Hong, S.-T.; Sleight, A. W. *J. Solid State Chem.* **1997**, *128*, 251.
(32) Le Bail, A. http://www.cristal.org/iniref/tutorial/part23a.html, 1997.
(33) Favre-Nicolin, V.; Cerny, R. *J. Appl. Crystallogr.* **2002**, *35*, 734.
(34) Carim, A. H.; Dera, P.; Finger, L. W.; Mysen, B.; Prewitt, C. T.; Schlom, D. G. *J. Solid State Chem.* **2000**, *149*, 137.
(35) Lufaso, M. W. *Chem. Mater.* **2004**, *16*, 2148.
(36) Mallinson, P. M.; Allix, M. M. B.; Claridge, J. B.; Ibberson, R. M.; Iddles, D. M.; Price, T.; Rosseinsky, M. J. *Angew. Chem. Int. Ed.* **2005**, *44*, 7733.
(37) Battle, P. D.; Kim, S. H.; Powell, A. V. *J. Solid State Chem.* **1992**, *101*, 161.
(38) Lightfoot, P.; Battle, P. D. *J. Solid State Chem.* **1990**, *89*, 174.
(39) Darriet, J.; Subramanian, M. A. *J. Mater. Chem.* **1995**, *5*, 543.
(40) Van Tendeloo, G.; Amelinckx, S.; Darriet, B.; Bontchev, R.; Darriet, J.; Weill, F. *J. Solid State Chem.* **1994**, *108*, 314.
(41) Abakumov, A. M.; Shpanchenko, R. V.; Antipov, E. V.; Lebedev, O. I.; Tendeloo, G. V.; Amelinckx, S. *J. Solid State Chem.* **1998**, *141*, 492.
(42) Dussarrat, C.; Fompeyrine, J.; Darriet, J. *Eur. J. Solid State Inorg. Chem.* **1994**, *31*, 289.
(43) Donohue, P. C.; Katz, L.; Ward, R. *Inorg. Chem.* **1965**, *4*, 306.
(44) Babel, D.; Pausevang, G.; Werner, V. *Z. Naturforsch., B: Chem. Sci.* **1967**, *22*, 1219.
(45) Castro, A.; Rasines, I.; Sanchez-Martos, M. C. *J. Mater. Sci. Lett.* **1987**, *6*, 1001.
(46) Orosel, D.; Jansen, M. *Z. Anorg. Allg. Chem.* **2006**, *632*, 1131.
(47) Collomb, A.; Gondrand, M.; Lehmann, M. S.; Capponi, J. J.; Joubert, J. C. *J. Solid State Chem.* **1976**, *16*, 41.
(48) Collomb, A.; Capponi, J. J.; Gondrand, M.; Joubert, J. C. *J. Solid State Chem.* **1978**, *23*, 315.
(49) Rodriguez, E. E.; Poineau, F.; Llobet, A.; Kennedy, B. J.; Avdeev, M.; Thorogood, G. J.; Carter, M. L.; Seshadri, R.; Singh, D. J.; Cheetham, A. K. *Phys. Rev. Lett.* **2011**, *106*, 067201.
(50) Mravlje, J.; Aichhorn, M.; Georges, A. *Phys. Rev. Lett.* **2012**, *108*, 197202.
(51) Hubbard, J.; Marshall, W. *Proc. Phys. Soc.* **1965**, *86*, 561.
(52) Witczak-Krempa, W.; Chen, G.; Kim, Y. B.; Balents, L. *Annu. Rev. Condens. Matter Phys.* **2014**, *5*, 57.
(53) Sardar, K.; Ball, S. C.; Sharman, J. D. B.; Thompsett, D.; Fisher, J. M.; Smith, R. A. P.; Biswas, P. K.; Lees, M. R.; Kashtiban, R. J.; Sloan, J.; Walton, R. I. *Chem. Mater.* **2012**, *24*, 4192.
(54) Sardar, K.; Fisher, J.; Thompsett, D.; Lees, M. R.; Clarkson, G. J.; Sloan, J.; Kashtiban, R. J.; Walton, R. I. *Chem. Sci.* **2011**, *2*, 1573.

Appendix

Appendix 1: Diffraction Patterns of $Ce_{1-x}Sb_xO_{2-\delta}$ made using $SbCl_3$ and $NaSbO_3$ as a precursor.

See next page.

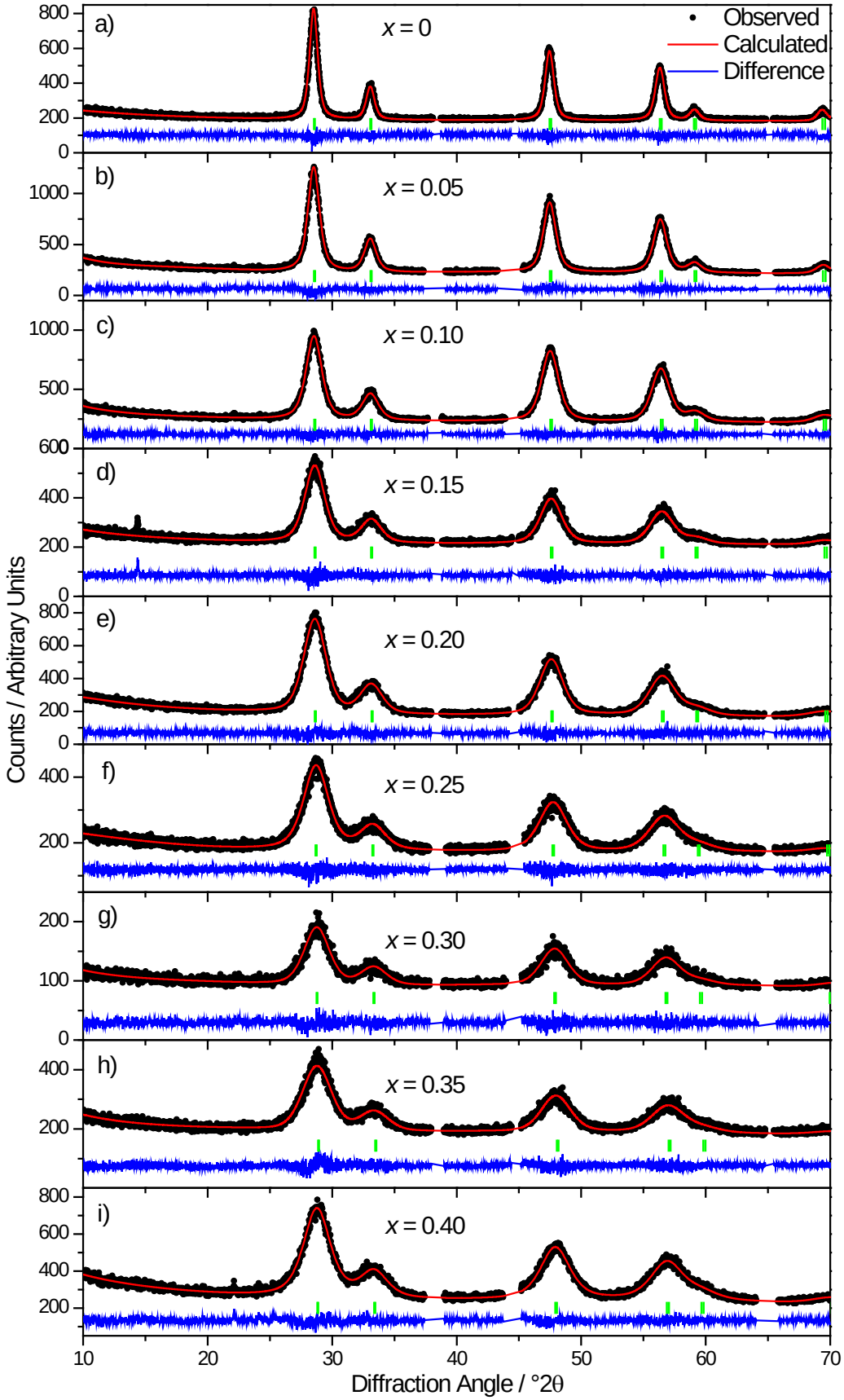

Figure A. 1) Le Bail fits to powder XRD data (λ = 1.54056 Å) of $Ce_{1-x}Sb_xO_{2-\delta}$ (0.00 ≤ x ≤ 0.40; respectively) made hydrothermally in NaOH solution (where $NaSbO_3$ is the Sb reagent).

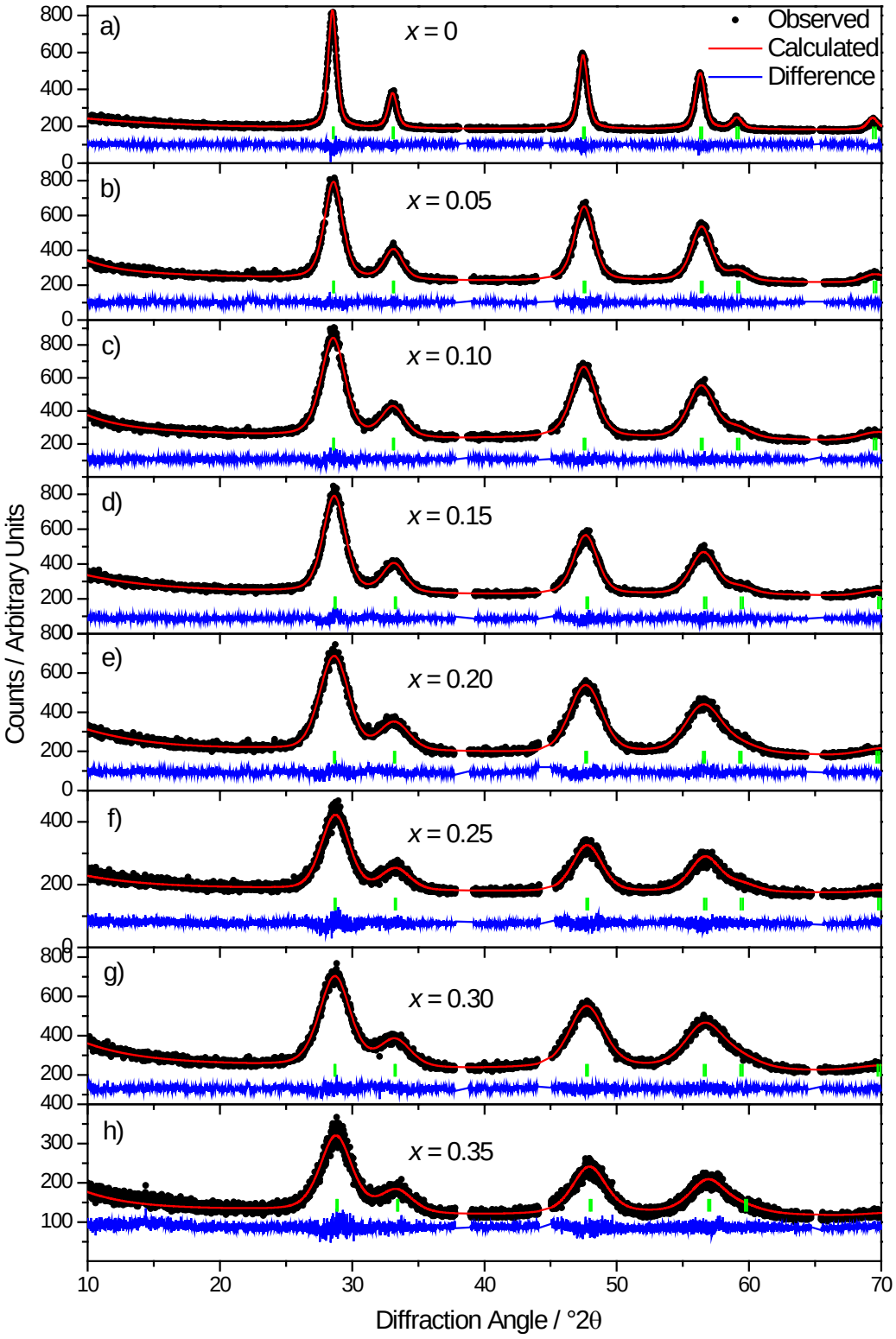

Figure A. 2) Le Bail fits to powder XRD data (λ = 1.54056 Å) of $Ce_{1-x}Sb_xO_{2-\delta}$ (0.00 ≤ x ≤ 0.35; respectively) made hydrothermally in NaOH solution (where $SbCl_3$ is the Sb reagent).

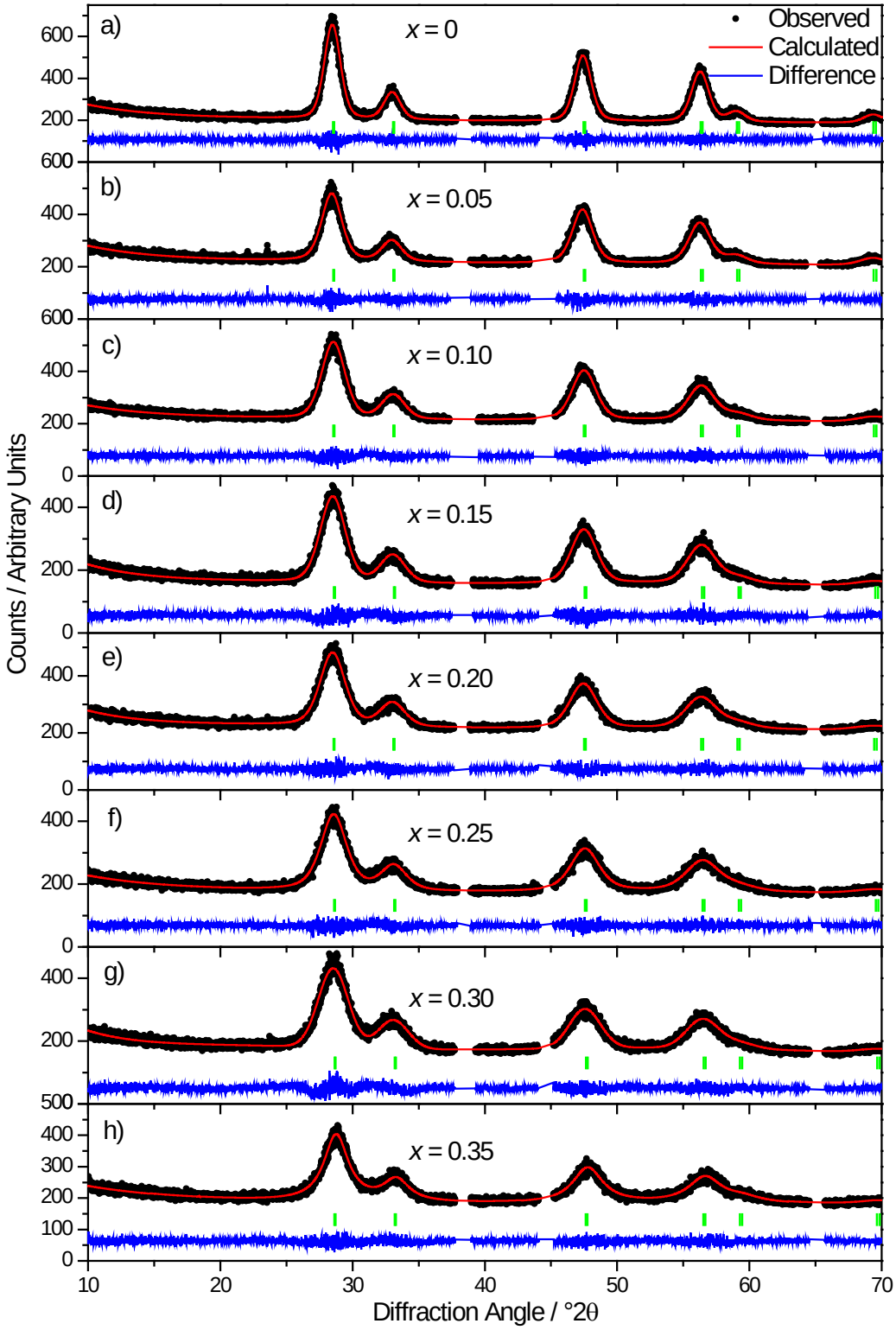

Figure A. 3) Le Bail fits to powder XRD data (λ = 1.54056 Å) of $Ce_{1-x}Sb_xO_{2-\delta}$ (0.00 ≤ x ≤ 0.35; respectively) made hydrothermally in NH_4OH solution (where $NaSbO_3$ is the Sb reagent).

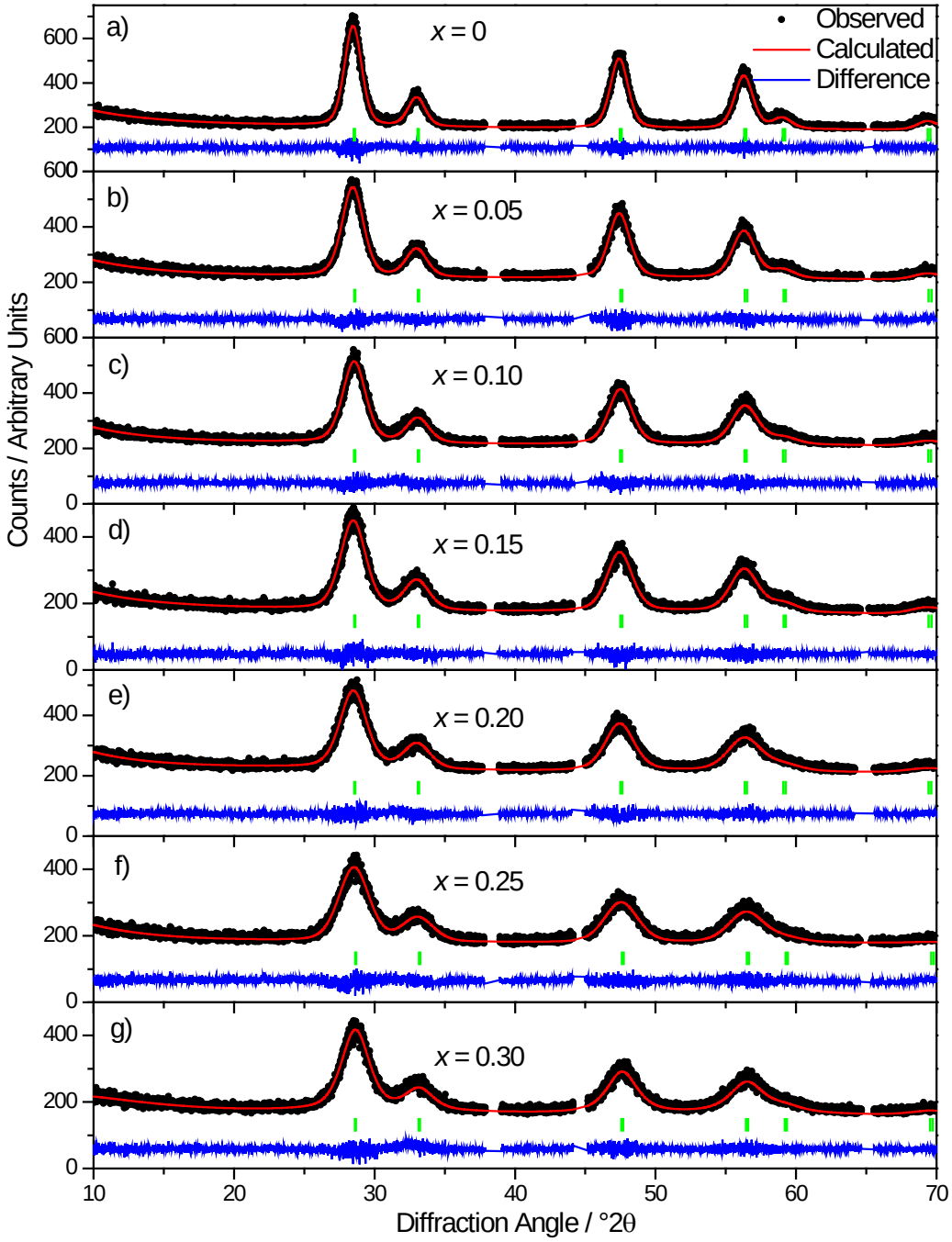

Figure A. 4 Le Bail fits to powder XRD data (λ = 1.54056 Å) of $Ce_{1-x}Sb_xO_{2-\delta}$ (0.00 ≤ x ≤ 0.30; respectively) made hydrothermally in NH_4OH solution (where $SbCl_3$ is the Sb reagent).

Appendix 2: ICP-OES Elemental Analysis of "$Ce_{0.70}Nb_{0.30}O_{2-\delta}$" Made Hydrothermally in NaOH Solution.

Table A. 1 ICP-OES elemental analysis by mass of $Ce_{0.70}Nb_{0.30}O_{2-\delta}$ (nominal composition) made hydrothermally in NaOH. Non-metals, Os and actinides were not tested for, and Na, Nb and Ce contents available in Table 3.2.

Analyte	Concentration / ppm
Li	3
Al	30
Si	< 50
Ca	60
V	2
Mn	2
Fe	40
Co	1
Cu	14
Zn	5
Sr	1
Mo	1
Ru	5
Pd	12
Ba	2
La	15
Eu	1
Tb	25
Ta	11
Ir	4
Hg	8
Pb	1
Bi	8